

Determination of the Gluon Polarisation from Open Charm Production at COMPASS

Susanne Koblitz



Institut für Kernphysik,
Johannes Gutenberg-
Universität Mainz

Fachbereich Physik der Johannes-Gutenberg Universität Mainz

Dissertation
zur Erlangung des Grades
„Doktor der Naturwissenschaften“

**Determination of the Gluon Polarisation
from Open Charm Production
at COMPASS**

vorgelegt von
Susanne Koblitz, geb. Hellwig
geboren am 25. Juni 1980 in Bonn

Oktober 2008

Berichtersteller

Tag der Prüfung 27. Januar 2009

Abstract

One of the main goals of the COMPASS experiment at CERN is the determination of the gluon polarisation in the nucleon, $\Delta G/G$. It is determined from spin asymmetries in the scattering of $160\text{ GeV}/c$ polarised muons on a polarised LiD target. The gluon polarisation is accessed by the selection of photon-gluon fusion (PGF) events. The PGF-process can be tagged through hadrons with high transverse momenta or through charmed hadrons in the final state. The advantage of the open charm channel is that, in leading order, the PGF-process is the only process for charm production, thus no physical background contributes to the selected data sample.

This thesis presents a measurement of the gluon polarisation $\langle\Delta g/g\rangle$ from the COMPASS data taken in the years 2002-2004. In the analysis, charm production is tagged through a reconstructed D^0 -meson decaying in $D^0 \rightarrow K^- \pi^+$ (and charge conjugates). The reconstruction is done on a combinatorial basis. The background of wrong track pairs is reduced using kinematic cuts to the reconstructed D^0 -candidate and the information on particle identification from the Ring Imaging Cerenkov counter. In addition, the event sample is separated into D^0 -candidates, where a soft pion from the decay of the D^* -meson to a D^0 -meson, is found, and the D^0 -candidates without this tag. Due to the small mass difference between D^* -meson and D^0 -meson the signal purity of the D^* -tagged sample is about 7 times higher than in the untagged sample.

The gluon polarisation $\langle\Delta g/g\rangle$ is measured from the event asymmetries for the for the different spin configurations of the COMPASS target. To improve the statistical precision of the final results, the events in the final sample are weighted. The use of a signal and a background weight allows the separation of $\langle\Delta g/g\rangle$, and a possible asymmetry in the combinatorial background.

This method results in an average value of the gluon polarisation in the x -range covered by the data. For the COMPASS data from 2002-2004, the resulting value of the gluon polarisation is $\langle\Delta g/g\rangle = -0.47 \pm 0.44$ (stat.) ± 0.15 (syst.), at an average $x = 0.11^{+0.11}_{-0.05}$ and a scale of $\mu^2 = 13\text{ GeV}^2$. This result points to small or negative values of $\Delta G/G(x)$ around a value of $x \sim 0.1$, which could point to a small gluon polarisation in the nucleon. The result is statistically compatible with the existing measurements of $\langle\Delta g/g\rangle$ in the high- p_t channel. Compared to these, the open charm measurement has the advantage of a considerably smaller model dependence.

Zusammenfassung

Ein Hauptziel des COMPASS Experiments am CERN ist die Bestimmung der Gluonpolarisation im Nukleon, $\Delta G/G$. Sie kann aus Doppelspinasymmetrien in der Streuung von polarisierten Muonen mit einem Strahlimpuls von $160 \text{ GeV}/c$ an einem polarisierten LiD-Target bestimmt werden. Durch die Selektion von Photon-Gluon-Fusionsereignissen (PGF) bekommt man Zugriff auf die polarisierte Gluonverteilung im Nukleon. Der PGF-Prozess kann über Hadronpaare mit hohem Transversalimpuls oder charmhaltigen Hadronen im Endzustand nachgewiesen werden. Der Vorteil der offenen Charmproduktion ist, dass in führender Ordnung der PGF-Prozess der einzige zur Charmproduktion beitragende Prozess ist. Untergrund von anderen physikalischen Prozessen tritt in den selektierten Daten nicht auf.

In dieser Arbeit wird eine Messung der Gluonpolarisation $\langle \Delta g/g \rangle$ mit den COMPASS-Daten der Jahre 2002-2004 vorgestellt. In der Analyse wird die Charmproduktion über ein rekonstruiertes D^0 -Meson nachgewiesen, das über den Kanal $D^0 \rightarrow K^- \pi^+$ (sowie den ladungskonjugierten Kanal) zerfällt. Die Rekonstruktion beruht auf der Kombination aller möglichen Spurpaare. Um den Untergrund von falschen Spurpaaren zu unterdrücken, werden Schnitte auf die D^0 -Kinematik sowie die Teilchenidentifikation mit dem „Ring-Imaging-Cerenkov“-Detektor genutzt. Darüber hinaus werden die Spurpaare in D^0 -Kandidaten, bei denen ein zusätzliches langsames Pion aus einem D^* -Zerfall in ein D^0 nachgewiesen werden konnte, und in D^0 -Kandidaten ohne diesen Nachweis unterteilt. Durch den geringen Massenunterschied zwischen D^* -Meson und D^0 -Meson ist die Reinheit des Signals in den Daten mit dem D^* -Nachweis sieben Mal größer als ohne den Nachweis.

Die Gluonpolarisation $\langle \Delta g/g \rangle$ wird aus den Zählratenasymmetrien für die verschiedenen Spineinstellungen des COMPASS-Targets bestimmt. Um die statistische Signifikanz des Ergebnisses zu verbessern, werden gewichtete Ereignisse verwendet. Durch die Verwendung von Signal- und Untergrundgewichten kann in der Messung zwischen der Gluonpolarisation $\langle \Delta g/g \rangle$ und einer möglichen Untergrundasymmetrie unterschieden werden.

Das Ergebnis der Messung ist ein Mittelwert für die Gluonpolarisation in dem von den Daten abgedeckten x -Bereich. Für die COMPASS-Daten aus den Jahren 2002-2004 ergibt sich ein Wert von $\langle \Delta g/g \rangle = -0.47 \pm 0.44 (\text{stat.}) \pm 0.15 (\text{syst.})$ für die Gluonpolarisation bei einem mittleren Impulsbruchteil von $x = 0.11^{+0.11}_{-0.05}$ und einer harten Skala von $\mu^2 = 13 \text{ GeV}^2$. Dieses Ergebnis deutet auf eine kleine oder negative Gluonpolarisation bei x ungefähr $x \sim 0.1$ hin, was als Hinweis gedeutet werden könnte, dass die Gluonpolarisation im Nukleon insgesamt klein ist. Das Ergebnis ist statistisch mit den präziseren Messungen über Hadronenpaare mit hohem Transversalimpuls kompatibel. Gegenüber diesen Messungen hat die „open charm“-Messung den Vorteil, erheblich weniger von Modellen abzuhängen.

Contents

Introduction	1
1 The spin structure of the nucleon	3
1.1 The nucleon structure in lepton-nucleon scattering	3
1.2 Inclusive polarised lepton-nucleon scattering	11
1.3 Measurements of the gluon polarisation	17
1.3.1 Polarised lepton-nucleon scattering	17
1.3.2 Polarised proton-proton scattering	20
1.4 Open Charm production in COMPASS	23
2 The COMPASS Experiment	27
2.1 The Muon Beam	27
2.2 The Polarised Target	30
2.3 The Spectrometer	32
2.4 The Ring Imaging Cerenkov Detector	35
2.5 The Data Acquisition System	36
2.6 Changes to the Spectrometer after 2004	37
3 The Trigger System in the Runs 2006 and 2007	39
3.1 The COMPASS Muon Trigger	39
3.1.1 The Hodoscope Systems	40
3.1.2 The Calorimetric Triggers	43
3.1.3 The Veto System	45
3.2 The Introduction of ECAL1 to the spectrometer	46
3.2.1 The Electromagnetic Calorimeter ECAL1	46
3.2.2 The Effect of ECAL1 on the Trigger	46
3.2.3 The ECAL1 trigger	54
3.3 Changes to the Veto System	57
4 Data Reconstruction and Stability Controlling	59
4.1 Data Reconstruction	59
4.1.1 Spectrometer Tracking	60
4.1.2 Cluster Reconstruction in the Calorimeters	62

4.1.3	Particle Identification	62
4.1.4	Event Reconstruction	65
4.2	The Detector Performance	67
4.2.1	Instabilities in the Detector Performance	67
4.2.2	Influence of individual detector	70
4.2.3	False asymmetries from instabilities	73
4.3	Procedures for stability controlling	74
4.3.1	Detection of bad spills	74
4.3.2	Data grouping	76
5	Reconstruction of D-mesons	79
5.1	Event Selection	81
5.2	Reconstruction of D -meson candidates	82
5.3	The D^* -tag	84
5.4	Background Suppression through Kinematics	85
5.5	The Use of Particle Identification	88
5.6	The final spectra	91
6	Cross-section for D^*-Production in COMPASS	95
6.1	The Luminosity Measurement	96
6.1.1	Target Thickness	96
6.1.2	Measuring the Muon Flux	97
6.1.3	Dead-times in Data Taking	98
6.2	Determination of the Acceptance Factor	99
6.3	Determination of the Number of Reconstructed D^*	102
6.4	The Resulting Cross Section	104
7	Determination of the Gluon Polarisation	107
7.1	Properties of the final data set	107
7.2	Measurement of the gluon polarisation	109
7.3	Observables needed for the measurement	113
7.3.1	Determination of the analysing power	114
7.3.2	Parametrisation of the signal strength	117
7.4	False Asymmetries	123
7.5	Result for the gluon polarisation	125
	Summary	131
	References	133

Introduction

Ever since the discovery in the 1960s that protons and neutrons, the constituents of the atomic nuclei, were themselves composed particles, their structure was the subject of intense investigations. The development of theoretical models describing the nucleon structure and the experimental efforts to measure its compositions are progressing in parallel.

The picture of the nucleon changed from a particle composed of exactly three quarks over the model of a particle composed of many quarks to the current model, that not only predicts quarks but also gluons as constituents of the nucleon. The current model, which is based on the quantum-chromo-dynamics, the quantum field theory of the strong interaction, describes the nucleon as a composition of a uncountable number of particles. Besides the three valence quarks, that are needed to explain the baryon number and the electrical and colour charge of the nucleon, the model predicts a large amount of so-called “sea-quarks” and gluons in the nucleon. The quarks and gluons are in constant interaction with each other, where the quarks emit gluons and the gluons convert to quark-antiquark pairs. Thus, the nucleon structure cannot be described by a static picture.

In contrast, the properties of the nucleon such as the electrical charge or the momentum are static quantities and show no dependence on the exact configuration of the nucleon’s content at a particular moment. It is therefore impossible to determine the contribution of one individual quark or gluon to the different properties of the nucleon. Instead, it becomes more interesting to investigate the contribution of ensembles of constituents, such as “valence quarks” or gluons. This is achieved through so-called “sum-rules”, that relate individual properties to integrated contributions of ensembles of quarks or gluons, called “sums”. These “sums” can be accessed through measurements of high-energetic scattering experiments that resolve the sub-structure of nucleons.

This thesis addresses the question of the spin-composition of the nucleon. The proton spin was first measured in 1927 (Demison) and its spin quantum number of $\frac{1}{2}$ * is well established. The composition of the spin projection, S_z , of the nucleon can be formulated by

$$S_z = \frac{1}{2} = \frac{1}{2}\Delta\Sigma + \Delta G + L \quad .$$

*Conventions used in this thesis:

- In this thesis, $\hbar = 1$ and $c = 1$ is used.
- If no explicit indication is given, all references to particles given in this thesis implicitly include the corresponding antiparticles.

where $\frac{1}{2}\Delta\Sigma$ and ΔG are the sums of the contributions from the spins of quarks and gluons and L corresponds to the contribution from orbital angular momentum of the nucleon's constituents. But, so far, so far no definite answer can be given to questions on the size of these three contributions. Before the first measurements were performed, it was believed that the contribution from the quark spins would add up to the full nucleon spin, similarly to the electrical charge. However, measurements have shown, that the contribution from quarks is not large enough to account for the entire nucleon spin. At the moment, different experiments are focussing on a precise determination of the contribution from the gluon spin.

In the past, high-energetic lepton-nucleon collisions have proven to be the most successful probe for the nucleonic sub-structure. Our current model for the nucleon is essentially build on the results of many lepton-nucleon scattering experiments. These experiments provide two ways to access the the gluon contribution in the nucleon. The scaling violation observed in the Q^2 -dependence of measured structure functions provided a first access to the role of gluons. A deeper understanding of the gluon contribution is achieved through measurements of interactions with a direct participation of the gluon. The most prominent candidate for such an interaction is the photon-gluon fusion process. It can be detected through the production of a heavy quark-antiquark pair.

This thesis was performed in the context of the COMPASS[†] collaboration. Its subject is the determination of the gluon contribution to the nucleon spin from an analysis of polarised lepton-nucleon scattering data taken in the years 2002-2004. The analysis is based on the detection of photon-gluon fusion events through the production of charm quarks. This method to access the nucleon structure and more particularly the gluon contribution to the nucleon spin will be presented in chapter 1. It will be compared to other possibilities to access the gluon contribution.

The next two chapters put a focus on the experimental setting of the measurement. The COMPASS collaboration analyses the interactions of a high-energetic muon beam with a fixed target of polarised nucleons to access their spin structure. In chapter 2, the muon beam and the polarised target will be introduced, as well as the large multi-purpose detector used to detect the collisions. Chapter 3 discusses the trigger system to detect interactions between beam muons and target nucleons. This chapter also describes the changes introduced to the trigger system between the years 2004 and 2006.

Chapters 4 and 5 turn to the analysis of the data taken in the years 2002, 2003 and 2004. In chapter 4 the reconstruction of the recorded events is presented followed by a discussion on the stability of the reconstructed data. Chapter 5 introduces the reconstruction of D -mesons, which provide the evidence for the production of charm quarks.

The last two chapters present the measurements obtained with D -mesons that were reconstructed in the data sets from 2002, 2003 and 2004. Chapter 6 discusses the cross-section for D^* -meson-production at the COMPASS experiment and gives a first estimate of this quantity. In chapter 7 the measurement of the gluon polarisation is presented. The chapter starts with an introduction of the method of the measurement discussing also the other ingredients needed for the extraction of the gluon polarisation. In the last section, the result for the gluon polarisation will be given and compared to other measurements of the gluon polarisation. The thesis is concluded with a short summary.

[†]COmon Muon Proton Apparatus for Structure and Spectroscopy

Chapter 1

The spin structure of the nucleon

This chapter discusses the possibilities to determine the gluon polarisation in the nucleon and thus to evaluate the contribution of gluons to the nucleon spin. The subject of this thesis is the measurement of the gluon polarisation through the production of charmed mesons in polarised lepton-nucleon scattering. Besides the measurement through the so-called “open charm” production, the gluon polarisation can be accessed by the observed scaling violations in polarised structure functions as well as direct measurements in other channels. These other possibilities to determine the gluon polarisation will also be discussed in this chapter.

So far, the most successful tool for the investigation of the nucleon structure has been the observation of inclusive lepton-nucleon scattering and the determination of the structure functions of the nucleon. This method to probe the content of the nucleon will be presented in the first section. In the second section, the inclusive measurements of polarised lepton-nucleon scattering will be introduced, and its possibilities to access the gluon polarisation will be discussed. The third section will present the different methods for direct measurements of the gluon polarisation through double spin asymmetries and give a brief overview of the existing results. In the last section, the production of charmed mesons and their detection in the COMPASS experiment will be discussed in more details.

1.1 The nucleon structure in lepton-nucleon scattering

In lepton-nucleon scattering point-like leptons are used to investigate the structure of nucleons. In the scattering process, the incoming lepton l interacts with the nucleon n through the exchange of a virtual photon γ^* giving access to the nucleon structure. A schematic view of the process is given in figure 1.1. From the measured initial and final four-momenta k and k' of the lepton, different Lorentz-invariant observables can be determined, which are generally used to characterise the process. The negative four-momentum transfer squared Q^2 is given by

$$Q^2 = -q^2 = (k - k')^2 \stackrel{\text{lab}}{\approx} -4EE' \sin^2 \frac{\theta}{2} , \quad (1.1)$$

where E (E') is the energy of the incoming (outgoing) lepton and θ its scattering angle in the laboratory system. In the approximation on the right side of the equation the mass of the lepton

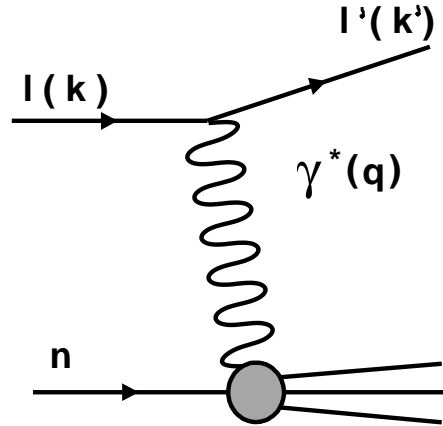


Figure 1.1: Schematic view of the lepton-nucleon scattering through a single photon exchange. The incoming lepton l scatters on the nucleon N through the exchange of a virtual photon γ^* . The diagram corresponds to the process in lowest order of perturbative QED calculations.

is neglected. Besides the momentum transfer, the energy of the exchanged photon ν and the inelasticity of the process y with

$$y \stackrel{\text{lab}}{=} \frac{E - E'}{E} = \frac{\nu}{E} \quad (1.2)$$

are determined from the kinematics of the lepton. To study the nucleon structure, the dependence of the differential scattering cross-section on these kinematic variables is measured.

The first measurements performed in 1968 [1] showed only a weak dependence on Q^2 for the inelastic lepton-nucleon scattering cross-section when it is normalised to the Mott cross-section [2]. This observation, which was the manifestation of a phenomenon called *scaling*, led to the conclusion, that, instead of scattering on the nucleon as a whole, the lepton is scattered incoherently on charged, point-like constituents of the nucleon. This discovery opened the way for the development of the parton model of the nucleon.

In the parton model [3], the nucleon is pictured as a collection of electrically charged, non-interacting, point-like constituents. In the *infinite momentum frame*, where the nucleon has a large momentum p_n compared to its mass ($p_n \gg M_n$), each constituent carries a fraction x of the nucleon's total momentum, where x is related to Q^2 and ν by

$$x = \frac{Q^2}{2M_n\nu} \quad (1.3)$$

Since in the parton model the virtual photon is absorbed by one of the partons without interference from the other constituents, the cross-section for the lepton-nucleon scattering is interpreted as the incoherent sum of the cross-sections for the scattering on all constituent quarks [4]. The lepton-nucleon scattering process in the parton model is illustrated in figure 1.2. The virtual photon only

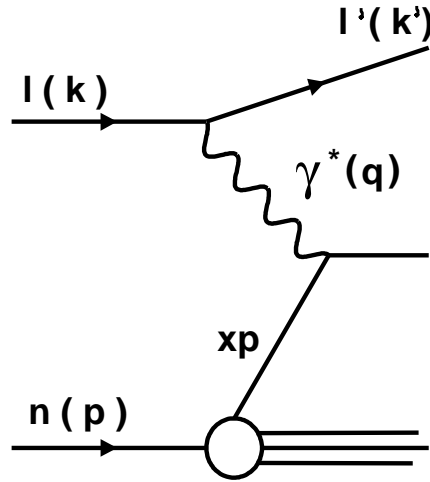


Figure 1.2: Schematic view of the lepton-nucleon scattering in the parton model. The virtual photon interacts with one of the constituents of the nucleon. The other constituents are spectators in the interaction.

interacts with one of the constituents of the nucleon, the others are spectators in the interaction. In the laboratory frame (proton at rest), the cross-section for the scattering of a lepton on a point-like constituent carrying the momentum fraction x , the electrical charge e_i and spin $\frac{1}{2}$ is given by [4]

$$\frac{d\sigma}{dy} = \frac{4\pi\alpha_{em}^2}{Q^4} 2M_n E x \left(1 - y + \frac{1}{2}y^2 \right) e_i^2, \quad (1.4)$$

where α_{em} is the coupling constant for electromagnetic interactions. Using this cross section, one can formulate the cross-section for lepton-nucleon scattering as the sum over the contributions from the constituents

$$\frac{d^2\sigma}{dx dy} = \frac{4\pi\alpha_{em}^2}{Q^2} \left\{ \frac{1-y}{xy} F_2(x) + y F_1(x) \right\}, \quad (1.5)$$

where the two structure functions $F_1(x)$ and $F_2(x)$ correspond to the charge-weighted distributions of the spin- $\frac{1}{2}$ constituents in the nucleon.

In a next step, the electrically charged partons of the nucleon were identified with the quarks used to explain the quantum numbers of hadron multiplets [6, 7, 8]. Besides their electrical charge e_i , quarks carry a flavour charge, which can be u, d, s, c, b or t , a colour charge and have a spin of $\frac{1}{2}$. In the Quark-Parton-Model (QPM), the structure functions F_1 and F_2 are interpreted as the sum over the contributions from the different quark flavours. For this purpose, the quark distribution function $q_i(x)$ is introduced, where $q_i(x)$ corresponds to the number of quarks with flavour i in the nucleon carrying a momentum between xp_n and $(x+dx)p_n$. The structure functions $F_1(x)$ and

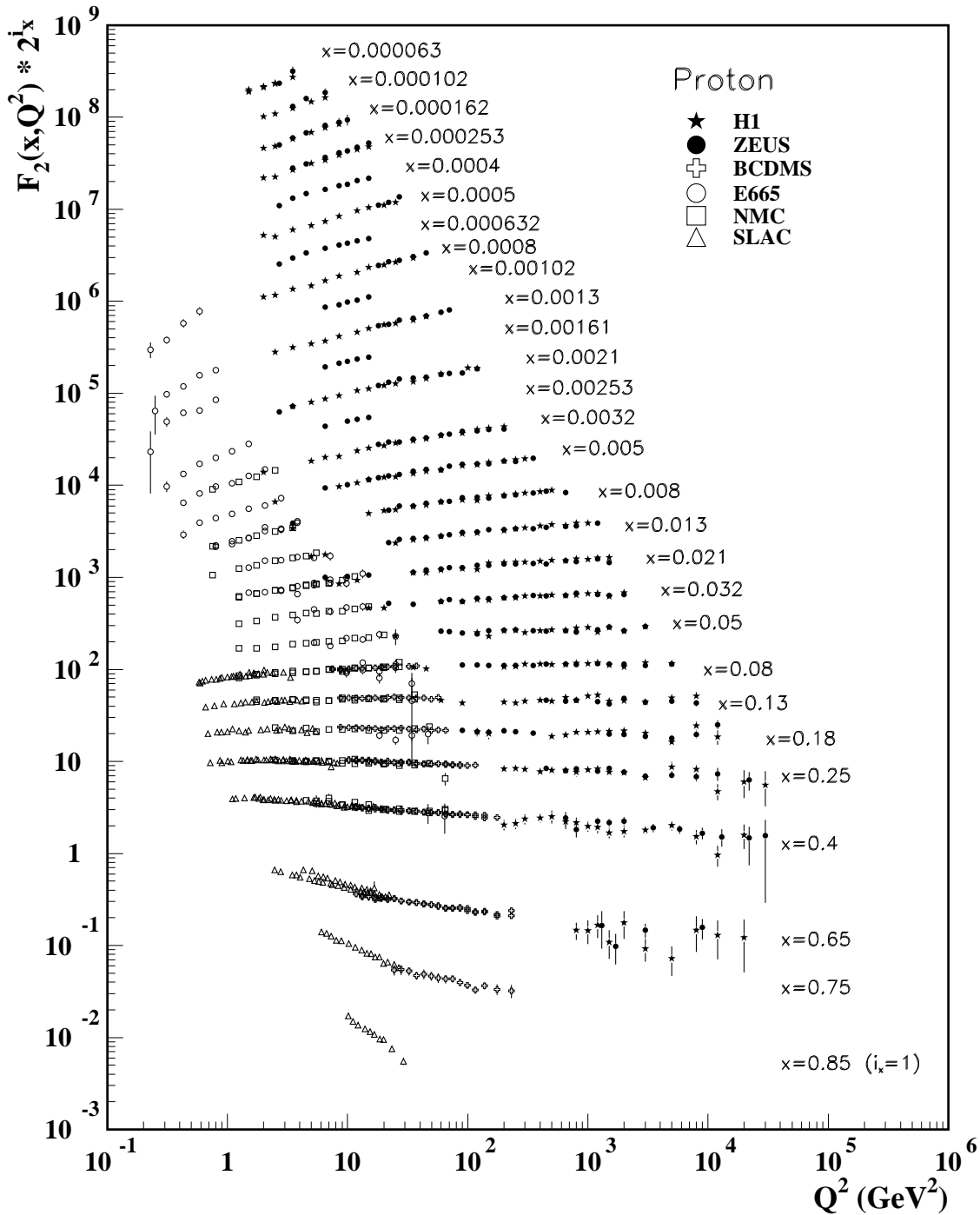


Figure 1.3: The proton structure function F_2 measured in electromagnetic scattering of positrons on protons (collider experiments ZEUS and H1), and for electrons (SLAC) and muons (BCDMS, E665, NMC) on a fixed target. Statistical and systematic errors added in quadrature are shown. The data are plotted as a function of Q^2 in bins of fixed x . Some points have been slightly offset in Q^2 for clarity. The vertical scale for F_2 has been adjusted in order to separate the values for different x . The plot was taken from [5], see references there for data points.

$F_2(x)$ can then be written as

$$F_1(x) = \frac{1}{2} \sum_i e_i^2 q_i(x) \quad (1.6)$$

$$F_2(x) = x \sum_i e_i^2 q_i(x) \quad , \quad (1.7)$$

where instead of summing over all constituents the summation is done over the different quark flavours. It has been established, that the dominant contributions to the nucleon structure are coming from quarks of flavours with light masses, i.e. u , d or s quarks. In the simple model of non-interacting quarks, the quark distribution only depends on x and not on Q^2 , which is the explanation for the observed scaling behaviour in early scattering data.

Figure 1.3 shows the existing measurements of F_2 for the proton as a function of Q^2 for a large range of x . The data are taken from fixed-target experiments (NMC, BCDMS, E665) as well as collider experiments, where a lepton beam is scattered off a high energetic proton beam (ZEUS, H1), and cover a remarkable range in x and Q^2 .

The data points in figure 1.3 show a logarithmic dependence of the measured structure function F_2 on Q^2 , which is in contrast to the expectation from the Quark-Parton-Model. This effect, also called *scaling violation*, can be explained, when considering, that Q^2 is also a measure for the resolution of the measurement. A larger momentum transfer provides the possibility to resolve smaller distances, or to distinguish between two close particles. This is illustrated in figure 1.4. In this

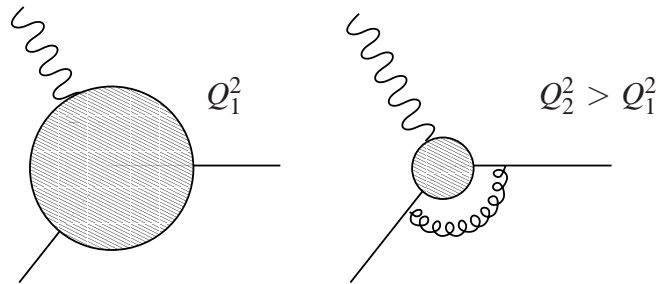


Figure 1.4: Illustration of the resolution. While a photon with Q_1^2 is scattered on a single quark, the photon with higher $Q_2^2 > Q_1^2$ resolves the quark and the gluon radiated by the quark.

figure, the photon with Q_1^2 is scattered on a single quark, while the photon with higher $Q_2^2 > Q_1^2$ resolves the quark and the gluon that was radiated by the quark and, thus, scatters on a quark with a smaller momentum fraction.

Thus, it is clear, that the interactions of quarks in the nucleon need to be taken into account, when formulating the Quark-Parton-Model. Quarks carry each a colour charge, which has three different varieties of colour or anti-colour. Because of the colour charge, quarks are subject to the strong interaction. As the electromagnetic interaction, the strong interaction is described by a quantum field theory, the Quantum-Chromo-Dynamics (QCD) with free quark fields and gluons as gauge

bosons. The gluon mediates the strong interaction coupling to colour charges. A principle difference between Quantum-Electro-Dynamics (QED) and QCD is, that gluons, unlike photons, carry also colour charge. Gluons couple therefore not only to quarks but also to gluons. As in any quantum field theory, the coupling strength of the QCD has a scale dependence, which originates in the interaction of colour charges with the vacuum. Because the QCD has six individual quark fields and eight different gauge bosons, the Q^2 -dependence of strong interactions is much stronger than for QED and has the opposite sign. For low Q^2 , the coupling constant α_S is very large and all quarks are trapped inside bound states, which is also called “confinement”. With increasing Q^2 , the coupling strength decreases until quarks can be regarded as quasi-free particles. This effect is called “asymptotic freedom”.

In nature, quarks and gluons can only be found in bound states. When discussing a high energetic scattering process, it is therefore not enough to calculate the hard interaction with the partons participating in the scattering. In addition, a description of the quark in the nucleon is needed as well as a formulation of, how the partons produced in the interaction form the bound states in which they are observed. In most cases, the Q^2 of the hard interaction of the scattering process is large enough to justify a perturbative approach for a calculation in QCD. In these cases, the interaction is calculated in orders of the coupling strength α_S , which needs to be small enough to permit the neglect of higher order contributions. This is not the case, when looking at the transition of asymptotically free quarks to quarks in bound states. This transition, called fragmentation, can therefore not be calculated perturbatively. Neither can the distribution of quarks in the nucleon be taken from a perturbative calculation. According to the *factorisation theorem* [9], the hard scattering process can be calculated independently of the fragmentation or the quark distributions. The quark distributions and fragmentation are determined from existing data. The fragmentation function is obtained from a phenomenological model, whose parameters are adapted to describe the data. The quark distribution are described through mathematical functions, whose parameters are determined through fits to the data. The factorisation theorem states, that the distribution of quarks in the nucleon and the fragmentation of quarks only depend on the momentum transfer Q^2 and not on the actual hard scattering process. It is therefore possible, to determine distribution and fragmentation functions from data of different scattering processes.

The QCD improved parton model takes the strong interaction of quarks into account. The quark distributions in the nucleon depend therefore not only on x , but also on the resolution with which the quarks are observed, leading to a Q^2 -dependence of the the measured structure functions $F_1(x, Q^2)$ and $F_2(x, Q^2)$ and the quark distributions in the nucleon $q_i(x, Q^2)$. Equations 1.6 and 1.7 are then rewritten as

$$F_1(x, Q^2) = \frac{1}{2} \sum_i e_i^2 q_i(x, Q^2) \quad (1.8)$$

$$F_2(x, Q^2) = x \sum_i e_i^2 q_i(x, Q^2) . \quad (1.9)$$

The quark distribution $q_i(x, Q^2)$ is now defined as the number of quarks of flavour i in the nucleon with a momentum between $x p_n$ and $(x + dx) p_n$ when viewed with a resolution determined by Q^2 [3]. In addition, in the QCD-improved parton model the nucleon not only consists of quarks, but also gluons. Since they do not carry electric charge, they do not interact with the photons probing

the nucleon, and do therefore, in lowest order of α_S , not contribute to the lepton-nucleon cross-section. But through their interactions with quarks, they influence the quark distribution functions in the nucleon. To account for the gluons in the nucleon, a gluon distribution function $g(x, Q^2)$ is introduced.

To compare the measured values of $F_1(x, Q^2)$ and $F_2(x, Q^2)$ at any given Q^2 with the predictions from the QPM, the Q^2 -dependence of the parton distribution functions (PDFs) needs to be determined. This dependence is given through a set of equations, describing how the PDFs change with Q^2 . Using these evolution equations the PDFs can be calculated for any Q^2 from a set of known or parametrised PDFs at a given Q_0^2 . The most prominent evolution equations are the DGLAP* equations [10, 11, 12].

To formulate the Q^2 -evolution of the PDFs the possible strong interactions of the partons in the nucleon are considered. Figure 1.5 illustrates these interactions as they are considered in the leading order DGLAP-evolution. For quarks, the only the radiation of a gluon is considered for the

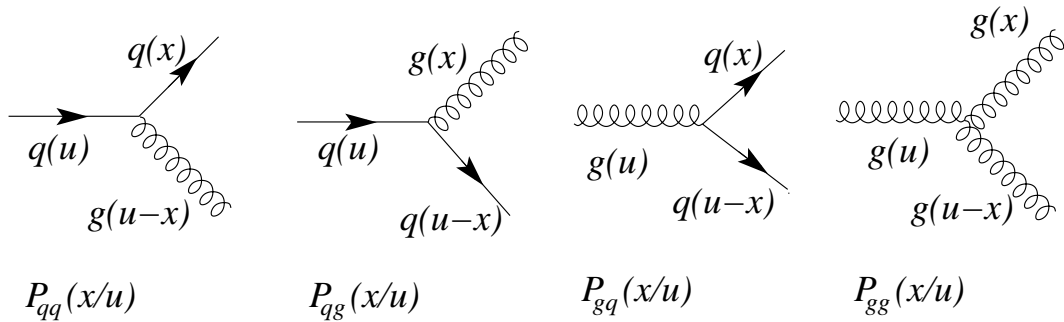


Figure 1.5: The four interactions of partons in the nucleon, that are considered in the leading order DGLAP-evolution.

leading order Q^2 -evolution. In figure 1.5, this interaction is represented by the two graphs on the left, to show, that it effects the quark and the gluon distribution in the nucleon. The gluons can radiate a gluon or split into a quark-antiquark pair, which is shown by the remaining two graphs in figure 1.5. The effect of each of the four processes on the PDFs is described by a splitting function, $P_{i,j}(\frac{x}{u})$. The splitting function, $P_{i,j}(\frac{x}{u})$, correspond to the probability that a parton j with the momentum fraction x of the nucleon momentum originates from a parton i with a momentum fraction u of the nucleon momentum. The splitting functions themselves are calculable in perturbative QCD. The leading order calculation of the splitting functions can be found in [12].

Using these splitting functions, the evolution equation of an individual quark distribution can be written as

$$\frac{dq_i(x, Q^2)}{d \ln Q^2} = \frac{\alpha_S}{2\pi} \int_x^1 \frac{du}{u} [q_i(u, Q^2) P_{qq}(x/u) + g(u, Q^2) P_{qg}(x/u)] \quad . \quad (1.10)$$

One can see, that the change in the quark distribution has one contribution from the quark splitting and a second contribution from gluon splitting. This second contribution only depends on the

*Dokshitzer, Gribov, Lipatov, Altarelli, Parisi

gluon distribution and not on the type of the quark distribution. Therefore, it is useful to regroup the PDFs from quarks and antiquarks into a singlet and several non-singlet contributions, with

$$q^S(x, Q^2) = \sum_i^{n_f} [q_i(x, Q^2) + \bar{q}_i(x, Q^2)] \quad (1.11)$$

$$q^{NS}(x, Q^2) = q_l(x, Q^2) - q_m(x, Q^2) \quad , \quad (1.12)$$

where n_f is the number of flavours in the nucleon. The quark distributions $q_l(x, Q^2)$ and $q_m(x, Q^2)$ stand for sums of several quark or antiquark distributions. The only condition put to the non-singlet distributions is, that the same number of quark and antiquark distributions enter $q_l(x, Q^2)$ and $q_m(x, Q^2)$. In this case, the gluon contributions cancel in the evolution equation of the non-singlet distribution and the evolution becomes independent of the gluon distribution. The three evolution equations for non-singlet, singlet and gluon distributions are given by

$$\frac{dq_i^{NS}(x, Q^2)}{d \ln Q^2} = \frac{\alpha_S}{2\pi} \int_x^1 \frac{du}{u} \left[q_i^{NS}(u, Q^2) P_{qq}(x/u) \right] \quad (1.13)$$

$$\frac{dq_i^S(x, Q^2)}{d \ln Q^2} = \frac{\alpha_S}{2\pi} \int_x^1 \frac{du}{u} \left[q_i^S(u, Q^2) P_{qq}(x/u) + 2n_f g(u, Q^2) P_{qg}(x/u) \right] \quad (1.14)$$

$$\frac{dg(x, Q^2)}{d \ln Q^2} = \frac{\alpha_S}{2\pi} \int_x^1 \frac{du}{u} \left[q_i^S(u, Q^2) P_{gq}(x/u) + g(u, Q^2) P_{gg}(x/u) \right] \quad . \quad (1.15)$$

The DGLAP equations can be used to extract the x -dependence of the PDFs from the measured data of F_2 shown in figure 1.3. For this, an initial parametrisation of the PDFs is formulated for a fixed Q_0^2 . The parametrised functions are then evolved to the different values of Q^2 of the measured data points of F_2 using the DGLAP equations. From equation 1.9, F_2 can be calculated from the evolved PDFs and can be compared to the measured value. The free parameters of the original set of functions are then optimised to minimise the difference between the measurements of F_2 and the calculated values. In most cases, the F_2 measurements from different experiments are fit together to obtain a large coverage in x and Q^2 . This makes the fitting procedures more complicated, because the different experimental and systematic errors from the different measurements have to be taken into account. Recent analysis of the existing structure function measurements have been performed by the GRV collaboration [13], the CTEQ [14] collaboration and the MRST [15] collaboration. Since for higher Q^2 the probability of observing a heavy quark in the nucleon can become non-zero, in some cases the QCD-fits are performed with additional structure functions for charm and bottom quarks in the nucleon [16].

To obtain the PDFs for a higher order perturbative calculation, the same fitting procedure is used. However, the splitting function and the relation between the parton distributions and the structure functions (see equations 1.8 and 1.9) depend on the order of the perturbative calculation and need to be adapted. In higher order, more processes contribute to the lepton-nucleon cross section. For example the PGF process (see section 1.3.1), where the gluon interacts with the virtual photon through the exchange of a quark-antiquark pair. To account for these possibilities, the gluon distribution function $g(x, Q^2)$ also contributes to the structure functions F_1 and F_2 .

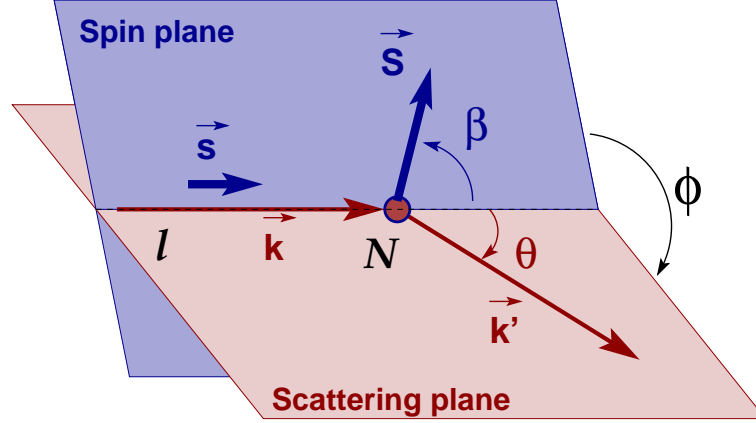


Figure 1.6: Kinematic planes in polarised deep-inelastic lepton-nucleon scattering.

1.2 Inclusive polarised lepton-nucleon scattering

Scattering experiments, where polarised leptons are scattered off a polarised nucleon target, address the question of the spin composition of the nucleon. The constituents of the nucleon, quarks and gluons, both carry spin and can have orbital angular momentum related to their movement inside the nucleon. The spin of the nucleon is therefore composed by the sum of all quark spins, the sum of all gluon spins and the sum over the orbital angular momenta. A sizeable contribution from all quark spin or all gluon spins is the result of a polarisation of quarks or gluons inside the nucleon.

Inclusive measurements of polarised deep inelastic scattering processes provide access to the contributions from quark spins and gluon spins. For this the cross-section for the scattering of a polarised lepton off a polarised nucleon target is evaluated. This cross-section can be separated into a spin-averaged contribution $\bar{\sigma}$, a contribution from longitudinally oriented nucleon spins σ_{\parallel} and a contribution from transversely oriented target nucleons σ_{\perp} by [17, 18]

$$\frac{d^3\sigma}{dx dy d\phi} = \frac{d^3\bar{\sigma}}{dx dy d\phi} + \mathcal{H}_l \cos\beta \frac{d^3\Delta\sigma_{\parallel}}{dx dy d\phi} - \mathcal{H}_l \sin\beta \cos\phi \frac{d^3\Delta\sigma_{\perp}}{dx dy d\phi} \quad (1.16)$$

In this equation the helicity of the incoming leptons is denoted by \mathcal{H}_l , with $\mathcal{H}_l = \pm 1$ for left and right handed particles. The angle between the incoming lepton momentum and the nucleon spin is $0 \leq \beta \leq \pi$, the second angle entering the equation, ϕ indicates the azimuthal angle between the scattering plane and the plane containing the lepton and the nucleon spins, as shown in figure 1.6. The spin-averaged cross-section $\bar{\sigma}$ as a function of the two unpolarised structure functions F_1 and F_2 was already given in equation 1.5. In an analogue way, two polarised structure functions, g_1

and g_2 , can be introduced to the spin-dependent cross-sections σ_{\parallel} and σ_{\perp} [18]

$$\frac{d^3\Delta\sigma_{\parallel}}{dx dy d\phi} = \frac{4\alpha_{em}^2}{Q^2} \left\{ \left(1 - \frac{y}{2} - \frac{y^2\gamma^2}{4} \right) g_1 - \frac{y}{2}\gamma^2 g_2 \right\}, \quad (1.17)$$

$$\frac{d^3\Delta\sigma_{\perp}}{dx dy d\phi} = \frac{4\alpha_{em}^2}{Q^2} \left\{ \gamma \sqrt{1 - y - \frac{y^2\gamma^2}{4}} \left(\frac{y}{2} g_1 + g_2 \right) \right\}, \quad (1.18)$$

where the kinematic factor $\gamma^2 = Q^2/v^2 = 4x^2M^2/Q^2$ vanishes for $Q^2 \rightarrow \infty$.

The spin-dependent structure functions, g_1 and g_2 , are accessed through the differences of the cross-sections for two opposite spin configurations. Since the spin-dependent part of the cross-section is relatively small compared to the total cross-section, cross-section asymmetries are measured. In the asymmetries systematic effects related to the absolute cross-section measurements cancel, thus facilitating the measurement of small spin-dependent contributions. For the scattering of a polarised lepton on a polarised target, two cross-section asymmetries can be determined. For longitudinal target polarisation, A_{\parallel} is given by

$$A_{\parallel}(x, Q^2; E) = \frac{\Delta\sigma_{\parallel}}{\bar{\sigma}} = \frac{\sigma_{\leftarrow\leftarrow} - \sigma_{\rightarrow\rightarrow}}{\sigma_{\leftarrow\leftarrow} + \sigma_{\rightarrow\rightarrow}}. \quad (1.19)$$

In the case of transverse target polarisation, A_{\perp} is

$$A_{\perp}(x, Q^2; E) = \frac{\Delta\sigma_{\perp}}{\bar{\sigma}} = \frac{\sigma_{\uparrow\rightarrow} - \sigma_{\downarrow\rightarrow}}{\sigma_{\uparrow\rightarrow} + \sigma_{\downarrow\rightarrow}}. \quad (1.20)$$

In both cases the arrows \rightarrow and \Rightarrow denote the orientation of the spin of lepton and nucleon in the scattering process. The symbol σ was chosen as a shorthand notation and stands for the differential cross-sections $d^3\sigma/dx dy d\phi$.

The spin-dependent structure functions, g_1 and g_2 , can be experimentally accessed through the measurement of the photon-nucleon asymmetries A_1 and A_2 [18]:

$$A_1(x, Q^2; E) = \frac{\sigma^{1/2} - \sigma^{3/2}}{\sigma^{1/2} + \sigma^{3/2}} = \frac{g_1 - \gamma^2 g_2}{F_1} \quad (1.21)$$

and

$$A_2(x, Q^2; E) = \frac{\sigma^{TL}}{\sigma^{1/2} + \sigma^{3/2}} = \gamma \frac{g_1 + g_2}{F_1}. \quad (1.22)$$

In the above expressions $\sigma^{1/2}$ ($\sigma^{3/2}$) stands for the cross-section of the interaction between a photon with helicity +1 and a nucleon with helicity +1/2 (-1/2) coupling to an angular momentum with a projection along the photon momentum of 1/2 (3/2). The cross-section σ^{TL} corresponds to the interference term for transverse and longitudinal photons.

The photon-nucleon asymmetries are related to the muon-nucleon cross-section asymmetries

through kinematic factors $\eta(Q^2, y, \nu)$, $\lambda(Q^2, y, \nu)$ and $\xi(Q^2, y, \nu)$, which depend on the kinematics of the photon emission from the lepton, and the depolarisation factor, $D(Q^2, y)$ [19]:

$$A_{\parallel} = D (A_1 + \eta A_2) \quad , \quad (1.23)$$

$$A_{\perp} = D\lambda (A_2 + \xi A_1) \quad . \quad (1.24)$$

The expressions for $\eta(Q^2, y, \nu)$, $\lambda(Q^2, y, \nu)$ and $\xi(Q^2, y, \nu)$ can be found in [18]. The depolarisation factor, $D(Q^2, y)$, stands for the polarisation transfer from the initial lepton to the photon probing the content of the nucleon. It can be expressed as a function of the kinematics of the lepton-photon interaction

$$D = \frac{y [(1 + \gamma^2 y/2) (2 - y) - 2y^2 m_{\mu}^2 / Q^2]}{y^2 (1 - 2m_{\mu}^2 / Q^2)(1 + y^2) + 2(1 + R)(1 - y - \gamma^2 y^2 / 4)} \quad , \quad (1.25)$$

where R is for the ratio of photo-absorption cross-sections for longitudinal and transverse photons $R = \sigma_L / \sigma_T$.

When only A_{\parallel} is measured, the polarised structure function, g_1 , can be accessed through

$$g_1 = \left[\frac{A_{\parallel}}{D} + (\gamma - \eta) A_2 \right] \frac{F_1}{(1 + \gamma^2)} = \left[\frac{A_{\parallel}}{D} + (\gamma - \eta) A_2 \right] \frac{F_2}{2x(1 + R)} \quad . \quad (1.26)$$

In the kinematic range of the COMPASS experiment, the factor $\gamma - \eta$ is small, so the contribution from A_2 can safely be neglected. For experiments with lower energies, where A_2 is larger, a parametrisation for A_2 is used [20]. To determine g_1 from measured values of A_{\parallel} , corresponding values of F_2 and R are needed, which are usually parametrised as functions of x and Q^2 . The parametrisations used by COMPASS were established by the SMC collaboration [21], which performed polarised inclusive scattering measurements with a similar beam energy than COMPASS. The structure function g_1 has been measured by different experiments as a function of x using the double-spin asymmetries in lepton-nucleon scattering at different values of Q^2 . Depending on the target material of the experiment, the measured asymmetries give access to the structure of proton, neutron or deuterons. In the case of the deuteron the measurement of g_1 corresponds to the isospin-symmetric structure of nucleons. For measurements of g_1^N with a deuteron target, only a correction of the target polarisation is needed, that takes into account the D -wave state of the deuteron. Measurements of the HERMES collaboration [22] have shown, that in measurements of g_1 the tensor structure of the deuteron can be neglected.

So far, the COMPASS collaboration has collected data on lepton-deuteron scattering during four years and data on lepton-proton scattering during one year. Of these recorded data, the inclusive asymmetries A_{\parallel} and g_1 were determined and published for the years 2002-2004 [23, 24]. The remaining data are still being analysed. Besides the COMPASS experiment, inclusive asymmetries of polarised lepton-nucleon scattering were measured by experiments at SLAC (E142 [25], E143 [26], E154 [27], E155 [28]), CERN (EMC [29], SMC [21, 30]), DESY (HERMES [31, 32]) and JLAB (HallA [33]). In figure 1.7 the the measurements of g_1 for protons, deuterons and neutrons are shown as a function of x .

To extract the polarisation of quarks and gluons in the nucleon from the measured values of g_1 , the

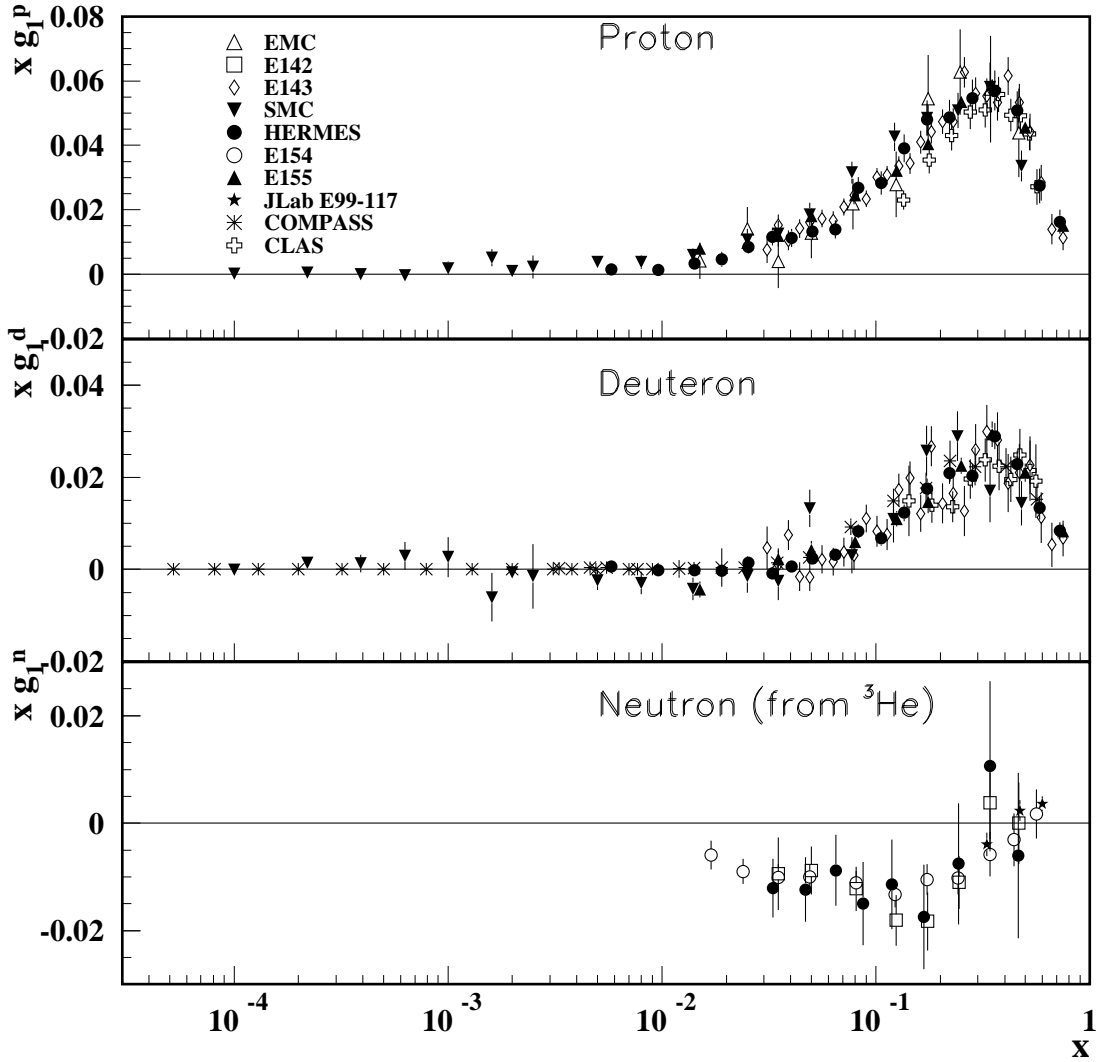


Figure 1.7: The spin-dependent structure function $xg_1(x)$ of the proton, deuteron, and neutron (from ${}^3\text{He}$ target) measured in deep inelastic scattering of polarised electrons/positrons: E142 ($Q^2 \sim 0.3 - 10\text{GeV}^2$), E143 ($Q^2 \sim 0.3 - 10\text{GeV}^2$), E154 ($Q^2 \sim 1 - 17\text{GeV}^2$), E155 ($Q^2 \sim 1 - 40\text{GeV}^2$), JLab E99-117 ($Q^2 \sim 2.71 - 4.83\text{GeV}^2$), HERMES ($Q^2 \sim 0.18 - 20\text{GeV}^2$), CLAS ($Q^2 \sim 1 - 5\text{GeV}^2$) and muons: EMC ($Q^2 \sim 1.5 - 100\text{GeV}^2$), SMC ($Q^2 \sim 0.01 - 100\text{GeV}^2$), COMPASS ($Q^2 \sim 0.001 - 100\text{GeV}^2$), shown at the measured Q^2 (except for EMC data given at $Q^2 = 10.7\text{GeV}^2$ and E155 data given at $Q^2 = 5\text{GeV}^2$). Note that $g_1^n(x)$ may also be extracted by taking the difference between $g_1^d(x)$ and $g_1^p(x)$, but these values have been omitted in the bottom plot for clarity. Statistical and systematic errors added in quadrature are shown. The plot was taken from [5]. Note that all measured points are at different Q^2 .

polarised quark distributions $q_i^+(x, Q^2)$ and $q_i^-(x, Q^2)$ are introduced. The distribution describes the number of quarks of flavour i , with a momentum fraction between x and $x + dx$ and with the same and opposite helicity as the nucleon. To parametrise the polarised structure function g_1 with polarised quark distributions the differences $\Delta q_i(x, Q^2)$ of the two helicity distributions are used. They are given by

$$\Delta q_i(x, Q^2) = q_i^+(x, Q^2) - q_i^-(x, Q^2) . \quad (1.27)$$

The integral of each difference $\Delta q_i(x, Q^2)$

$$\Delta Q_i = \int_0^1 \Delta q_i(x) dx \quad (1.28)$$

is interpreted as the total spin contribution of all quarks of flavour i divided by $1/2$. The quark polarisation can be obtained by dividing ΔQ_i with the integral over the unpolarised quark distribution. In the QCD improved QPM, the relation between the polarised structure function $g_1(x, Q^2)$ and the polarised quark distributions is given in leading order by

$$g_1(x, Q^2) = \frac{1}{2} \sum_i e_i^2 [\Delta q_i(x, Q^2) + \Delta \bar{q}_i(x, Q^2)] . \quad (1.29)$$

From the measured values of $g_1(x, Q^2)$, the polarised quark distributions are extracted by performing a global fit as described for the unpolarised case. However, due to the limited kinematic range covered by the data, additional constraints are needed for a good convergence of the fit-functions. Using the flavour decomposition of the first moment of g_1^p , Γ_1^p , one obtains [34]

$$\Gamma_1^p = \int_0^1 g_1^p(x, Q^2) dx \quad (1.30)$$

$$= \frac{1}{2} \left[\frac{4}{9} (\Delta \mathcal{U} + \Delta \bar{\mathcal{U}}) + \frac{1}{9} (\Delta \mathcal{D} + \Delta \bar{\mathcal{D}}) + \frac{1}{9} (\Delta \mathcal{S} + \Delta \bar{\mathcal{S}}) \right] . \quad (1.31)$$

Equation 1.31 can be rearranged into a singlet contribution, $\Delta \Sigma$, and two non-singlet contributions, $\Delta \mathcal{A}_3$ and $\Delta \mathcal{A}_8$, to the first moment of g_1^p

$$\Gamma_1^p = \frac{1}{12} \Delta \mathcal{A}_3 + \frac{1}{36} \Delta \mathcal{A}_8 + \frac{1}{9} \Delta \Sigma , \quad (1.32)$$

where

$$\Delta \mathcal{A}_3 = \Delta \mathcal{U} + \Delta \bar{\mathcal{U}} - \Delta \mathcal{D} - \Delta \bar{\mathcal{D}} \quad (1.33)$$

$$\Delta \mathcal{A}_8 = \Delta \mathcal{U} + \Delta \bar{\mathcal{U}} + \Delta \mathcal{D} + \Delta \bar{\mathcal{D}} - 2(\Delta \mathcal{S} + \Delta \bar{\mathcal{S}}) \quad (1.34)$$

$$\Delta \Sigma = \Delta \mathcal{U} + \Delta \bar{\mathcal{U}} + \Delta \mathcal{D} + \Delta \bar{\mathcal{D}} + \Delta \mathcal{S} + \Delta \bar{\mathcal{S}} \quad (1.35)$$

The values from $\Delta \mathcal{A}_3$ and $\Delta \mathcal{A}_8$ are related to the decay constants of the β decays in the baryon octet and have been measured previously [5, 35, 36]. They provide additional constraints, when fitting the polarised parton distributions to the measurements of g_1 . A detailed description of a fitting procedure and the application of these constraints can also be found in [37].

An example for the polarised parton distributions of the proton obtained with a global fit of the g_1

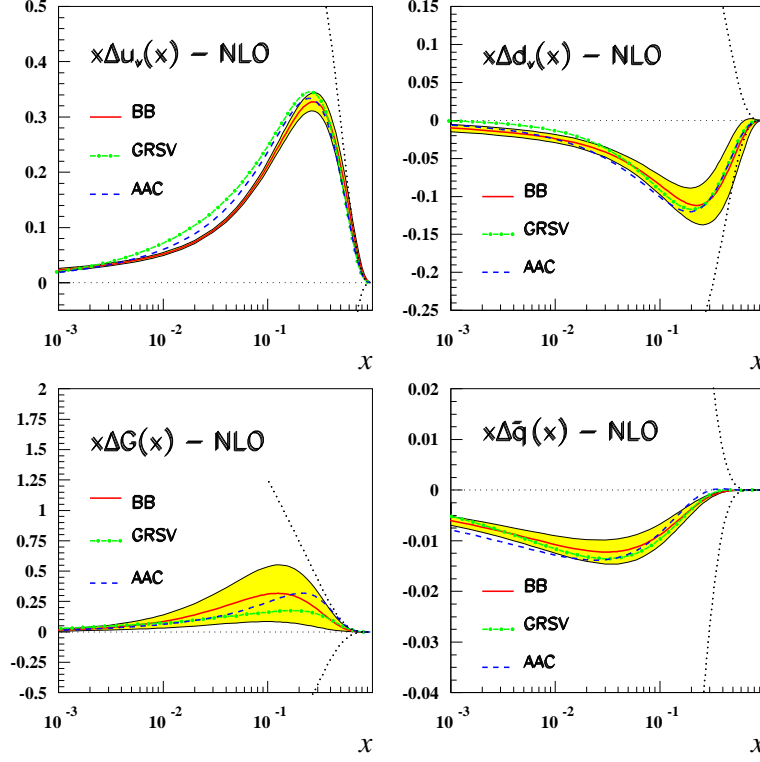


Figure 1.8: Recent analysis of polarised parton distributions of the proton. The distributions are shown for $Q^2 = 4 \text{ GeV}^2$. The plot is taken from [38] ('BB'). The additional curves represent the central fits from [39] ('GRSV') and [40] ('AAC').

data is shown in figure 1.8. The figure shows the fit results from three different groups and a band that indicates the uncertainty of the curves from 'BB' [38]. The quark distributions obtained from three different fits are in good agreement. The situation is very different for the polarised gluon distribution, where much larger uncertainties are observed.

From the polarised quark distributions the total contribution of the quarks to the nucleon spin, $\frac{1}{2} \Delta\Sigma$, can be determined. In [24] this contribution was determined to be

$$\Delta\Sigma(Q^2 = 3 \text{ GeV}^2) = \int_0^1 \Delta q^{SI} dx = 0.30 \pm 0.01 (\text{stat.}) \pm 0.02 (\text{evol.}) . \quad (1.36)$$

From this result, which is consistent with the results from previous fits, one can conclude, that the quarks have a significant polarisation in the nucleon, but the quark spin does not fully explain the spin of the nucleon. The gluon contribution and orbital angular momenta are therefore essential in the understanding of the spin composition of nucleon. Thus, a precise determination of the gluon polarisation is required.

The large uncertainty of the polarised gluon distribution determined through the QCD-fit is related to the fact, that so far, polarised lepton-nucleon scattering measurements were only performed by fixed-target experiments. This limits the available range in Q^2 and x . The polarised gluon distribution contributes to g_1 through the Q^2 -evolution of the polarised quark distributions. It is mainly

determined from the slope of g_1 in Q^2 . Because of the small range of Q^2 of the existing data, this slope cannot be determined precisely. The gluon polarisation can therefore not be determined very precisely from a QCD-fit of the existing g_1 data. Thus, additional measurements are necessary.

1.3 Measurements of the gluon polarisation

Measurements of the polarised gluon distribution in the nucleon are being performed in polarised lepton-nucleon scattering and polarised proton-proton collisions. Both measurements are based on interactions, where a gluon in the nucleon participates in the hard scattering process. This is achieved through different approaches. This section will present these approaches and discuss their sensitivity to the gluon polarisation.

1.3.1 Polarised lepton-nucleon scattering

In lepton-nucleon scattering, the dominant contributions to the cross-section are the quark-parton model (QPM) process contributing at the order α_{em} , the QCD-Compton (QCD-C) process contributing at the order $\alpha_{em}\sqrt{\alpha_S}$ and the photon-gluon fusion (PGF) contributing at $\alpha_{em}\sqrt{\alpha_S}$. The three processes are illustrated in figures 1.9 and 1.10. In the QPM process, the virtual photon is absorbed by one of the quarks in the nucleon. In the QCD-C process, the virtual photon is absorbed by a quark that emitted a gluon immediately before or afterwards. In both processes, only quarks from the nucleon participate in the interaction. The dominant process involving a gluon from the nucleon in lepton-nucleon scattering, is the photon-gluon fusion process (PGF). In this process, the virtual photon emitted by the lepton interacts with a gluon from the nucleon via the production of a quark-antiquark pair, as shown in figure 1.9.

The gluon polarisation is extracted from the double spin asymmetry for PGF events. This double spin asymmetry has a similar definition as the inclusive double spin asymmetry, $A_{||}$, (see equation 1.19) with the difference, that it is given by the PGF cross-section. For the COMPASS experiment, where PGF events are observed in muon-nucleon scattering, the asymmetry can be written as

$$A_{PGF}^{\mu N} = \frac{\Delta\sigma_{PGF}}{\bar{\sigma}_{PGF}} = \frac{\sigma_{PGF}^{\leftarrow\leftarrow} - \sigma_{PGF}^{\rightarrow\rightarrow}}{\sigma_{PGF}^{\leftarrow\leftarrow} + \sigma_{PGF}^{\rightarrow\rightarrow}}, \quad (1.37)$$

where the arrows indicate the spin orientations of the muon and the nucleon. According to the factorisation theorem [41], the polarised and unpolarised PGF cross-section $\Delta\sigma_{PGF}$ and $\bar{\sigma}_{PGF}$ can be expressed through the two gluon distributions in the nucleon $g(x, \hat{s})$ and $\Delta g(x, \hat{s})$ and the partonic cross-section, describing the muon-parton interaction

$$d\bar{\sigma}_{PGF} = d\sigma_{PGF}^{\mu g}(x, \hat{s}, \dots) g(x, \hat{s}) \quad (1.38)$$

$$d\Delta\sigma_{PGF} = d\Delta\sigma_{PGF}^{\mu g}(x, \hat{s}, \dots) \Delta g(x, \hat{s}) \quad (1.39)$$

where the variable x stands for the momentum fraction of the nucleon carried by the gluon and \hat{s} is the invariant mass of the photon-gluon system. For PGF processes, the invariant mass of the photon-gluon system, \hat{s} , is used instead of the momentum transfer to the virtual photon, Q^2 , to

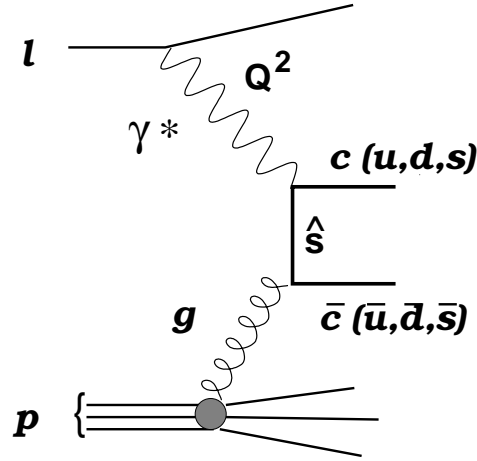


Figure 1.9: Illustration of the photon-gluon fusion process, where the virtual photon and the gluon interact by creating a quark-antiquark pair, which can be detected in the final state. The hard scale of this process is given by the invariant mass of the photon-gluon system, \hat{s} .

describe the scale of the scattering process. This reflects the fact, that the gluon distribution in the nucleon is probed with \hat{s} . The invariant mass, \hat{s} , can be calculated from the four-momenta of the photon \mathbf{P}_γ and of the gluon \mathbf{P}_g using $\hat{s} = (\mathbf{P}_\gamma + \mathbf{P}_g)^2$. It is also worth mentioning, that for PGF processes the variable x describing describing the momentum fraction of the nucleon, that is carried by the gluon participating in the interaction, does not correspond to the “Bjorken x ”, x_{BJ} , calculated from the lepton kinematics using equation 1.3.

The PGF asymmetry from equation 1.37 can then be related to the gluon distributions in the nucleon $g(x, \hat{s})$ and $\Delta g(x, \hat{s})$ through [42]

$$A_{PGF}^{\mu N} = \frac{\int d\Delta\sigma_{PGF}^{\mu g}(x, \hat{s}, \dots) \Delta g(x, \hat{s})}{\int d\sigma_{PGF}^{\mu g}(x, \hat{s}, \dots) g(x, \hat{s})}, \quad (1.40)$$

where the integration is done over x , \hat{s} and other observables the partonic cross-section depends on. To relate the measured cross-section asymmetry with the gluon polarisation in the nucleon $\Delta G/G = \int \Delta g(x, \hat{s}) / \int g(x, \hat{s})$ the analysing power a_{LL}^{PGF} is introduced. It corresponds to the partonic spin asymmetry for the $\mu g \rightarrow q\bar{q}$ scattering process in PGF and is given by

$$a_{LL}^{PGF} = \frac{\Delta\sigma_{PGF}^{\mu g}}{\sigma_{PGF}^{\mu g}}. \quad (1.41)$$

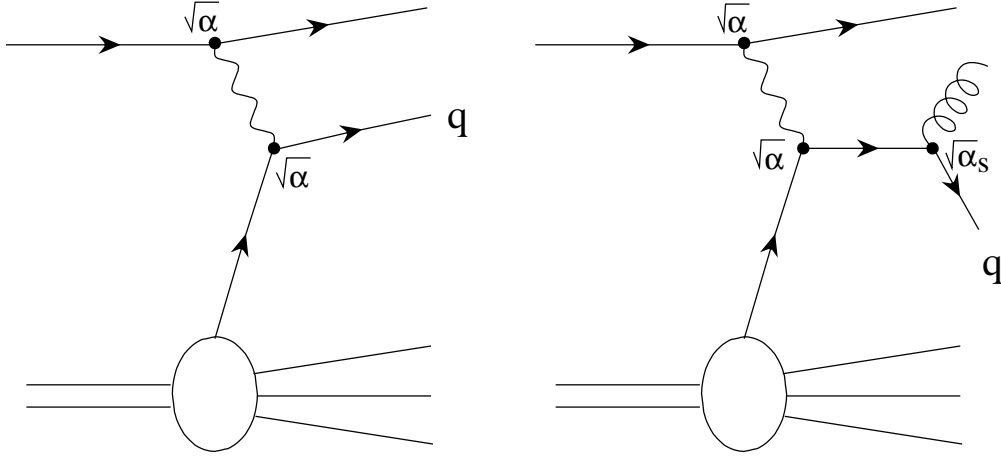


Figure 1.10: Illustration of the QPM process (left) and the QCD-C process (right).

Using the analysing power, equation 1.40 can be simplified

$$A_{PGF}^{\mu N} = \frac{\int d\Delta\sigma_{PGF}^{\mu g}(x, \hat{s}, \dots) \Delta g(x, \hat{s})}{\int d\sigma_{PGF}^{\mu g}(x, \hat{s}, \dots) g(x, \hat{s})} \quad (1.42)$$

$$= \frac{\int d\sigma_{PGF}^{\mu g}(x, \hat{s}, \dots) g(x, \hat{s}) a_{LL}^{PGF} \Delta g(x, \hat{s}) / g(x, \hat{s})}{\int d\sigma_{PGF}^{\mu g}(x, \hat{s}, \dots) g(x, \hat{s})} \quad (1.43)$$

$$A_{PGF}^{\mu N} = \left\langle a_{LL}^{PGF} \cdot \frac{\Delta g}{g} \right\rangle \quad (1.44)$$

For the measurement of $\left\langle \frac{\Delta g}{g} \right\rangle$ it is assumed that

$$A_{PGF}^{\mu N} = \langle a_{LL}^{PGF} \rangle \left\langle \frac{\Delta g}{g} \right\rangle, \quad (1.45)$$

where $\left\langle \frac{\Delta g}{g} \right\rangle$ is the average value of $\Delta g/g(x, \hat{s}, \dots)$ of the event sample used for the determination. Thus, $\left\langle \frac{\Delta g}{g} \right\rangle$ is only measured in the limited range of x covered by the data. Without this assumption, the effects of the partonic asymmetry and the gluon polarisation to the measured PGF asymmetry could not be disentangled. However, the simplification is only permitted in the case $\Delta g(x, \hat{s})/g(x, \hat{s})$ has a weak or linear dependence on x in the range of x covered by the data [43]. In the x -range of the data analysed in this thesis, the existing models describing the x -dependence of the polarised gluon distribution can reasonably well be approximated by a linear function.

For the scattering of a muon beam with polarisation P_μ off a polarised nucleon target with polarisation P_T , the cross-section asymmetry $A_{PGF}^{\mu N}$ is related to the measured asymmetry, A_{PGF}^{meas} , by

$$A_{PGF}^{meas} = P_\mu P_T f(R_{PGF} A_{PGF}^{\mu N} + (1 - R_{PGF}) A_B), \quad (1.46)$$

where the dilution factor f indicates the fraction of polarised nucleons in the target. The asymmetry is determined from an event sample, selected with an enhanced fraction of PGF-events R_{PGF} . For the case, where $R_{PGF} < 1$, a possible asymmetry of the background events A_B has to be taken into account.

In COMPASS, two channels are used to enhance PGF events. In the “open charm” channel, PGF events are identified by a charm quark in the final state. The leading order process for charm quark production is PGF, since charm quarks are not constituents of the nucleon and their production through the fragmentation process is strongly suppressed by their large mass. By requiring a D -meson, containing a charm quark, in the final state, a sample of PGF-events can be selected, where no second production process contributes. The challenge in this channel is to select a sample of D -mesons with as little combinatorial background from the reconstruction procedure as possible. In the “high- p_t ” analysis, a pair of hadrons with high transverse momenta is used to tag the PGF-events. This event signature is not unique for PGF processes. Besides PGF also the QPM and the QCD-C process can produce two hadrons with high transverse momenta. In addition, in photo-production events, where a quasi-real photon ($Q^2 \approx 0 \text{ GeV}^2$) is exchanged, resolved photon processes, where the photon fluctuates into a $q\bar{q}$ pair before interacting with the gluon, have to be considered. The fraction of PGF-events is enhanced through cuts on the transverse momenta of the two hadrons, as well as the sum of the two transverse momenta squared $p_{t1}^2 + p_{t2}^2$. To extract $\langle \frac{\Delta g}{g} \rangle$ from an event sample with high- p_t hadrons, the relative event fractions of the different processes have to be determined. This is done using events generated in Monte Carlo simulations. The high- p_t channel is not limited by the available event statistics. Instead the measurement is strongly model dependent, since it relies on information from Monte Carlo simulations to determine the relative contributions from the different processes.

The COMPASS experiment was the first experiment to publish a measurement of $\langle \frac{\Delta g}{g} \rangle$ from the open charm channel in lepton-nucleon scattering [44]. In the high- p_t channel, measurements of $\langle \frac{\Delta g}{g} \rangle$ have been published by the COMPASS collaboration [45], the SMC collaboration [46] and HERMES collaboration [47]. All three measurements agree within their precision, but on the basis of these measurements the polarised gluon distribution cannot be determined. It is however to be expected, that the significance of the results from the data taken in COMPASS until 2007 will make a distinction between different solutions for the gluon polarisation possible.

1.3.2 Polarised proton-proton scattering

Since the year 2000 a high energy proton-proton collider with polarised proton beams, called RHIC [48], is in operation at the Brookhaven National Laboratory. It offers the possibility to study the interaction of polarised protons at a centre-of-mass energy of 200 GeV.

In proton-proton collisions several processes involving gluons from the nucleon are available, however, they do not have unique event signatures. The processes studied to measure the gluon polarisation are shown in figure 1.11. The most prominent process for the measurement of the gluon polarisation is the prompt-photon production, shown in the upper left diagram. In this process the interaction of a quark from one proton with the gluon from the other proton is coupled to a photon emission. The photon provides a direct probe of the hard subprocess, since unlike the quarks and gluons it can be directly observed in the detector.

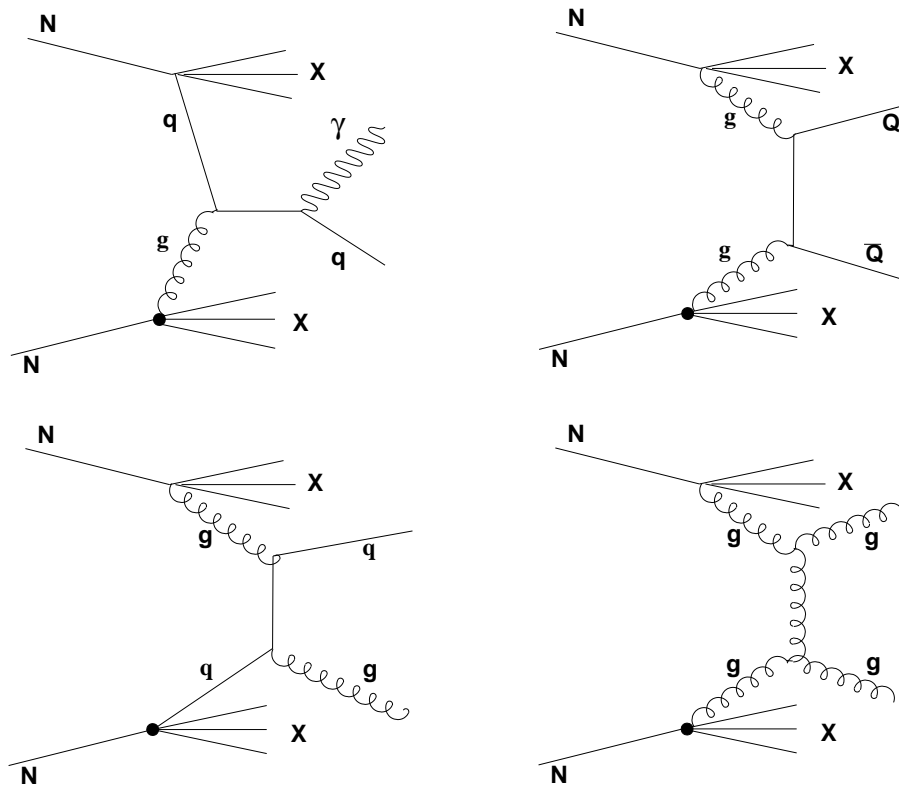


Figure 1.11: Proton-proton scattering processes where a gluon participates in the hard interaction. Upper left: prompt photon production, upper right: heavy-flavour production, lower left and lower right: jet or hadron production

The other three processes consist of parton-parton scattering events, where at least one parton is a gluon. The resulting quarks or gluons can be observed either as high energetic hadrons in the final state or in the form of jets. This makes the distinction of processes, where one gluon, two gluons or no gluons participated in the hard scattering difficult. One possibility for this distinction would be the detection of heavy quark production (upper right plot). Similar to the lepton-nucleon scattering, the dominant process for heavy quark production is gluon-gluon scattering, so heavy quarks can be used to select events where two gluons participated in the interaction. However, this channel is limited in statistics due to the requirements of charm production and detection.

Light quarks in the final state can be produced in quark-quark, quark-gluon or gluon-gluon scattering. It is, a priori, not possible to distinguish between the underlying scattering processes. Therefore all events are used for the asymmetry measurements. The separation of the contributions from the three different processes is done using a Monte-Carlo model. For this the data are divided into several bins of the transverse momentum of the observed hadron or jet. For each bin, the contribution from the gluon-gluon, the quark-gluon and the quark-quark process can be determined. Since the relative strengths of the three processes change as a function of the transverse momentum, the contributions of the three production mechanisms can be disentangled.

The measurement of the gluon polarisation follows the same principle as in lepton-nucleon scat-

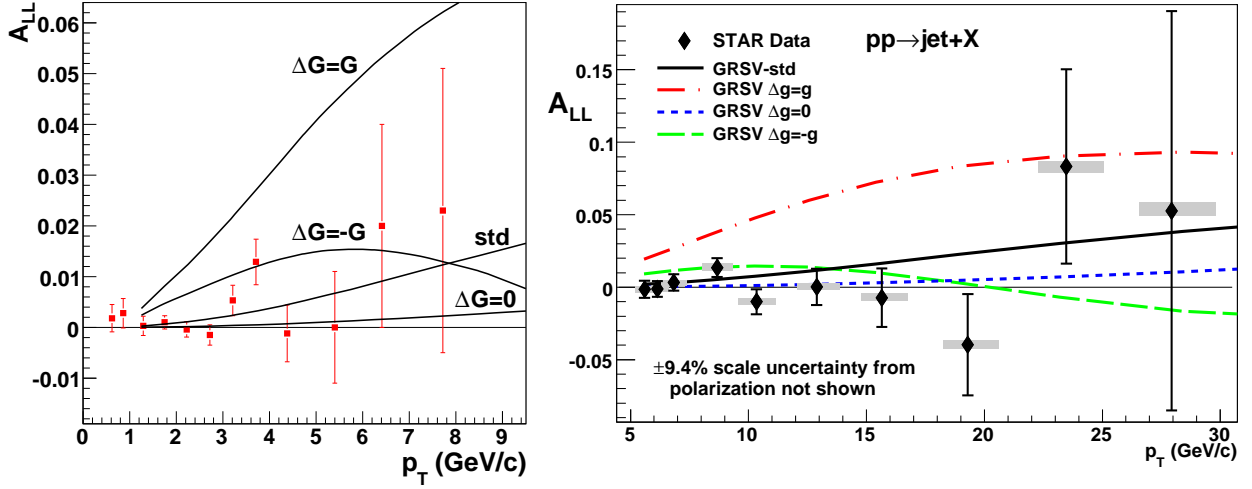


Figure 1.12: Measured proton-proton asymmetry A_{LL} from inclusive jet production [49] (right) and inclusive π^0 production [50] (left) as a function of p_T . The measurements are compared to the expectations for different gluon polarisations.

tering. From a preselected event sample, where the fraction of events with gluons in the hard interaction was enhanced through the selection cuts, the longitudinal cross-section asymmetry $A_{LL} = \Delta\sigma/\sigma$ is determined. When looking at a process $a + b \rightarrow c + X$, where a and b are partons in the initial state, c in the final state, the spin-dependent cross-section of the pp scattering process $\Delta\sigma$ can be decomposed to [34]

$$d\Delta\sigma = \sum_{a,b,c} \Delta f_a \otimes \Delta f_b \otimes d\Delta\hat{\sigma}_{a,b}^c \otimes D_c^h, \quad (1.47)$$

where Δf_i is the polarised parton distribution function of parton i , $\Delta\hat{\sigma}_{a,b}^c$ the spin-dependent partonic cross-section and D_c^h the fragmentation function for parton c to a the hadron or jet h through which it is observed. In the case, where the helicity of the hadrons in the final state is not observed, the D_c^h corresponds to the spin-independent fragmentation function and cancels in the asymmetry. The determination of the polarised parton distributions from the measured asymmetries then requires the knowledge of the spin-dependent partonic cross-sections.

One can see from equation 1.47 that in the case where both initial partons are gluons, the asymmetry is proportional to $(\langle\Delta g/g\rangle)^2$. In this case, the sign of the gluon polarisation cannot be determined. The processes with two initial gluons contribute to the heavy flavour production and to the jet and hadron production.

The extraction of the gluon polarisation from the measured asymmetries is done in several steps. From a Monte-Carlo simulation the event fractions of the different production mechanisms are determined as a function of p_T . The partonic asymmetries of the contributing processes are also calculated as a function of p_T . Using the partonic asymmetries, it is therefore possible to calculate the expected longitudinal proton-proton asymmetries as a function of p_T for different models of the polarised gluon distribution. The comparison of the calculated values and the measurements

allow a conclusion about the gluon polarisation in the proton. This is shown in figure 1.12, where the measured asymmetries from inclusive jet production (right) and inclusive π^0 production are shown as a function of p_t . The figures also show different curves corresponding to different gluon polarisations. One can see, that these measurements prefer low or negative gluon polarisations for the kinematic ranges of the measurements.

At RHIC, the PHENIX and the STAR collaboration are working on the determination of $\langle \frac{\Delta g}{g} \rangle$ from high energetic pp collisions. They have so far published results from π^0 and jet production [51, 52, 49, 50] (see also figure 1.12). As for these measurements the contributions of the different underlying scattering processes need to be very well understood, the first publications from both collaborations discussed the unpolarised cross-sections and their agreement with next-to-leading order calculations [53, 54, 55].

Results from the cleaner heavy flavour and prompt-photon production channels are not published yet. These channels require more statistics for an extraction of $\langle \frac{\Delta g}{g} \rangle$. The comparison of the published results with the different theoretical predictions give a similar picture as for the high- p_t channel. At the moment no definitive conclusion about the gluon polarisation can be drawn, but it is clear that, when more data are available, the measured asymmetries allow a determination of the polarised gluon distribution in the proton [56] using the results on the polarised quark distributions from inclusive lepton-nucleon measurements.

1.4 Open Charm production in COMPASS

This section discusses the production and the detection of charm quarks in the kinematic regime of the COMPASS experiment. The first part of this section is dedicated to a discussion of the exclusiveness of the open charm production via photon-gluon fusion. The second part of this section will then examine the possibilities for charm detection in more details.

The measurement of the gluon polarisation from open charm production in COMPASS makes use of two advantages of heavy quarks with respect to lighter quarks. As mentioned above, heavy quarks can only be produced in the hard scattering process. They are too heavy for production during the fragmentation of lighter quarks. Thus, unlike lighter quarks, a heavy quark can be directly identified as a quark from the hard scattering process. In addition, due to the heavy mass, the charm quarks preserve most of their initial momentum during the fragmentation process. The observed kinematics of the charmed meson can therefore be related to the parton kinematics.

The dominant process for charm production in lepton-nucleon scattering is the photon-gluon fusion process, shown in figure 1.9. A second conceivable process with a charm quark in the final state, would be a QPM process (see figure 1.10) with an intrinsic charm quark in the nucleon. This process is however strongly suppressed, as shown in figure 1.13. It displays the measurement of the structure function $F_2^{cc}(x_{BJ})$ for charm production from muon-nucleon scattering at three different photon energies ν , which are comparable to the photon energies in COMPASS. The data are compared to curves showing the expectations of F_2^{cc} from PGF and intrinsic charm. The data points agree with the PGF production mechanism of the observed charm quarks. For this diagram, the difference between the variable x_{BJ} calculated from the muon kinematics through equation 1.3

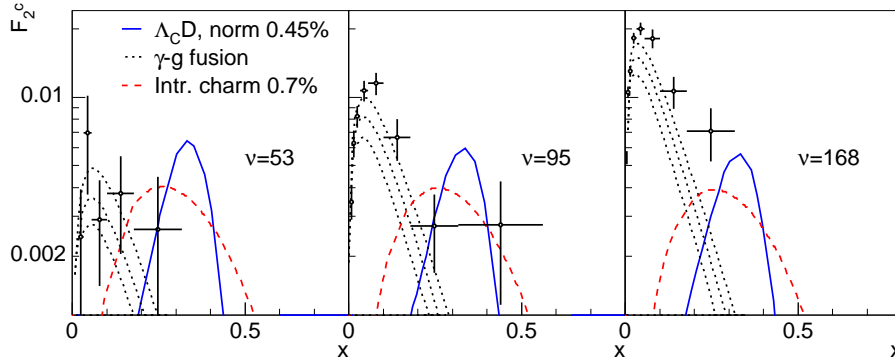


Figure 1.13: Measurements of F_2^c by the EMC collaboration [57] compared to the expected distributions of charm production in PGF and from intrinsic charm in NLO [58, 59]. This plot was taken from [58].

and the x , which describes the momentum fraction of the nucleon carried by the parton, should be remembered. The data points are shown for different values of x_{BJ} , which is only for the QPM process, the same as x . For the PGF process, the actual momentum fraction carried by the gluon has larger values than the x_{BJ} that is shown in the plots.

A second background contribution in a sample, where charm production was detected, could be “resolved-photon” processes. In the resolved-photon processes, the photon emitted by the muon fluctuates into a quark-antiquark pair before interacting with one of the gluons from the nucleon. Resolved photons appear mostly in interactions with $Q^2 \approx 0 \text{ GeV}^2$. At larger values of Q^2 their contribution is suppressed. For a measurement of the gluon polarisation in the nucleon, a large contribution from resolved-photon processes is problematic, because the quark polarisations in the photon could introduce a background asymmetry. Several studies [60, 61] have shown, that the resolved photon contribution to charm production is expected to be below 1% in COMPASS kinematics and can therefore be neglected.

Thus, the photon-gluon fusion process is not only the dominant process for charm production in leading, but all other processes can be neglected. Figure 1.14 shows the estimated charm-production cross-section through photo-production processes as a function of the photon-nucleon centre-of-mass energy W [62]. One can clearly see the steep rise in the cross-section at values of $W < 10 \text{ GeV}$. This threshold is related to the fact, that a minimum energy of $\hat{s} = 4m_c^2 = 9 \text{ GeV}^2$ is needed in the photon-gluon system to produce the two charm quarks. For the 160 GeV muon energy used in COMPASS, the energy range for the photons is approximately $30 < \nu < 130 \text{ GeV}$. This corresponds to an average W around 15 GeV, which is similar to the values of W of the fixed-target experiments shown in the diagram. The values of W are above the threshold for the production of a charmed quark-antiquark pair through the PGF process.

Besides the unambiguous production process, heavy quarks have the advantage, that they carry information about the hard scattering process, where they were produced. In the case where both charm quarks from the PGF process are detected, it would be possible to determine \hat{s} , the invariant

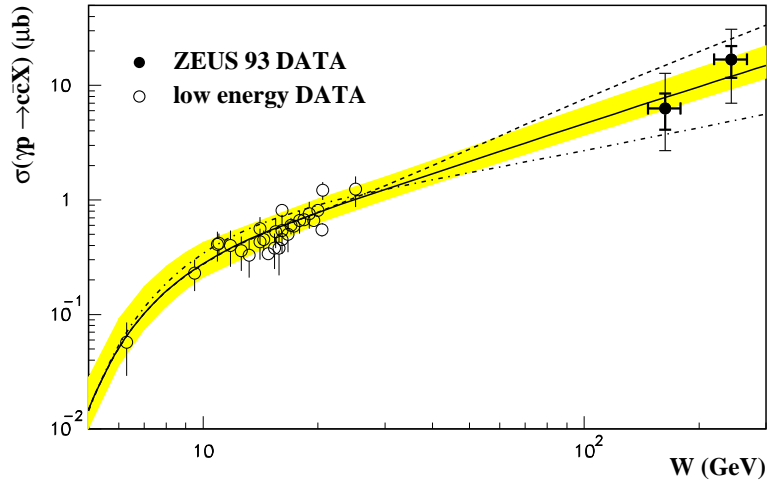


Figure 1.14: Total photo-production cross section as a function of W . The solid dots are the ZEUS measurements from the data taken in 1993 and the open dots are earlier measurements from fixed target experiments. The solid line represents the central prediction of NLO calculations. The shaded band represents the theoretical uncertainties coming from varying this scale in the range. This plot was taken from [62]

mass of the photon-gluon interaction. From \hat{s} the momentum fraction of the nucleon carried by the gluon can directly be calculated. Thus, charm quarks provide a unique possibility to access the properties of the gluons in the nucleon. Unfortunately, in COMPASS the probability to observe both charm quarks from the PGF-process is very low and the event samples with two detected charm quarks are by far too small for an asymmetry determination. The gluon polarisation is therefore measured from events, where only one charm quark was detected. It is therefore important to detect this charm quark in such a way, that the four-momentum of the charm quark can be reconstructed. For the extraction of the gluon polarisation, the partonic photon-gluon asymmetry has to be calculated. This asymmetry is a function of the kinematics of the photon-gluon system and can be expressed by the Mandelstam variables of the photon-gluon interaction \hat{s} , \hat{t} and \hat{u} , which can be approximated, when the four-momentum of one charm quark is known. For such an approximation, also the event variable, such as Q^2 or y , are used as well as the D -meson four-momentum.

In many experiments charm quarks are detected either through the secondary vertex of their decay or through a lepton produced in a semi-leptonic decay channels. For the analysis presented here, neither method can be applied. Secondary vertices from charm decays are excluded, because due to the thick solid state target they cannot be resolved. The semi-leptonic decays of charm quarks are not considered, because in this channel the momentum of the charm quark cannot be fully reconstructed. Charm quarks are therefore only detected through their fragmentation into charmed mesons. At COMPASS energies, the meson most frequently produced in the fragmentation of a charm quark is the D^0 -meson. About 55% of the charm quarks fragment into a D^0 -meson [63], the other hadrons produced in charm fragmentation are the D^\pm (23%), D_s^\pm (10%) and Λ_C^\pm (7.6%). This means, that for every PGF-event in COMPASS at least one D^0 -meson is expected. About half

of these D^0 -mesons are produced in the decay of a $D^{*\pm}$ -meson [63]. During the fragmentation process, about 80% of the initial momentum of the charm quark is transferred to the D -mesons, which leads to a very good correlation between the D -meson and the charm momentum. Thus, from the D -meson momentum the kinematics of the initial scattering process can be approximated.

The charmed mesons are detected through their hadronic decay channels. These decays are essentially weak decays, where the charm quark is transformed into a strange quark and a kaon is produced. For example, in $(53 \pm 4\%)$ of D^0 -decays a charged kaon, in $(42 \pm 5\%)$ a neutral kaon is produced [5]. Thus, for a successful analysis of open charm production from PGF processes, a detector for particle identification of great importance. For this reason COMPASS is equipped with a Ring-Imaging Cerenkov detector providing the distinction between pions and kaons.

Chapter 2

The COMPASS Experiment

The COMPASS experiment is located in the north area experimental zone of the SPS* accelerator at CERN. It is designed to observe interactions between high energetic muons or hadrons with nucleons in a fixed target. A two stage spectrometer is used to detect and measure all particles produced in the scattering processes. As the COMPASS collaboration pursues different physics programmes, the exact setup of the experiment depends on the actual ongoing measurement.

This chapter is dedicated to the description of the experimental set-up used in the measurement of the gluon-polarisation in the years 2002-2004. The polarised beam and the polarised target play an essential role in this measurement. They will be introduced in sections 2.1 and 2.2. The following sections will present the detectors used to measure and identify the particles produced in the interactions. A particular emphasis is given to the RICH detector, since its information about the particles identity is vital in the detection of charmed mesons. The data acquisition system used to collect the data from the spectrometer will be shortly described in section 2.5. The last section of this chapter will give a short overview over the changes introduced to the spectrometer between 2004 and 2006.

The description of the experimental set-up in this chapter puts a focus on the detector systems of interest for the measurement presented here. A detailed description of all components in the COMPASS experiment can be found in [64].

2.1 The Muon Beam

The COMPASS experiment uses the μ^+ -beam provided by the CERN muon beam-line M2 [65]. This beam-line uses protons from the SPS accelerator. The 400GeV proton beam produced in SPS is directed on a 500mm thick Beryllium target, shown as “T6” in figure 2.1. In the interaction between the primary protons and the target material high energetic hadrons are produced. A system of acceptance quadrupoles and dipoles (“B1-B3”) selects pions within a momentum band of up to 225 GeV. These pions are led into a 600m long decay tunnel containing an array of focusing and defocusing magnet (FODO) for a better focusing of the beam. After travelling this distance, a fraction of the pions will have decayed through the parity violating weak decay into a muon and a

*Super Proton Synchrotron

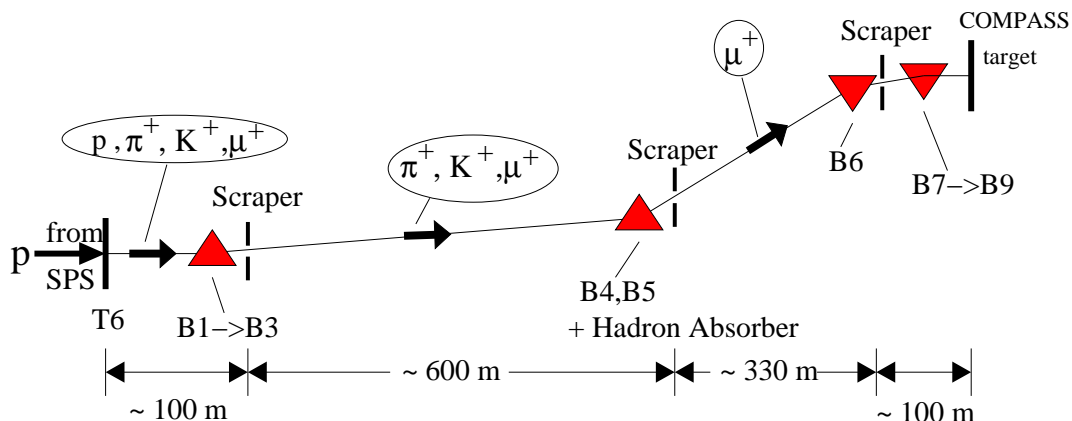


Figure 2.1: The set-up of the M2 beam-line. T6 stands for the beryllium target used to produce the secondary hadron beam, the bending magnets guiding the beam on the COMPASS target are marked with triangles. For the hadron physics programme the hadron absorber between B4 and B5 is removed.

μ -neutrino. A hadron absorber system at the end of the tunnel absorbs undecayed hadrons, while the muons penetrate its material. The SPS accelerator system is situated about 20m under ground. Hence, two systems of deflecting magnets are needed to direct the beam onto the COMPASS target located at ground level. The first system (“B4, B5”), surrounding the hadron absorbers, directs the beam upwards towards the surface. The second set of magnets (“B6 - B9”) guides the beam parallel to the surface and onto the target. At the same time, the two systems of bending magnets are also used to select the momentum of the muon beam. For this selection a relative precision of 5% can be achieved. For a more precise determination of the incoming muon momentum the second dipole system is also used to measure the momentum of the incoming beam particle. During the years 2002 - 2004, the different dipoles of the M2 beam-line were set to provide a muon beam of $160 \text{ GeV} \pm 5\%$.

The profile of the muon beam arriving on the target is shown in figure 2.2. The principle beam component, indicated by the shaded area in figure 2.2, is surrounded by an intense halo. This halo consists of muons with not only a different trajectory but in most cases different momenta than the principle beam component. As seen in figure 2.2, most halo muons can be found in the “near halo”, covering an area of up to 30cm around the principle beam component. The “far halo” consisting of significantly less particles extends over a much larger surface and covers the sensitive areas of all detector components in the COMPASS spectrometer. A veto system installed before the COMPASS target is used to distinguish between interactions of the principle beam component and beam halo.

The muons of the M2 beam-line are naturally polarised due to their production in the parity violating weak decay of pions $\pi^+ \rightarrow \mu^+ \nu_L^\mu$. The conservation of momentum and spin in the pion rest frame requires the decay muons to have negative helicity, i.e. the muon spin compo-

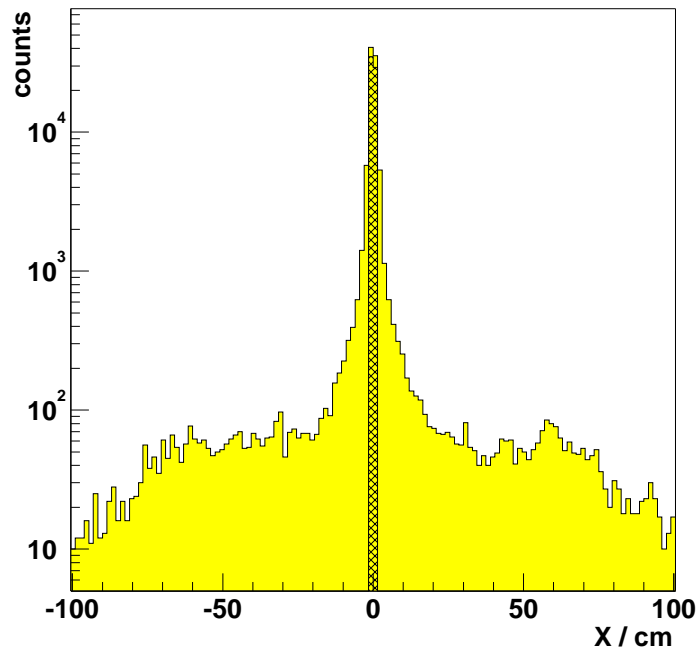


Figure 2.2: Horizontal profile at the target centre for incoming particles obtained with a random trigger. The shaded area corresponds to particles passing through both target cells.

ment parallel to the momentum is negative. Since for muons the helicity is not conserved under Lorentz-transformations, not all muons have negative helicity in the laboratory frame. The fraction of muons with negative helicity corresponding to the beam polarisation, P_μ , depends on the ratio of the energies of pions, E_π , and muons, E_μ . It can be calculated using

$$P_\mu = \frac{-m_\pi^2 + (1 - 2E_\pi/E_\mu)m_\mu^2}{m_\pi^2 - m_\mu^2} \quad (2.1)$$

For the so-called muon programme, a beam momentum of 160 GeV was chosen. With this muon momentum an average beam polarisation of $(-80 \pm 4)\%$ was achieved in 2004, where a pion beam energy of 172 GeV was used. In 2002 and 2003, a pion energy of 177 GeV was selected leading to an average beam polarisation of $(-76 \pm 4)\%$ for the same muon energy.

Since the beam optics allow for a spread of up to 5% of the muon momentum, a measurement of the incoming beam particle is needed. This is achieved with the beam momentum station (BMS). It consists of six detectors that are placed before and after the system of bending magnets providing the horizontal direction in front of the target (B6 in figure 2.1). The three dipoles provide a total deflection by 30 mrad. In combination with the BMS, they also function as spectrometer magnets and are used for a momentum determination. Four BMS detectors are scintillator hodoscopes with 64 horizontal strips, which have a width of 5 mm each. They are complemented by two scintillating

fibre hodoscopes with 64 and 128 channels. All detectors are read out with photo-multiplier tubes leading to a very high time resolution of 300 ps. The sizes of the different BMS detectors are adapted to the beam cross sections at the different positions. By measuring in the 6 BMS detectors the position in the bending plane of dipoles, the momentum of each incoming beam muon can be determined.

The data taking in COMPASS is organised along the time structures given by the SPS. The proton beam from the SPS is structured into spills. For the duration of a spill, the beam particles enter the experiment continuously. A spill lasts typically 4.8 s and it is repeated every 14.8 s. During normal beam operation, the proton intensity on the beryllium target “T6” is in the order of $\sim 10^{13}$ particles. With this proton intensity, a muon intensity of about $2 \cdot 10^8$ muons on the COMPASS target is achieved with the 500 mm thick beryllium target.

A second time structure coming from the SPS operation are the data taking periods. Each data taking period corresponds to several days of continuous data taking. In most cases, the data taking periods are defined by the SPS schedule, which foresees interruptions in the SPS operation once per week. For stability reasons, all asymmetry measurements in COMPASS are performed for each data taking period separately.

2.2 The Polarised Target

For a precise measurement of cross-section asymmetries, a high rate of polarised scattering events is needed. Because of the low cross-section of muon-nucleon interactions and the limitations in the intensity of the muon beam, the nucleon target was designed to obtain a high luminosity. This is achieved using a thick target of solid state material providing a high material density. The target is organised in two target cells of 60 cm each, which are oppositely polarised. This allows a simultaneous measurement of interactions with both nucleon spin directions.

Besides the high interaction rate, it is important for a good asymmetry measurement to have a large fraction of polarisable material and a high polarisation of the target material. Both quantities scale directly with the inverse of the statistical error, while the number of detected events enters the precision of the measurement with a square-root. The target material was therefore chosen for a large maximum polarisation and a large dilution factor, indicating the amount of polarisable material. In the years 2002-2004 ${}^6\text{LiD}$ was used as a target material. It has a high dilution factor, because not only the deuteron can be polarised. The Lithium nucleus basically consists of an unpolarisable Helium core and a deuteron. Thus, the total fraction of polarisable nuclei in ${}^6\text{LiD}$ is around 40%. Figure 2.3 gives a schematic view of the different components needed for the operation of a polarised target. In the following a short introduction to the target operation will be given. A detailed description can be found in [66].

For the measurements with polarised nucleons, the two target cells are installed inside a system of two magnets. The solenoid magnet holds a longitudinal field leading to a longitudinal polarisation of the nucleons. In addition, a dipole magnet is used for a transverse spin orientation of the target nucleons. During the actual polarisation process only the field of the solenoid is used. To obtain a good polarisation, the solenoid generates a field of 2.5 T with a homogeneity of better than

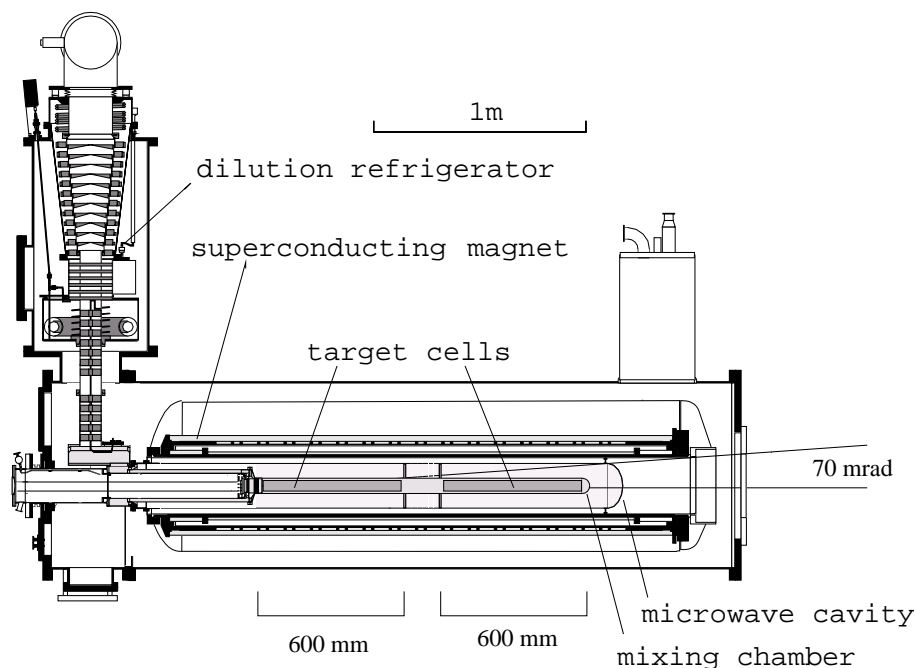


Figure 2.3: Schematic view of the COMPASS target system.

2 ± 10^{-5} . The field of the dipole magnet is 0.5 T, which is sufficient to hold the polarisation of the already polarised nucleons. Only after the target material was polarised, the spins of the target nucleons are rotated into the direction needed for the measurement by changing the direction of the net magnetic field using a super-composition of the solenoid and the dipole fields. This procedure is also used to inverse the longitudinal spin orientations.

The polarisation of the target material is achieved with the method of dynamic nuclear polarisation [67]. For this, electrons are injected into the target material during its production. During operation, target material is kept at very low temperatures in a strong magnetic field of 2.5 T. In this environment the free electrons are polarised to about 96%, while the deuteron nuclei have a natural polarisation of 0.052%. The high polarisation of the electrons is transferred to the nucleons through microwave irradiation of a suitable frequency close to the spin resonance frequency of the electrons. The microwaves incite a coupled spin-flip of a nucleon and an electron. While the electron spin flips back almost instantaneously, the nucleon spin remains in the new state for a longer time. This process continues for as long as there are nucleons whose spins are pointing in the same direction as the electron spins. However, as more and more nucleons have opposite spin directions, the increase of polarisation will slow down. Once the desired polarisation has been achieved, the spin configuration can be “frozen” by cooling the target to 50 mK.

The degree of polarisation of the target material is measured through a system of NMR coils. Around each cell up to five individual coils are installed. Since only a part of the target volume is monitored through the NMR coils, the polarisation in the remaining volume is extrapolated from the measured values.

The operation of the polarised target requires extremely low temperatures. They are provided by a dilution refrigerator, in whose mixing chamber the two target cells are installed. The dilution refrigerator uses the mixing properties of liquid ^3He and ^4He . When cooling a mixture of the two Helium isotopes below a critical temperature of 0.86 K the mixture will develop two phases, which differ in the concentration of ^3He in the liquid ^4He . The cooling mechanism is based on a phase transition between the phase with a high concentration of ^3He to the other phase. For this phase transition additional energy is required. Thus, by forcing this transition to take place continuously, the mixture of ^3He and ^4He can be cooled down to temperatures as low as 50 mK. At these temperatures, the relaxation time of the nucleon spin is several months, which explains the name “frozen spin mode” for the target operation at this temperature.

2.3 The Spectrometer

The layout of the COMPASS spectrometer is shown in figure 2.4. It is organised in two spectrometer stages combining a high momentum resolution with high angular acceptance. The large angle spectrometer (LAS), immediately after the target, detects particles that are scattered at large angles of up to 180 mrad. The small angle spectrometer (SAS) is used for fast particles with angles smaller than 30 mrad. Both spectrometers are equipped with detectors for track measurements. The two spectrometer magnets, SM1 and SM2, are used for the momentum determination. The magnet in the first spectrometer, SM1, has an integrated field-strength of 1.0 Tm. In the second spectrometer, SM2, is used for the measurement of higher momenta and has therefore a higher field-strength of 4.4 Tm.

The fixed-target geometry of the spectrometer entails a large gradient of the particle rates in the plane perpendicular to the beam direction. This gradient is reflected in the choice of tracking detectors covering the different segments of this plane. For detectors in regions with high particle rates, high spacial and temporal resolution are needed besides the ability to operate under high particle fluxes. At larger distances from the beam, the requirements on the resolution become less important than the need to cover large surfaces. As a result, many different technologies are used for the tracking detectors.

In the beam region, tracking detectors are exposed to very high particle rates. In this region, detectors are used to measure the beam and to detect particles that are scattered at very small angles with respect to the beam. These detectors require good time-resolution and short dead-time because of the high rates they have to withstand. In COMPASS, this is achieved with 8 scintillating fibre hodoscopes placed over the full length of the spectrometer. These hodoscopes consist of stacks of scintillating fibres, that are read out through photo-multiplier tubes. The distance between two channels lies between 0.4 cm and 0.7 cm leading to an overall resolution of the measured position of $130\mu\text{m}$ to $210\mu\text{m}$.

In addition, in the zone before the target three stations of silicon micro-strip detectors are used to measure the position of the incoming beam particles with a resolution of about $15\mu\text{m}$. Because of their relatively bad time resolution, they are combined with two scintillating fibre hodoscopes to the so-called beam telescope. The position of the incoming beam particle measured by the beam

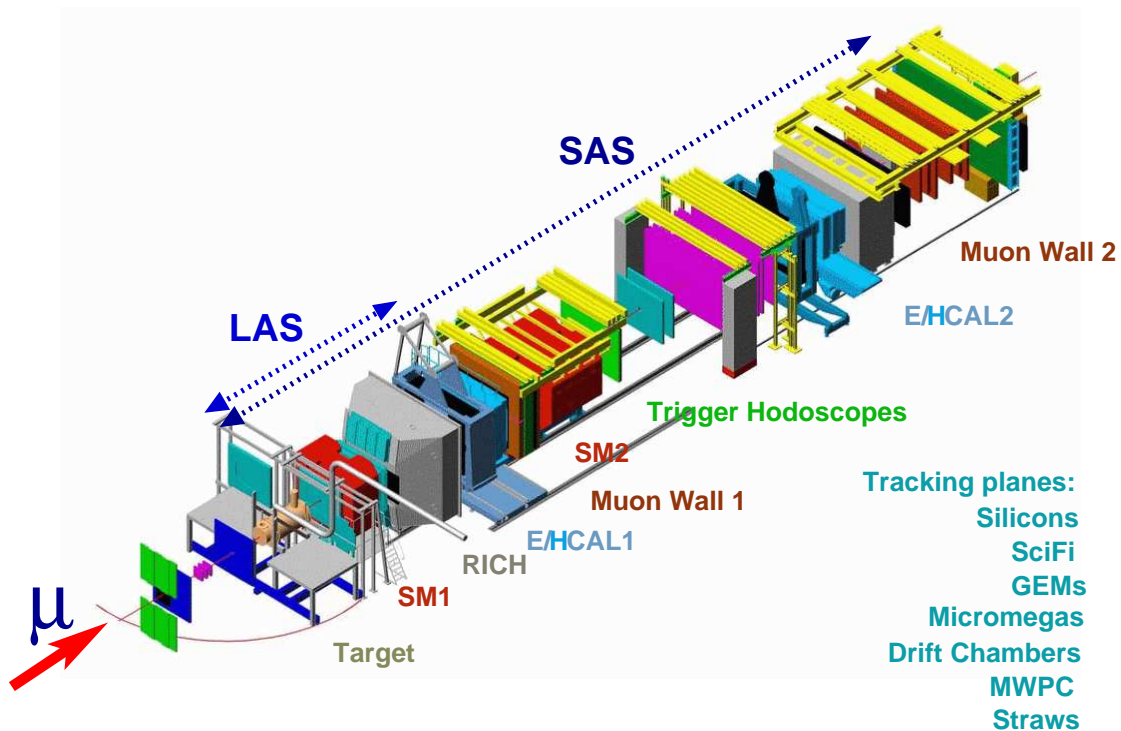


Figure 2.4: Schematic view of the COMPASS spectrometer.

telescope has such a high resolution, that it determines the two transverse coordinates X, Y [†] of the measured interaction vertex.

The Z -coordinate of the interaction vertex is determined from the crossing of the beam-trajectory and the trajectory of outgoing particles. To obtain a good track resolution for the outgoing tracks, 12 micro-mesh gas detectors (“Micromegas”) are placed immediately behind the target. These gas detectors use a micro-strip read-out, with which a spatial resolution of $90\mu\text{m}$ was achieved. The technological speciality of the Micromegas is a micro-mesh that divides the gas volume of the detector into two regions. In the larger conversion region, the space charge induced by a passing particle is collected. In the only $100\mu\text{m}$ thick amplification region, this charge is amplified using a very high potential. The micro-mesh limits the amplification process to the region close to the anode, which ensures a fast evacuation of positive ions. In combination with the high granularity of the detector, this results in a high rate capability and an improved time-resolution of around 9ns . The active area of the detectors is $40 \times 40\text{cm}^2$ with a central hole of $5 \times 5\text{cm}^2$. Together with scintillating fibre stations covering their central hole, the Micromegas can be used to detect all outgoing particles up to angles of 70mrad .

At larger distances from the target, GEM detectors are used to cover the area of up to 20cm around the beam-line. These detectors use a different technology to limit the electron amplification to a

[†]In COMPASS, a right handed coordinate system is used. The Z -direction of this system is given by the horizontal direction of the beam at the position of target, the X -axis is the horizontal direction, the Y -axis the vertical direction in the plane transverse to the beam. The origin of the coordinate system lies in the COMPASS target.

very confined region with a strong electric field. The amplification region of the GEM detectors are small holes in copper-coated Capton foils. Across the foils, a potential difference is applied. Inside the holes, the strong electric field multiplies the charges by up to a factor 20. Each detector uses a stack of three foils to guarantee a safe and stable operation. The read-out of the electric signal is done via anode strips, providing a spacial resolution of $50\mu\text{m}$ and a time resolution of around 12 ns.

To cover the angular acceptance of 180 mrad, larger area tracking detectors are used. To this class of detectors belong multi-wire proportional chambers, drift chambers and straw drift tubes. All of these detectors detect crossing particles by collecting the electrons from ionisation on signal wires. The read-out electronic records the time of the arrival of the signal on the wire, thus measuring the drift time of the electrons in the detector. This allows a spacial resolution that is better than the resolution obtained from the wire spacings. The time resolution of the measurement is therefore directly related to the spacial resolution. The use of these detectors is possible, because in the outer regions of the spectrometer the detectors are not exposed to high particle rates. To ensure their safe operation, the large area tracking detectors have holes around the centre where the particle flux becomes too high.

Each of the two spectrometer stages is equipped with a calorimeter system. Before 2006, the system in the large angle spectrometer consisted of only a hadronic calorimeter (HCAL1), while in the small angle spectrometer an electromagnetic calorimeter (ECAL2) and a hadronic calorimeter (HCAL2) were installed. The hadronic calorimeters absorb the incident hadrons and measure the deposited energy. They are build as sampling calorimeters, consisting of several layers of iron and scintillating material. Inelastic reactions in the iron plates cause a cascade of secondary particles. The secondary particles are detected through the radiation of photons in the scintillator layers of the calorimeter. The photons are detected by photo-multipliers and converted to electronic signals. The integral of all light signals is a measure of the energy deposited in the calorimeter. The quick response of the scintillators in the hadron calorimeter makes it suitable as an energy trigger signal for the spectrometer.

The electromagnetic calorimeter ECAL2 in the second spectrometer is a homogeneous lead glass calorimeter, where the energy deposition and detection occur in the same medium. The electromagnetic shower is produced in the interaction between the incoming particle and the heavy nuclei of the lead glass. The shower electrons are detected through their emission of Cerenkov light. The light produced in the lead glass modules is converted to electronic signals by photo-multipliers.

Behind the two calorimeter systems so-called “Muon Walls” are used to unambiguously identify muons in the spectrometer. These detectors take advantage of the fact, that muons, unlike hadrons, penetrate large amounts of material before being stopped. To identify muons by this characteristics, the two Muon Walls consist of a combination of tracking detectors and hadron absorbers. In the large angle spectrometer, Muon Wall 1 has two tracking stations separated by a 60 cm iron absorber. Each detector stations consists of four layers of mini drift tubes covering an area $400 \times 200\text{cm}^2$. Muon Wall 2 in the second spectrometer has a 2.4 m thick concrete absorber, which is placed directly behind HCAL2. Behind the absorber, two stations with each six layers of steel drift tubes covering an area $447 \times 202\text{cm}^2$ are installed. In the beam region, these detectors have a whole of $100 \times 80\text{cm}^2$ which is covered by multi-wire proportional chambers.

In COMPASS, more than 300 tracking planes are installed in the two spectrometers. They are

arranged in different detector stations with at least two different wire-orientations. Besides the X and Y orientation with vertical and horizontal read-out wires, inclined planes U and V are used, where the wires have a angle between 5° and 45° with the horizontal and vertical directions. The inclined planes are needed to resolve ambiguities caused by two or more particles crossing the same detector plane. Many detector stations have therefore planes with at least three different orientations. In addition, on many stations more than one detector plane is used with the same orientation. Through this arrangement of more than one tracking plane at the same Z -position, the redundancy in the tracking system is ensured.

2.4 The Ring Imaging Cerenkov Detector

The Ring Imaging Cerenkov Detector [68, 69] is used to separate the outgoing hadrons into pions, kaons and protons. It is placed behind SM1 and covers the full angular acceptance of the first spectrometer. Its main component is a large gas vessel with a volume of about 80m^3 .

A high energetic particle crossing this gas vessel emits Cerenkov photons along its path. The emission angle of the photons θ_C depends on the momentum and the mass of the particle and is given by

$$\cos\theta_C = \frac{1}{n\beta} = \frac{1}{n} \sqrt{1 + \frac{m^2c^2}{p^2}} \quad (2.2)$$

In COMPASS, the particle momentum is determined from the particle's track in the spectrometers. Thus, a measurement of θ_C provides the means to identify the particle from its rest mass.

The momentum range, where this particle identification method can be applied, is limited. Before a particle will emit Cerenkov photons, its momentum has to exceed the threshold for Cerenkov emission. From equation 2.2 it is clear, that Cerenkov emission only takes place, when

$$\frac{1}{n\beta} \leq 1 \quad . \quad (2.3)$$

Thus, the Cerenkov threshold depends on the refractive index n of the gas mixture used, as well as on the particles mass. For the radiator gas C_4F_{10} used for the RICH, the refractive index is $n_{\text{C}_4\text{F}_{10}} = 1.00153$ at 1 bar and a temperature of 20°C . The corresponding Cerenkov thresholds are 2.5 GeV, 8.9 GeV and 16.9 GeV for pions, kaons and protons, respectively.

The upper momentum limit for the particle identification is related to the fact, that the RICH provides a measurement of β . For high momenta, the difference in β between a pion and a kaon becomes very small. Thus, the particle identification through a measurement of β is no longer reliable. In the analysis presented in this thesis, an upper momentum cut for the particle identification of 50 GeV is used.

Figure 2.5 gives a schematic overview of the RICH detector. The Cerenkov photons emitted by the particles crossing the gas vessel are focussed onto the read out systems on the upstream side of the detector. On this read-out plane, the photons emitted by one particle build ring segments. The radius of these rings are a measure of the Cerenkov angles.

The focussing of the Cerenkov photons is achieved using a system of 116 spherical mirrors. The

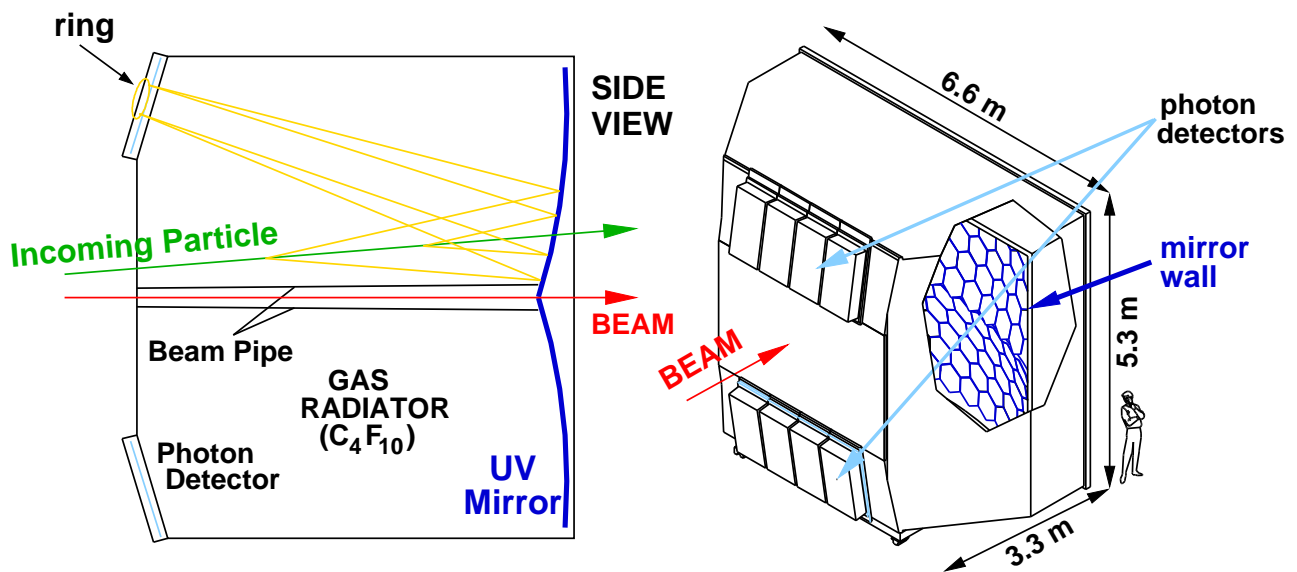


Figure 2.5: Schematic view of the RICH detector. The photons emitted by the particles are focussed onto a read-out system on the upstream side of the detector. This is achieved with a system of two spherical mirrors.

mirror plane is split into an upper and a lower part, which have a small tilt relative to the vertical plane, so that the photons are reflected either up- or downwards onto the two photo-detectors. With this geometry, the photo-cathodes are installed outside the acceptance of the spectrometer in a region with lower particle rates.

For the detection of the Cerenkov photons, multi-wire proportional chambers with CsI photo cathodes are used. The two systems in the upper and lower part of the detector consist each of 4 chambers. Their sensitive surface of 5.3 m^2 is covered with CsI photo cathodes of $8 \times 8\text{ mm}^2$, giving a total of 84000 read-out channels.

2.5 The Data Acquisition System

The COMPASS data acquisition system (DAQ) [70] collects the data produced in the over 200000 detector channels of the COMPASS spectrometer and combines them to the detector events stored on tape.

This is done in several steps. In the front-end electronics, which are mounted directly on the detectors, the information is digitised immediately on reception from the detector channels. After the arrival of a trigger signal from the trigger control system (TCS), the data are transferred via fast links to readout-driver modules named CATCH and GeSiCA. These modules combine the data from up to 16 front-end cards into sub-events, before transmitting them via optical fibres into the

central DAQ.

The computer system of the DAQ is organised in two separate clusters. The read-out buffers (ROBs) collect the data sent by the CATCHES and store them on spill-buffer cards. Each ROB only receives the data from the detector components it is connected to. The spill-buffers are capable of storing the data from more than one spill at the same time.

The detector events are assembled from the information of the ROBs by the event builders (EOB). The events builders constitute a cluster of 12 computers working in parallel to process the data delivered by the spectrometer. After their combination, the online filter is applied to the detector events. This software is run on all event builders. It has two components. The software trigger selects good events using algorithms for the raw detector information. In 2004, the algorithm consisted in a verification, that the event contained a beam track with enough hits in the BMS to reconstruct its momentum. In addition, a quality filter is used to remove events with too many errors in the collected data.

From the event builders the data are directly transferred to the CERN computer centre, where they are stored on tape. The DAQ stores the collected data in samples of about 200 spills, called run. Each spill contains around 50000 event with an average size of 40kB, corresponding to a data volume of around 2 GB per spill. During one year of data taking, several hundred Terabyte of data are recorded.

2.6 Changes to the Spectrometer after 2004

The long SPS-shutdown between the run in 2004 and 2006 made it possible to introduce several large improvements to the spectrometer. Here, only the most important changes will be mentioned. Additional information about the upgrade projects can be found in [64].

The most significant improvement was the installation of a new target solenoid with an increased angular acceptance of 180mrad instead of the 70mrad available for the previous target magnet. To ensure track reconstruction over the enlarged acceptance the tracking detectors in the LAS were rearranged and new tracking stations were added. Since the spectrometer was originally designed for a 180mrad acceptance, the RICH detector in the LAS already covered this acceptance. The same was true for the hadronic calorimeter and the muon wall installed in the first spectrometer.

The RICH detector was improved significantly during the break in 2005. The system for photo-detection in the inner four sectors of the RICH was replaced. The new system based on MAPMTs allows a more efficient background rejection due to a high time resolution of a few ns. Besides the photon-detectors also new optical telescopes were installed reducing the signal distortion in this region. In the outer parts of the RICH, the electronic read-out of the photo-cathodes was exchanged to reduce the time gates used in the read-out. With the improvements of the RICH detectors a better association of detected photons to the particles of the event was achieved and a better suppression of uncorrelated background was obtained. This has greatly enhanced the signals of hadrons in the RICH. Most importantly, the efficiency and purity of the kaon identification have increased strongly leading to an improvement by a factor of about 2 in the effective signal of the reconstructed D -mesons.

The third big improvement of the spectrometer was the completion of the calorimeter system of

the LAS with the installation of an electromagnetic calorimeter, providing the possibility to detect photons and neutral pions, that were scattered at large angles. The lead glass calorimeter, ECAL1, with similar properties as ECAL2, was installed in the free space between the RICH and HCAL1. Before the calorimeter, a pre-shower detector, so-called “RichWall”, was installed. The shower process of electromagnetic and hadronic particles start in this detectors, which is a combination of drift chambers and lead plates, allowing a better detection of the impact point of the particles on the calorimeters. The effect of the completion of the calorimeter system in the first calorimeter will also be discussed in the next chapter, where the trigger system is presented.

Chapter 3

The Trigger System in the Runs 2006 and 2007

The COMPASS experiment uses a single layer trigger system to detect inelastic interactions between the incoming muons and the target material. The main event signature used for triggering is a muon, whose momentum and angle are changed during the scattering in the target. The second trigger criterion are energy deposits in the calorimeters indicating that high energetic hadrons were produced. Because of the large halo component, a veto system is used to ensure the sensitivity of the trigger to interactions inside the COMPASS target only.

As described in section 2.6, several changes were introduced to the COMPASS spectrometer before 2006. As a consequence, the trigger system was adapted to the new situation. On one hand, a new veto detector was build, that could be operated in the magnetic field of the new target. On the other hand, the new electromagnetic calorimeter ECAL1 was added to the trigger scheme. The addition of ECAL1 to the spectrometer introduced a considerable change in the trigger setup. Therefore, several studies were performed to optimise the use of information from ECAL1 and HCAL1 in the trigger.

This chapter puts a special focus to the changes introduced to the trigger system before the runs 2006 and 2007. It starts with a short introduction to the muon trigger system, as it was used in 2004 and with some changes also in 2006 and 2007. A detailed description of the trigger system as it was used in the year 2004 can be found in [71]. The second section of this chapter is then dedicated to a discussion of ECAL1 and its integration to the muon trigger. The last section will present the new veto station build for the operation close to the new target magnet.

3.1 The COMPASS Muon Trigger

The COMPASS muon trigger system is designed to be sensitive for deep-inelastic scattering events with large momentum transfers $Q^2 > 0.5 \text{ GeV}^2$ as well as quasi-real photo-production events ($Q^2 \approx 0 \text{ GeV}^2$). To cover such a large kinematic range of interactions, the trigger uses several hodoscope systems to detect and identify the scattered muon. Each hodoscope system is composed of two hodoscopes located at different Z -positions in the spectrometer. In the case of horizontal

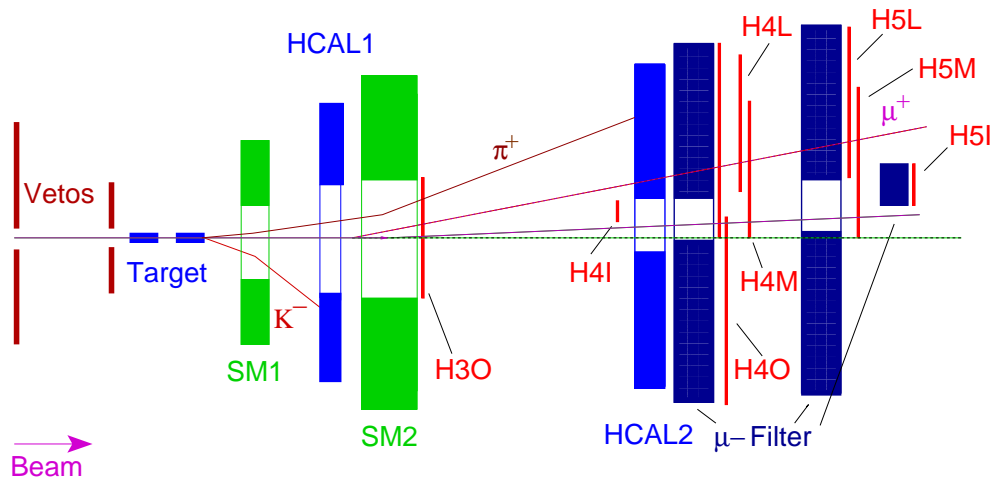


Figure 3.1: Location of the different trigger components in the spectrometer.

strips, the information of the two hodoscopes can be combined to measure the vertical component of the scattering angle (vertical target pointing). Hodoscopes with vertical strips are used for an estimation of the energy of the scattered muon. For this, the vertical strips provide two positions in the bending plane of the spectrometer magnets. This measurement is used for the quasi-real photo-production, where the scattering angles are extremely small.

Besides the information from the hodoscopes, the energies deposited in the calorimeters are used for triggering. Large energies in the calorimeters are a sign for an inelastic interaction. Thus, the information about energies in the calorimeters can be used to improve the selectiveness of the hodoscope triggers. In addition, one can directly trigger on large energy deposits of the calorimeters. Such a stand-alone calorimeter trigger is sensitive to events, where the scattered muon is not seen. It contributes mainly in kinematic regions that are geometrically not covered by the hodoscope systems. In the years 2002-2004, the trigger only used information coming from the hadron calorimeters HCAL1 and HCAL2. After 2006, the signals from ECAL1 were also available, which will be presented in section 3.2.3.

Because of the large beam halo, neither the hodoscope triggers nor the calorimetric trigger can be used without a veto system. The veto system consists of scintillator detectors, covering the region outside the target. All muons, that do not enter the target at the nominal position, will fire the veto, which will block the trigger system.

The following three sections will give more details about these three systems of the trigger.

3.1.1 The Hodoscope Systems

The trigger system uses four different hodoscope systems. Their positions are shown in figure 3.1. The hodoscope triggers for quasi-real photo-production are the “Inner Trigger” (H4I and H5I) and the “Ladder Trigger” (H4L and H5L). They have vertical strips and are used for an estimation of the energy loss nu in the interaction. The hodoscopes for “Outer Trigger” with horizontal strips (H30

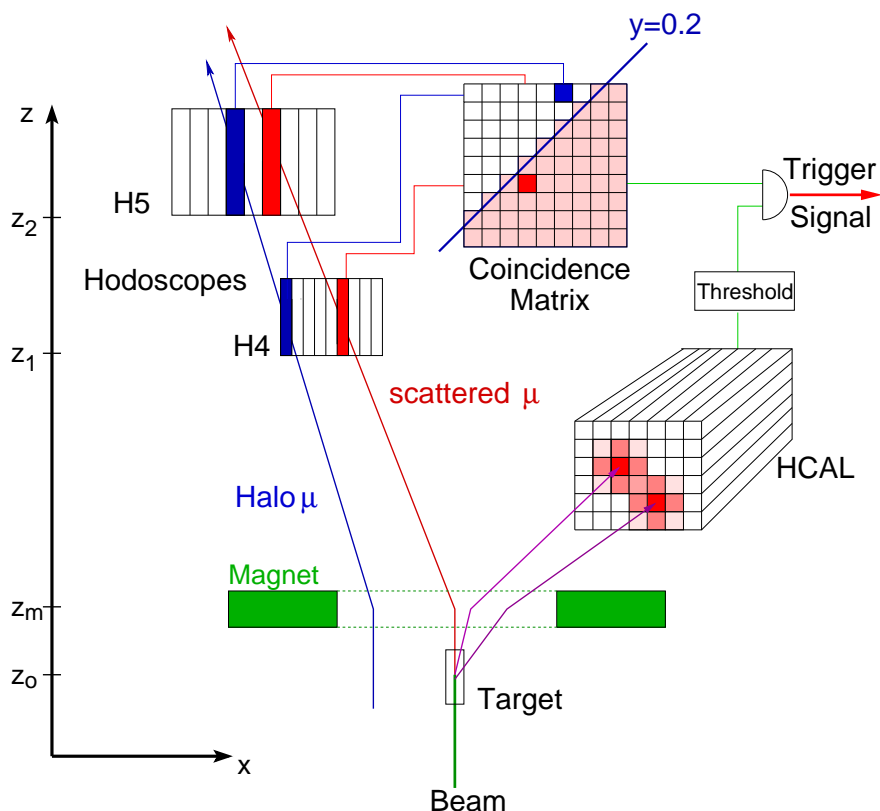


Figure 3.2: Illustration of the trigger concept of the energy loss trigger.

and H4O) are used for vertical target pointing. The “Middle Trigger” consists of four hodoscopes, two of which have horizontal (H4MH and H5MH) strips and two with vertical strips (H4MV and H5MV). It can be used for an estimation of the muon energy as well as the vertical component of its scattering angle.

As shown in figure 3.1, at least one hodoscope of each system is placed behind a hadron absorber. These hodoscopes are therefore also used to separate the scattered muon from outgoing hadrons. A trigger can only be produced, if both hodoscopes detect the particle.

For triggering on the energy loss of the muon in the target, the energy of the scattered muon is estimated from its horizontal deflection in the spectrometer magnets. The trigger scheme for quasi-real photo-production is constructed to efficiently select muons with a minimum energy loss above $y > 0.2$. Events with a smaller energy loss are not interesting for the asymmetry measurements performed by COMPASS, because the depolarisation factor D (see equation 1.25) becomes small for very low y . The principle of the energy loss trigger is illustrated in figure 3.2. The two muon hits in the hodoscopes are correlated electronically using a coincidence matrix. In this matrix a check is done, whether the hit is coming from a muon scattered in the target, or a beam particle. A muon, that has lost energy in the target, is deflected differently in the spectrometer magnets than the beam and will therefore have different hit combinations on the hodoscopes. The

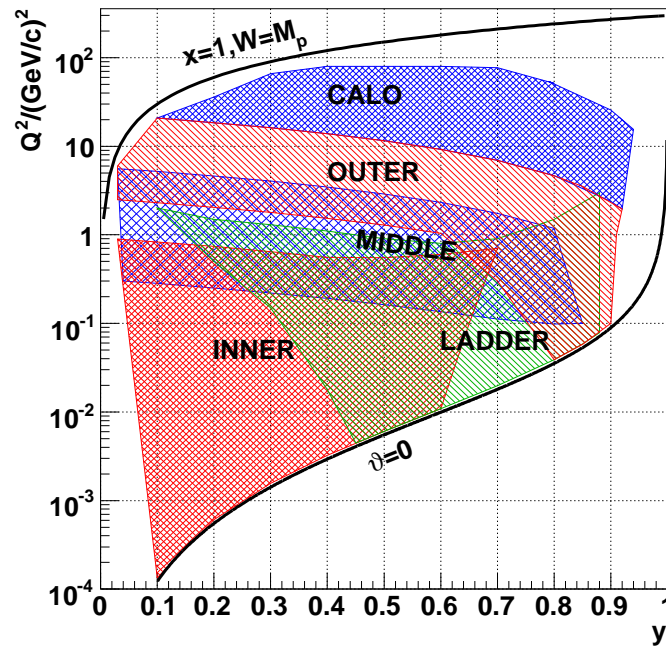


Figure 3.3: The kinematic plane and its coverage by the different trigger systems.

illustration of the coincidence matrix shows the pattern of allowed hit combinations. For each strip in the first hodoscope, there is one strip in the second hodoscope corresponding to $y = 0.2$. This strip combination corresponds to a good combination for the energy loss trigger. In addition, all combinations where the strip in the second hodoscope is farther left, are also allowed. They correspond to an energy loss $y > 0.2$.

Figure 3.2 also indicates, that the information from the hodoscopes is combined with signals from the calorimeters to build the trigger. This additional requirement is needed due to the strong background from elastic-scattering off target electrons, radiative interactions with nuclei and the beam halo. None of the background processes are expected to produce hadrons with large energies. Therefore, the addition of the calorimeters to the energy loss trigger provides a good possibility to increase the trigger purity.

The vertical target pointing of the triggers for deep-inelastic scattering has a similar set-up as the energy loss trigger. The signals of the two hodoscopes are combined to the trigger signal using a coincidence matrix. The pattern of allowed hit combinations is different. For each horizontal strip of the first hodoscope, only one strip in the second hodoscope can be fired, if the muon is coming from the target. Thus, the matrix pattern for the vertical target pointing corresponds to one band of allowed combinations.

The geometry of the four hodoscope systems of the COMPASS muon trigger was chosen to fully cover the kinematic $y - Q^2$ plane. This is shown in figure 3.3, where the kinematic ranges of the different triggers are shown. The “Inner Trigger” is used to cover the range of smallest y and Q^2 . To access really small y , the two “Inner” hodoscopes are located close to the nominal beam

position. To cope with the high particle flux at this position their strips have a width of 6 mm (H4I) and 12 mm (H5I), keeping the rates of individual strips and, thus, the rate of random coincidences to a reasonable level. The “Ladder Trigger” complements the “Inner Trigger” in the low Q^2 range. It is placed farther away from the beam and is used to detect larger energy losses. The strips of the “Ladder” hodoscopes are increasing in width for larger angles. This allows a coverage up to very large values of y with the 32 channels available for the coincidence matrices.

The geometries of the two hodoscope systems for vertical target pointing reflect the accuracy with which the angle of the outgoing muon can be measured. Due to multiple coulomb scattering inside the solid state target as well as inside the hadron absorbers, the angles of the scattered muons display a Gaussian smearing around their true value. At the level of the hodoscopes, this smearing amounts to several centimetres. The widths of the hodoscopes were therefore set to 6.2 cm and 7.7 cm for the “Middle Vertical” hodoscopes (H4MV and H5MV). For the “Outer Trigger” the scintillator strips with 7 cm are used for H3O, which is placed before the hadron absorber, and strips with 15 cm are used for H4O.

3.1.2 The Calorimetric Triggers

The trigger concept for the calorimeter trigger is based on the energy deposits in clusters of calorimeter modules. The use of clusters instead of an energy sum of each calorimeter is necessary, because of the large amount of halo muons crossing the calorimeters and leaving small energy deposits. By looking only at small regions of the calorimeters, a fake trigger produced by two or more halo muons crossing the calorimeter at the same time can be suppressed.

The clustering of calorimeter modules is done using the analogue sums of the modules. The summation electronic takes a small fraction of the analogue signals of each module before the rest of the signals are converted into digital signals for the standard read-out. The trigger uses the energy deposited in regions of 4×4 calorimeter cells calculated from the sum of the analogue signals. To avoid inefficiencies at the edges of the 4×4 -cell regions, the summing is done in two steps and four layers, as illustrated in figure 3.4. In a first step, the analogue signals coming from 2×2 -cells are summed up. Four copies of the resulting sums are then used to build four different sums with 4×4 -cells, where it contributes the upper right, upper left, lower right and lower left part of the sum. In figure 3.4 the sum of 2×2 -cells shown by the four filled squares is used for the four sums of 4×4 -cells that are shown by the four big hatched squares. This is also illustrated in the sketch showing the two summation steps. The signal from the first summation step is used in four of the second summations steps.

The result of this staggered summation are four complete layers of sums of 4×4 -cells. Inefficiencies for cluster detection occurring between two summation regions of one layer are compensated in the other layers. For triggering purposes, the signals in the 4×4 -cells are discriminated using constant-fraction discriminators. The discriminator electronics provides two useful features for the trigger. First, not one threshold, but two independent thresholds can be applied to each sum providing also two independent signals for the trigger. In addition, the discriminator information of all sums from one layer can be evaluated together to apply conditions on the number of clusters, that were found. This requirement on the cluster multiplicity is useful in situations, where more than one hadron is produced in the primary interaction.

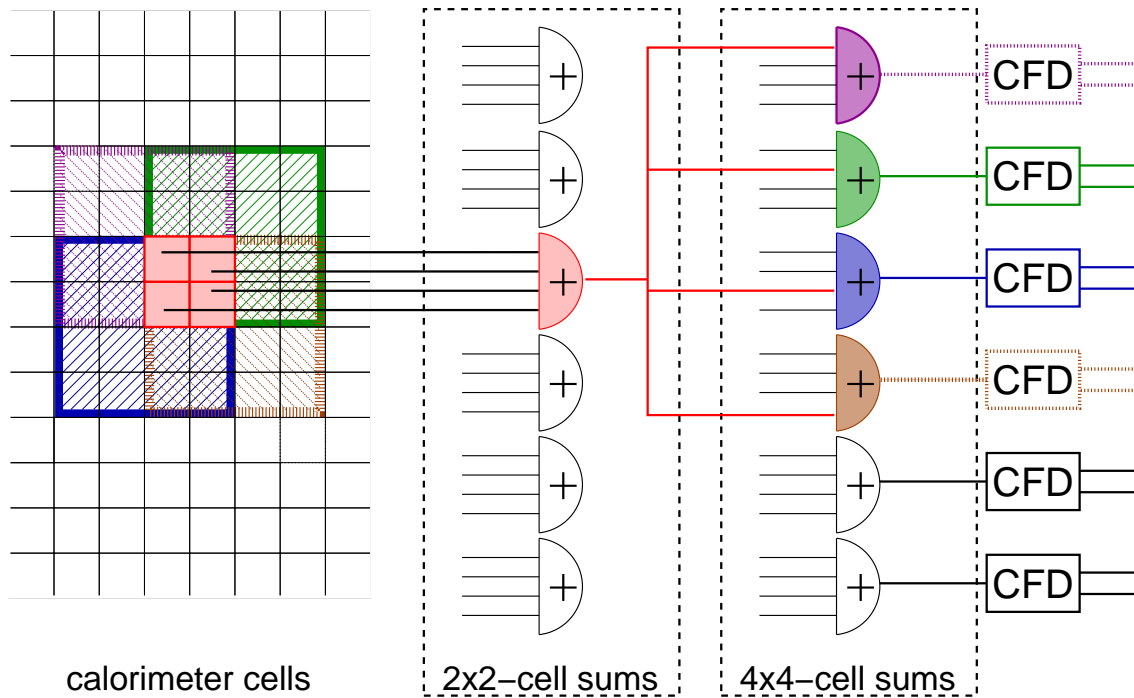


Figure 3.4: The summation scheme of the two calorimetric trigger systems: From the analogue signals of the individual cells the amplitudes of 2×2 -cell squares are built. Each amplitude is used in the determination of four 4×4 -cell squares, where it takes up the lower right lower left, upper right and upper left parts of the larger sums. In this example, the sum of 2×2 -cells indicated by the filled square is used in the four sums of 4×4 -cells illustrated by the four hatched boxes.

The information of the calorimetric trigger contributes to the full trigger system in two ways. On one hand, the calorimeter information helps to suppress background in triggers, that also use hodoscope systems. On the other hand, the pure calorimetric trigger is used as a stand-alone trigger to reach regions of higher Q^2 . The trigger thresholds used for the two applications are chosen independently. The threshold for the stand-alone trigger is set to higher values than for the signal, which is combined with the hodoscopes. This reflects the fact, that in the combined trigger the information of two systems is used together, which already provides a better background suppression.

The thresholds for the energy deposition are chosen as a multiple of the minimum ionising particle energy deposit (MIP) in the calorimeters as the largest background signal in the calorimeters is coming from halo muons. One MIP corresponds to 1.8 GeV in HCAL1 and 2.3 GeV in HCAL2. For the calorimetric contribution to the hodoscope triggers a low threshold of 3 MIP was used. This threshold was applied on one of the discriminators of each layers. A second contribution to this signal was coming from the second discriminators of two layers, where in addition to an energy threshold of 2 MIP the requirement for a cluster multiplicity of two was implemented.

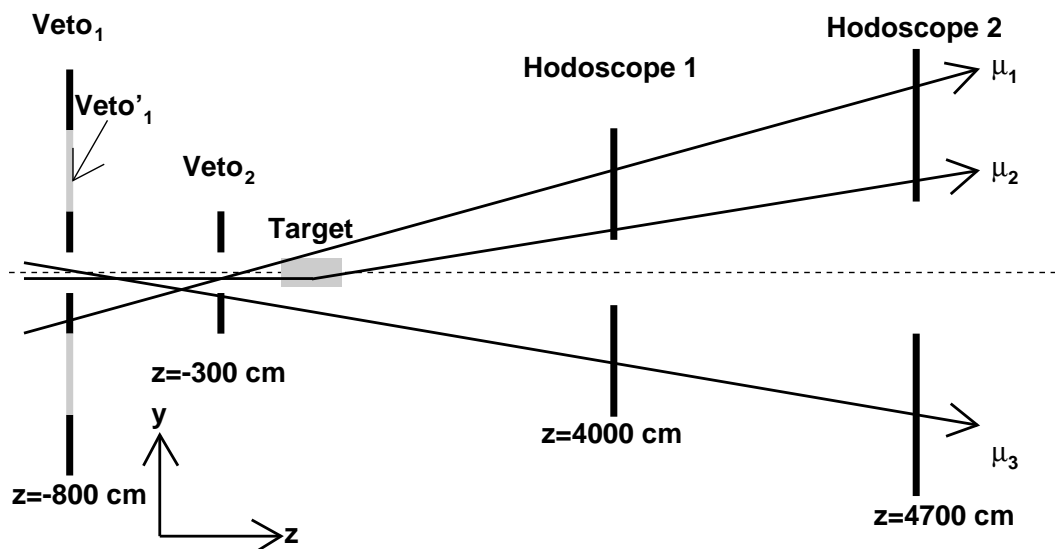


Figure 3.5: The principle of the veto system for fake scattered muons. The trajectory labelled μ_2 corresponds to a beam muon scattering in the target, that causes a trigger in the hodoscopes. The two other trajectories (μ_1 and μ_3) are from halo muons, that would cause a trigger, which is suppressed by the veto system.

The second discriminators of the remaining two layers were used for the pure calorimetric trigger. Because of the strong dependence of the trigger rate on the selected threshold, the threshold was adapted to the capacity of the data acquisition. In 2004 a value of 4 MIP was selected, while in the years before a much higher threshold around 9 MIP was used. The threshold setting of 2006 and 2007 will be discussed in the context of the new trigger using the electromagnetic calorimeter ECAL1.

3.1.3 The Veto System

The purpose of the veto system is to suppress triggers that were induced by halo muons. For the triggers based on vertical target pointing, they constitute the main source of background. For their suppression the veto system before the target is very important.

Halo muons cause triggers in two ways. They can interact with material in the spectrometers producing hadrons that deposit enough energy in the calorimeters to provoke a trigger. Secondly, a muon crossing the spectrometer under a certain angle can fake a scattered muon in one of the hodoscope systems and, by this, cause a trigger. This is illustrated in figure 3.5. To suppress these fake triggers, several veto detectors are placed in front of the target. If any of the veto detectors is hit by a halo muon, the veto system blocks all triggers.

The veto system essentially consists of two stations, Veto₁ and Veto₂ placed at 8 m and 2 m before the target. Veto₂ consists of one detector with 4 small scintillators covering a surface of $30 \times 30 \text{ cm}^2$ with a beam hole of 4 cm diameter. Veto₁ is a composition of several detectors. The smallest, inner

detector is of similar size as Veto₂, while two detectors with larger scintillator strips are used to cover a surface similar to that of the calorimeters. This choice of detector sizes was done to obtain a good time resolution in the region, where the halo has high rates. With a good time resolution, small veto gates can be applied, which reduces the dead time of the veto system.

While Veto₁ essentially suppresses all muons outside the beam spot, Veto₂ was added to limit the beam divergence. The two holes of Veto₁ and Veto₂ allow the maximum divergence of the beam to be 7 mrad. Since this is too large for an efficient suppression of halo induced triggers in the “Middle Trigger”, a third veto station with 4 small detectors around a beam hole of 10 cm diameter was placed 20 m upstream of the target.

From the different veto detectors, two veto signals are build. The so-called V_{tot} is the logical “OR” of all veto detectors. It is used for the pure “Calorimeter Trigger”, the “Outer Trigger” and the “Middle Trigger”. The systems triggering on energy loss are less sensitive to halo muons. Therefore, no veto is applied on the “Inner Trigger”. The “Ladder Trigger” is combined with different veto signal, that only contains the information of the outer two detectors of Veto₁. This is needed due to the geometrical overlap of the “Ladder Trigger” and the hadron calorimeters.

3.2 The Introduction of ECAL1 to the spectrometer

Before the data taking in 2006 the electromagnetic calorimeter ECAL1 was installed in front of HCAL1. For the trigger, this resulted in two changes of the set-up compared to 2004. On one hand, a trigger for ECAL1 was installed, on the other hand, the trigger conditions for HCAL1 needed to be revised. Because of the additional material in front of HCAL1, the energy deposited by hadrons in HCAL1 is decreased. For HCAL2, the introduction of ECAL1 had no effect.

3.2.1 The Electromagnetic Calorimeter ECAL1

The electromagnetic calorimeter ECAL1 consists of 1500 lead glass modules that are read out with photo multipliers. To cover its surface of $4 \times 2.9 \text{ m}^2$ three different module types with different cell sizes are used. The geometry of ECAL1 is shown in figure 3.6. The largest cells, called OLGA blocks, are used to cover the outer parts of ECAL1. In this region only small particle rates are expected, therefore, only a moderate space resolution is needed. In the central region, the upper and lower parts of the calorimeter are filled with so-called MAINZ blocks and the central part is covered with even smaller modules, named GAMS blocks. The three types of lead glass modules and their properties are presented in table 3.1. All three modules have been used in previous experiments, where their properties were determined, and who gave the modules their names.

3.2.2 The Effect of ECAL1 on the Trigger

Before ECAL1 was introduced to the spectrometer, the Muon-Trigger System, as presented in the previous section, was performing with high efficiency, selecting not only events within a large kinematic region, but also with one or more hadrons in the final state. Therefore, it was very desirable that the properties of the trigger should change as little as possible between the runs in 2004

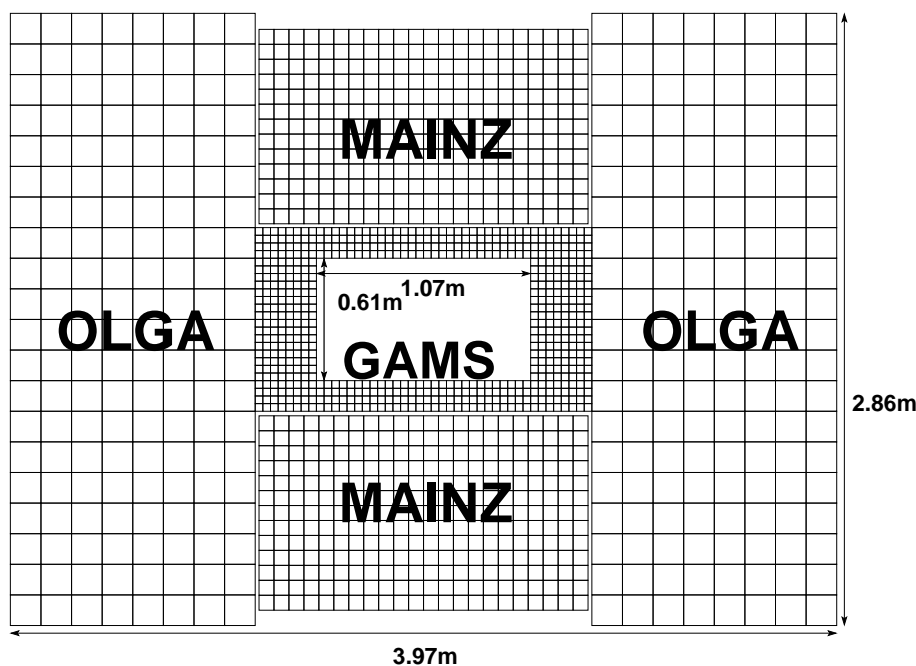


Figure 3.6: The layout of the electromagnetic calorimeter ECAL1.

and in 2006.

The introduction of ECAL1 had, however, a large effect on the trigger, since it changed the hadronic energy deposits in HCAL1. Therefore, some effort was made to understand the behaviour of hadrons being stopped in the double-calorimeter ECAL1-HCAL1 and, as a consequence, to adjust the trigger system to the new situation. This adjustment was done in two steps. During the run in 2006, the settings for HCAL1 were adapted to the new situation and a new trigger system for ECAL1 was designed and tested [76]. Only after these test were finished, a full trigger system for ECAL1 was developed and added to the trigger in 2007.

Results of Monte Carlo Studies

Before the installation of ECAL1, Monte Carlo generated events were studied for a first estimation of the effect. For the generation, the open-charm production process in photon-gluon fusion was chosen, because this channel is used in the evaluation of the gluon polarisation, the main physics goal of the COMPASS experiment. The analysis uses events where at least two hadrons are produced. Open charm events are therefore well-suited to study the effect of ECAL1 on hadrons. For each generated Monte Carlo event, the detector response was simulated twice, once with and once without the ECAL1 in the spectrometer. The reconstructed events from the two simulations were compared and from the number of reconstructed D^* -mesons in the two Monte Carlo samples, a possible effect of ECAL1 was estimated. A total of 25000 events were processed in this way. For this study, a preliminary description of ECAL1 in the COMPASS spectrometer was used, which

ECAL1 Modules

	OLGA	MAINZ	GAMS
Lead Glass type	SF5	SF57	TF1
PbO-Content (mass)	55	75	50
Density [g/cm ³]	4.08	5.51	3.86
Radiation length X0 [cm]	2.54	1.55	2.74
Molière radius [cm]	4.3	2.61	4.7
Surface [cm ²]	14 × 14	7.5 × 7.5	3.82 × 3.82
Length [cm]	47	36	45
Length [X0]	18.5	23.3	16.42
Energy resolution: $\frac{\sigma(E)}{E}$	$\frac{0.15}{\sqrt{E[\text{GeV}]}} \oplus 0.08$	$\frac{0.070}{\sqrt{E[\text{GeV}]}} \oplus 0.02$	$\frac{0.1}{\sqrt{E[\text{GeV}]}} \oplus 0.015$
Previous Experiments	NA14 [72], WA92 [73]	WA98 [74]	NA12 [75]

Table 3.1: Properties of the three lead glass modules used in ECAL1

did not yet incorporate the full simulation of the response of ECAL1. However, the material of ECAL1 was correctly described, so the energy loss of hadrons in ECAL1 and the change of signals in HCAL1 could be estimated in this study.

The first result of this study was a reduction of the D^* signal by about 15%, when ECAL1 was part of the detector. Since the D^* -mesons are reconstructed using only the information from the tracking system, this loss in the signal was produced in the trigger system. The majority of the events with a D^* -meson in the final state are produced at very low Q^2 , where in the trigger a hodoscope signal and a signal from the calorimeters is needed. The second largest contribution is coming from the pure calorimetric trigger, which was fired by a high energetic hadron.

The same event reduction as in the D^* -signal was also observed for the background events. This confirms the connection with the trigger. The event loss itself could be reduced by applying stricter cuts on the selected D^* candidates. These selection cuts mostly result in requiring higher particle momenta for the decay products of the D^* . The dependence of the event loss on the kinematics of the D^* candidate is shown in figure 3.7. In this figure, the ratio of reconstructed events with ECAL1 to reconstructed events without ECAL1 in the Monte Carlo simulation is shown as a function of Q^2 and y (blue points, scale on the right). While this ratio is relatively flat over the range of Q^2 , a clear slope can be observed in the dependence on y . For small y , a much larger fraction of the events is not detected by the trigger. For events with a small muon energy loss y , the hadrons in the final state have small momenta, since the available energy in the final state is small. In figure 3.7, the points with the event ratios are also compared to the distribution of events

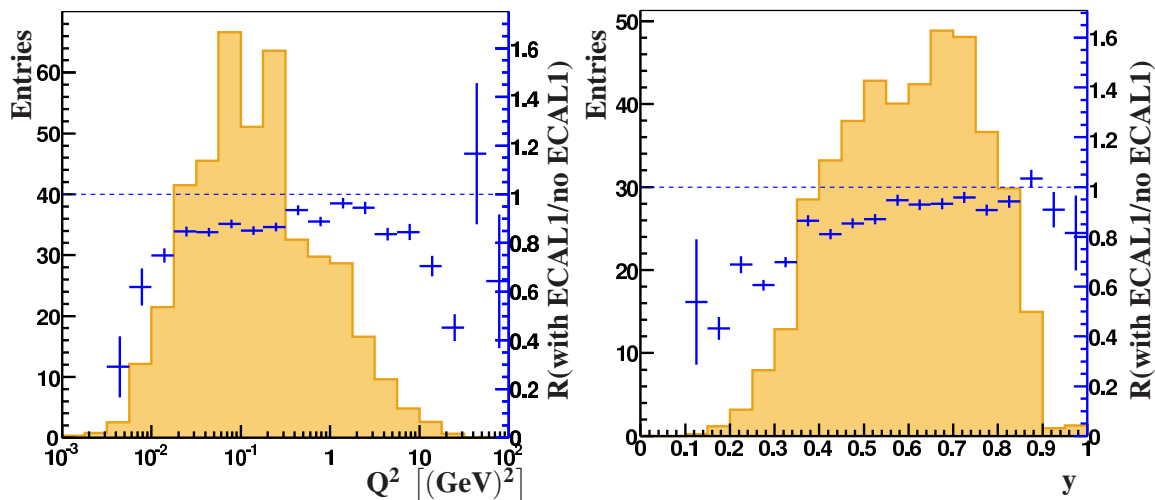


Figure 3.7: The dependence of the event loss on Q^2 and y . The blue points (scale on the right) show the ratio of reconstructed D^* events from the simulation with ECAL1 in the spectrometer to the reconstructed D^* events without ECAL1 in the spectrometer as a function of the event kinematics Q^2 and y . The filled histograms show the distribution of the events used in the asymmetry determination. The events were weighted with the analysing power a_{LL} used in the $\langle \frac{\Delta g}{g} \rangle$ analysis.

from real data taken in 2003 (filled histograms). The events in the histograms were weighted with their analysing power a_{LL}^{PGF} (see section 7.3.1). This quantity describes the sensitivity of the event to the gluon polarisation. The weighting was applied, because a_{LL} depends strongly on y . From the weighted events the overall effect on the open charm analysis can be more easily evaluated. The figure shows, that the largest relative losses appear in regions that do not contribute much to the measurement of the gluon polarisation. Therefore, only a small effect of ECAL1 on the measurement of the gluon polarisation from the open charm channel is expected. At this point it should be noted, that for other physics channels analysed in COMPASS, larger effects of ECAL1 could be expected. This is particularly the case for semi-inclusive measurements with transversely polarised target nucleons, where the sensitivity for the asymmetry is largest for small y . Therefore, a trigger system including signals from ECAL1 was designed and included in the installation of ECAL1.

As a next step, a deeper study was performed to learn more about the behaviour of the hadrons in the double-calorimeter ECAL1-HCAL1. The aim of this study was to evaluate the possibilities for triggering on the energy deposited in the two calorimeters. Due to the complex geometry of ECAL1, the possibility of a combined trigger for HCAL1 and ECAL1 was ruled out very early. The search for geometrically correlated clusters in the two calorimeters is too complex to be performed in the limits given for the trigger system. However, the possibility of including this search to the tasks of the online filter system (see section 2.5) is being investigated for the data taken for the future hadron programme.

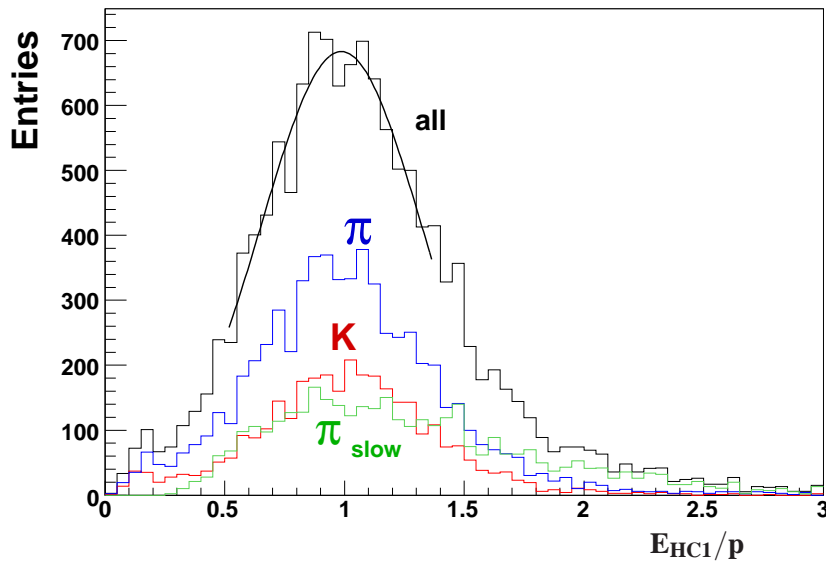


Figure 3.8: The ratio of cluster energy and track momenta in the sample without ECAL1 in the simulation. The four curves show the histograms of all hadrons together and the distributions of pions and kaons and slow pions separately. For all three decay particles of the D^* more than 95% of the particles energy is reconstructed.

The main goal of the Monte Carlo study was therefore to understand better the individual energy deposits in the two calorimeters. For this purpose energy clusters belonging to the kaons from the D^* decay were used. The momenta of these kaons are high enough to expect large energy deposits in the calorimeters. As mentioned before, the simulated events could only be used to study the clusters in HCAL1.

The most important result of this investigation is illustrated in figures 3.8 and 3.9. In both figures, the ratio of the reconstructed cluster energy E to the track momentum p is shown. Figure 3.8 displays the distribution of E/p for events from the simulation without ECAL1. The diagram contains four histograms: The black histogram is the combined distribution for all decay products from the D^* -mesons. The three other histograms show the distributions of pions, kaons and slow pions produced in the simulated D^* -events. All four histograms show a rather broad Gaussian distribution peaking at values around 0.95. Thus, for this event sample almost the full energy of the hadrons is found in the reconstructed clusters.

Figure 3.9 shows the distribution of E/p for the kaon candidates of the sample produced with ECAL1 included in the simulation. In this case, the sample is subdivided into kaons, where the standard track-cluster matching algorithm did find the corresponding cluster in HCAL1, and those kaons, where the automatic procedure did not find a cluster, but a simple minimal distance requirement could be used to find the HCAL1 clusters. In the course of this study, it was noticed, that the standard track-cluster matching failed in the case, where the hadronic shower started in ECAL1. So, the black histogram in figure 3.9 corresponds to the kaons, which started showering in ECAL1, while the red histogram is from the kaons, which only showered in HCAL1. The

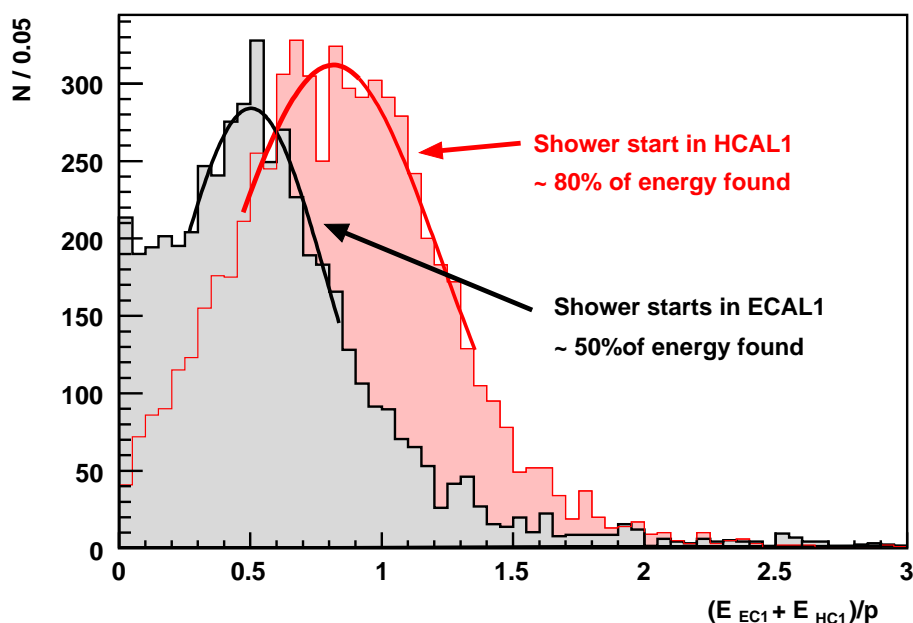


Figure 3.9: The ratio of cluster energy and track momenta in the sample with ECAL1 in the simulation. The sample of kaons from the D^* -decay was divided into kaons, where the shower started in ECAL1, and those, where it only started in HCAL1 (see description in the text for more details).

distributions show again Gaussian-like peaks, however their maxima are shifted towards significantly lower values. In the case, when the showering starts in HCAL1 and the full shower should be contained in this calorimeter, the reconstructed cluster energy only corresponds to 80% of the particles energy. For the sample, where the shower started in ECAL1, even smaller fractions of the energy are detected. The peak is at a value of 50%. In average, for the kaons observed in this sample, only 70% of the particle energy is found in the reconstructed clusters.

These results from the Monte Carlo simulation correspond roughly to the expectations for ECAL1. The depth of ECAL1 corresponds to about 1-1.2 nuclear interaction length, depending on the calorimeter modules. Therefore, one expects, that only $\sim \frac{1}{3}$ of the hadrons reach HCAL1 without starting to shower. For the particles, where the shower did start in ECAL1, one still expects to observe a significant part of the energy in HCAL1. This agrees with the findings from the Monte Carlo simulation.

Changes for 2006

From the Monte Carlo studies it was concluded, that the expected loss of hadronic events from the introduction of ECAL1 in the calorimeter could be recovered by lowering the thresholds in the trigger logic in HCAL1. For the D^* -signal it was estimated, that a lowering of the thresholds to 60 – 70% of their values in 2004 most of the loss induced by ECAL1 would be recovered.

The lowering of the thresholds was done in 2 steps. At the beginning of the data taking the lower thresholds for HCAL1, contributing to the energy loss triggers, were lowered from 3 MIP to 2 MIP. The pure calorimetric trigger was kept at its original value from 2004. The lowering of the thresholds resulted in a very strong increase of the trigger rates. For this reason, the thresholds of the pure calorimetric trigger were only lowered to a value of 3 MIP, when the online filter was activated, which increased the capacity of the DAQ. The threshold for HCAL2 were kept at the old values of 3 MIP and 4 MIP, because the situation for HCAL2 did not change between 2004 and 2006.

In addition, a test trigger system was installed in ECAL1. This system was not included to the normal physics triggers, but provided a good possibility to study the trigger signals from ECAL1. One important contribution from the test run in 2006 was, that the signals from all 1500 individual calorimeter modules were investigated.

Results from data taken in 2006

The data from the 2006 run were used to study the double-calorimeter ECAL1-HCAL1 with real data. For the development of a trigger scheme including ECAL1 signals in the muon trigger, two main questions had to be answered. The energy deposited in ECAL1 and HCAL1 by hadrons had to be measured. Secondly, the cluster sizes and shapes in HCAL1 were studied, especially for particles with a shower starting in ECAL1. A detailed report of these studies can be found in [76]. Figure 3.10 provides a summary of the studies on energy deposits in ECAL1 and HCAL1. It shows the energy sharing between both calorimeters for pion tracks in different trigger conditions. To suppress background from electromagnetic showers, only pions identified in the RICH were used. Their momentum was selected to be between 5 GeV and 10 GeV, which is the energy range, where most effects from ECAL1 are expected. The diagrams show the distribution of the relative energy $\eta = E_{cell}/p$ in the calorimeters around the impact point of the tracks. The cell energies E_{cell} from the cluster cells were divided by the track momentum p to obtain distributions that are independent of the track momentum. The distribution of the relative energy deposited in ECAL1 is shown on the left and for HCAL1 on the right. The black box shows approximately the area used in the summation schemes of the trigger electronics.

The top row shows the two distributions for events, where the “Calorimeter Trigger” was active, which indicates that a high energetic cluster was found in HCAL1. In the middle row, the “Middle Trigger” was active. This trigger requires a cluster with an energy above the lower threshold in HCAL1. The bottom row shows the diagrams, where the “Inclusive Middle Trigger” was active, but no signal was seen in the “Middle Trigger”. The “Inclusive Middle Trigger” only requires the hodoscope signals for a trigger signal, but no calorimeter information. Thus, the bottom row shows events, where a hadronic track was present in the first calorimeter, but it was not seen by the trigger system for HCAL1.

The diagrams allow several conclusions. First, and most directly visible, is the fact, that in ECAL1 and HCAL1 the deposited energies are well contained within the area used by the trigger summation schemes. Especially in the lower right plot, there is no indication, that the lower threshold of HCAL1 did not give a signal, because too much energy was lost in cells outside this area.

Furthermore, the plots show the sharing of the deposited energy in the two calorimeters. Going

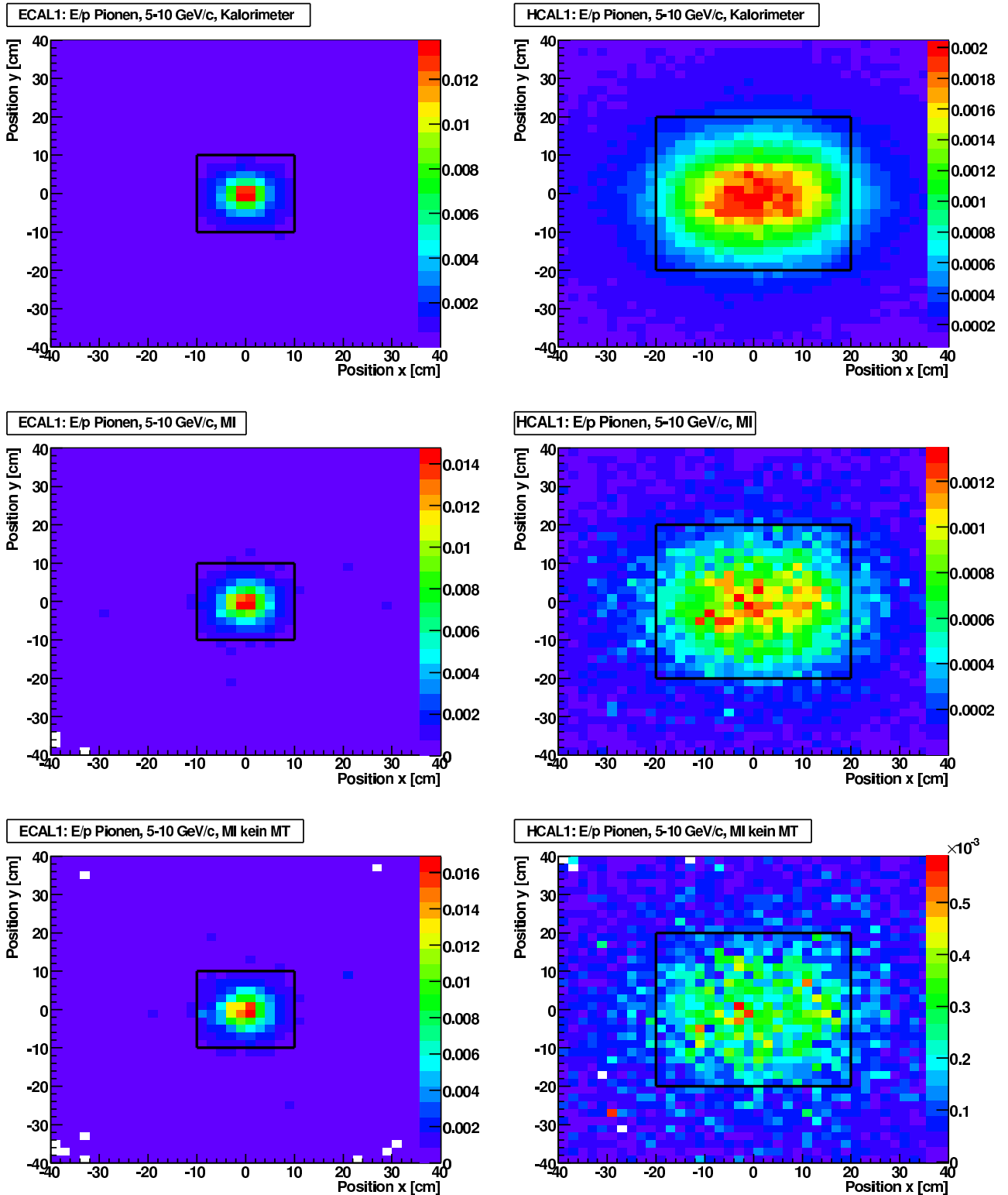


Figure 3.10: The distribution of energy from hadrons in ECAL1 and HCAL1 for data taken in 2006. Each diagram shows the average energy fraction $\eta = E_{cell}/p$ deposited by a hadron (5-10 GeV) around the track impact point. The left (right) plots show the distributions in ECAL1 (HCAL1). For a description of the different trigger conditions, see text. Note that the colour scales vary between the plots. This plot was taken from [76].

from the upper to the lower plot one can see, that the energy deposits in ECAL1 increase slightly, while the deposits in HCAL1 decrease significantly. This trend becomes much more pronounced when looking at the energy deposits within the triggering regions of $20 \times 20 \text{ cm}^2$ for ECAL1 and $40 \times 40 \text{ cm}^2$ for HCAL1. In the events, where a hadronic trigger signal was required, around 40% of the particles energy is found in the HCAL1 cluster. This fraction goes down to about 10% in the lowest diagram. These numbers are smaller than what was seen in the Monte Carlo study. However, the selection of the tracks entering the two studies were different. In the Monte Carlo sample, only one process was considered. In this study from real data, no specific event selection was applied, allowing all tracks from all kinds of processes to enter the study. In addition, the momentum range used for the real data was also chosen differently. These differences in the track selection can account for some of the differences in the two results. However, a study using reconstructed D^* -mesons would require the complete production of the data taken in 2006, which was not available for this study. Another explanation for the observed discrepancies in the energy deposits is the so-called “RichWall” detector, that was installed in front of ECAL1. It was constructed as a pre-shower for ECAL1 and is build as a sandwich of tracking planes and lead-steel plates. This detector was not simulated in the Monte Carlo simulations. Since the total thickness of the converter material amounts to 3 radiation length, it should have an effect on the energy deposits in ECAL1 and HCAL1.

In the meantime, a complete description of the response of ECAL1 and the RichWall for Monte Carlo simulations is in preparation. This will provide the possibility for a detailed comparison of the energy sharing in data and Monte Carlo. In addition, test beam studies were performed to measure the energy distribution in ECAL1 lead glass cells and HCAL1 modules for hadronic tracks with high statistics. The first results of these studies are summarised in [77].

3.2.3 The ECAL1 trigger

During the run in 2006, a test trigger for the signals of ECAL1 was used to study the properties of ECAL1 as well as the possibilities for a trigger on ECAL1 signals. In 2007, this system was improved and adapted to the existing muon trigger. The test performed with the set-up in 2006 and the installation of the full trigger system in 2007 are described in [76].

For the ECAL1 trigger system, a small fraction of the analogue signal is split from the standard read-out and used for triggering. The analogue signals from 16 individual lead glass modules are summed together in specially designed summation cards. Because of the different shapes of the OLGA, MAINZ and GAMS modules, only modules of the same type are grouped together for this summation. Where possible, regions of 4×4 cells are used for one analogue sum. The arrangement of the 90 sums used for the trigger is shown in figure 3.11. Each cross corresponds to one sum of 16 modules. The zones with the modules of the MAINZ type cannot entirely be covered with regions of 4×4 cells, therefore in two cases a sum of 2×8 modules is used.

For triggering, the signals of the analogue sums are split into 3 signals. The first signal is discriminated using a discriminator with a low threshold. The second signal is discriminated using a high discriminator threshold. The discriminator output of all first signals are combined in a logical “OR”. The same is done for the second signals. The output of these two “OR”s are combined with the calorimeter signals of the physics trigger. The “OR” from the low threshold discriminators is

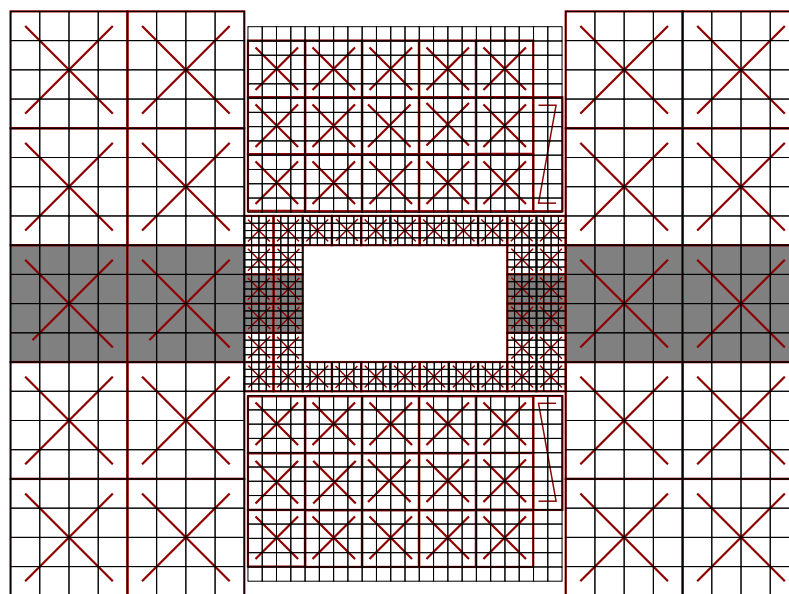


Figure 3.11: The summation scheme for the ECAL1 trigger. Each little square corresponds to one module in ECAL1. The summation is done for 4×4 cells, indicated by the red crosses. In the regions of the MAINZ cells, two sums of 2×8 modules were used to best cover the two regions. The shaded area is excluded from the trigger set up to suppress background from electrons.

added to the trigger information used in combination with the hodoscopes. The output of the high thresholds is added to the “Calorimeter Trigger”.

The trigger thresholds for ECAL1 were selected to be comparable to the thresholds in HCAL1 in the data taking in 2006 and 2007. Those were around 3.5 GeV for the semi-inclusive contribution and around 5.5 GeV for the pure calorimetric trigger. The thresholds were selected for a good separation to the background from halo muons, which deposit of 1.8 GeV in HCAL1.

For ECAL1, only around 0.5 GeV are expected on average for a minimum ionising particle. However, in this calorimeter large background contributions are expected from electromagnetic showers. The main source for this background are photons produced in radiative interactions of the muon beam with nucleons from the target or the detectors. Another source of background photons are π^0 -decays. Most photons are produced in the target region. Due to the many detectors between target and SM1, many photons convert into e^+e^- -pairs before reaching SM1.

Figure 3.12 shows the distribution of reconstructed energies for electrons and pions, that were both identified using the RICH. The two spectra cover a very similar range and both show maxima at energies around 1 GeV. A suppression of the signals from electrons based on the trigger threshold is therefore not possible. To suppress this background in the ECAL1 trigger, the so-called central plane is excluded. Because of the bending direction of SM1, the conversion electrons are mainly detected in a horizontal band, which is indicated by the shaded area in figure 3.11. Before the installation of ECAL1, the same electromagnetic background directly reached HCAL1. To suppress

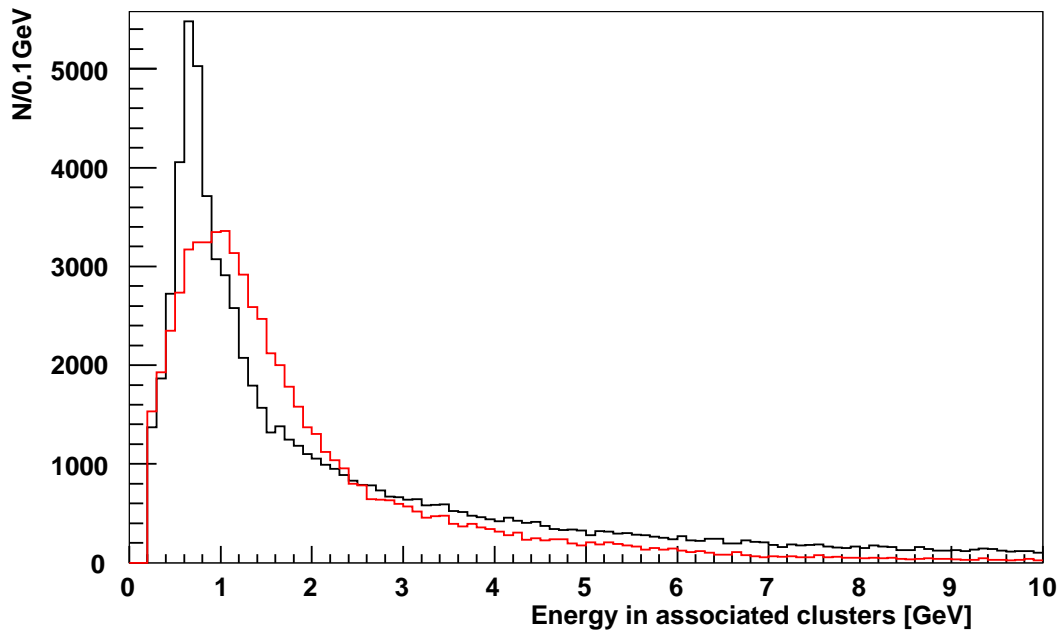


Figure 3.12: Apparent energy depositions for electrons (red) and hadrons (black) in ECAL1. For each track, the sum of the energy of all associated clusters is shown. For a better comparison, a correction for hadronic energy deposits was not applied. This plot was taken from [76].

this background in the calorimetric trigger signals, a lead shielding was used in front of HCAL1, covering a surface similar to the horizontal band shown in figure 3.11.

With the exclusion of the central band, lower thresholds could be selected for ECAL1. For the lower threshold a value of 2 GeV was set, for the higher threshold, used for the stand-alone “Calorimeter Trigger”, a threshold of 4 GeV was applied. As for the HCAL1 thresholds in 2006, the final values for the ECAL1 thresholds were selected taking into account the capacities of the DAQ.

The inclusion of the ECAL1 signals to the hadronic trigger system in 2007 improved the trigger efficiency for hadrons. For a final conclusion about the contribution of ECAL1, more data taken in 2007 need to be produced. However, a first study was performed using a preliminary production of small data samples [76]. The result is shown in figure 3.13, where the trigger efficiency of the calorimetric trigger system is displayed as a function of y . With the inclusion of the ECAL1 trigger to the calorimetric trigger system, the trigger efficiency from 2004 was not only reached in the range of y used by the physics analysis $0.2 < y < 0.9$. For a large fraction of the events the trigger efficiency was even higher in 2004.

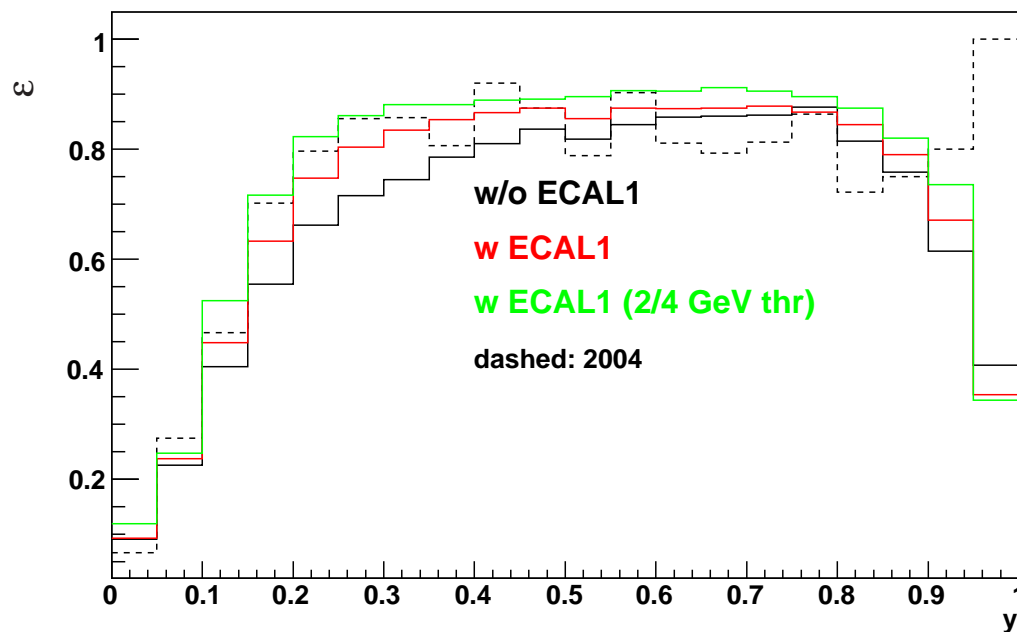


Figure 3.13: The trigger efficiency, ϵ , of the calorimetric trigger system as a function of y . The dashed line corresponds to the status in 2004, the three solid lines show the efficiencies obtained in 2006 with different threshold settings for ECAL1.

3.3 Changes to the Veto System

The installation of the large aperture new target magnet before the run in 2006 made it necessary to change veto₂. Being only 2m away from the magnet, this veto is now exposed to a high magnetic field. This field is due to a stronger fringe field component of the new magnet and significantly larger than with the old target magnet.

The geometry of the new Veto₂ is displayed in figure 3.14. It consists of eight trapezoidal shaped detectors. They cover a circular surface with a radius of 14cm around a beam hole. The frame allows a movement of the detectors in radial direction. This provides the possibility to adjust the diameter of the beam hole between 2.2cm and 4.5 cm.

The light produced in the scintillators is collected in fishtail light guides and then directed via long s-shaped guides onto the photo-multipliers. Due to the special shape of the light guides the photo multipliers can be installed with their longest axis perpendicular the strongest component of the fringe field, which is radial. This special orientation of the photo multiplier and additional layers of shielding with mu-metal made it possible to operate photo multipliers close to the target.

Further information about the installation and operation of the new veto detector can be found in [78].

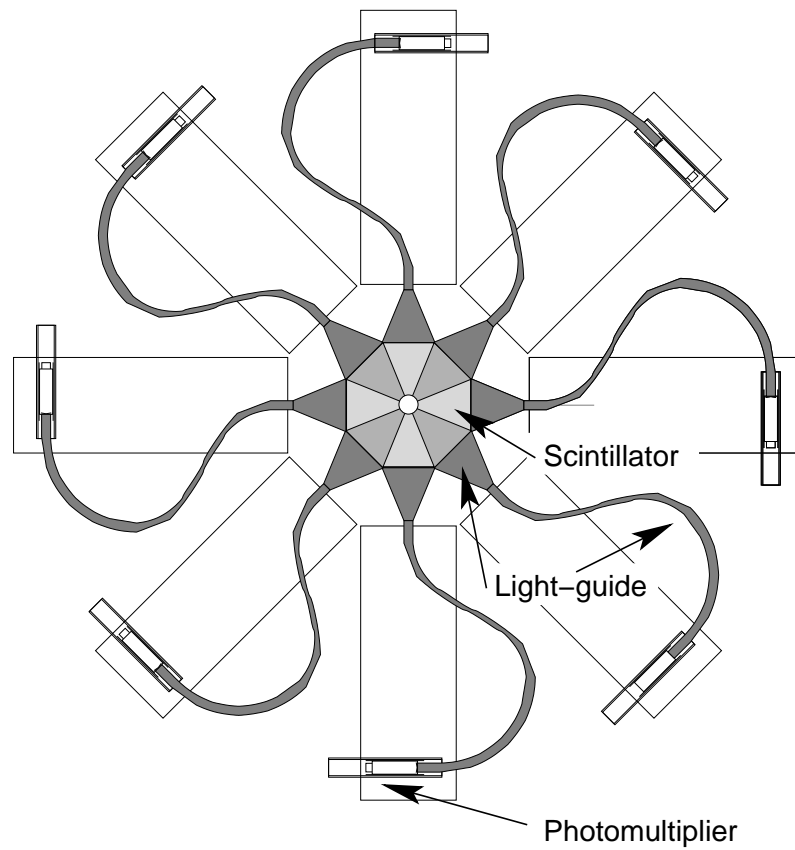


Figure 3.14: The layout of the new Veto₂ station.

Chapter 4

Data Reconstruction and Stability Controlling

For the determination of asymmetries, the detailed knowledge of the detector performance is essential. Since detector instabilities could cause false asymmetries, the stability of the spectrometer has to be monitored closely during data taking. It also has to be checked for reconstructed events. Only after the reconstruction, the stability of the event sample used for the asymmetry measurement can be verified.

In this chapter, the effect of spectrometer instabilities will be discussed. The first section will give an introduction to the different algorithms used in the event reconstruction. This will be followed by a discussion on how the instability of a single detector plane could affect the measurement. The last section will then present a method to exclude events, in which the detector performance might introduce a bias to the asymmetry measurement.

4.1 Data Reconstruction

The event reconstruction is performed by the object oriented software package CORAL [79]. It is build in a modular architecture, where each reconstruction task is represented by an individual module. The three steps necessary to get from the recorded data words to a reconstructed physics event are displayed in figure 4.1.

The event reconstruction starts with the decoding of the recorded information. During the data taking, the information from each detector is stored in data words comprising the information about the observed signal of a detector hit and the active detector channels. The detector hit is either recorded using a TDC* or an ADC[†] module, giving the information about the timing or the amplitude of the signal. All information is extracted from the recorded data and combined with the geometry information of the detectors. From this, two-dimensional detector hits can be obtained, where one coordinate corresponds to the Z-position of the detector. The second coordinate from the active wire is measured in the orientation of the detector plane. For X and Y planes these are X

*time-to-digital converter

[†]analogue-to-digital converter

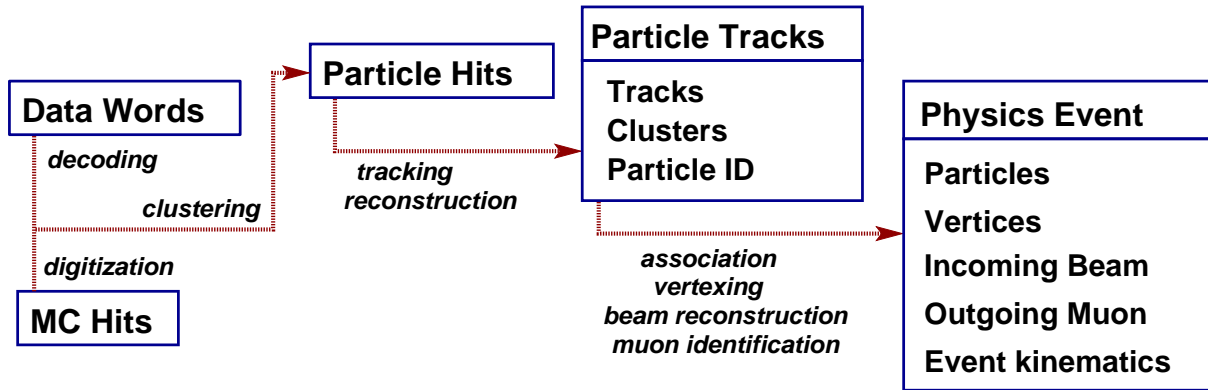


Figure 4.1: The three steps needed in event reconstruction. The raw data are first transformed into hit clusters, before particle traces in forms of tracks and cluster can be reconstructed. The full physics event is reconstructed from all particle traces.

and Y coordinates, for U and V planes the transformation into X and Y coordinates takes place at a later stage. Before the different reconstruction algorithms are applied, a clustering procedure is used to cluster together those hits in each detector plane, that were produced by the same particle, sharing its signal on two wires.

On the hits obtained in the clustering process, different reconstruction algorithms are applied to reconstruct particles tracks, clusters and the identification information in the RICH. Those tracks are then associated to reconstructed particles. In addition, a reaction vertex is reconstructed and the incoming and outgoing muon is identified. After that all information of the physics event was reconstructed.

The following sections will discuss the different algorithms applied in the event reconstruction in more detail.

4.1.1 Spectrometer Tracking

The reconstruction of charged particle tracks plays the most important role in the event reconstruction. The reconstruction algorithm is organised in three steps [80, 81]. A pattern recognition algorithm is used to find track segments. This search is limited to track segments without deflection from a magnetic field or multiple scattering in material. Therefore the pattern search is applied in five spectrometer zones separately. The zone boundaries are given by the target magnet, the two spectrometer magnets and the muon absorber in the second spectrometer. The different track segments are then combined using a bridging algorithm. This algorithm compares the track parameters of the track segments at the zone boundaries and, in a second step, the information of a preliminary track-fit of two combined track-segments to select all matching combinations of track segments. The bridging procedure is applied to each zone boundary independently. For track segments reconstructed behind SM2, where no matching track segment was found between SM1 and SM2, a recovery procedure is used to find all track hits between the target and SM2. Finally,

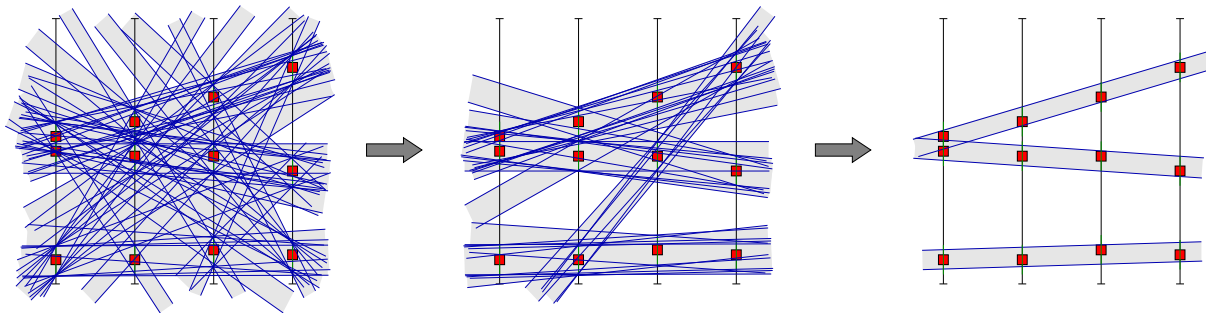


Figure 4.2: The recombination of straight tracks is done on a combinatorial basis.

the track parameters are obtained from a fit to all hits of the track. With this fit the reconstructed track parameters for an eventual vertex reconstruction, as well as the determination of the track momentum are obtained. Due to the large number of detector planes, a simple least- χ^2 -method would be too time consuming for the standard event reconstruction. Therefore, a Kalman filter [82] is used for the track reconstruction.

For the discussion of the stability of the spectrometer, the last two steps play a less important role, because they do not depend directly on the presence of individual detector hits. This is much different for the first step, where a missing hit can lead to a track segment not being reconstructed. Therefore, the reconstruction of individual track segments will be presented with a few more details in the following.

The procedure for the pattern search is shown in figure 4.2. The algorithm starts with all possible combinations of two hits. For each combination the track segment is extrapolated over the full zone, to search for additional hits belonging to this candidate. As shown in the left diagram of figure 4.2, at this stage there are a very large number of track candidates. From these candidates, all those tracks are rejected, that have less than a minimum number of hits belonging to the track segment or a track angle that is outside the angular range of tracks coming from the target. The required minimum number of hits is smaller than the number of tracking planes that can be reached by this track segment. This provides the redundancy needed for a track reconstruction with only a small dependence on the efficiency of individual planes.

The remaining candidates (middle picture of figure 4.2) are then sorted and selected based on a quality function. This function evaluates the number of particle hits belonging to the track segment as well as the χ^2 for the hypothesis of a linear track. The selection removes track candidates, that have too many hits in common with tracks of higher quality, leaving the algorithm with a set of good track segments (right picture of figure 4.2).

To properly treat the different detector orientations present in the spectrometer, the pattern recognition is applied in two steps. First only particle hits from detectors with the same orientation are considered. This leads to two-dimensional track segments that are, in the next step, combined to three dimensional tracks. This second step follows the same procedure, selecting the good candidates from all combinations based on the quality of a track-fit.

Spectrometer alignment

The position of the individual detectors, as well as their orientations and wire spacings, play an important role in the procedure of event reconstruction. Their absolute position is surveyed before the start of each run. During data taking this geometrical information of the detectors is monitored using specific alignment procedures. This alignment procedure is performed at least once per data taking period.

The procedure uses events with halo-muons, where the magnetic field in the spectrometer magnets is off. The track reconstruction is then reduced to the reconstruction of straight tracks. The positions of the reconstructed tracks are compared to the detector hits. This comparison yields the corrections to be applied to the detector positions, angles and wire spacings.

To improve the accuracy of the alignment, the procedure is repeated with physics events and bent tracks, once the preliminary alignment with straight tracks is done. Since there are much more physics events than alignment events, this provides the necessary statistics for the desired precision.

4.1.2 Cluster Reconstruction in the Calorimeters

The energy depositions in the calorimeter are obtained from reconstructed clusters. The cluster algorithm uses the knowledge of the shower shapes to determine the total energy deposited in the cluster and the cluster position.

The algorithm selects cells with high energy depositions as seeds for the cluster reconstruction. For each so-called hot cell, the energy deposited in the surrounding cells (3×3 or 5×5 depending on the cluster energy) is considered. The algorithm assumes, that the energy in the hot cells was deposited by a single particle, while energy deposits in the cells surrounding the hot cells can be coming from two particles. In the case, where one cell is the neighbour of two hot cells, the energy in the cell is shared between the two clusters. A model of the shower profile is used to determine the energy fractions of the two clusters.

After assembling the cells of the clusters, the cluster energy and position are determined. For the cluster energy, the sum of the cell energies is corrected for eventual losses at the edges of the cells. For this correction a model of the shower profile is used. The determination of the cluster position is done independently for the two coordinates. It is based on an inverse one dimensional cumulative shower profile function [83]. In this approach, the horizontal and vertical shower projections are analysed using analytic functions describing the shower profiles for hadronic and electromagnetic showers.

4.1.3 Particle Identification

Outgoing particles are identify based on three different principles. The most extensive means for particle identification are provided by the RICH detector, see section 2.4. However, due to their very similar rest masses, the RICH cannot be used to distinguish between pions and muons in the final state. They are distinguished using the tracking and clustering information of reconstructed particles.

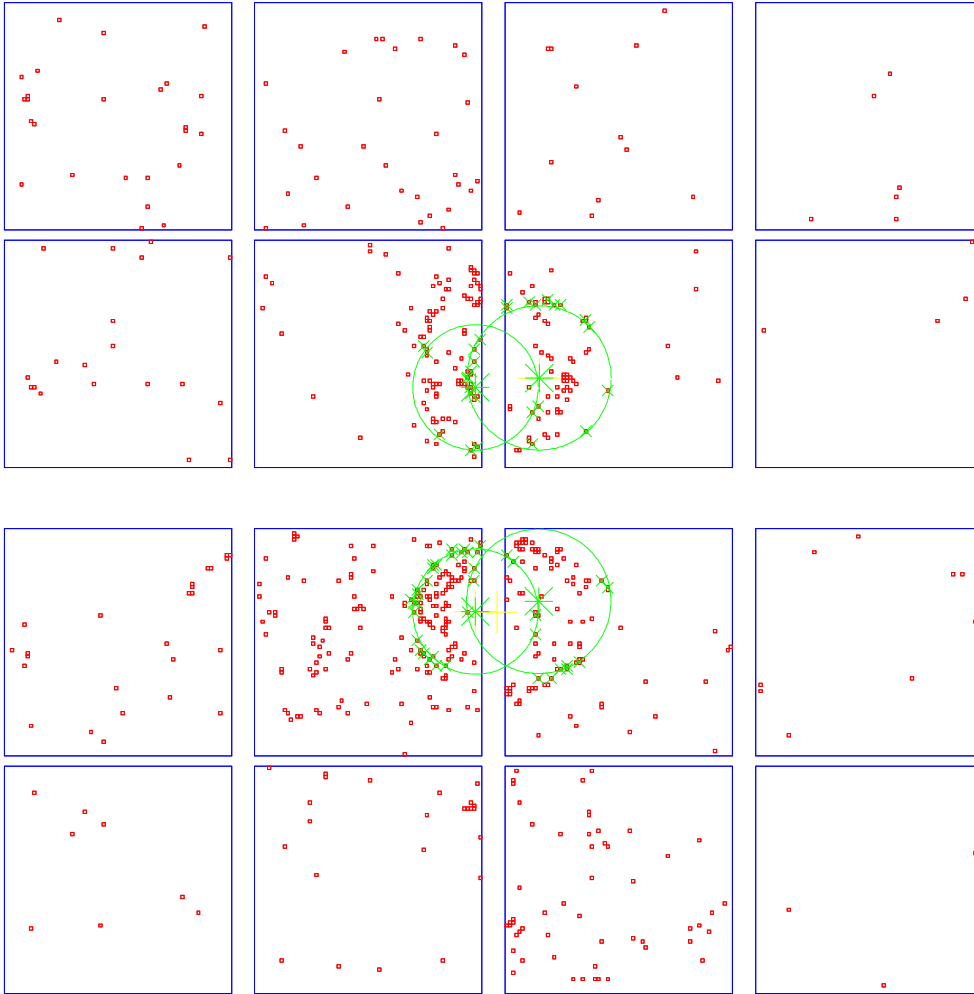


Figure 4.3: A typical event in the RICH. The red clusters indicate the hits seen by the photon detectors, the green circles show the reconstructed rings.

Muons are identified by the amount of material the particle passed on its trajectory in the spectrometer. If this amounts to more than 30 radiation length the particle is identified as a muon. 30 radiation lengths imply, that the particle crossed at least one of the calorimeters or hadron absorbers. In practice, this means, that the particles track needs at least one hit behind an absorber to be identified as a muon. Hadrons, on the other hand, are identified by the ratio of energy deposited in the calorimeters, E , to the particles momentum, p . Since they are stopped in the calorimeters, a large fraction of their energy should be found in reconstructed clusters. A typical cut on E/p for hadron identification is $E/p > 0.3$.

Hadron Identification in the RICH

The main purpose of the RICH is distinction between the different charged hadrons in the final

state. The identification procedure is based on the distribution of detected photons in the RICH. Figure 4.3 shows the distribution of hits on the photo cathodes for a typical event. The reconstruction procedure [84, 85] starts by clustering these detector hits to photon clusters.

To measure the Cerenkov angle of the photons emitted by a particle crossing the RICH, first the photons belonging to the particle track are collected. For each photon the azimuthal (θ_γ) and polar (ϕ_γ) angles of the photon relative to particle track are calculated. Photons belonging to the Cerenkov-cone of the particle are expected to be uniformly distributed in ϕ_γ and to show a clear maximum for θ_γ . The photons around this maximum are associated to the track.

In a next step, the angles of the detected photons are corrected for misalignments in the mirror system or distortions in the quartz windows. For these corrections, a preliminary determination of the particles Cerenkov angle is done using a ring fit to the detected photons. Only with this preliminary θ_C the photon angles θ_γ and ϕ_γ can be corrected.

For the particle identification, the distribution of the corrected θ_γ of each photon is compared to the expected θ_C for different mass hypothesis. θ_C can be calculated from equation 2.2 using the reconstructed track momentum and the rest masses of pions, kaons and protons. To compare the calculated θ_C^π , θ_C^K and θ_C^p to the detected photons, a probability function is used. For the first production of COMPASS data, this function was determined from a χ^2 -method. This was later replaced by a likelihood method.

The χ^2 -method calculates a χ^2 for each mass hypothesis using

$$\chi_i^2 = \frac{1}{N_{DOF}} \sum_{k=1}^{N_\gamma} \frac{(\theta_C^i - \theta_{\gamma k})^2}{\sigma_\gamma^2} \quad i \in \pi, K, p \quad , \quad (4.1)$$

where N_γ is the number of photons in the Cerenkov signal and σ_γ is the resolution of the photon angle. The mass hypothesis with the smallest χ^2 is taken to be the particles identity, if this χ^2 value is smaller than a given upper limit. This last requirement excludes identifications from a random distribution of photons.

With the progressing analysis of COMPASS data, a new identification method was developed using likelihood functions to verify the different mass hypothesis [86]. The calculation of the likelihood functions is based on the probability distributions of photons for the different mass hypothesis. In addition it also takes into account the distribution of background hits. Figure 4.4 shows the distribution of hits in the photon detectors, that are not associated to particle tracks crossing the RICH. While these photons are rather uniformly distributed in the outer regions of the RICH, large background contributions are observed around the beam pipe. This background contribution is mainly coming from photons emitted by the large beam halo present in the detector. Due to this large inhomogeneity, the consideration of the background improves the particle identification significantly. The expected distribution of background photons is stored in so-called background maps. These two-dimensional maps store for each detector pixel the probability to observe a background photon in an event. They are determined from reconstructed events and look very similar to the diagram in figure 4.4.

In the likelihood-method, a likelihood value \mathcal{L}_i is calculated for each mass hypothesis i using

$$\mathcal{L}_i = \frac{e^{-B}}{N_\gamma} e^{-S_i} \prod_{k=1}^{N_\gamma} s_i(\theta_{\gamma k}, \phi_{\gamma k}) + b(\theta_{\gamma k}, \phi_{\gamma k}) \quad i \in \pi, K, p \quad , \quad (4.2)$$

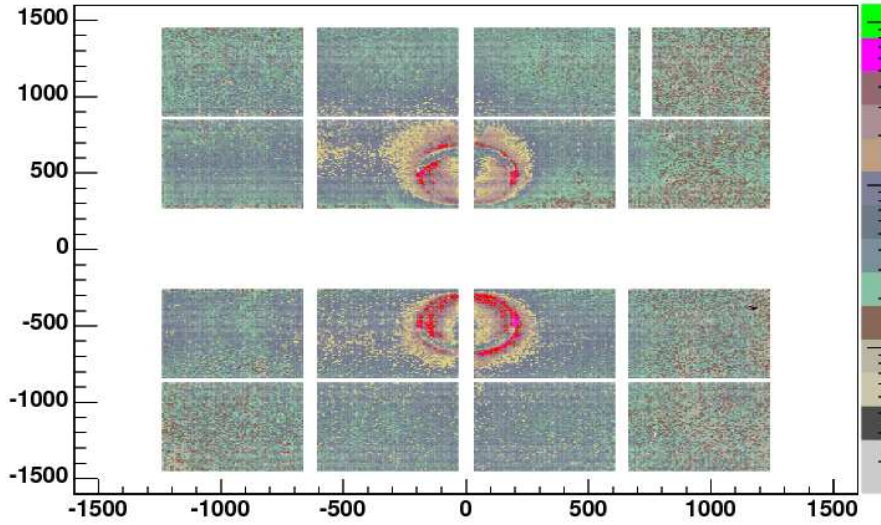


Figure 4.4: A map of the distribution of background hits in the photo detectors of the RICH. The logarithmic colour scale illustrates the large inhomogeneity of the background distribution. This figure is taken from [86].

where the $s_i(\theta_{\gamma_k}, \phi_{\gamma_k})$ and $b(\theta_{\gamma_k}, \phi_{\gamma_k})$ are the signal and background probability distributions for a photon with the coordinates θ_{γ_k} and ϕ_{γ_k} and S and B stand for the number of expected signal and background photons.

The signal probability distribution $s_i(\theta_{\gamma_k}, \phi_{\gamma_k})$ corresponds to a Gaussian distribution with the expected Cerenkov angle for the mass hypothesis as a mean and the angular photon resolution as width of the curve. The background probability $b(\theta_{\gamma_k}, \phi_{\gamma_k})$ is taken from a background map. Besides the likelihoods for the different Cerenkov signals, a background likelihood indicating no Cerenkov signal was observed, is also calculated.

For the particle identification the hypothesis with the largest likelihood value is used. To improve the purity of the identification using the likelihood method, additional cuts on the ratios of likelihood are introduced.

4.1.4 Event Reconstruction

From the reconstructed tracks, clusters and the RICH information the full events are build. The fully reconstructed particles of the event are obtained from the association of tracks and clusters. Among the reconstructed tracks, the incoming and outgoing muon of the interaction are identified and the momentum measurement of the BMS is combined with the track of the incoming muon. The interaction vertex is then reconstructed using all reconstructed tracks. Secondary vertices from decaying neutral particles are searched in all pairs of oppositely charged tracks.

While the RICH information was evaluated using the information about the reconstructed tracks, the calorimeter clusters were reconstructed independently. A track-cluster matching procedure is

used, to combine the clusters and tracks from the same particle. This procedure uses the extrapolated track coordinates on the calorimeter surface as the most probable impact point of the particle. Using these coordinates all clusters are associated to a track, that have a maximum distance of 3σ from the track impact point, where σ corresponds to the combined position resolution of the track and cluster coordinates.

Beam Track Reconstruction

The beam reconstruction is used to combine the information from the beam momentum station (BMS, see section 2.1) and the tracking stations upstream of the target. The beam track entering the target is reconstructed in the beam telescope that provides a very precise measurement of the track direction as it enters the target. The beam reconstruction combines this information with the momentum measurement in the BMS.

The BMS uses the deflection in the bending magnets of the beam-line, that provide the horizontal beam direction before the target (B6 in figure 2.1), to measure the beam momentum. For the momentum determination, the hits in the BMS detectors coming from the same particle are selected using the time information of the hits. A fit to the hits is used to determine the momentum of the muon. After the fit, all beam candidates in the same event are compared, and only those candidates that have a good agreement in the timing of their hits and a good fit quality are kept.

To correlate the momentum measurement in the BMS with the reconstructed track measurement from the beam telescope only the time information from the two measurements is used. A spatial correlation of the different hits is not possible, since the two detector groups are about 100m apart. The comparison of the time measured in the BMS detectors with the time measured in the scintillating fibres of the beam telescope allows the assignment of a momentum from the BMS to the reconstructed beam track of the beam telescope.

Tagging of Scattered Muon

The scattered muon is selected from the reconstructed, positively charged tracks. In events, where the signal from a hodoscope system triggered the read-out, the track of the scattered muon candidate has to contain hits from the two triggering hodoscopes. For events with the pure calorimeter trigger, where the muon provoking the trigger cannot be identified, the scattered muon is only detected from track segments behind the hadron absorber. To ensure, that the muon originates from the target, the scattered-muon candidate needs to pass the entrance and exit of the target no more than 5 cm from the beam axis.

In the case, where more than one outgoing particle fulfils the identification criteria for the scattered muon, all scattered muon candidates are marked as a possible candidate. However, only the candidate for the scattered muon with the largest momentum is used in the event.

Vertex Reconstruction

The final step in the event reconstruction is the determination of the interaction and decay vertices. The interaction vertices, called primary vertices, are reconstructed starting from the reconstructed

beam tracks. The so-called secondary vertices, from decays of a neutral particle into two oppositely charged particles, are reconstructed in a second step using pairs of reconstructed tracks.

For each incoming beam particle, one primary vertex is reconstructed. Using the distance-of-closest-approach (dca) between the outgoing particles and the incoming muon all tracks are selected, that could possibly belong to the primary vertex. The outgoing muon is always added to the vertex, irrespectively of its dca to the beam track. It will also not be removed in the later steps of the reconstruction procedure.

A vertex fit is performed using all selected tracks, and the χ^2 contribution of each track is determined. The track with the largest contribution is removed if the contribution is above a given threshold. After the removal the fit is redone and the χ^2 contributions are reevaluated. These steps are repeated until no more track has a χ^2 contribution above the threshold. Since wrongly contributed tracks could have introduced a bias in the vertex position that could have caused a good track to be lost in the filtering process, a recovery procedure is applied to tracks that were filtered out. This recovery looks at the chi-square contribution of a previously removed track, when it is added to the final vertex. If this contribution is below the threshold, the track will be added to the vertex.

To reconstruct the secondary vertices from the decay of neutral particles, the dca of each pair of oppositely charged outgoing tracks is considered. If this distance is small enough a vertex fit is performed to obtain the position of the decay vertex. The χ^2 -value of the fit is also used as a selection criterion for decay vertices.

4.2 The Detector Performance

The object of the data stability studies is to investigate how the asymmetry measurement depends on the stability of the reconstructed data. Before discussing how a reliable data set for an asymmetry measurement can be obtained, this section discusses the possible instabilities in the detector and their effect on the data.

The asymmetry measurements in COMPASS are based on four counting rates. These are the rates for the two target cells obtained for two different settings of the magnetic fields of the target. Four instead of two rates are used, because the two acceptances for events from the two target cells are different. By calculating the asymmetry from four rates, this acceptance effect cancels in a static detector environment, because the ratio of the two acceptances enter the asymmetry calculation twice. However, this cancellation only occurs, when the spectrometer was stable during the measurement for the two field orientations. In case of spectrometer instabilities, false asymmetries can be introduced to the measurement. False asymmetries are unphysical asymmetries caused by problems during data taking.

4.2.1 Instabilities in the Detector Performance

The physics asymmetries are determined for each data taking period separately. The result for the full data set is afterwards calculated as a weighted mean over the different periods. This procedure was adapted, because in between two data taking periods, access to the experiment is possible,

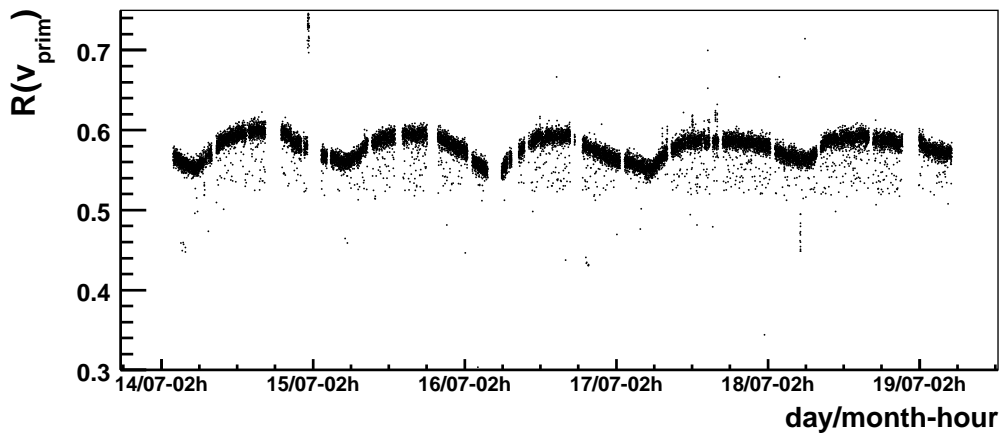


Figure 4.5: Example for day-night effect. The histogram shows the number of primary vertices per reconstructed event with at least one secondary vertex. Each point represents the value average over all events of one spill. The plot shows the data of one period in July 2004.

which may introduce changes in the setup.

During one data taking period, the access to the detectors is kept at the possible minimum. Nevertheless, on many occasions direct interventions are necessary resulting in changes of the detector performance. The four most common sources of instabilities are discussed in the following.

External Influences

External problems have their sources outside the experimental set-up. While they cannot be avoided, it might be possible to reduce their effect on the data.

A prominent example for an externally induced instability are temperature effects. During summer the temperature in the experimental hall changes by about 10°C between day and night time. This temperature change causes a clearly visible effect in the spectrometer performance, as shown in figure 4.5, where an indicator for the performance of the vertex reconstruction is shown for a full period. The oscillation between day and night time can clearly be seen.

To suppress asymmetries related to the day-night-effect the change of the target field is organised such that the field orientation is different every afternoon. An odd number of rotations per day reduces the possibility that an accumulated day-night instability produces a false asymmetry.

Another frequent external problem during data taking are instabilities in the beam-line. However, for the asymmetry calculation they play a minor role, because this instability occurs upstream of the target, and is completely independent of the target cells.

Hardware problems

The most common instability occurring during data taking is induced from hardware problems. These instabilities include everything from a very short high voltage trip in a tracking detector to a

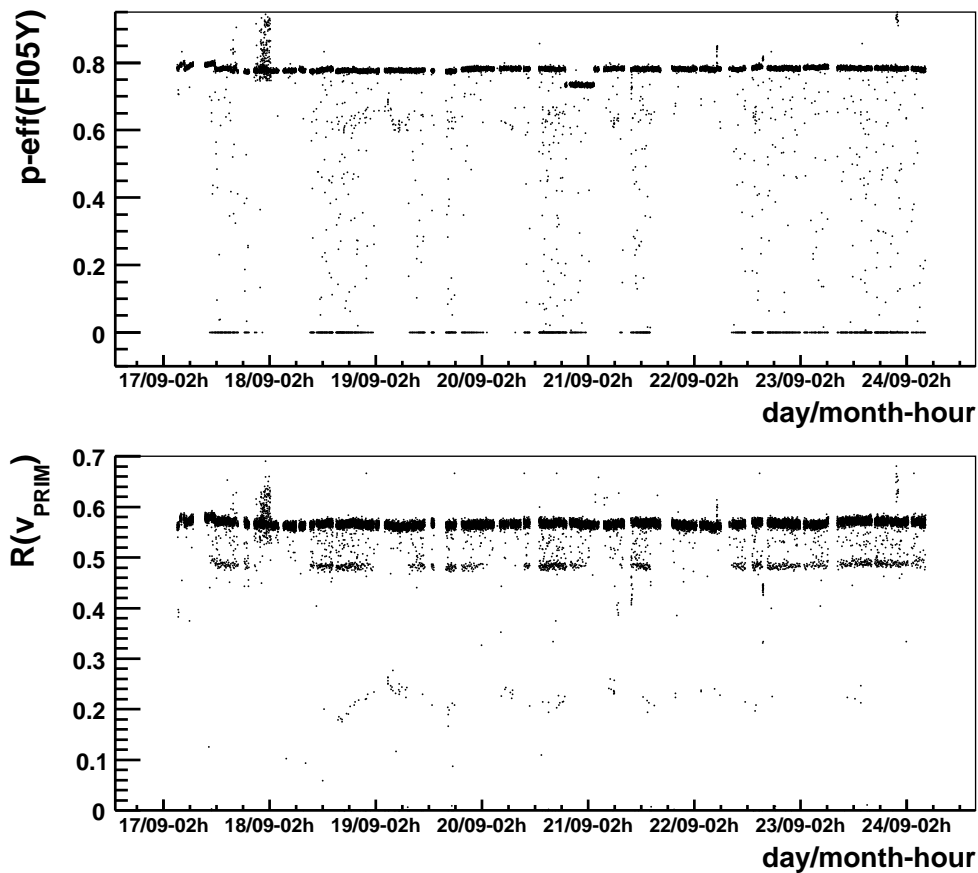


Figure 4.6: Example for hardware problem. A malfunctioning temperature sensor switched this plane of scintillating fibre on and off for short time intervals (upper plot). For the affected spills, the overall performance of the spectrometer is significantly reduced, as shown in the lower plot, where an indicator for the vertex reconstruction efficiency is shown for the same spills.[§]

recurring malfunction of a hardware device. The difficulty of properly treating these problems lies in their detection. Therefore a careful check of all detectors and of the recorded data during data taking is indispensable.

While a short trip in a power supply doesn't reduce the overall performance of the spectrometer, a lasting detector malfunction can cause serious problems for the data quality. This is illustrated in figure 4.6. The upper plot shows the pseudo-efficiency (see section 4.2.2) for one plane of scintillating fibres for each spill of one period. One can clearly see, the plane was regularly off

[§]There are several reasons, why this problem was not detected during data taking despite the careful checks done by detector experts and the shift crew. The most important is, that for technical reasons the main monitoring programme is always looking at several spills simultaneously. This software shows the hit-distributions in all detectors, which allows a verification the quality of the recorded data. Since the problematic station was never off for many spills in a row, the missing hits from the station were not visible in the data monitoring.

during full or partial spills. The lower plot illustrates the consequences of this malfunction on the overall performance. It displays the behaviour of the vertex reconstruction for the same spills. One can see, that in the spills, where the malfunction occurs, the vertex reconstruction is less efficient. Besides the instabilities coming directly from the hardware, the changes made to cure problems or improve the overall performance need to be considered. These operational instabilities include the adjustment of high voltage settings, switching on and off of detector channels or the loading of new thresholds to suppress noise.

A large effort is made, to avoid any action on detectors that could introduce a bias in the asymmetry measurement. If a change in the setup is needed it is applied in a way, that the data before and after the action do not enter the same asymmetry calculation. Unfortunately, this rule can not always be applied, since sometimes urgent problems need immediate response.

Software induced Problems

Software induced problems are introduced in the reconstruction process of the data. To avoid problems from the software, all data from the same period are produced with the same reconstruction software. However, due to the strong magnetic field of the target solenoid, some reconstruction options depend on the orientation of the field. The most prominent example, are positions of detectors, that change slightly when the field orientation changes. A large effort is made, to accurately align the detectors in both field orientations and thus, avoid false asymmetries induced by software settings.

For each instability observed in the data, it would be desirable to identify the cause. This is however only feasible for larger problems affecting many spills. A simple trip in a tracking detector can rarely be connected to a spill with a worse performance. The bigger the problem is, the more important it is to identify its origin, for the simple reason, that only when it was identified, it can be avoided in the future. For the analysis of the data containing the instabilities, it is then evaluated whether the data can be used in the analysis. In principle there are two options: For a smaller effect, the data will be used in spite of the problem. Data showing larger instabilities are removed from the data sample for the asymmetry measurement. For all data used for the analysis it is then estimated, how much these instabilities could affect the measurement. This estimate is taken into account in the systematic error of the result.

4.2.2 Influence of individual detector

When observing an instability in an individual detector, it is difficult to predict, how this instability can affect the reconstructed data. There are two reasons for this difficulty. One is, that the tracking system was built with a lot of redundancy. A single faulty detector plane should therefore not be visible in the data. Only, when several detectors have simultaneous problems, the tracking performance should be affected. The second reason is more complex. Even if the problem affects the performance of the event reconstruction, it only has an effect on the asymmetry calculation, if it affects the two cells differently.

These two aspects were investigated in more details, to be sure that instabilities in the data are

treated correctly. This is done studying the behaviour of pseudo-efficiencies and macro-variables, two important tools for data stability studies.

Pseudo-efficiencies

The so-called pseudo-efficiency are calculated for each detector plane. The pseudo-efficiency is an approximation to the real efficiency of the detectors. It is determined from all reconstructed tracks passing the detector planes and corresponds to the ratio of the number of hits found in the detector to the expected number of hits. It is not a real efficiency, because the detector planes are all used for the track reconstruction, which biases the number of expected hits. Nevertheless, the pseudo-efficiencies can be used for stability studies, where the interest lies more on their fluctuations than on the absolute values.

Macro-variables

To obtain a measure of the stability of the detector performance as a whole, so-called macro-variables are used. A macro-variable is a variable describing the properties of the reconstructed event. In general, they are not motivated by physics. Examples for macro-variables are the number of reconstructed tracks, the number of vertices per event or the total energy reconstructed in ECAL2. While these macro-variables change from one event to the next, one can expect, that the mean value of each spill (~ 15000 events) should remain constant. These means of the macro-variables from each spill are therefore good indicators for the stability of the event reconstruction. A good choice of macro-variables allows, in addition, to localise the origin of a problem.

Study of the Redundancy of the Tracking System

The aspect of the redundancy of detector planes was investigated using the correlations between pseudo-efficiencies and the macro-variables. Since pseudo-efficiencies and macro-variables are determined for each spill, one can check for correlated behaviour between a pseudo-efficiency and a macro-variable by looking at the two-dimensional distributions and from the correlation coefficient, that can be determined for the spills of one period. Figure 4.7 shows the distribution of the correlation coefficients for the correlation between the pseudo-efficiency of all individual detector planes and the number of vertices per reconstructed event. As can be seen in the example, the correlation coefficients were found to be small for all detector planes, independently of the plane's location or orientation. This indicates, that indeed, the redundancy of tracking stations provides the independence on the individual tracking planes needed for a stable spectrometer.

Soon after this study, one exception to its result was discovered. The problem observed in one of the scintillating fibre stations (see figure 4.6) had a unexpectedly strong effect on the spectrometer performance. Since the scintillating fibres (SciFi) are the only detectors withstanding the high rates in the regions, where the beam is crossing, the 8 SciFi stations have to cover this region over the whole length of the spectrometer. Thus, between SM1 and SM2 only two stations with each one X and one Y orientation are installed. When one of the planes did not work, no track segment crossing the SciFis was found in this zone. Therefore only those scattered muons at very

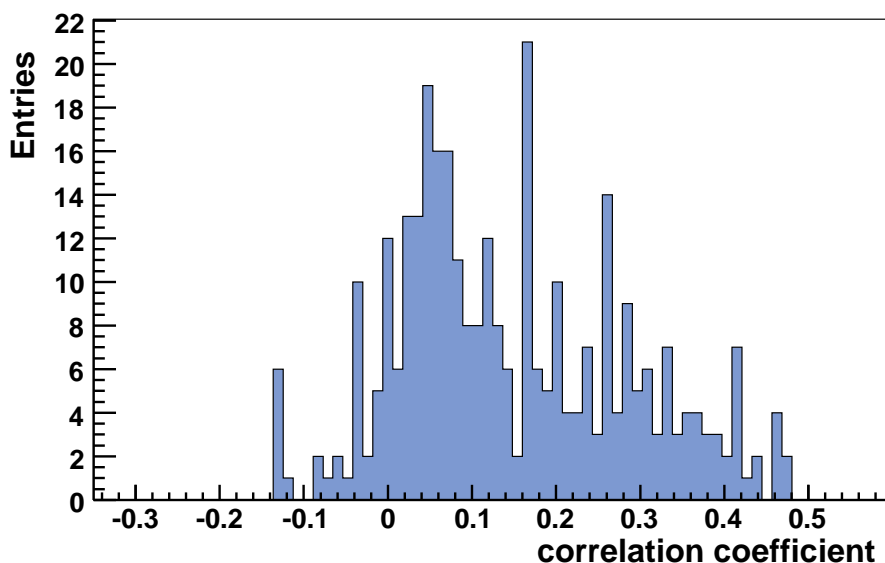


Figure 4.7: Distribution of the correlation coefficients of the pseudo-efficiencies of all 324 detector planes and the macro-variable giving the “number of primary vertices per reconstructed event with at least one secondary vertex”.

low angles were reconstructed, that could be recovered at a later step. As a result, in those spills, where the problem occurred, much less scattered muons and primary vertices were found.

This strong correlation between the SciFis and the spectrometer performance was not seen, when looking at the correlation coefficients, because in normal operations, the fibre stations are very stable detectors and rarely show any fluctuation, which would be needed to observe correlations. After the origin of this problem was understood, it was cured in the next run through the installation of an additional SciFi station in the zone between SM1 and SM2.

Acceptance Difference of upstream and downstream Cell

The main origin of false asymmetries in the measurement are instabilities in the detector performance with a significantly different effect on the two target cells. Therefore, it is interesting to see, if individual detectors have a different impact on the reconstruction of events depending on the cell, in which the scattering occurs.

This was studied using the hits from reconstructed tracks in the individual detector planes. For each detector plane, the number of hits of tracks from the upstream and the downstream cell were counted separately and their ratio was observed. The idea of the study was to see, if there are detector planes that have significantly more hits from tracks originating in one of the cells. Such a detector could be more liable to cause a false asymmetry than others, since it is likely that an instability of this detector will effect the reconstruction efficiencies of tracks of the downstream cell differently than the efficiency of tracks from the upstream cell.

For all detector planes the observed number of hits from track of the downstream cell was about

15% larger than the number of hits from tracks of the upstream cell. This is not surprising, since also more primary vertices are found in the downstream cell. Besides this general difference between the two cells, the observed hit-ratios showed a dependence on the angular regime of the detectors. Especially the so-called large-area detectors, covering the full angular acceptance of COMPASS, showed larger differences between the two cells, than the small angle detectors. This difference is not surprising, since the angular acceptance of the upstream cell is smaller than the one of the downstream cell.

The most important result of this study was, that for no detector plane exceptionally large differences between the two cells were observed. For the treatment of detector instabilities this means, that no detector is significantly more liable to cause false asymmetries than the other detectors. However, the general difference between the two cells implies, that an instability in any detector can cause a false asymmetry.

4.2.3 False asymmetries from instabilities

To verify that no false asymmetries are present in the data set used for the asymmetry measurement, fake asymmetries are calculated, where no physical asymmetry is expected. For example, in each analysis a series of fake asymmetries is calculated, between data taken during day time and night time, or between two data sets, divided according to the momentum direction of an outgoing particle. Besides the kinematic of the outgoing particles also different cell geometries, different cell geometries are used to divide the sample for a fake asymmetry calculation. With this check, the sensitivity of the different spectrometer acceptances of the two target cells to spectrometer instabilities can be verified.

From these fake asymmetries it is possible to determine the degree of stability of the spectrometer acceptance also for the true physics asymmetry that is analysed. If all calculated fake asymmetries are consistent with 0, the statistical precision of the fake asymmetries can be used to estimate the level up to which false asymmetries in the data can be excluded. Because the acceptance of the spectrometer is a function of the event selection, these studies have to be performed for each physics analysis independently. In the case significant deviations from 0 are observed, the source of the false asymmetry is investigated. In general, it can be located within one subsample of the data, which is then excluded for the physics asymmetry measurement.

One known source of false asymmetries is related to the strong magnetic field of the target magnet. Due to this strong field, the performance of the detectors close to the target changes between two field rotations, which can cause a false asymmetry. Therefore, two different microwave configurations are used to polarise the target material, changing the orientation of the target spins relative to the magnetic field. The false asymmetries in the measurement with one microwave orientation can then be cancelled in the measurement with the other orientation, provided both measurements are done with equal event statistics.

4.3 Procedures for stability controlling

To ensure that the measurements of the physical asymmetries are not influenced by detector instabilities, a stability check of the data used in the measurement is performed and instable data is removed.

A first preselection of stable data is achieved with the production run lists. These run lists are based on the logbook informations and exclude all runs, where the beam or a magnet in COMPASS was not at its nominal setting. A detector problem does not lead to the exclusion of a run from production. Detector problems are only treated, when their effect to the reconstructed data can be seen.

The check of the data stability is based on the reconstructed data. It is done in two steps. A bad spill selection is applied to detect and remove individual spills, where a problem can be observed in the reconstructed data. During a second procedure, called data grouping, the time evaluation of the detector performance is checked, and the runs taken with different target field orientations are grouped into configurations for asymmetry calculation.

4.3.1 Detection of bad spills

To reduce possible influences of detector instabilities, a bad spill selection is used to remove unstable spills from the data set. Although bad spills have their origin in detector problems, the check for bad spills is done using macro-variables, not pseudo-efficiency. This reflects the fact, that many problems of individual detectors are masked by the redundancy of the tracking system. The macro-variables used in the standard bad spill procedure are “the number of reconstructed primary vertices per reconstructed event with secondary vertex”, “the number of tracks in the primary vertex” and “the number of beam particles per reconstructed event”.

The definition of a bad spill is obvious. A bad spill does not have the same properties, than the good ones, and deviates therefore in at least one observable from the majority of other spills. Using this criterion, a bad spill selection “by hand” is easily done. However, the large quantity of data available makes it necessary to devise an automated procedure for bad spill selection.

The challenge for an automated bad spill recognition lies in the fact, that also so-called good spills are not entirely stable throughout the whole data taking period. Instead, drifts or oscillations of the mean values of the used observables as seen in figure 4.5, are frequently observed. It can even happen, that the good spills are clustered around two mean values, as shown in figure 4.6. Thus, the definition of bad spills should take these fluctuations into account.

Number-of-Neighbours algorithm

The Number-of-Neighbours algorithm makes use of the fact, that the majority of spills in each period are good and have similar properties. The few bad spills on the other hand are expected to deviate in at least one observed value from the majority of the other spills. Thus, the number of spills with similar properties than a given spill is large for a good spill and very small for a bad spill. This is also illustrated in figure 4.8, where randomly generated good (dark markers) and bad (light markers) spills are shown. The good spills are surrounded by many similar spills, while

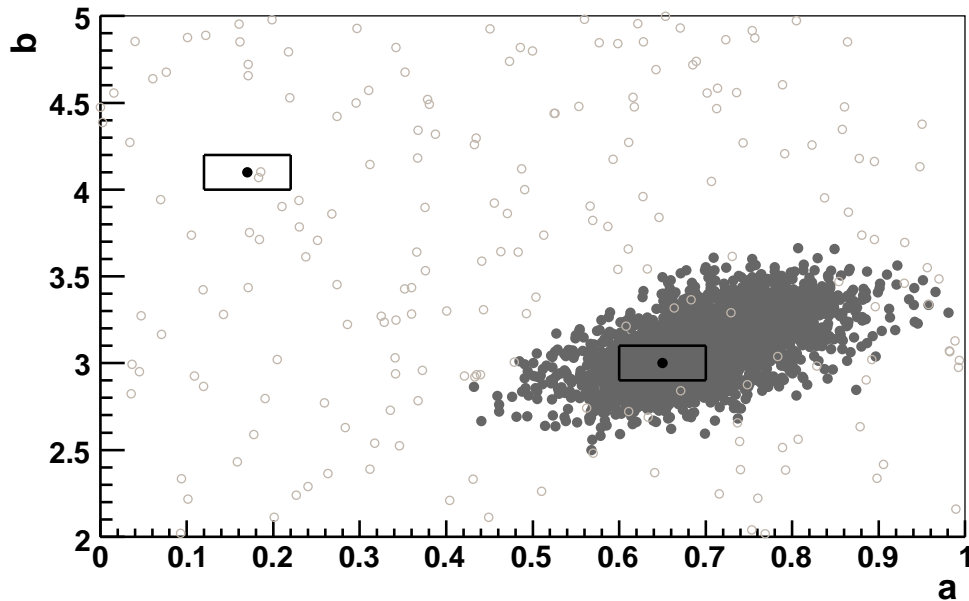


Figure 4.8: Illustration of the distribution of good spills (dark points) and bad spills (light points). The distributions in the variables a and b are randomly generated. Inside the left box very few spills are seen, while many spills lie inside the right box. The edges of the boxes correspond to the size of the statistical spreading of good spills.

hardly any spills can be found in the surroundings of bad spills.

To quantify the number of surrounding spills, an observable called “Number-of-Neighbours” is introduced. The definition of a neighbour Y for a spill X with properties \vec{x} uses the information about the statistical spread of good spills $\vec{\sigma}$,

$$Y \in \{\text{neighbours of } X\} \Leftrightarrow \vec{y} - \vec{x} < \vec{\sigma} \quad , \quad (4.3)$$

where \vec{y} stands for the observed properties of spill Y . Thus, all spills are neighbours of spill X , whose properties not deviate more than the expected statistical spread from the properties of X . The definition of a neighbour is also illustrated in figure 4.8. For the two black spills, the neighbours are all spills, that lie inside the two boxes. One can see, that the left spill has hardly any neighbours, while the right spill has many.

The statistical spread of good spills can in most cases not be easily determined. However, it was studied, that the result of the bad spill algorithm, does not depend on the exact choice of the range used for the counting of neighbour spills provided it is in the same order than the statistical spread of good spills. Therefore, the RMS of all observed spills is used to determine the range, in which neighbours are counted.

The Number-of-Neighbours algorithm counts the numbers of neighbour spills for each given spill X and uses this result to select bad spills. The counting procedure in the multi-dimensional phase space is based on a binary search tree algorithm, which is presented in [87, 88]. The use of a binary

search tree is essential in this application, because a simple approach, where the neighbourhood condition is checked for every existing spill combination, needs much more computer time. The advantage of the binary search tree is, that the tree structure itself already stores information about the spill properties. Therefore, not all the spill combinations have to be checked, some spills can be directly excluded from their position in the binary tree.

The determination of the “Number of neighbours” does not in itself constitute a selection of bad spills. It only provides a criterion, that can be used for the bad spill removal. The minimum number of neighbours for a good spill is determined for each data set independently. It depends critically on the spectrometer conditions during data taking. For a typical data taking period between 5% and 10% of the spills are considered bad. In the case of persistent detector problems, this number goes up to 20%. In some cases, when a detector problem occurs constantly during data taking and affects the data with both target field orientations equally, it is decided to keep the spills affected by this problem.

Figure 4.9 gives an example for the application of the bad spill procedure. The figure shows “the number of primary vertices per reconstructed event” as a function of the recording time for each spill of a data taking period in 2004. The upper plot shows all spills of this period, the lower plot only the spills that survived the bad spill procedure. One can see, that the bad spill procedure successfully removes the spills with deviations in this macro-variable. In addition, some spills are removed, that do not seem to have a problem, when looking at “the number of primary vertices per reconstructed event”. These spills have a problem, that can only be seen in one of the other two macro-variables. The good spills show a good overall stability, free from the main detector problems.

4.3.2 Data grouping

After the removal of bad spills, the data taken during one data taking period are grouped together for the asymmetry calculation. For the data grouping, the information from several different sources are combined. The logbook is used to get an overview of the different incidents during data taking, such as periods, where no data was recorded, or periods, where a specific detector had a problem. In addition, the reversals of the magnetic field in the target magnet are checked.

With the information about the general occurrences during the data taking period, the stability information from the reconstructed data is checked. The spill-by-spill values of the macro-variables and the pseudo-efficiencies are checked for the overall stability of the data. Since bad spill procedure removed all short instabilities, the focus now lies on larger structures, such as step-like discontinuities of pseudo-efficiencies or macro-variables or the observed fluctuations from the day-night effects. The findings from the reconstructed data are compared to the information from the logbook, to identify the origin of observed instabilities. In some cases, a bad run was mistakenly produced, which is removed by adding its spills to the bad spill list.

For the asymmetry calculation the data from one period are grouped in time intervals with stable detector performance, called run-configurations. For the two target-spin orientations needed for the asymmetry measurements, each run-configuration has to include a field reversal of the target magnet.

The grouping of the available data into run-configurations is done taking into account the re-

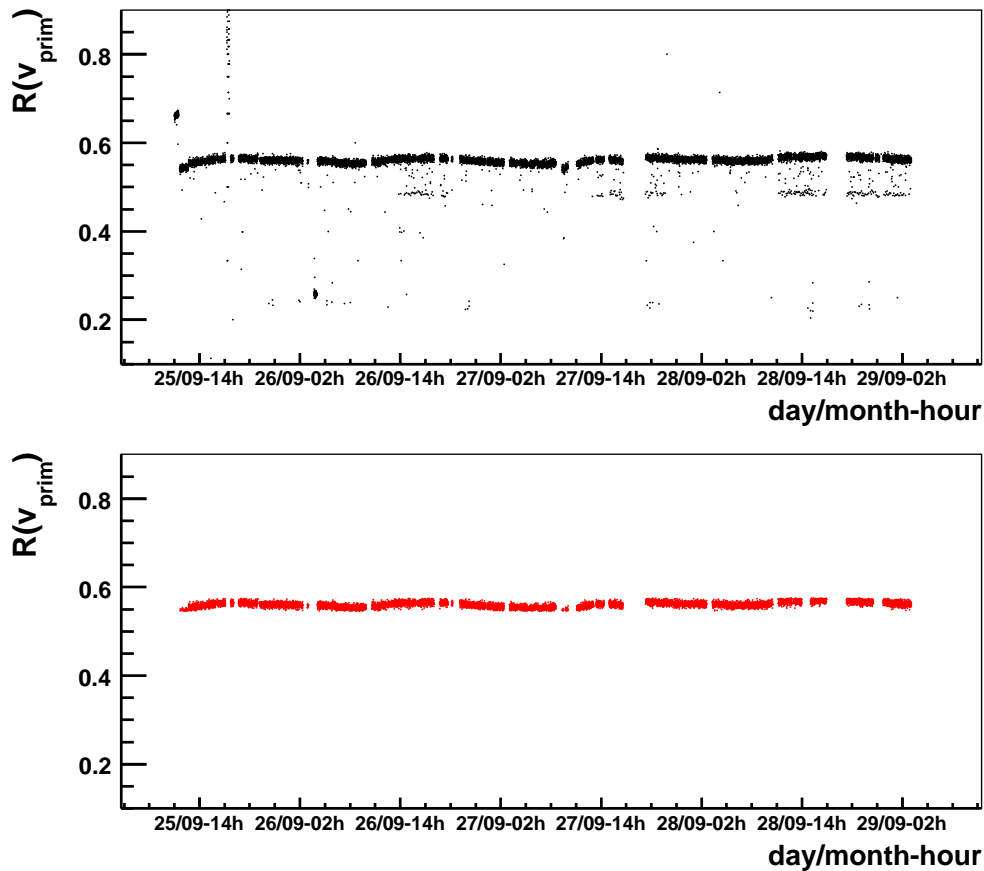


Figure 4.9: Result of the bad spill procedure. The black markers show the mean values of “the number of primary vertices found per reconstructed event” as a function of time. Upper plot shows the distribution of all spills of the data taking period, the lower plot only the good spills that survived the bad spill procedure.

maintaining instabilities in the reconstructed data. Two incidents, that should not be contained in a run-configuration are discontinuities in macro-variables or pseudo-efficiencies and long interruptions in the data taking. No data taken before the discontinuity or interruption should be combined with data taken afterwards. Both type of incidents are therefore strict limits of run-configurations. In most cases, the data taken after a discontinuity can be combined with the data taken after the next field reversal. However, if more than one discontinuity or interruption occurs between two field reversals, the data between the two incidents cannot be combined with data from a different spin orientation and is therefore lost for the asymmetry measurement.

Thus, the data entering the run-configurations are selected with stricter requirements on the stability as the data passing the bad spill removal. For the run-configurations it is ensured, that for all spills taken with one field orientation there exist some spills taken with the opposite field orientation and the same detector situation. The amount of the two groups of spills is equalised as much as possible.

For a physics analysis where a lot of data are available, such a strict treatment of instable data is indispensable, to reduce the systematic uncertainty coming from instabilities. Otherwise, the uncertainty due to instabilities could have a comparable size with the uncertainty coming from statistics.

This is not the case, for physics analysis, where only a limited amount of data is available. In these cases, instable data are treated less strict to keep a sufficiently large data set. Instead, checks for false asymmetries are used to verify, that to a precision that is better than the statistical precision of the data no false asymmetries can be observed. The open charm analysis, where a reconstructed *D*-meson is needed for the asymmetry calculation is the most prominent example for such a situation. The number of *D*-meson-candidates found in one data taking period is so small, that for the asymmetry calculation the data of the whole period are combined. A subdivision of the events into run-configurations is not possible.

Chapter 5

Reconstruction of D -mesons

The measurement of the gluon polarisation presented in this thesis is based on the asymmetry measured for events with charm production. Charm production is detected through fully reconstructed D -mesons. In COMPASS two channels of D -meson-decays are considered. Those are

$$D^0 \longrightarrow K^- \pi^+$$

$$D^{*+} \longrightarrow D^0 \pi_{slow}^+ \longrightarrow K^- \pi^+ \pi_{slow}^+ ,$$

and their charge conjugates. The decays are solely detected via the signal in the invariant mass spectrum of combinations of reconstructed particles. The decay vertex itself cannot be resolved, since the vertex resolution inside the thick solid state target is at least 5 times larger than the decay length of the D^0 -mesons. The D^0 -mesons are reconstructed from oppositely charged track pairs. The decay of D^* -mesons is detected in events with a reconstructed D^0 -meson through the slow pion, which is produced in the decay of the D^* -meson into a D^0 -meson. The requirements on the slow pion improve the selectivity of the D^* -reconstruction compared to the D^0 -reconstruction. Therefore, the two decays are reconstructed and analysed separately.

To improve the signal of the reconstructed D^0 -mesons, additional cuts on its kinematic properties are applied. In both cases – the D^0 -decay and the D^* -decay – these requirements are applied on the kinematics of the reconstructed D^0 -mesons. The kinematic variables, that are interesting in this context are the momentum $p(D^0)$ and the transverse momentum with respect to the direction of the virtual photon $p_t(D^0)$ of the D^0 . The decay angle of the D^0 -meson, θ^* , is defined as the angle of the kaon with respect to the boost-direction of the D^0 determined in the rest frame of the D^0

$$\theta^* = \angle(\vec{p}(K), \vec{v}_{boost}(D^0)) . \quad (5.1)$$

To compare the energy of the D^0 with the total energy available in the interaction, the fragmentation variable

$$z(D^0) = \frac{E(D^0)}{v} \quad (5.2)$$

is used. For the decay of the D^* -meson the invariant mass difference δm between D^* and D^0 is defined by

$$\delta m = m(D^*) - m(D^0) . \quad (5.3)$$

Besides the cuts on the kinematic properties of the D^0 -meson, the information from the RICH to identify the decay products as kaon and pion is used. Especially the identification of the charged kaon is needed for a good event selection.

The final event sample used for the asymmetry calculation contains not only the signal events S , where a D -meson could be reconstructed, but also events B , where a fake (K , π) candidate from combinatorial background was found. This background dilutes the signal from the charm events, which reduces the overall significance of the measurement. To obtain the best possible significance of the asymmetry measurement, the selection cuts were chosen to maximise the effective signal S_{eff}

$$S_{\text{eff}} = \frac{S^2}{S+B} . \quad (5.4)$$

The effective signal reflects how the precision of the measured $\langle \frac{\Delta g}{g} \rangle$ depends on the selected data sample. This can be seen from combining equations 1.45 and 1.46 to

$$\langle \frac{\Delta g}{g} \rangle = \frac{1}{P_\mu P_T f \langle a_{LL} \rangle} \frac{1}{R_{PGF}} A_{PGF}^{\text{meas}} , \quad (5.5)$$

assuming $A_B = 0$. From $R_{PGF} = S/(S+B)$ and $\delta A_{PGF}^{\text{meas}} \approx 1/\sqrt{S+B}$ one obtains for the statistical uncertainty of the measurement of $\langle \frac{\Delta g}{g} \rangle$

$$\delta \langle \frac{\Delta g}{g} \rangle \approx \frac{1}{P_\mu P_T f \langle a_{LL} \rangle} \frac{1}{\frac{S}{S+B}} \frac{1}{\sqrt{S+B}} \propto \frac{1}{\sqrt{S_{\text{eff}}}} . \quad (5.6)$$

Thus, by selecting the cuts for a maximal S_{eff} , the statistical uncertainty of the measured $\langle \frac{\Delta g}{g} \rangle$ is minimised. While for the cuts on the D^0 -kinematics the optimal values only show little dependence on selection through other cuts applied to the sample, the best criteria for the particle identification in the RICH depend on the mixture of signal and background events, this selection is applied to. Therefore, the RICH selection was only optimised, after all cuts were applied.

It should be noted, that it was verified for all cuts used in this analysis, that they cannot artificially create a signal or change the shape of an existing signal of D^0 -mesons. In particular the cuts used for the particle identification were also validated using kaon and pion samples from other decays. However, within their range of good values, the improvement of the effective signal through these cuts can vary. The optimisation of S_{eff} uses this variation to obtain the best possible selection of D -mesons for the asymmetry calculation. This optimisation was also verified on independent data sets to exclude the influence of a statistical fluctuation in one particular event sample.

The reconstruction starts with selecting events fulfilling all stability criteria for the asymmetry measurement. The primary vertex of these events should have at least two outgoing hadrons in addition to the scattered muons. Otherwise, a D^0 -meson cannot be reconstructed. The D^0 -meson and D^* -meson are then reconstructed from the possible combinations of hadron tracks in the event. To suppress the contributions from wrong combinations first kinematic cuts are applied. The last selection step uses the RICH information to identify the kaon and pion from the D^0 -decay and, thus, improve the observed signal of D^0 -mesons.

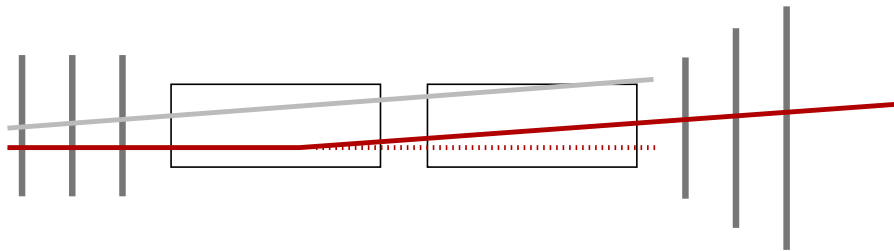


Figure 5.1: The selection criterion for the incoming beam: the extrapolated beam track has to cross both target cells, as shown by the dark line. The gray line corresponds to a beam track, that does not fulfil the criterion.

5.1 Event Selection

To obtain a event sample, that can be used for the asymmetry measurement, the stability procedures introduced in chapter 4 are used. To ensure a good stability of the data, bad spills detected from the bad spill algorithm (see section 4.3.1) are removed. The same is done for spills from bad runs, that had been produced by mistake. Because of the small event statistics in the final sample, the asymmetry is calculated for all the data from each data taking period and not for the run-configurations described in section 4.3.2.

To ensure a cancellation of the muon flux, only events are selected, where the incoming muon would cross the full target volume. This is verified from the position of the extrapolated beam trajectory at the entrance and exit window of the target. At both windows, the trajectory should lie within the fiducial target volume. This is illustrated in figure 5.1. It displays the example of a beam particle with an interaction in the first cell, whose trajectory before the interaction can be extrapolated through the second cells. A second, gray line gives the example of a beam track, that does not cross the two cells.

The reconstructed primary vertices are the basis for the D -meson reconstruction. Since the D -production and decay take place within the solid state target volume, a distinction between the production and decay vertices is not possible. In the reconstruction of charm decays all particles are joined to the primary vertex.

For the reconstruction, primary vertices are selected that clearly lie within the volumes of the polarised target cells. Besides the selection of vertices with Z -positions inside one of the two target cells, the distance from the cell axis, r , is required to be less than 1.4 cm and the absolute Y -position should not exceed 1.0 cm. The first requirement is used to suppress the influence of unpolarised material at the edges of the target cells, that have a radius of 1.5 cm. The second requirement reflects the fact, that the target cells are not completely filled with polarised material. The upper cut of 1.0 cm for the vertices ensures that the measurement is not affected by the incomplete filling. Both cuts were applied taking into account the inclination of the target axis with respect to the spectrometer.

Figure 5.2 shows the distribution of primary vertices in the final sample. The left plot gives the distribution in the transverse plane, the right plot displays the distribution in Z . In this plot one can

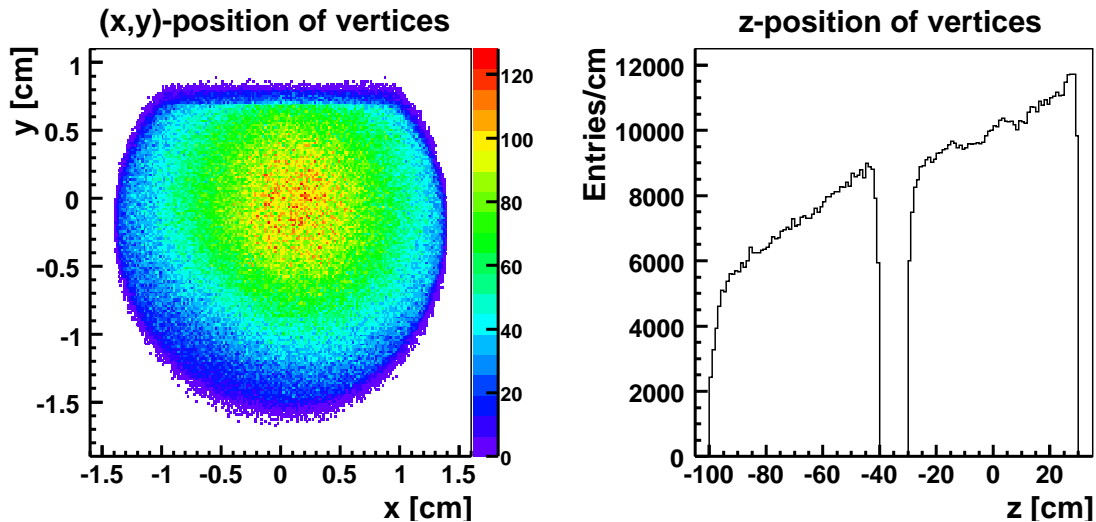


Figure 5.2: Distributions of primary vertices transverse to the beam (left) and along the beam direction (right) for the final event sample of the 2004 data. This means, only vertices where one D^0 -candidate was found are shown and also the target selection cuts were applied.

clearly see the strong increase of reconstructed vertices when going toward the downstream end of the target. This increase is an result of the multiple coulomb scattering of outgoing particles with the target material. As a result of these interactions, low energetic hadrons might not be detected by the COMPASS spectrometers, and in addition, the scattering also reduces the vertex reconstruction efficiency.

Apart from the requirements of the position of the primary vertex, some selection is also applied for the D -reconstruction. Since the D -mesons are reconstructed from at least two oppositely charged hadrons, a minimum number of three outgoing particles is required. This includes the scattered muon. The particle tracks for the incoming and outgoing muon need also to be reconstructed for the event to be considered. Both are needed to determine the kinematics of the scattering process.

5.2 Reconstruction of D -meson candidates

The reconstruction procedure for the D -meson candidates from the two decay channels starts from the reconstruction of the decaying D^0 -meson. In the first channel only the D^0 -meson is detected, in the second channel an additional soft pion is needed.

The D^0 -meson is reconstructed through its decay into charged kaon and a charged pion. This decay has a branching ratio of $3.8 \pm 0.07\%$ [5]. There are decay channels of the D^0 -meson with higher branching ratios. However, they have the disadvantage, that more than two hadrons have to be reconstructed in the final state, which reduces the overall reconstruction efficiency. This reduction is related to the reconstruction efficiency of the additional hadrons as well as to the fact, that

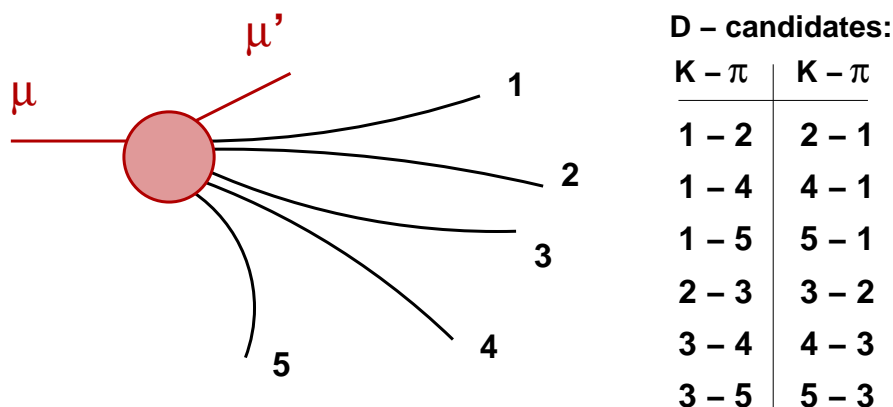


Figure 5.3: Reconstruction of D^0 -candidates. Each pair of oppositely charged outgoing hadrons in the event is used to reconstruct a D^0 -candidate assuming the first hadron to be a kaon, the second a pion the mass of the D^0 is calculated and the other way around.

in these decays all decay products have smaller momenta. Since the efficiency for the detection of a charged hadron in the COMPASS spectrometer decreases with decreasing momentum [64], this effect becomes quite important when looking at D^0 -decays into three or more hadrons. Therefore, the largest number of reconstructed D -mesons is expected from the D^0 -decay into a kaon and a pion.

In the second decay analysed in this study, besides the reconstructed D^0 , the soft pion, a very low energetic hadron, whose momentum is typically below 10 GeV, is also reconstructed. Due to the thick solid state target, the detection of the outgoing hadrons with such low momenta becomes increasingly difficult. This is reflected in the number of D^* -mesons reconstructed in the spectrometer, which is less than 1/3 of the number of reconstructed D^0 -mesons. However, a similar amount of D^* -mesons and D^0 -mesons would be expected, since D^* -mesons have a similar production probability, than the D^0 s, and the branching ratio of the decay soft pion and a D^0 is $67.7 \pm 0.5\%$. Because of the very good background suppression trough the D^* -tag, the sample with reconstructed D^* -mesons is still very interesting for the determination of $\langle \frac{\Delta g}{g} \rangle$.

Since the D^0 -production vertices cannot be distinguished from the decay vertices, the reconstruction of the D -mesons is done only on a combinatorial basis. This is also illustrated in figure 5.3. For each event all outgoing particles from the primary vertices are considered. The scattered muon is first identified and excluded from the further procedure. For the outgoing hadrons, each possible pair of oppositely charged tracks is used to reconstruct two D^0 -candidates by assuming the first track to belong to a kaon, the second track to belong to a pion and vice versa. For both assumptions the invariant mass of the two-particle system is calculated. For a true D^0 -meson this mass should lie at 1864.5 MeV [5]. In the further steps, all D^0 candidates with an invariant mass, that does not differ more than 400 MeV from the expected mass, are considered. Their mass distribution is shown in figure 5.4. In this distribution no signal from the D^0 decay can be observed. Instead a very large amount of background from wrong combinations is present. This combinatorial background has to be suppressed in order to get a usable signal of D^0 -mesons. To suppress the wrong

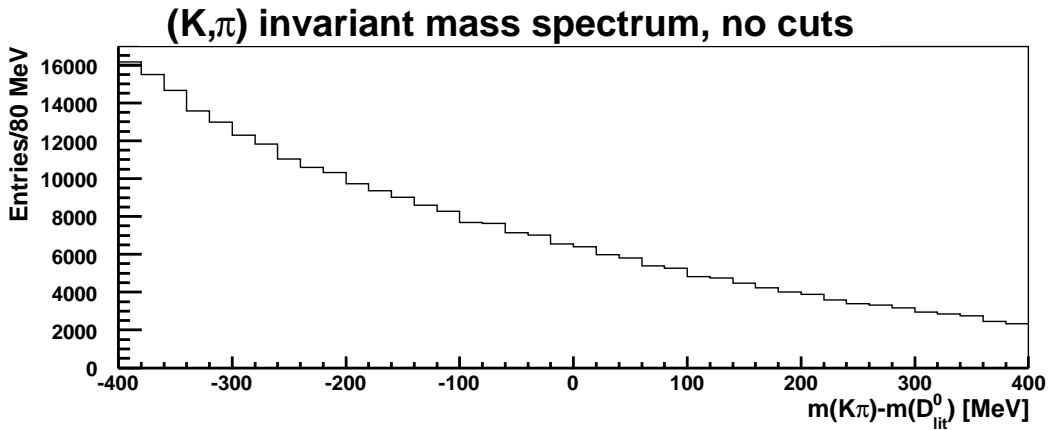


Figure 5.4: Invariant mass spectrum of all possible $K - \pi$ combinations. The data sample shown corresponds to several runs of one period in 2004.

combinations kinematic cuts on the D^0 -candidates are used as well as the information from the RICH. The signals from the RICH allow the identification of good (K, π) -pairs in the sample. The reconstruction of the D^* -meson follows the same procedure as the D^0 -reconstruction. In this case combinations of three outgoing particles are considered, where for the first two the same requirements are applied as for the other D^0 -candidates. The third outgoing hadron corresponds to the soft pion. It has to be oppositely charged to the kaon-candidate. In the example of figure 5.3, this is the case for the track combinations (1,2,5) or (2,1,3). For the D^* -candidates, where three three particles are grouped together, more combinations are possible. In the example shown in figure 5.3, there are 18 possible D^* -candidates, compared to 12 possible D^0 -candidates. However, the requirement for the soft pion to be really soft, drastically reduces the possible combinations.

5.3 The D^* -tag

The advantage of the D^* compared to the D^0 lies in the high selectivity of the soft pion reconstruction. Due to the small difference of the invariant masses of the D^* -meson (2010.0 MeV) and the D^0 -meson (1864.5 MeV), only very little energy is available for the decay of the D^* -meson. Taking into account the mass of the additional pion produced in this decay, one arrives at

$$m_{D^*} - m_{D^0} = 2010.0 \text{ MeV} - 1864.5 \text{ MeV} = 145.4 \text{ MeV} = m_{\pi} + 5.8 \text{ MeV} .$$

In the rest frame of the decaying D^* only 5.8 MeV are available for the kinetic energy of this decay. This also limits the phase space of kinematic combinations for the decay products. Since the amount of combinatorial background found for a decay is related to the phase space available to the decay, the mass difference of D^* and D^0 can be used to effectively suppress combinatorial background.

This is also illustrated in figure 5.5. It shows the distribution of $\delta m = m_{D^*} - m_{D^0} - m_{\pi}$. For this figure D^0 -candidates were used, that have a reconstructed invariant mass that is closer than

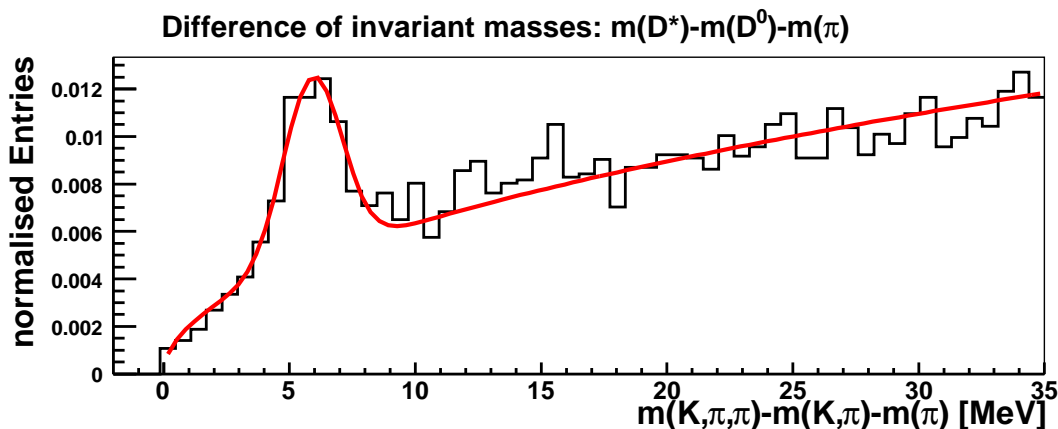


Figure 5.5: The distribution of $m_{D^*} - m_{D^0} - m_{\pi}$ for an event sample, which was preselected with cuts on the D^0 -mass and the kaon identification. This preselection was necessary to enhance the D^* -mesons in the sample such, that the signal in the δm distribution becomes visible. The histogram was fitted with the sum of a Gaussian and a root function.

10 MeV to the literature value, and, whose kaon could be identified in the RICH. Without this preselection, the signal in the δm -distribution would not have been visible on top of the large combinatorial background.

The figure shows, that the distribution of δm has two components. On one hand, there is the contribution from combinatorial background, which gradually rises with increasing values of δm and follows the shape of a root function. On top of this, a Gaussian like signal can be observed around $\delta m = 6$ MeV. The signal from the D^* -decay is lying at the very beginning of the region accessible by combinatorial background. Therefore, this background can be significantly reduced with the application of a cut on δm . In this analysis, δm is selected to lie between 3.1 MeV and 9.1 MeV. With this cut, the background contribution in the signal region of the D^0 -mass is reduced by a factor 10, compared to the event sample without the δm -cut.

This large difference in the ratio of signal to background is the reason to perform the analysis separately in the two event samples. Because of the high selectivity of the D^* -tag, the other cuts applied to the D^0 -mesons are less strict for the D^* -tagged sample. Despite the different cuts used in the two samples, there is still a significant difference in the signal purity of the two event samples. As a result, the effective signal of the D^* -tagged sample is about twice as large as the effective signal of the untagged sample, although almost 4 times more D^0 -mesons are observed in the untagged sample. Because of this very different ratio of signal and background events in the two samples, they are also analysed separately to determine the gluon polarisation.

5.4 Background Suppression through Kinematics

The cuts on the kinematics of the D^0 -meson use differences of D^0 -mesons compared to the combinatorial background, that are coming from the production and decay process. The two kinematic

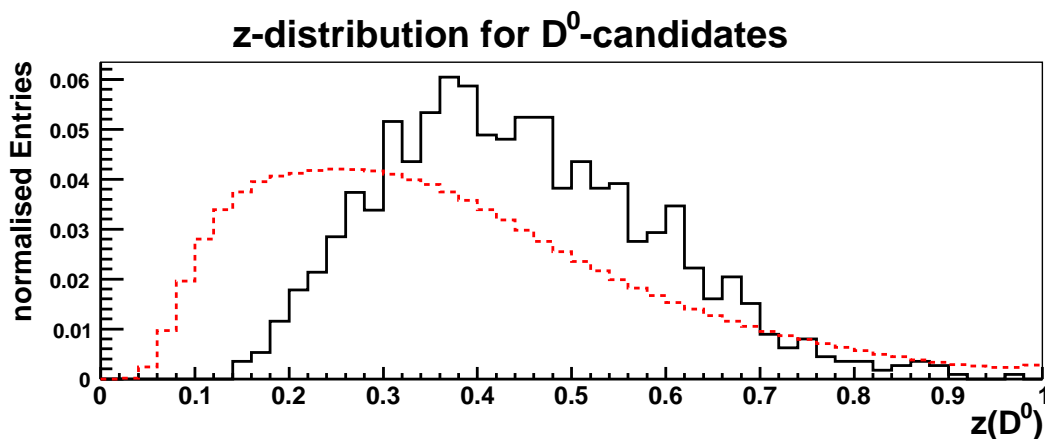


Figure 5.6: The z -distribution for D^0 -candidates shown for a sample of pure background events (red, dashed histogram) and a sample, where the signal fraction was enhanced (black, solid histogram). Both distributions are shape normalised.

variables used in this context are $z(D^0)$ and $\cos(\theta^*)$. Both cuts are explained in the following. The underlying production process for D -mesons is the fragmentation of a heavy quark. Due to their heavy mass charm quarks behave differently in the fragmentation process than light quarks. The essential difference is, that the meson carrying the heavy quark also carries most of the momentum of the original quark. In the fragmentation of light quarks the quark momentum is more evenly distributed over the produced hadrons. Since the combinatorial background is essentially coming from events with light quarks, this difference between light and heavy quarks can be used to suppress the background. This is done with a cut on $z(D^0)$ which indicates how much of the energy available in the event is reconstructed in the D^0 -meson. In the case of a true D^0 , this fraction is expected to be high, while for background events much smaller values of $z(D^0)$ are observed. In figure 5.6 the distribution of $z(D^0)$ for a sample, where the D^0 -signal was enhanced, (black solid line), and for a sample of background (K, π)-pairs (red, dashed line) are shown. In the sample with enhanced signal, the signal purity was increased to $\sim 50\%$ to illustrate the properties of the expected signal. The selection criteria used for the enhancement do not correspond to the final selection cuts. Instead much stricter cuts for the kaon identification (see section 5.5) and the invariant masses are used. With these cuts a high signal purity could be achieved, without cutting in the distributions of the variables discussed in this chapter. The sample with background candidates was obtained by simply requiring the mass of the (K, π) pair to lie outside the expected signal region. In the figures 5.6, 5.7 and 5.8 both histograms are normalised to have an integral of 1 to show the differences in the distribution of the two samples. One should keep in mind, that in the original sample of D^0 -candidates, there are about 50 background events per signal event. Figure 5.6 shows, that a cut on $z(D^0) > 0.2$ can be used to suppress background candidates without losing many signal events. For the D^* -tagged sample a cut of $z(D^0) > 0.2$ was used. For the untagged sample a stricter cut was needed, thus $z(D^0) > 0.25$ is required. Besides the energy fraction $z(D^0)$, one could also expect differences in the transverse momentum $p_t(D^0)$ between the signal and the background events. The high transverse momentum of the pro-

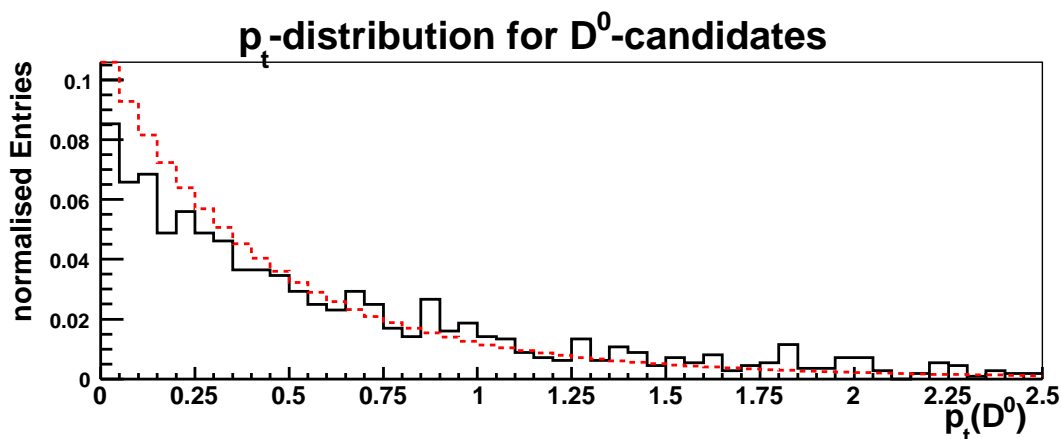


Figure 5.7: The p_t -distribution for D^0 -candidates shown for a sample of pure background events (red, dashed histogram) and a sample, where the signal fraction was enhanced (black, solid histogram). Both distributions are shape normalised.

duced hadrons is used in other analyses to identify photon-gluon fusion events [45]. Thus, one might expect the D -mesons, that are also produced through photon-gluon fusion, to have higher transverse momenta than the combinatorial background, that is produced in other processes. The distributions for the signal enhanced sample (black, solid line) and the background sample (red, dashed line) are shown in figure 5.7. It is obvious, that a distinction between the two samples using this variable is not possible. Both distributions show a strong rise towards low p_t . This can be understood from looking at the production mechanism. In the case of charm production, most of the energy available in the photon-gluon system is used to produce the heavy quark pair. Therefore, in contrast to the light quark pairs produced in PGF, high transverse momenta are not expected for the two charm quarks.

The second quantity that is effectively used to suppress the combinatorial background in the D^0 -decay angle θ^* . In the rest frame of the D^0 -decay, an isotropic distribution of the decay products in all directions is expected. Since for the combinatorial background the (K, π) -pair was not produced in a real decay, a peaked angular distribution is expected. The peak is coming from the boost into the rest frame of the assumed (K, π) -pair. In the case, where no kaon is present, the boost vector will still be calculated assuming the kaon mass for one of the hadrons, which then leads to very small angles between the direction of the kaon candidate and the boost vector. Therefore the D^0 -decay angle θ^* can be used to suppress background events.

This is also illustrated in figure 5.8, where the solid histogram shows the distribution of $\cos\theta^*$ for the signal enhanced sample and the dashed histogram shows the distribution for the background. The signal enhanced sample is rather uniformly distributed over the full angular range, while the background events are mainly lying close to $\cos\theta^* \approx 1$. Thus, a cut of $|\cos\theta^*| < 0.85$ is used for the D^* -tagged candidates, while for the untagged candidates the stricter requirement of $|\cos\theta^*| < 0.5$ is applied.

With the selection cuts described in this section, the signal purity could already be enhanced significantly. However it is not yet high enough to allow the samples to be used in the asymmetry

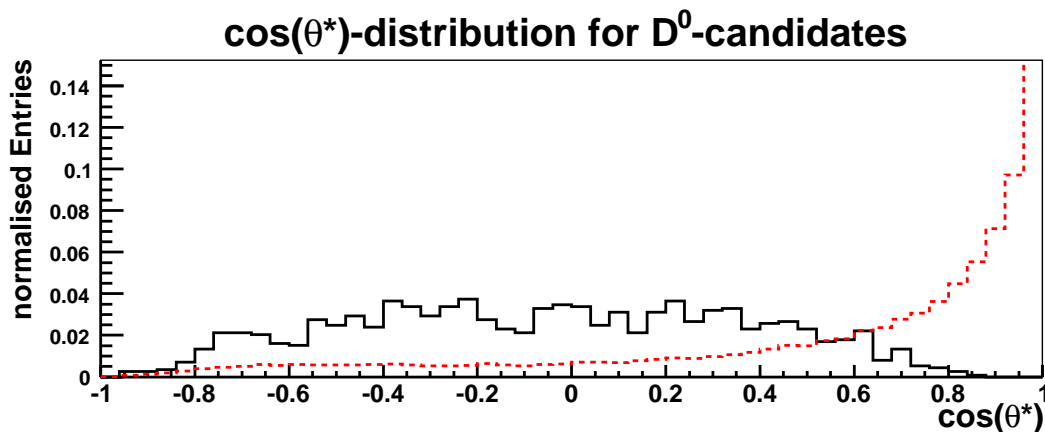


Figure 5.8: The $\cos\theta^*$ -distribution for D^0 -candidates shown for a sample of pure background events (red, dashed histogram) and a sample, where the signal fraction was enhanced (black, solid histogram). Both distributions are shape normalised.

determination. The selection of the D^0 -candidates can be greatly improved with the application of the RICH selection, which will be discussed in the next section.

5.5 The Use of Particle Identification

In figure 5.9 the invariant mass distribution for the D^* -tagged sample is shown after the application of the kinematic cuts described in the previous section. When looking at the signal region, i.e. about 2σ around the peak of the Gaussian signal, the ratio of signal to background events is around 0.24. In the case of the untagged sample the situation is a lot worse. Without the background suppression through the D^* -tag, the signal of the D^0 -meson is hardly visible. It is estimated, that the ratio of background to signal events in this sample is larger than 20.

For a further suppression of the background (K, π) pairs, the information recorded in the RICH for the selected track pairs is used. This allows the suppression of all track pairs where the kaon and pion candidate could not be identified in the RICH. Especially for the kaon a large suppression factor is expected, since only about 10% of the original background combinations contain a real kaon [86]. For the identification of the two hadrons the reconstructed RICH information (see section 4.1.3) is used. Here, both methods described in section 4.1.3 were used. The χ^2 -method was applied to the data taken in 2002 and 2003, for the data from 2004 the likelihood method was applied.

Both methods can only be applied to particles with a momentum above the Cerenkov thresholds for the RICH detector (see section 2.4). The momentum ranges, that can be used for the particle identification, are shown in figure 5.10, where the reconstructed Cerenkov angles are plotted versus the momentum of the reconstructed tracks. The figure shows the three bands for the three mass hypothesis of pion, kaon and proton. In the upper left corner, a small fraction of the electron band can also be seen. From the figure one can deduce the momentum ranges, in which the dif-

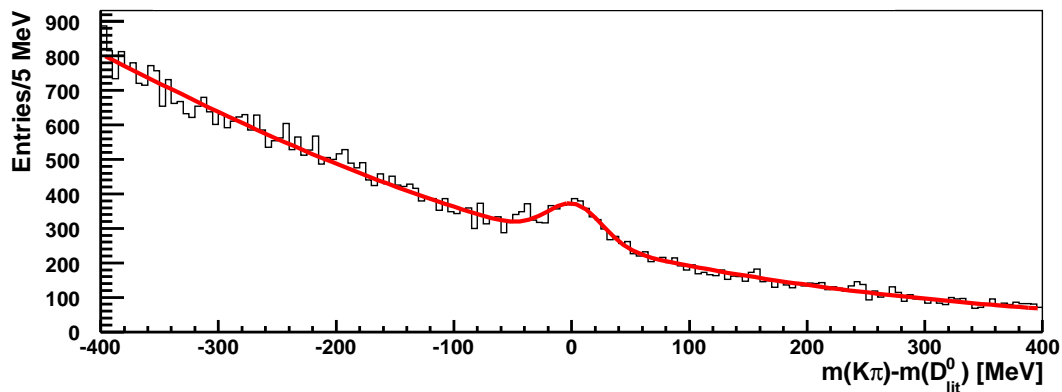


Figure 5.9: Invariant mass spectrum of the (K, π) -pairs for the D^* -tagged sample before the RICH cuts were applied. The curve shows the result of a fit to the data, where the sum of a Gaussian and an exponential background function was used. The signal to background ratio is about 1:4 in the signal region ($\pm 2\sigma$). The data sample shown here corresponds to 7 data taking periods of 2004.

ferent particle types can be identified. To identify kaons, the momentum has to be above the kaon threshold of around 9 GeV, for pions the threshold lies around 2.5 GeV and for protons it is around 17 GeV. The upper momentum limits for a good particle identification are not as clearly visible. One can see in figure 5.10, that the separation of kaon and pion band is increasingly difficult when going to momenta higher than 40 GeV. However, at these high momenta much less combinatorial background contributes to the two D^0 -samples. Therefore, it was decided to use an upper limit for particle momenta for the RICH identification of 50 GeV.

The identification criteria for kaon and pion depend on the method available for the data set. To identify a kaon based on the χ^2 -method (see section 4.1.3), the different χ^2 -values calculated for the kaon-candidate are examined. For a positive identification, the χ^2 -value for the kaon hypothesis has to be the smaller than all others and smaller than 5, to ensure a reliable fit of the Cerenkov signal.

For the identification with the likelihood method, all likelihood values belonging to the kaon-candidate are used. In general, a particle was identified as a kaon, when the likelihood for the kaon hypothesis was larger than all other likelihoods, including the background likelihood. However, for the open charm analysis it was observed, that for the kaon-candidates, the kaon-likelihood and the pion-likelihood are very close. Many kaons have reconstructed momenta in the region, where the two Cerenkov bands already overlap and the signal from the RICH becomes ambiguous. To avoid losing too many good kaons from this region, a cut on the likelihood-ratio of kaons and pions to be larger than 0.98 (1.02) was applied. Here, the second value was used for a subset of the data from 2004, that were produced with a different version of the likelihood analysis. In addition, the ratio of the kaon-likelihood to the background likelihood was used, to improve the quality of the RICH selection. With a cut on this ratio to be larger than 1.24 (1.06) all those candidates are removed, where the observed Cerenkov signal does not show much difference from a background

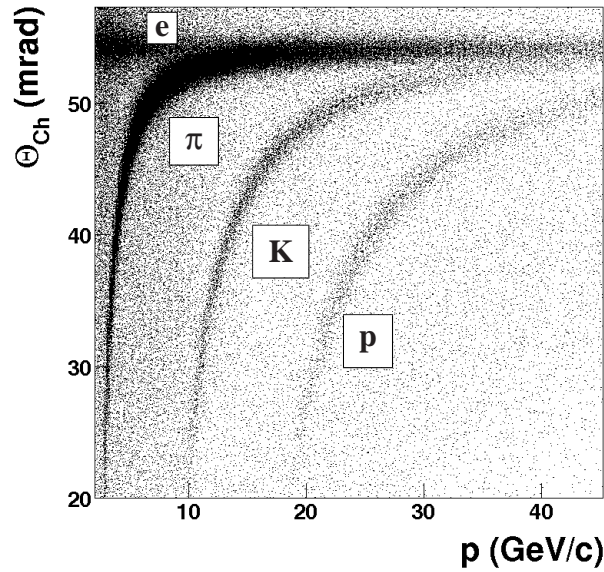


Figure 5.10: Reconstructed Cerenkov angles versus the momentum of the particle's tracks. The entries referring to particles identified as pions have been suppressed by a factor of 3; those referring to particles identified as protons have been multiplied by a factor of 4.

event. The values of the two cuts were chosen to optimise the effective signal of the selected D^0 -mesons. It is clear, that they were tuned to the requirements of the open charm analysis, where a small amount of signal is surrounded by a very large combinatorial background. The cuts were therefore also checked on other kaon samples, e.g. from Φ -decays.

For the identification of the pion-candidate, the available reconstructed RICH information – likelihood or χ^2 values – of the reconstructed track are used. For the identification through the likelihood method, the likelihood of the pion hypothesis has to be the largest likelihood for this track. Additional requirements, as for the kaon identification, are not used for the pion identification, since most pion-candidates are expected to be pions.

For a positive identification from the χ^2 method, the χ^2 -value for the pion hypothesis should be smaller than all other χ^2 -values and smaller than 5. In the untagged sample an additional background suppression is achieved by requiring the momentum of the pion candidate to be larger than 9 GeV. For the χ^2 -method the requirements for the pion identification in the D^* -tagged sample are a bit more relaxed. Instead of requiring a full identification of the pion based on the χ^2 -values, it is only required, that the pion cannot be identified as a kaon. This change was added to improve the efficiency of the RICH selection.

Figure 5.11 shows an invariant mass spectrum of D^* -tagged D^0 -candidates after the application of the RICH selection. The improvement in the observed signal obtained with the RICH is evident, when comparing figure 5.9 and figure 5.11. The background in the sample is suppressed by a factor 5, while the signal of the D^0 -meson is reduced by less than 10%. For the untagged sample

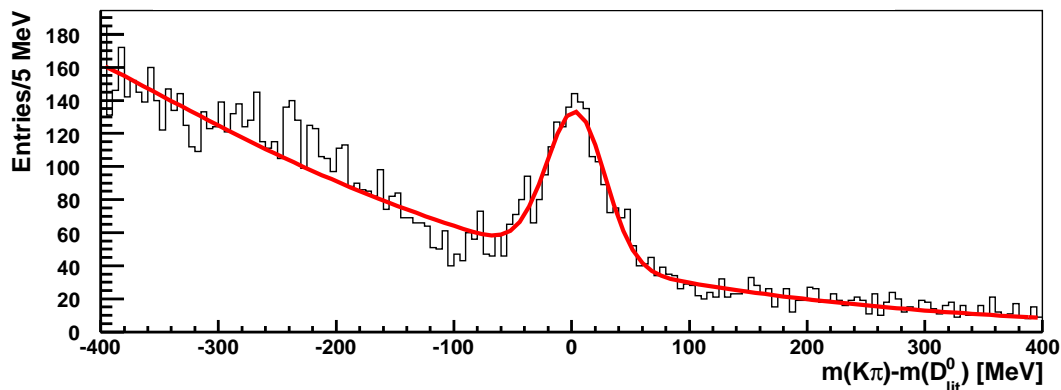


Figure 5.11: Invariant mass spectrum of the (K, π) -pairs for the D^* -tagged sample after the RICH cuts were applied. The curve shows the result of a fit to the data, where the sum of a Gaussian and an exponential background function was used. The signal to background ratio is about 1.2:1 in the signal region ($\pm 2\sigma$). The data sample shown here corresponds to 7 data taking periods of 2004.

the effect of the background suppression is even larger.

5.6 The final spectra

Before the extraction of $\langle \frac{\Delta g}{g} \rangle$, the two event samples are scanned for events with two D^0 -candidates in both samples. For the asymmetry calculation every event is only used once. So, events that have two candidates are treated in the following way: If one of the candidates belongs to the D^* -tagged sample, the other candidate to the untagged sample, the candidate of the D^* -tagged sample is kept, the other candidate discarded. If both candidates belong to the same sample neither of them is used and the event is discarded. This procedure follows the principle, that the candidate with the higher signal probability should be used in the analysis. However, a selection of one of the two candidates, i.e. based on kinematic criteria or the particle identification, could introduce a bias in the invariant mass distribution. To select the candidate with the higher probability to belong to a signal event, would introduce a difference in the treatment of signal and background events. This should however be avoided, because the information of signal and background fractions from the mass spectra will be used in the determination of $\langle \frac{\Delta g}{g} \rangle$. The only other possible treatment for events with double entries would be a random selection of one candidate. This was however not implemented, because of the very small event fraction affected by this cut (below 4% in the untagged sample, below 3% in the D^* -tagged sample).

The final events samples for the three years of data taking analysed in this thesis are presented in figures 5.12 for the D^* -tagged candidates and in figure 5.13 for the untagged sample. They correspond to a total statistics of 13300 untagged D^0 -mesons and 3450 D^* -tagged D^0 -mesons. For the D^* -tagged sample an average signal-to-background ratio was reached for candidates within 2σ of

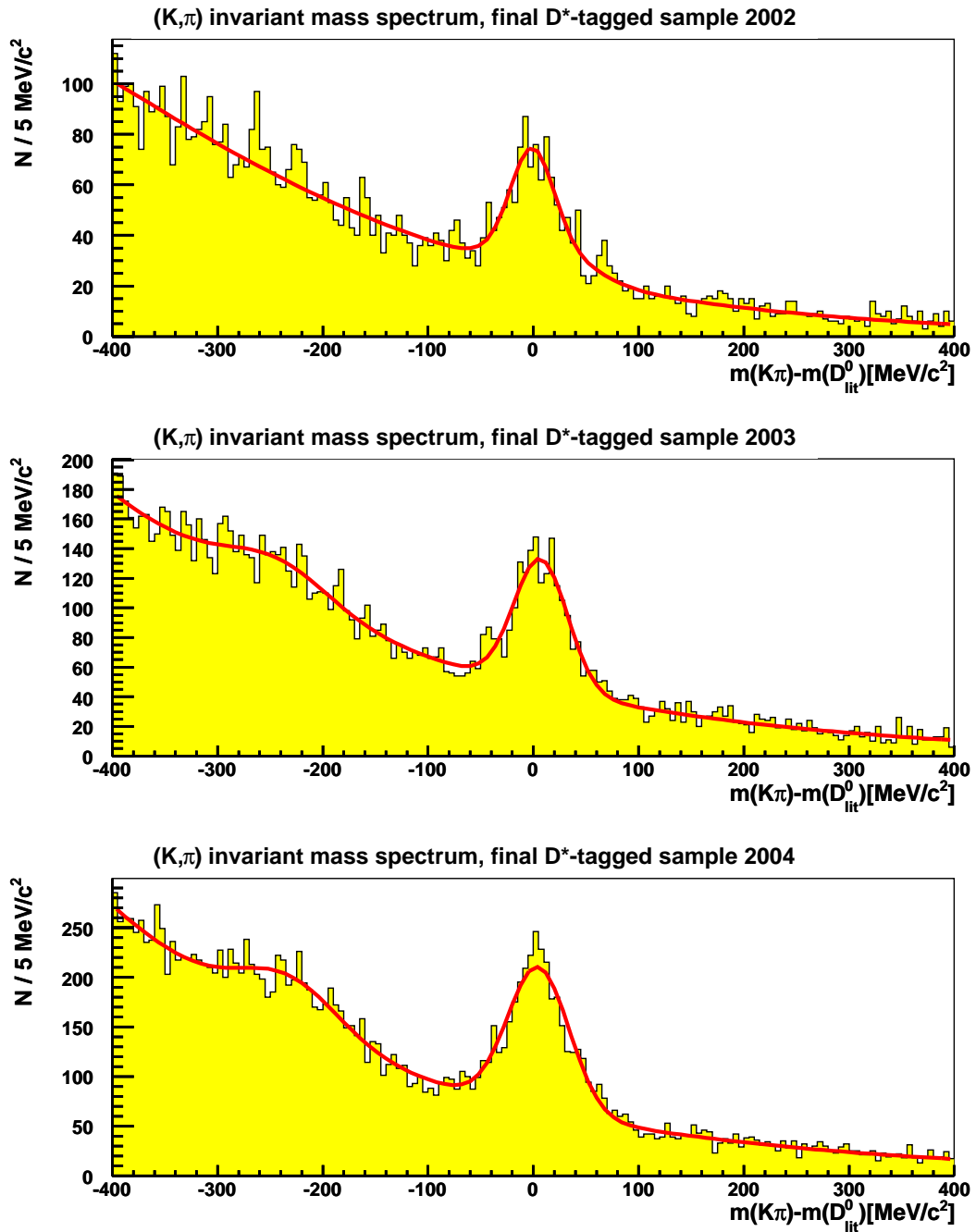


Figure 5.12: Invariant mass spectrum of the of the (K, π) -pair for the D^* -tagged event samples from the data taken in 2002, 2003 and 2004.

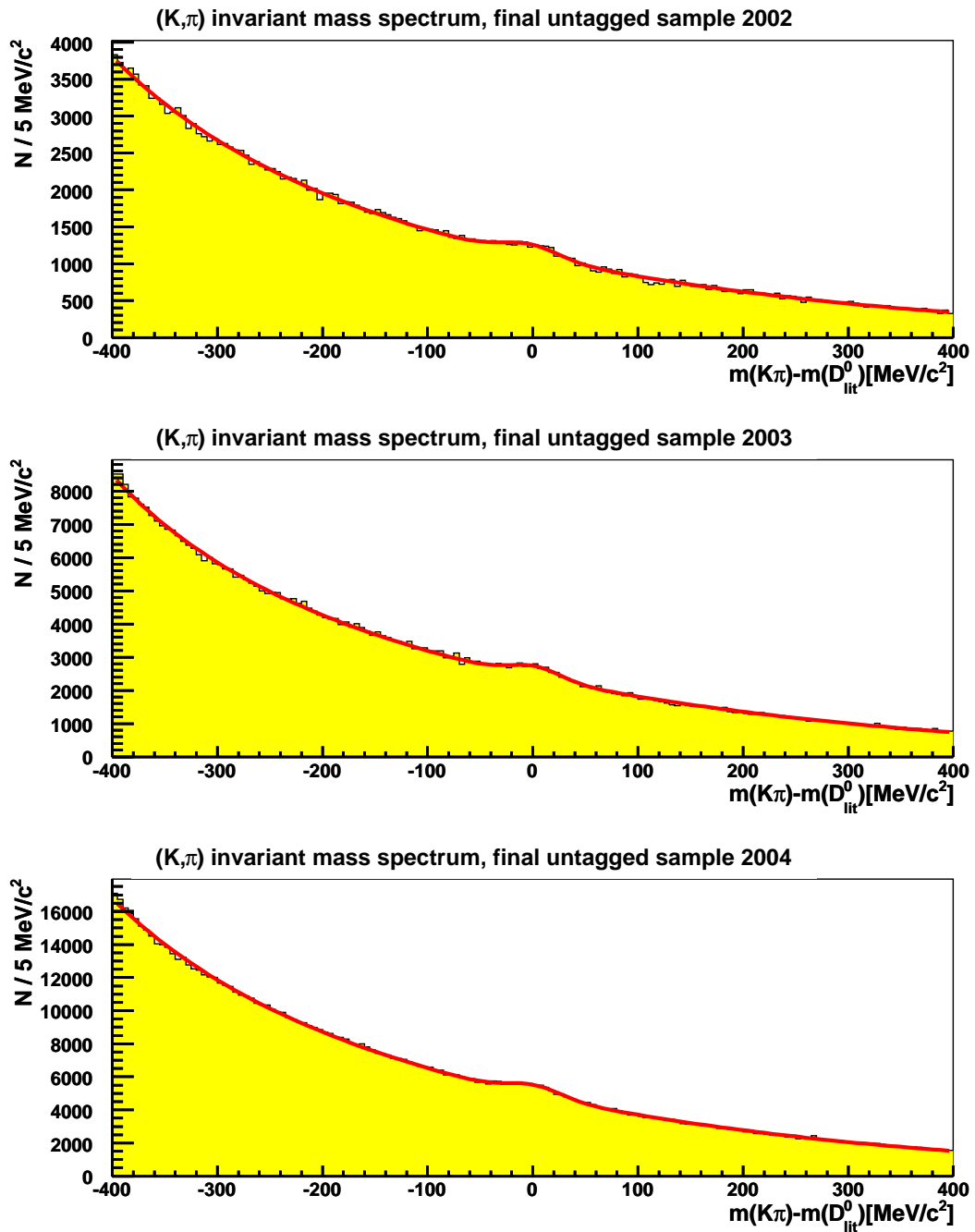


Figure 5.13: Invariant mass spectrum of the of the (K, π)-pair for the untagged event samples from the data taken in 2002, 2003 and 2004.

the maximum signal in the invariant mass, for the untagged sample the average ratio was 0.077. Table 5.1 gives an overview over the contributions of the three different years in terms of statistics and figure-of-merit. As can be seen, the largest contributions are coming from the data taken in 2004.

	$N(D^0)$	$N(BG)$	FOM	D^0/BG
2002 untagged	2032 \pm 260	24194 \pm 141	157 \pm 42	0.084 \pm 0.011
2002 D^* -tagged	386 \pm 159	557 \pm 500	158 \pm 178	0.693 \pm 0.695
2003 untagged	3855 \pm 358	46892 \pm 185	293 \pm 56	0.082 \pm 0.011
2003 D^* -tagged	1064 \pm 59	938 \pm 239	565 \pm 104	1.13 \pm 0.29
2004 untagged	7427 \pm 512	100702 \pm 277	510 \pm 73	0.074 \pm 0.005
2004 D^* -tagged	2001 \pm 68	1554 \pm 188	1127 \pm 114	1.29 \pm 0.16

Table 5.1: Overview of the statistics of the tagged and untagged samples from 2002-2004. All number are determined from the fitted curves to the invariant mass distributions shown in figures 5.12 and 5.13. The event numbers are determined from the integrals over a 2σ -region of the Gaussian signals. The figure-of-merit and the signal-to-background ratio are calculated from the event numbers.

Chapter 6

Cross-section for D^* -Production in COMPASS

In this chapter the procedure for the D^* -meson production cross-section measurement is described and a first estimation for the result is given. This estimation is based on the event sample, where one D^* -meson was reconstructed. Thus the cross-section for the process

$$\mu N \longrightarrow \mu' D^{*\pm} X$$

is determined. The event sample used in this study corresponds to a subsample of the 2004 data set. The D^* -mesons were selected with the same selection cuts as for the asymmetry measurements described in chapter 5. A Monte Carlo sample was analysed in parallel, where the same software and selection cuts were applied.

The study was restricted to the D -meson sample with D^* -tag. In the untagged D^0 -sample the large background under the D^0 -signal introduces large uncertainties. Therefore, this second sample was not used.

The production cross section is determined from the number of reconstructed D^* -mesons in the event sample $N(D^{*\pm})$, the integrated luminosity of the event sample \mathcal{L} , an acceptance factor ϵ , which was determined from the Monte Carlo sample and the branching ratio (BR) of the D^* -decay that is reconstructed, using

$$\sigma_{\mu N \rightarrow \mu' D^{*\pm} X} = \frac{N(D^{*\pm})}{\mathcal{L} \cdot \epsilon \cdot BR} \quad . \quad (6.1)$$

In this chapter, the procedures used to determine the different factors in the cross-section determination will be presented. To estimate the accuracy of this cross section measurements, two analysis were performed. In one analysis, the information from the RICH was used, in the second analysis it was discarded. The same procedure was followed for the real data sample and the Monte Carlo sample, thus the resulting values for the cross-section should agree.

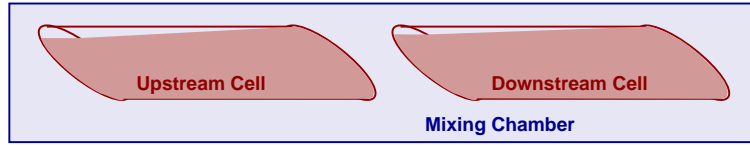


Figure 6.1: The materials in the target cells. The two cells are filled with ${}^6\text{LiD}$. Because of the incomplete filling ${}^3\text{He}$ and ${}^4\text{He}$ from the mixing chamber also contribute to the area density.

6.1 The Luminosity Measurement

The luminosity is a scaling factor, that relates the number of observed events with the cross section:

$$N_{event} = \mathcal{L} \sigma \quad . \quad (6.2)$$

Here N_{event} is the number of observed events, σ the cross-section and \mathcal{L} the integrated luminosity for the data sample. The luminosity is a function of the amount of particles crossing the interaction point and the size of the interaction point. It can be calculated from

$$\mathcal{L} = N_1 \frac{N_2}{A} \quad , \quad (6.3)$$

where N_1 and N_2 are the number of particles from beams or targets in the interaction point and A is the area of the particle crossing.

For a fixed target experiment the luminosity is determined by measuring the intensity of the beam for N_1 and the area density of the target to determine N_T/A . For most experiments, the beam has a beam spot of a much smaller size compared to the cross section of the target. In these cases, the measured beam flux can be directly multiplied with the mass density of the target to determine the luminosity.

In COMPASS, the size of the beam spot is in the same order than the cross-section of the target. The cross-section of the target is therefore the size of the interaction point A entering the luminosity calculation. Since the beam flux is measured for all beam particles, it has to be corrected for the part of muons that do not fully cross the target.

6.1.1 Target Thickness

The area density of the target N_T/A entering the luminosity has to be determined using all nucleons in the target, not only the polarisable fraction of the target material used in the asymmetry measurements. Therefore not only the target material ${}^6\text{LiD}$ and its isotopes are taken into account, but in addition the contribution from the liquid ${}^3\text{He}$ and ${}^4\text{He}$ in the mixing chamber of the dilution refrigerator is considered (see figure 6.1).

The number of nucleons in the target N_T is determined from the weight of the target material m_T using

$$m_T = N_T \cdot m_{nucl} \quad , \quad (6.4)$$

where the mass of one nucleon is $m_{nucl} = 1.6738 \cdot 10^{-27}$ kg [5]. The weight is determined using a special scale, permitting the weight of the target material to be measured at temperatures below 100 K, which is necessary to preserve the material. A full description of these measurements can be found in [89]. The typical mass of the target material in both cells is about 350 g, to this are added about 60 g of liquid helium. The exact amount of target material in the target varies between different target fillings by a few grams.

The target density is obtained by dividing the number of nucleons in the target by the surface of the target,

$$\rho_T = \frac{N_T}{A} = \frac{N_T}{\pi r^2} , \quad (6.5)$$

where A is the surface of the target, that is perpendicular to the beam and illuminated by beam particles. Since the width of the muon beam is larger than the surface of the target, A is simply size of the entrance window of the target. For the cylindrical COMPASS target, A corresponds to a circle with a radius of 1.5 cm.

For the data taking in 2004 a target density of $3.49 \cdot 10^{25}$ N/cm² was obtained [90]. The relative error on the area density of the target of 2% is coming from the uncertainty of the mass and volume measurements.

This procedure to measure the area density assumes, that the density of the target nucleons is homogeneous over the full surface of the target. This assumption is correct for a completely filled target. However, in the years 2002-2004 the target was not completely filled. Therefore, in the analysis strict cuts are applied on the fiducial target volume, for which a homogeneous target filling can be assumed.

6.1.2 Measuring the Muon Flux

To determine the number of muons crossing the target, hits from muons in a scintillating fibre station installed directly in front of the target are counted. This detector has a surface of a similar size to that of the target. The standard read-out of the 96 channels of the detectors y-plane is done via photo-multipliers. To count the muons crossing this detector, an analogue signal is picked up at the last dynode of each photo-multiplier and combined to six individual analogue signals, each comprising 16 original detector channels in a logical "OR". The analogue signals are discriminated and directed on an electronic scaler, which counts the number of hits in each spill. At full beam intensity, the rate counted by this scaler was about $2 \cdot 10^8$ muons per spill. The uncertainty on the scaler count is related to the electronics used to count the muons. The largest effect especially for high beam intensities is coming from the dead time of the electronics, which reduces the counting efficiency. On the other hand, muons can also produce two hits on neighbouring strips of the fibre station, which the electronics cannot detect. Since all these effects have not yet been fully investigated, an upper limit of 10% was deduced from the rough estimations of the two effects.

The scaler provides an estimate of the number of muons present in the spectrometer in each spill. However, not every muon hitting the scintillating fibre station contributes to the luminosity. Therefore, a correction factor has to be applied to the number of muons counted by the scaler [91]. This correction factor takes several effects into account. The largest correction is coming from the geometric difference of the fibre station and the target. Only muons that cross the full target length

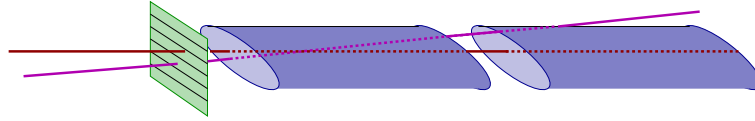


Figure 6.2: The origin of the correction factor for the beam flux counted by the scintillating fibre stations. The upper track hits the station but not the target, the lower track hits both. A correction factor is used to correct for these geometric effects.

inside the fiducial volume should enter the luminosity determination. This is illustrated in figure 6.2, where two beam tracks entering the target zone are shown. Both hit the fibre station, but only one of them fully crosses the target. The other one should not be used in this measurement. The ratio of hits in the fibre station versus usable beam tracks is determined from random trigger events using reconstructed beam muons that do not interact in the target. To determine the fraction of usable beam tracks, all beam tracks in a time window around the trigger signal of the random trigger events are reconstructed. Then it is checked, how many tracks hitting the fibre station also cross both target cells.

An additional correction comes from the reconstruction efficiency of the beam momentum station. It was also determined using random trigger events. For beam tracks without interaction in the target two momentum measurements are available in COMPASS. The measurement of the BMS can be compared to a measurement in the small angle spectrometer, using the field of SM2 for the momentum determination. From such a comparison, the reconstruction efficiency of the BMS was identified to be 96% [92].

For 2004, the correction factor for the scaler rate of the scintillating fibre station 2 was determined to be 0.58 ± 0.03 . The uncertainty of this number has two origins. On one hand, a slight difference in the result was observed, when using two differently generated random triggers [91]. On the other hand, for the study presented here, not all random trigger events recorded in 2004 were available, resulting in a higher statistical uncertainty of the result.

6.1.3 Dead-times in Data Taking

Another factor entering the luminosity of an experiment, is the data taking efficiency. This efficiency is related to the fact, that the detectors cannot record a new event at any given moment. In particular, when the data acquisition is already busy recording a previous event, the detector is blind to what happens in the target. This dead-time of the spectrometer is induced by the data acquisition system. In 2004, the dead-time of the COMPASS DAQ in 2004 was 5%. The luminosity determined from the beam flux and the target mass is corrected by this dead-time, to obtain the luminosity for the recorded events. The relation between the recorded luminosity $\mathcal{L}_{recorded}$, that is used for the cross-section measurement, and the true luminosity \mathcal{L}_{true} obtained from beam and target is

$$\mathcal{L}_{recorded} = (1 - T_{dead}) \mathcal{L}_{true} \quad , \quad (6.6)$$

where T_{dead} is the dead-time of the spectrometer.

The second dead-time appearing during data taking is the dead-time of the veto system. When a halo muon hits one of the veto detectors, the veto signal will become active. While the veto is active, all good muons interacting in the target are prevented from causing a trigger. To reduce this so-called veto dead-time as much as possible, the veto signals are kept as short as possible. Moreover, different veto signals with different rates are used for the different physics triggers. Thus, one single dead-time factor cannot be given for the full trigger system. The different dead-times induced by the veto system are also reported in [71]. When determining a cross section, the veto dead-time is not included in the luminosity. Instead, the different values for the veto dead-time are included in the Monte Carlo simulation of the spectrometer. Depending on the physics trigger of the event, the event can be rejected with a probability that corresponds to the dead-time of the veto used for this trigger.

For the data set used for this cross section determination a total flux of $N_{\mu}^{counted} = 22.5 \cdot 10^{12} \pm 10\%$ muons was counted by the fibre station. This number is multiplied with the correction factor and DAQ dead-time to obtain the corrected muon flux of $N_{\mu}^{corr.} = 12.4 \cdot 10^{12} \pm 11\%$. The integrated luminosity obtained for this data sample is

$$\mathcal{L} = 0.43 \text{ fb}^{-1} \pm 12\% .$$

6.2 Determination of the Acceptance Factor

The acceptance factor ε comprises the probability of a D^* -meson produced at COMPASS energies to have three reconstructible decay products within the COMPASS acceptance and the efficiency for the D^* to be reconstructed in the COMPASS spectrometer. It is determined using Monte Carlo events generated with the AROMA generator [93]. This generator simulates events where a heavy quark is produced in the PGF process (see section 1.3.1), which is the principal process for charm production in COMPASS.

To determine ε the detector response for the generated events is simulated. The four-vectors of the generated particles were fed into a simulation of the COMPASS spectrometer, in which the interactions of the particles with the different detectors were simulated. These simulated detector events were then reconstructed using the standard CORAL data reconstruction as described in section 4.1 to obtain reconstructed events. From these events D^* -candidates were reconstructed using the all selection cuts described in chapter 5. An exception is made for the RICH selection, which is only used in one of the two analysis. In the second analysis for the cross-section measurement the generated RICH information was not used. The final spectrum of the D^0 -mass of the generated event sample with RICH selection is shown in figure 6.3. In this spectrum practically no background is present under the D^0 -signal, because the Monte Carlo event sample only contained signal events.

During the full procedure the number of events passing each simulation or reconstruction step were recorded. A total of 72028 events were generated in the AROMA generator. Of these, 60000 sim-

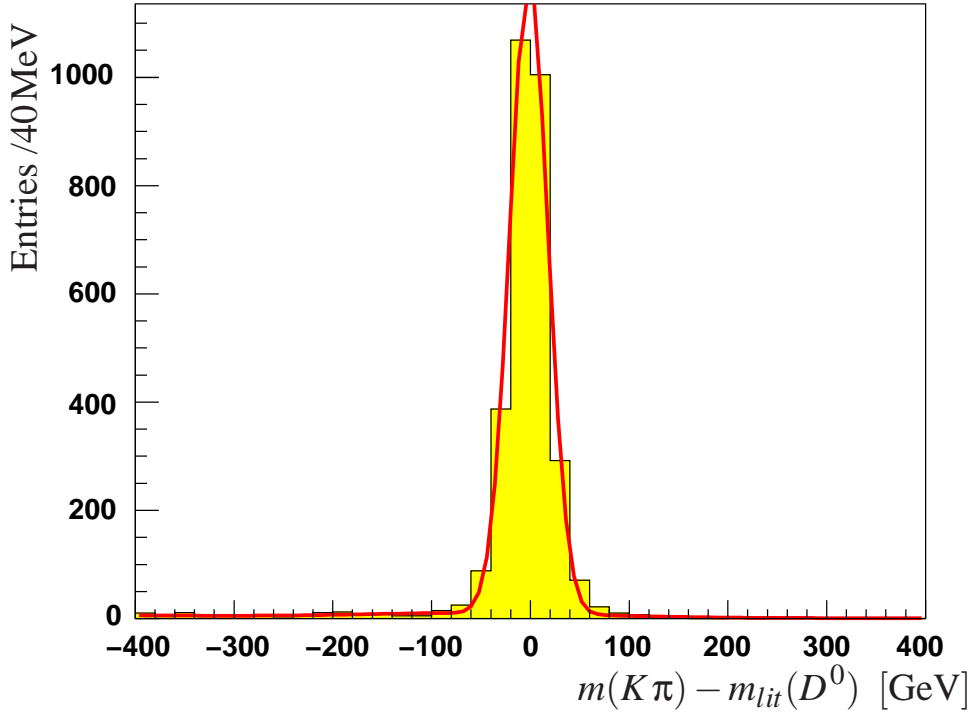


Figure 6.3: The invariant mass distribution of the D^0 -candidates of the D^* -mesons from the Monte Carlo sample. The plot shows the distribution for the sample where RICH selection was also applied.

ulated events passed the selection criteria for reconstructed events. The D^* -meson reconstruction procedure reduces this number very strongly. With no RICH selection applied, only 4189 ± 68 D^0 -mesons were found in the signal, when the RICH cuts are applied this number is reduced to 2839 ± 54 . Both numbers are taken from a fit to the spectrum, the error corresponds to the error from the fit. This large reduction of the produced D -mesons is related to the fact, that a large fraction of the D^* -mesons are produced with relatively small momenta which is reflected in the decay products. Especially the slow pion, which has in many cases a momentum around or below 1 GeV, is often stopped before exiting the thick target.

From the numbers given above, the acceptance factor for the D^* -mesons produced in COMPASS can be determined using

$$\epsilon = \frac{N(D^*_{reconstructed})}{N(D^*_{generated})} . \quad (6.7)$$

For the D^* -reconstruction without the particle identification in the RICH, an acceptance factor of $\epsilon_{no\ RICH} = 0.058 \pm 0.001$ was obtained. For the sample, where also the RICH selection was applied, this factor was $\epsilon_{with\ RICH} = 0.039 \pm 0.001$.

Before these acceptance factors are used to obtain the cross sections for the D^* -production, the reliability of the Monte Carlo information is verified. For that purpose the distributions of Monte Carlo generated events and real data were compared. To both samples all selection cuts were

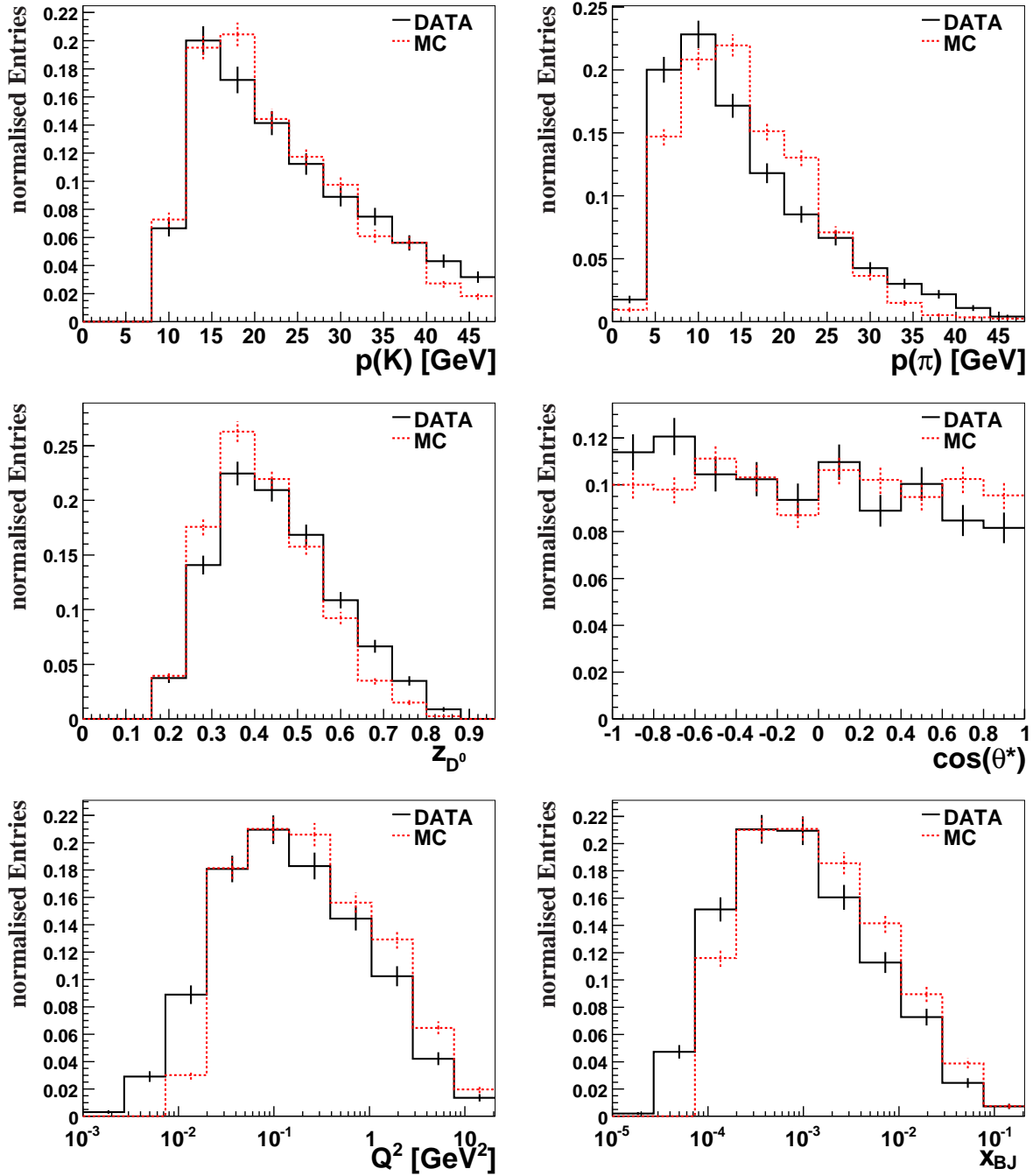


Figure 6.4: Comparison of the distributions of the Monte Carlo and the real data samples for kaon momentum $p(K)$ and pion momentum $p(\pi)$ in the upper row, the momentum fraction $z(D^0)$ and the D^0 -decay angle $\cos\theta^*$ in the middle row, and Q^2 and x_{BJ} in the lower row.

applied and the comparison was restricted to events, where the mass of the D^0 -candidate was in the region of the expected signal. This was done to suppress the influence of the combinatorial background in the real data sample. It was also tried to compare the Monte Carlo distributions with the background subtracted signal distributions from real data. However the statistical error in the distribution introduced by the background subtraction was so large, that a comparison with the Monte Carlo sample was not possible. In figure 6.4 the distributions for the Monte Carlo and the data sample are shown for some of the variables. One can see, the the agreement between the two samples is reasonable, but not perfect. While in the regions with large statistic the agreement is generally good, at the edges of the distributions larger discrepancies can be observed.

As a consequence, a larger error needs to be assigned to the acceptance factors. To quantify the effect of different distributions on the final number of D^* -mesons, a simple estimation was made. Since for most of the variables, the agreement between the real data and the Monte Carlo events was better than 20%, an additional relative uncertainty of 20% was assigned to the acceptance factors, leading to total errors of 0.0012 (0.008) for the analysis without (with) RICH selection. The final values for the acceptance factor are

$$\epsilon_{withRICH} = 0.039 \pm 0.008$$

and

$$\epsilon_{noRICH} = 0.058 \pm 0.012 \ .$$

6.3 Determination of the Number of Reconstructed D^*

For the measurement of the D^* -production cross section, a subsample of the data taken in 2004 was used. This subsample was selected from periods that had been produced with the same version of CORAL. From the events collected during the 7 data taking periods the D^* -candidates were reconstructed, using the procedures described in chapter 5 with the same selection cuts on the events, vertices and the reconstructed D^* -candidates as for the Monte Carlo sample. To determine the number of D^* -mesons in the final event samples, the mass distribution of the D^0 -candidates is considered. A fit is applied to the mass-spectra of D^0 -candidates. The fit function was formulated in such a way, that the number of D^0 -mesons in the signal of the Gaussian is one of the fit parameters. The fit provides therefore directly the number of D^* -mesons produced in the sample and its uncertainty including the correlations with the other fit-parameters.

The two analyses with and without the RICH selection result in two different numbers of reconstructed D^* -mesons. The number of D^* -mesons in the final samples are

$$N(D^{*\pm})_{withRICH} = 1194 \pm 55$$

and

$$N(D^{*\pm})_{noRICH} = 1408 \pm 105 \ .$$

For the cross-section determination the selection criterion to have exactly one D^* -meson per reconstructed event was also applied. At first sight, this criterion does not seem necessary, since the

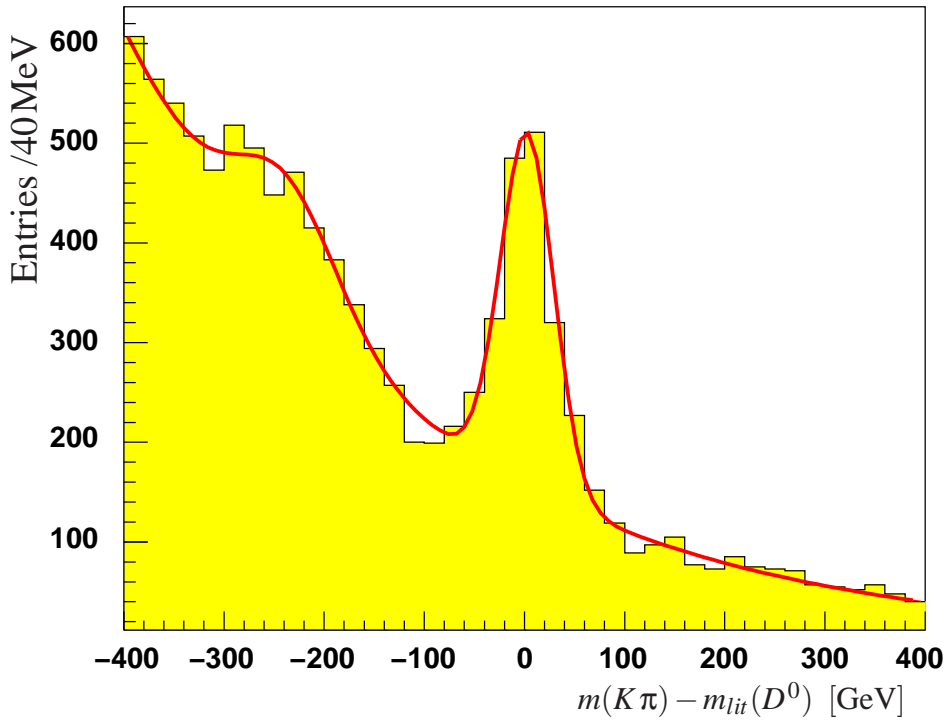


Figure 6.5: The invariant mass distribution of the D^0 -candidates of the real data D^* -meson sample used for the cross-section determination. The plot shows the distribution for the sample where RICH selection was applied.

cross-section is determined for the process

$$\mu N \longrightarrow \mu' D^{*\pm} X$$

independently of the question whether X contains a second D^* -meson. However, the treatment of events with two D^* -candidates is not straightforward in this analysis. This is mainly because the cross-section is determined for the process, where at least one D^* -meson was produced in the μN scattering. So, an event where two D^* -mesons were produced should enter the final sample only once.

The decision to reject events with more than one D^* -candidate is based on the following consideration. The number of reconstructed true D^* -mesons is taken from the amplitude of the signal in the invariant mass distribution. For a perfect fit, this number is independent of the amount of background below the signal. Of course, the fit applied here still shows fluctuations in the background description, but their influence on the size of the signal is neglected in the following.

Therefore, only events, where a true D^* -meson was produced, are considered for the cross-section analysis. For these events it is generally assumed, that their production is well described by the AROMA event generator. The events from the Monte-Carlo sample used in the analysis and the events from real data with a true D^* -meson have therefore the same properties. This holds not only for the kinematics of the produced D^* -meson but also for the other particles in the event. Thus,

the generated and the real events have the same probability, that a second D^* -candidate is found in the sample irrespective of whether this is a true D^* -meson or background. The rejection of events with more than one D^* -meson-candidate reduces therefore the signal in the real data and in Monte-Carlo by the same factor, which then cancels in the cross-section calculation.

Of course, this cancellation only occurs for a perfect description of the real events by the Monte Carlo generated sample. However, as shown in figure 6.4, there are still some discrepancies between the events from real data and the generated events. The work to improve the description of the real data by the simulated events is ongoing. For this first estimate of the D^* -production cross-section, the existing discrepancies between data and Monte Carlo are the reason for large systematic uncertainty assigned to the acceptance factor ϵ . This uncertainty also includes the effect of the rejection of events with two D^* -candidates.

6.4 The Resulting Cross Section

The final ingredient needed to determine the cross section for D^* -production in the COMPASS experiment is the branching ratio for the D^* -decay

$$D^{*\pm} \longrightarrow D^0 \pi_{slow}^{\pm} \longrightarrow K^{\mp} \pi^{\pm} \pi_{slow}^{\pm} .$$

This branching ratio is taken from [5] and has the value

$$BR = 2.5 \pm 0.06\% .$$

For the analysis where the information from the RICH was not used, the result of the cross section is

$$\sigma_{without\ RICH} = 2.26 \pm 0.56\text{ nb} ,$$

for the analysis with the RICH selection cuts the result is

$$\sigma_{with\ RICH} = 2.85 \pm 0.68\text{ nb} .$$

The relative errors of the different contributions were added in quadrature to obtain the final errors. Within the limited precision of the final values, the two results agree. The study has shown, that the limiting factor for a more precise prediction of the D^* -production cross section is the agreement between Monte Carlo and real data. The 20% uncertainty assumed for the acceptance factor is the largest error and makes up most of the total error which is about 24% for the final result. The statistical uncertainty of the number of reconstructed D^* -mesons, which is the limiting factor in the measurement of the gluon polarisation discussed in chapter 7, only contributes with 5% (7%) in the analysis with (without) the RICH.

From the values above one can conclude, that in COMPASS the D^* -production cross-section is probably around 2 – 3nb. This result can be compared to other measurements of the D^* -production cross-section in lepton-nucleon scattering. The mean Q^2 obtained from the final D^* -sample used in the cross-section determination in COMPASS is $\langle Q^2 \rangle = 0.6\text{ GeV}^2$. The Q^2 of

the COMPASS measurement lies therefore between the photo-production region and the DIS region from measurements at HERA. The H1-experiment has published a measurement of the D^* -production cross-section for both regimes [94, 95]. The inclusive D^* -cross section measured by H1 for photo-production events ($Q^2 < 0.01 \text{ GeV}^2$) is $6.45 \pm 0.46 \text{ (stat.)} \pm 0.69 \text{ (syst.) nb}$, for the DIS regime ($2 \text{ GeV}^2 < Q^2 < 100 \text{ GeV}^2$) the inclusive D^* -production cross-section was measured to be $2.90 \pm 0.20 \text{ (stat.)}^{+0.58}_{-0.44} \text{ (syst.) nb}$.

The measurement presented here shows a good agreement with the measurement from H1 in the DIS regime. The difference between the value from COMPASS and the measurement from H1 for photo-production events is a bit larger, but the two values are in a reasonable agreement considering the large uncertainty of this first estimation of the D^* -production cross-section in COMPASS.

Chapter 7

Determination of the Gluon Polarisation

In this chapter the extraction of the gluon polarisation from the event samples selected in chapter 5 will be explained and the result for $\langle \frac{\Delta g}{g} \rangle$ will be presented. Before entering into the details of the extraction method, a few kinematic plots from the final event samples are shown allowing conclusions about the production process of the observed D -mesons. In the next section the extraction method will be explained. To determine $\langle \frac{\Delta g}{g} \rangle$ from the selected events, additional quantities are needed. Their determination will also be discussed. In the last section the results obtained for the gluon polarisation are presented and compared to other measurements of the gluon polarisation.

7.1 Properties of the final data set

In figure 7.1 the distributions of the muon inelasticity y , the “Bjorken x ”, $x_{BJ} = Q^2 / 2Mv$, and the negative four-momentum transfer squared Q^2 for the final D^* -tagged and untagged event sample are shown. These distributions can be compared with the expectations related to the PGF production mechanism.

The muon inelasticity y of the events, where a reconstructed D -meson candidate was found, covers a range between ~ 0.25 and ~ 0.9 . From these values of y the average centre-of-mass energy W of the photon-nucleon system can be calculated in the proton rest frame [96]

$$W^2 = -Q^2 + M_n^2 + 2vM \quad . \quad (7.1)$$

The values of W lie between 11 GeV and 18 GeV which is the expectation for fixed target interactions (see figure 1.14). The range of W covered by the selected events is clearly above the threshold for the production of a charm quark pair through the PGF process.

The middle diagram of figure 7.1 shows the distribution of x_{BJ} . This diagram should be compared to figure 1.13, showing the different predictions for charm production via the PGF process and via the QPM process with intrinsic charm in the nucleon. When comparing the distribution of x_{BJ} from figure 7.1 to the curves from figure 1.13 it is clear, that the hypothesis of intrinsic charm in the nucleon can be excluded. The observed values of x_{BJ} are much smaller than they would be in the case of D -meson-production by intrinsic charm.

As explained in section 1.4, x_{BJ} does not correspond to the momentum fraction of the nucleon

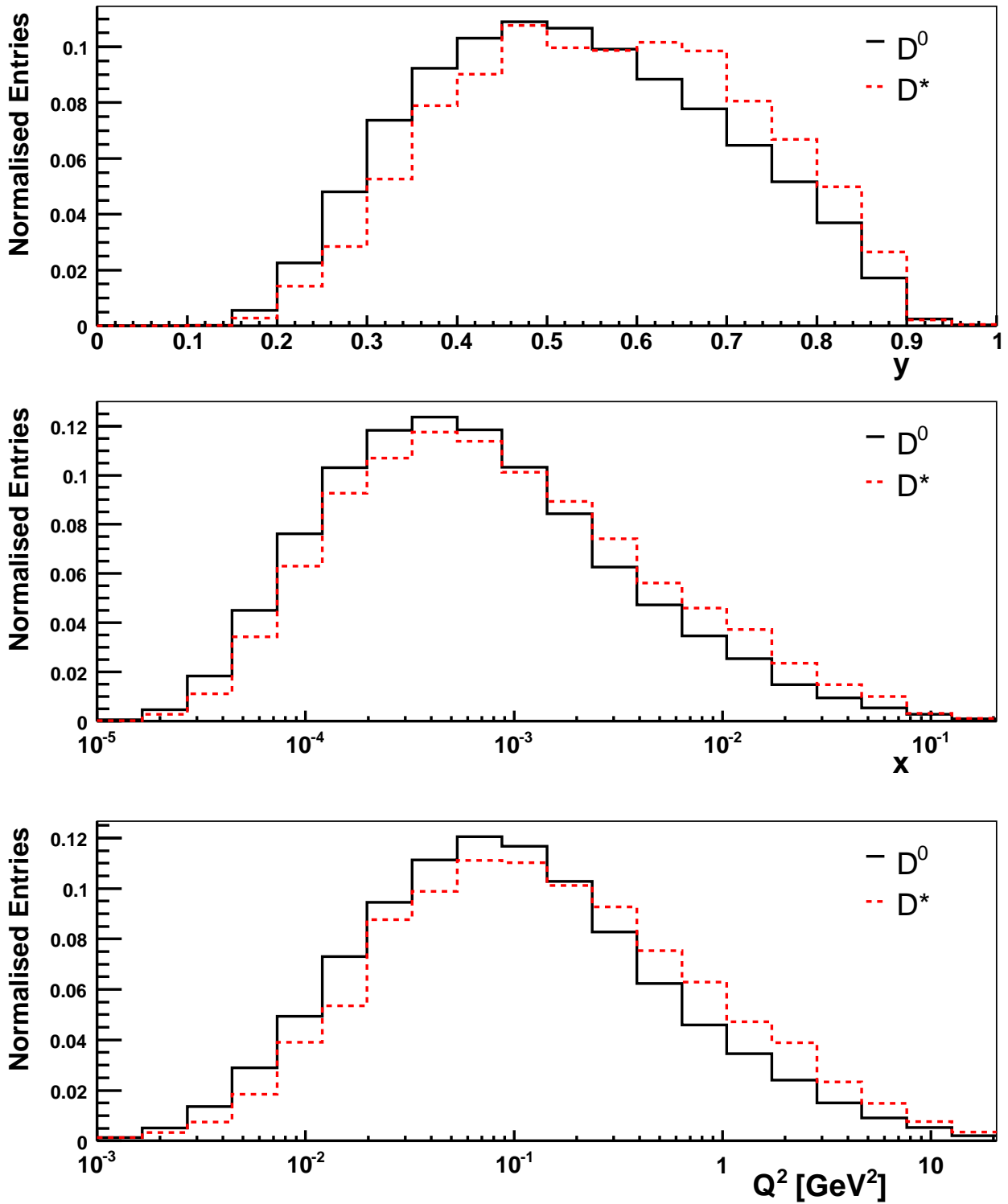


Figure 7.1: Distributions of y , x_{BJ} and Q^2 for the sample of selected D -mesons. The red, dashed lines show the histograms of the D^* -tagged sample, the black solid line the untagged D^0 sample.

carried by the gluon. The momentum fraction of the gluon, x , cannot be measured from the reconstructed events, because only one of the charm quarks from the PGF process was reconstructed. Instead, x has to be determined from events generated with the AROMA Monte Carlo generator. For the generated events, where the reconstructed D^* -meson passed all selection cuts that are also applied to the real data, the generated x was used. The mean was determined for the weighted generated events using

$$\langle x \rangle = \frac{\sum_{events} \omega_i x_i}{\sum_{events} \omega_i} , \quad (7.2)$$

where the same event weights as in the determination of $\langle \frac{\Delta g}{g} \rangle$ from real data (see equation 7.11) are applied to take into account the correlation between x and the analysing power a_{LL}^{PGF} (see section 7.3.1). The mean value of x obtained for the weighted Monte Carlo events is

$$\langle x \rangle = 0.11_{-0.05}^{+0.11} .$$

The last plot in figure 7.1 shows the distribution of Q^2 for the final event sample. The mean value is $\langle Q^2 \rangle \approx 0.5 \text{ GeV}^2$, but one can see from the distribution, that a lot of events take place at much smaller Q^2 . The samples extends therefore from quasi-real photo-production to deep-inelastic events. In this context, the most significant difference between the exchange of a quasi-real or a virtual photon is the contribution of resolved photon processes, which is larger for photo-production events. The overall fraction of resolved-photon events is estimated to be below 1% for the events in this channel (see section 1.4). Thus, their contribution was neglected.

For charm production, the scale of the hard process, $\gamma g \rightarrow c\bar{c}$, is not given by Q^2 . Instead \hat{s} , the invariant mass of the γ - g system is relevant. Since in this system two charm quarks are produced, \hat{s} has much larger values than Q^2 . Like x it cannot be calculated from the reconstructed data, and is determined from Monte Carlo generated events. The mean value of \hat{s} for this analysis is

$$\langle \hat{s} \rangle = 13 \text{ GeV}^2 .$$

Since the value of \hat{s} is essentially determined from the high mass of the two charm quarks produced in the γ - g system the correlation with a_{LL}^{PGF} is less strong, so this mean was determined for unweighted events.

7.2 Measurement of the gluon polarisation

To measure the gluon polarisation from the reconstructed D^* -mesons in the final sample, the counting rates for the different target orientations are used. The counting rate for events from interactions with a polarised beam (P_μ) and a polarised target (P_T) is given by

$$N = \varepsilon \Phi N_T (\sigma_{PGF} + \sigma_{CBG}) \left(1 + P_T P_\mu f \left[a_{LL}^{PGF} \frac{\sigma_{PGF}}{\sigma_{PGF} + \sigma_{CBG}} \langle \frac{\Delta g}{g} \rangle + a_{LL}^{CBG} \frac{\sigma_{CBG}}{\sigma_{PGF} + \sigma_{CBG}} A_{CBG} \right] \right) , \quad (7.3)$$

where ε , Φ and N_T are the acceptance factor (see section 6.2), the muon flux crossing the target and the number of nucleons in the target material. The dilution factor f and the analysing power,

a_{LL}^{PGF} and a_{LL}^{CBG} will be described in the next section. σ_{PGF} (σ_{CBG}) is the production cross-section for D -mesons (combinatorial background) in the final event sample.

The counting rate in equation 7.3 is composed from the counting rate for an unpolarised target or beam ($P_\mu = 0$ or $P_T = 0$) and a polarisation dependent part, which depends on the gluon polarisation $\langle \frac{\Delta g}{g} \rangle$ for the events with the D -mesons and on a possible background asymmetry A_{CBG} for the combinatorial background in the sample. To extract $\langle \frac{\Delta g}{g} \rangle$ and A_{CBG} these contributions are separated with the help of weighted events [97].

The spin-independent part contains the information about the number of target nucleons, the muon flux and the acceptance factor. This unpolarised part of the counting rate N_{unpol} is given by

$$N_{unpol}^{u,d} = \sum_{i=1}^{N_{EXP}^{u,d}} \varepsilon_i^{u,d} \quad (7.4)$$

$$= \varepsilon^{u,d} \Phi^{u,d} N_T^{u,d} (\sigma_{PGF} + \sigma_{CBG}) \quad , \quad (7.5)$$

where $N_{EXP}^{u,d} = \Phi^{u,d} N_T^{u,d} (\sigma_{PGF} + \sigma_{CBG})$ is the expected number of events with a D -meson from a PGF (σ_{PGF}) or from combinatorial background (σ_{CBG}), that are produced in the interaction of $N_T^{u,d}$ target nucleons and $\Phi^{u,d}$ beam muons. The acceptance factor $\varepsilon_i^{u,d}$ indicates the probability for each event to be detected and reconstructed in the final event sample. It depends on the event kinematics as well as the properties of the produced D -meson. The overall acceptance for the events is given by $\varepsilon^{u,d}$ and is the average of all $\varepsilon_i^{u,d}$.

The measurement of the gluon polarisation uses the event rates of four different event samples simultaneously. They correspond to the events in the upstream cell, when the cell was polarised parallel (N^u) or anti-parallel (N'^u) to the beam, and the equivalent rates from the downstream cell (N^d and N'^d). When comparing the unpolarised parts of the four counting rates, one obtains

$$\frac{N_{unpol}^u}{N_{unpol}^d} = \frac{\varepsilon^u \Phi^u N_T^u (\sigma_{PGF} + \sigma_{CBG})}{\varepsilon^d \Phi^d N_T^d (\sigma_{PGF} + \sigma_{CBG})} = \frac{\varepsilon^u \Phi^u N_T^u}{\varepsilon^d \Phi^d N_T^d} = \frac{\varepsilon^u N_T^u}{\varepsilon^d N_T^d} \quad \text{and} \quad (7.6)$$

$$\frac{N_{unpol}'^u}{N_{unpol}'^d} = \frac{\varepsilon'^u \Phi'^u N_T^u (\sigma_{PGF} + \sigma_{CBG})}{\varepsilon'^d \Phi'^d N_T^d (\sigma_{PGF} + \sigma_{CBG})} = \frac{\varepsilon'^u \Phi'^u N_T^u}{\varepsilon'^d \Phi'^d N_T^d} = \frac{\varepsilon'^u N_T^u}{\varepsilon'^d N_T^d} \quad (7.7)$$

Here, the requirement, that each beam muon should cross both target cells (see section 5.1), leading to $\Phi^d = \Phi^u$ and $\Phi'^d = \Phi'^u$, was applied for the last simplification. To further simplify the expressions for the unpolarised contribution, it is assumed, that changes in the acceptance between the two settings of the magnetic field, affect both cells in the same way,

$$\frac{\varepsilon^u}{\varepsilon^d} = \frac{\varepsilon'^u}{\varepsilon'^d} \quad . \quad (7.8)$$

The validity of this assumption is checked during the data stability procedures described in chapter 4. In the course of the data stability studies, all data are removed, where instabilities in the spectrometer from data taking could be observed. For the final results various additional checks are performed to determine the possible systematic error introduced through this assumption (see section 7.4).

Using this assumption, the unpolarised parts of the four counting rates can be related through

$$\frac{N_{unpol}^u}{N_{unpol}^d} = \frac{N_{unpol}^{\prime u}}{N_{unpol}^{\prime d}} . \quad (7.9)$$

To separate the contributions of $\langle \frac{\Delta g}{g} \rangle$ and A_{CBG} a double event weighting is applied. When looking at

$$N^k = N_{unpol}^k \left(1 + \beta_{PGF}^k \langle \frac{\Delta g}{g} \rangle + \beta_{CBG}^k A_{CBG} \right) , \quad k \in \{u, \prime u, d, \prime d\} , \quad (7.10)$$

which is a simplified expression of equation 7.3 where $P_T P_\mu f a_{LL}^{PGF} \sigma_{PGF} / (\sigma_{PGF} + \sigma_{CBG})$ and $P_T P_\mu f a_{LL}^{CBG} \sigma_{CBG} / (\sigma_{PGF} + \sigma_{CBG})$ were replaced by β_{PGF} and β_{CBG} , it becomes clear, that $\langle \frac{\Delta g}{g} \rangle$ (A_{CBG}) is most apparent in events where β_{PGF} (β_{CBG}) is large. Therefore, weighting each event with β_{PGF} enhances the effect of $\langle \frac{\Delta g}{g} \rangle$ in the data, whereas the background asymmetry A_{CBG} is enhanced for events weighted with β_{CBG} . This effect of the event weighting is further described in [98, 99]. The ideal choice of the event weights for a good determination of $\langle \frac{\Delta g}{g} \rangle$ and A_{CBG} are therefore the diluting factors β_{PGF} and β_{CBG} . However, one requirement for an event weight is, that it should be constant in time [98]. This is not the case for the target polarisation, P_T . During the measurements, the target was either still radiated with microwave to increase the polarisation or in the frozen spin mode, where the nucleon spins slowly relaxed. Thus, the degree of polarisation in the target is changing with time. The target polarisation was therefore excluded from the weights. The event weights used for the analysis are given by

$$\omega_S = P_\mu f a_{LL}^{PGF} \frac{\sigma_{PGF}}{\sigma_{PGF} + \sigma_{CBG}} \quad (7.11)$$

$$\omega_B = P_\mu f a_{LL}^{CBG} \frac{\sigma_{CBG}}{\sigma_{PGF} + \sigma_{CBG}} \quad (7.12)$$

With these event weights, we can formulate two relations between a measured sum-of-weights, $\sum_{i=1}^{N^k}$ and $\langle \frac{\Delta g}{g} \rangle$ and A_{CBG} for each of the four event samples. This gives us eight equations like

$$\sum_{i=1}^{N^k} \omega_S^i = \alpha_S^k \left(1 + \langle \beta_{PGF}^k \rangle_S \langle \frac{\Delta g}{g} \rangle + \langle \beta_{CBG}^k \rangle_S A_{CBG} \right) \quad (7.13)$$

$$\sum_{i=1}^{N^k} \omega_B^i = \alpha_B^k \left(1 + \langle \beta_{PGF}^k \rangle_B \langle \frac{\Delta g}{g} \rangle + \langle \beta_B^k \rangle_B A_{CBG} \right) \quad (7.14)$$

with

$$\langle \beta_P^k \rangle_W = \frac{\sum_{i=1}^{N^k} \omega_W \beta_P^k}{\sum_{i=1}^{N^k} \omega_W} \quad (7.15)$$

where the index $k \in \{u, \prime u, d, \prime d\}$ stands for the four event samples, $W \in \{S, B\}$ stands for the two different weights and $P \in \{PGF, CBG\}$ stands for the two process types, producing the data in the final samples.

As before, the unpolarised part, α_W^k , of each sum-of-weights is factored out. From equation 7.4, one can see, that α_W^k can be written as

$$\alpha_W^k = \sum_{i=1}^{N_{EXP}^k} \epsilon_i^k \omega_{Wi}^k . \quad (7.16)$$

The relation between the unpolarised parts of the counting rates, equation 7.9, remains valid in the case of weighted events. This gives two additional equations constraining the unpolarised contributions by

$$\frac{\alpha_S^u}{\alpha_S^d} = \frac{\alpha_S'^u}{\alpha_S'^d} \quad \text{and} \quad \frac{\alpha_B^u}{\alpha_B^d} = \frac{\alpha_B'^u}{\alpha_B'^d} \quad (7.17)$$

Equations 7.13, 7.14 and 7.17 provide a set of 10 equations for 10 quantities, that cannot be directly measured. Those are the eight unpolarised contributions α_S^k and α_B^k ($k \in \{u, 'u, d, 'd\}$) and $\langle \frac{\Delta g}{g} \rangle$ and A_{CBG} .

The eight sums-of-weighted events, $\sum_{i=1}^{N^k} \omega_S^i$, and $\sum_{i=1}^{N^k} \omega_B^i$ and the mean value of the diluting factors, $\langle \beta_p^k \rangle_S$ and $\langle \beta_p^k \rangle_B$ are obtained directly from the reconstructed events. Technically, they are determined from sums over the bins of weighted histograms of the invariant D^0 -mass spectrum. The summation limits were chosen to well contain the signal of the D^0 -meson and part of the background on each side. It was verified, that the result of the asymmetry determination does not depend on the actual choice of the integration limits.

To extract $\langle \frac{\Delta g}{g} \rangle$ and A_{CBG} from the final event samples, the 10 equations are solved for the unknown quantities. This was done using minimisation procedure from MINUIT [100]. The procedure fits a set of 10 parameters to describe the measured quantities obtained from the final event sample. It takes into account the statistical errors of all measured quantities, as well as the correlation between the sum-of-signal-weights and the sum-of-background-weights of the same event sample.

To increase the accuracy of the result, one additional constraint was introduced. This constraint is again based on an assumption concerning the stability of the acceptance during data taking. It is assumed, that a change in the acceptance of one cell affects signal and background events in the same way. This leads to the following constraint on the unpolarised contributions

$$\frac{\alpha_S^u}{\alpha_S'^u} = \frac{\alpha_B^u}{\alpha_B'^u} , \quad (7.18)$$

which implies through equation 7.17 that $\alpha_S^d/\alpha_S'^d = \alpha_B^d/\alpha_B'^d$. This is a much weaker assumption on the stability of the acceptance, than equation 7.8. Nevertheless, it was verified, that this additional constraint does not introduce a bias on the result of $\langle \frac{\Delta g}{g} \rangle$ [97, 101]. The introduction of this last constraint makes the system over-determined, since 11 constraints are given for 10 parameters. Therefore it is possible to evaluate the compatibility of the data with the fit result [97].

The extraction of $\langle \frac{\Delta g}{g} \rangle$ and A_{CBG} is done separately for each data taking period and the two channels. In 2002-2004 there were 29 data taking periods. The final result is the average of the 29 different values using the statistical error of each result in the calculation of the average.

7.3 Observables needed for the measurement

This section discusses the determination of the different values needed for the extraction procedure from the data. Several of the observables are not only used for the measurement of the gluon polarisation, but also in other asymmetry measurements by COMPASS [23]. Their determination is done in the standard way for COMPASS. Only the analysing powers, a_{LL}^{PGF} and a_{LL}^{CBG} , and the parametrisation of the signal strength $\sigma_{PGF}/(\sigma_{PGF} + \sigma_B)$ are specific to this analysis and will be discussed in more detail.

Target Polarisation

The target polarisation P_T is measured with NMR coils around the target cells [102], which are calibrated from thermal equilibrium measurements once for every data taking year. For each cell only one value is used in the analysis, which is the mean of the calibrated measurements from all coils of this cell. In the years 2002, 2003 and 2004 very similar target polarisations were achieved. The average value of the polarisation in the upstream cell was 50%, in the downstream cell it was 48%. The NMR coils measure the polarisation of the deuterons in the target. To obtain the polarisation of the nucleons of the deuterons, this polarisation is corrected for the D -wave state of the deuteron

$$P_T^N = P_T^{d,meas} (1 - 1.5\omega_D) \quad (7.19)$$

with $\omega_D = 0.05 \pm 0.01$ [24].

A 5% systematic uncertainty is assigned to the values of the target polarisation. This uncertainty corresponds to the spread of the NMR measurements in the same cell.

Beam Polarisation

In COMPASS, the beam polarisation P_B is not measured. Instead it is determined from the momentum of the incoming muon using a parametrisation obtained in a Monte Carlo simulation, which describes the transport of beam particles from the production target (“T6” in figure 2.1) to the experiment and parametrises the polarisation from the ratio E_μ/E_π (see also equation 2.1). The validity of this simulation was verified by measurements of the beam polarisation by the SMC collaboration [103, 104]. For the data taken in 2002 and 2003, the average beam from the parametrisation was 76%, in 2004 it was 80%. A systematic uncertainty of 5% is attributed to the values of the beam polarisation from the simulation used in this analysis.

Dilution factor

The dilution factor describes the fraction of polarisable nucleons participating in the interaction with the muon beam. It depends on the number of nucleons in the different materials inside the target and on the cross-sections for the muon-scattering on the nucleons in the different materials. The main target material, ${}^6\text{LiD}$, contains 8 nucleons per molecule of which only 4 are in a deuteron-like spin state and can be polarised. Besides ${}^6\text{LiD}$ other materials can be found in the target. The second largest contribution is the liquid helium of the dilution refrigerator, but small traces from

other elements can also be found [89].

Taking into account the number of nucleons from the deuteron n_d and from the different other materials n_A , the dilution factor f can be calculated with

$$f = \frac{n_d}{n_d + \sum_A n_A \left(\frac{\sigma_A}{\sigma_d} \right)} , \quad (7.20)$$

where the cross-section ratios (σ_A/σ_d) are approximately proportional to the ratios of unpolarised structure functions (F_2^A/F_2^d) . F_2^A and F_2^d are expressed per nucleon.

In COMPASS, the dilution factor is calculated as a function of x_{BJ} and y to account for the dependence of the cross-sections σ_A and σ_d on the kinematics of the scattering process [105]. This is done with a parametrisation, which is based on routines developed in the SMC collaboration [30]. The average value of the dilution factor for the data analysed in this thesis is $f = 0.41$. Because of the remaining uncertainties in the composition of the material inside the two target cells, a systematic uncertainty of 5% is associated to this value.

7.3.1 Determination of the analysing power

The analysing power a_{LL} is the asymmetry for the $\mu g \rightarrow c\bar{c}X$ process for the signal events. For the combinatorial background it corresponds to the asymmetry of the muon-parton scattering process. It essentially describes the sensitivity of an observed event to the gluon polarisation or the background asymmetry. It can be factorised into a contribution from the muon-photon vertex and a contribution from the photon-parton interaction:

$$a_{LL}^{PGF} = D \cdot \frac{\Delta\hat{\sigma}}{\hat{\sigma}} . \quad (7.21)$$

Here, D is the depolarisation factor introduced in section 1.2 and $\Delta\hat{\sigma}$ ($\hat{\sigma}$) the polarised (unpolarised) cross-section of the underlying photon-parton interaction. For the combinatorial background it is not clear, which parton interacts with the incoming photon. It was therefore decided, to use the depolarisation factor for the analysing power

$$a_{LL}^{CBG} = D . \quad (7.22)$$

For the signal events the underlying partonic interaction is the photon-gluon fusion process $\gamma g \rightarrow c\bar{c}X$. For this process, the partonic asymmetry $\Delta\hat{\sigma}/\hat{\sigma}$ can be calculated as a function of the Mandelstam variables \hat{u} , \hat{s} and \hat{t} of the hard subprocess [106]

$$\hat{s} = (\mathbf{P}_\gamma + \mathbf{P}_g) = (\mathbf{P}_c + \mathbf{P}_{\bar{c}}) \quad (7.23)$$

$$\hat{t} = (\mathbf{P}_\gamma - \mathbf{P}_c) = (\mathbf{P}_g - \mathbf{P}_{\bar{c}}) \quad (7.24)$$

$$\hat{u} = (\mathbf{P}_\gamma + \mathbf{P}_{\bar{c}}) = (\mathbf{P}_g + \mathbf{P}_c) \quad (7.25)$$

where \mathbf{P}_x is the four-momentum of parton x .

Thus, to calculate $\Delta\hat{\sigma}/\hat{\sigma}$ the kinematics of the two outgoing charm quarks are needed. For the

open charm events in the final sample, this information is not available, since only one of the two charm quarks is detected through the reconstructed D -meson. Therefore $\Delta\hat{\sigma}/\hat{\sigma}$ cannot be calculated from reconstructed events. Instead, $\Delta\hat{\sigma}/\hat{\sigma}$ is parametrised from measurable quantities using a neural network [107]. The parametrisation is based on Q^2 , x_{BJ} , y , $z(D^0)$ and the transverse momentum $p_t(D^0)$ of the D^0 with respect to the photon direction.

To train the neural network, events generated with the AROMA generator [93] were used. This event generator simulates heavy quark production in unpolarised lepton-nucleon scattering using the leading order matrix element for the PGF-process. In order to keep the analysis in the leading order regime, no parton showers were applied to the partons of the hard interactions. To describe the distribution of partons inside the nucleon before the interaction, a set of parton distribution functions from a global QCD-analysis (see section 1.1) was used. For this analysis the PDFs from a leading order analysis performed by the GRV collaboration [13] was chosen. The fragmentation of the produced hadrons was simulated using the JETSET 7.4 [108] program in its standard setting. Only generated events, where one of the charm quarks fragmented into a D^* -meson, were selected. For these D^* -meson, the decay in the channel

$$D^{*+} \longrightarrow D^0 \pi_{slow}^+ \longrightarrow K^- \pi^+ \pi_{slow}^+$$

was required. For the second charm quark produced in the hard interaction, no requirements were applied. No additional event sample was generated, where instead of a D^* -meson a D^0 -meson is required for the fragmentation of the first charm quarks. The main production process for D^0 -mesons is the decay of D^* -mesons, which contributes about 50% [63] of the produced D^0 -mesons. The other D^0 -mesons are produced directly in the fragmentation of the charm quark or through the decay of a different D -meson. It was studied, that the difference in the production of D^0 -mesons has no effect on the kinematic properties of the D^0 -meson. Therefore it was decided to use only one sample of Monte Carlo events for the training of the neural network. More details on the different setting of the Monte Carlo generation can be found in [107].

For the generated partons of the PGF-process, \hat{u} , \hat{s} and \hat{t} can be calculated from the available parton kinematics, making it possible to calculate a_{LL}^{PGF} . To build a parametrisation of a_{LL}^{PGF} from observables, the generated events were processed with a full simulation of the COMPASS detector and then reconstructed using the same reconstruction software as for the real data. A comparison of the simulated D^* -events and the reconstructed events from the D^* -tagged sample is shown in figure 6.4. The plots show a reasonable agreement between the two samples. The discrepancies, that can be observed, are mainly related to differences in the distributions of the event kinematics, i.e. Q^2 or x_{BJ} . Since in this context, the generated Monte Carlo events are only used to relate the properties of the reconstructed D -meson with the kinematics of the partons of the hard interaction, the event kinematics determined from the scattered muon play a less important role. This would be very different, if the generated events were used to determine relative contributions of different production processes as in the high- p_t analysis. Nevertheless, work is ongoing to improve the Monte Carlo description of the data for future analysis.

For the parametrisation of a_{LL}^{PGF} a neural network was trained. It used the reconstructible variables Q^2 , x_{BJ} , y , $z(D^0)$ and $p_t(D^0)$ from the simulated events and the true a_{LL}^{PGF} , calculated for the generated partons. The quality of the parametrisation was checked using a second Monte Carlo sample and comparing a_{LL}^{PGF} from the neural network to the calculated a_{LL}^{PGF} . Figure 7.2 shows the

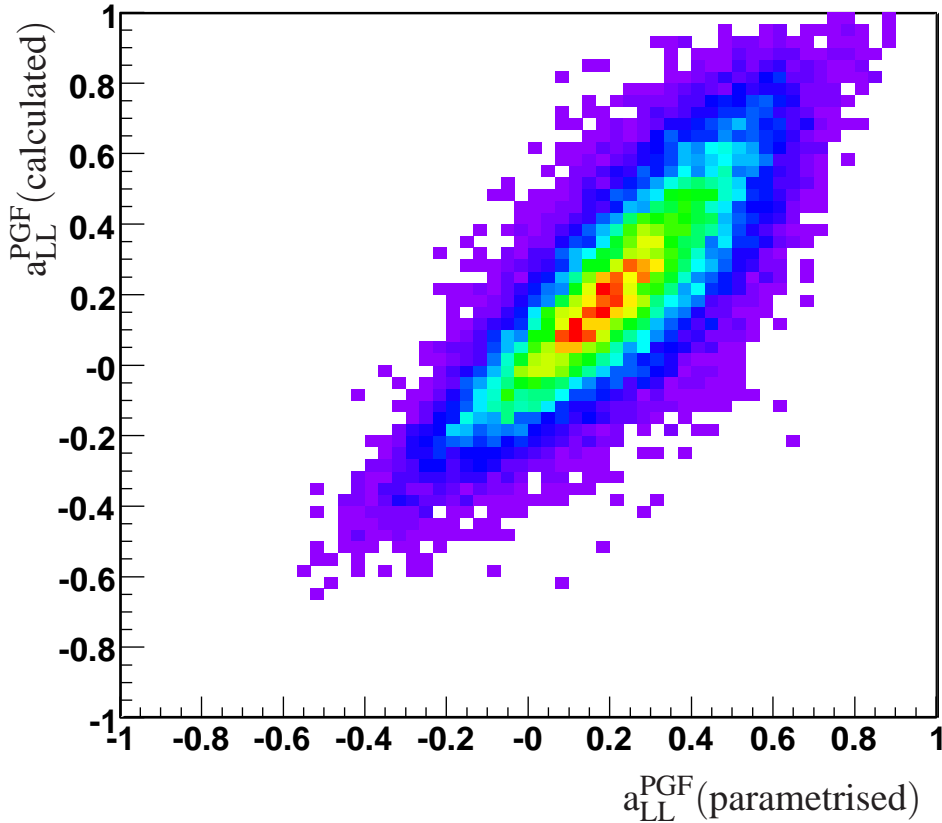


Figure 7.2: Correlation between the a_{LL}^{PGF} calculated from the generated event kinematics and the a_{LL}^{PGF} parametrised with the neural network for a control sample of generated Monte Carlo events.

correlation obtained with the neural network for such a control sample of generated Monte Carlo events. A very good correlation of 82% between the calculated and the parametrised values was achieved.

To estimate a possible bias introduced to the measurement of $\langle \frac{\Delta g}{g} \rangle$ through the use of this parametrisation of the analysing power, several checks were performed. The main source of such an uncertainty is coming from the use of Monte Carlo generated events when establishing the neural network parametrisation. Therefore, several neural networks were trained on different Monte Carlo samples, generated with different options. The neural networks were then used in the extraction of $\langle \frac{\Delta g}{g} \rangle$ and the effect of the different parameters on $\langle \frac{\Delta g}{g} \rangle$ was studied. The parameter showing the largest effect was the mass of the charm quarks m_c . In the standard setting, the value is $m_c = 1.5 \text{ GeV}$, for this study it was modified between 1.3 GeV and 1.6 GeV . The effect of the choice of the parton distribution function was also studied. The standard choice was GRV98 [13], but PDFs from CTEQ [14] and MRST [15] were also used in the course of this study.

All checks showed no evidence for a systematic bias on the extracted $\langle \frac{\Delta g}{g} \rangle$. The largest differences between two values of $\langle \frac{\Delta g}{g} \rangle$ observed during this study was 0.05, which was used as an estimate for the contribution from the analysing power to the systematic error.

7.3.2 Parametrisation of the signal strength

The signal strength $\sigma_{PGF}/(\sigma_{PGF} + \sigma_B)$ is determined from a fit to the unweighted D^0 -mass spectra of the final samples. To obtain a good description of the signal strength for all data, the samples are subdivided based on the target cell and the analysing power of the event. The separation of the events from the two target cells is done, because it was observed (see also figure 5.2) that the D^0 -signal in the invariant mass spectra had less statistic in the upstream cell than in the downstream cell. In addition, the ratio of signal-over-background also differs between the two cells.

The sample is further subdivided into bins of the analysing power a_{LL}^{PGF} . The reason for this division lies in an anti-correlation between the signal strength and the analysing power, which can also be seen in figures 7.3 and 7.4. The origin of this anti-correlation is related to the dependence of the analysing power on the kinematics of the D^0 -meson, in particular on the transverse momentum $p_t(D^0)$. For large values of $p_t(D^0)$, where the purity of the D^0 -sample is very high, the analysing power has small or negative values, which explains the anti-correlation. It not only has to be taken into account for a good description of the data. It can also introduce a bias to the estimation of $\langle \frac{\Delta g}{g} \rangle$, when weighted events are used. Therefore, the combined sample of D^* -tagged mesons from the three years is subdivided into five bins of a_{LL} times two bins for the target cells. For the untagged sample only three bins of a_{LL} times two bins for the target cells are used, because for more bins the weak signal of the D^0 -mass could not be fitted reliably. The ten (six) histograms are fitted in one fitting procedure, allowing some parameters of the fit functions to be correlated.

The fit-function used for the fit corresponds to a sum of a signal and a background function. For the description of the signal a Gaussian is used. The background in the mass-spectra is composed of a contribution from the combinatorial background and a reflection of the $D^0 \rightarrow K^- \pi^+ \pi^0$ decay, where only the K^- and the π^+ were detected in the spectrometer. This reflection can clearly be seen in the D^* -tagged sample, but it is not visible in the untagged sample. Therefore, only the background function of the D^* -tagged sample has an additional component describing this reflection with a Gaussian. To describe the shape of the combinatorial background an exponential function multiplied by a polynomial is used. The final fit-functions for the 10 (6) histograms of the D^* -tagged (untagged) sample are shown in figures 7.3 and 7.4.

To decide on the best fit-function to describe the data and also understand the dependence of the result for $\langle \frac{\Delta g}{g} \rangle$ on the chosen fit-function, a study was performed, where all possible options were varied. The most important option was the choice for the background shape in the fit function. In addition, a correlation of fit-parameters from different histograms was considered. Another option studied concerned the minimisation method of the fitting procedure, where in one case χ^2 was determined from the value of the function at the bin centre and the value of the histogram, and in the other case the average value of the function in the bin was compared to the value of the histogram. The last choice considered in this study was the size of the histogram bins, which was varied between 1 MeV and 20 MeV.

For every possible combination of options a fit was performed for the D^* -tagged and the untagged sample. Then all fits were checked for a reasonable description of the data. Bad fits were excluded from the study to find the best choice of fit-options.

From the good fits, the dependence of the resulting $\langle \frac{\Delta g}{g} \rangle$ on the fit options was determined. Figure 7.5 shows the distribution of the results for $\langle \frac{\Delta g}{g} \rangle$ obtained using all good fit-functions for the

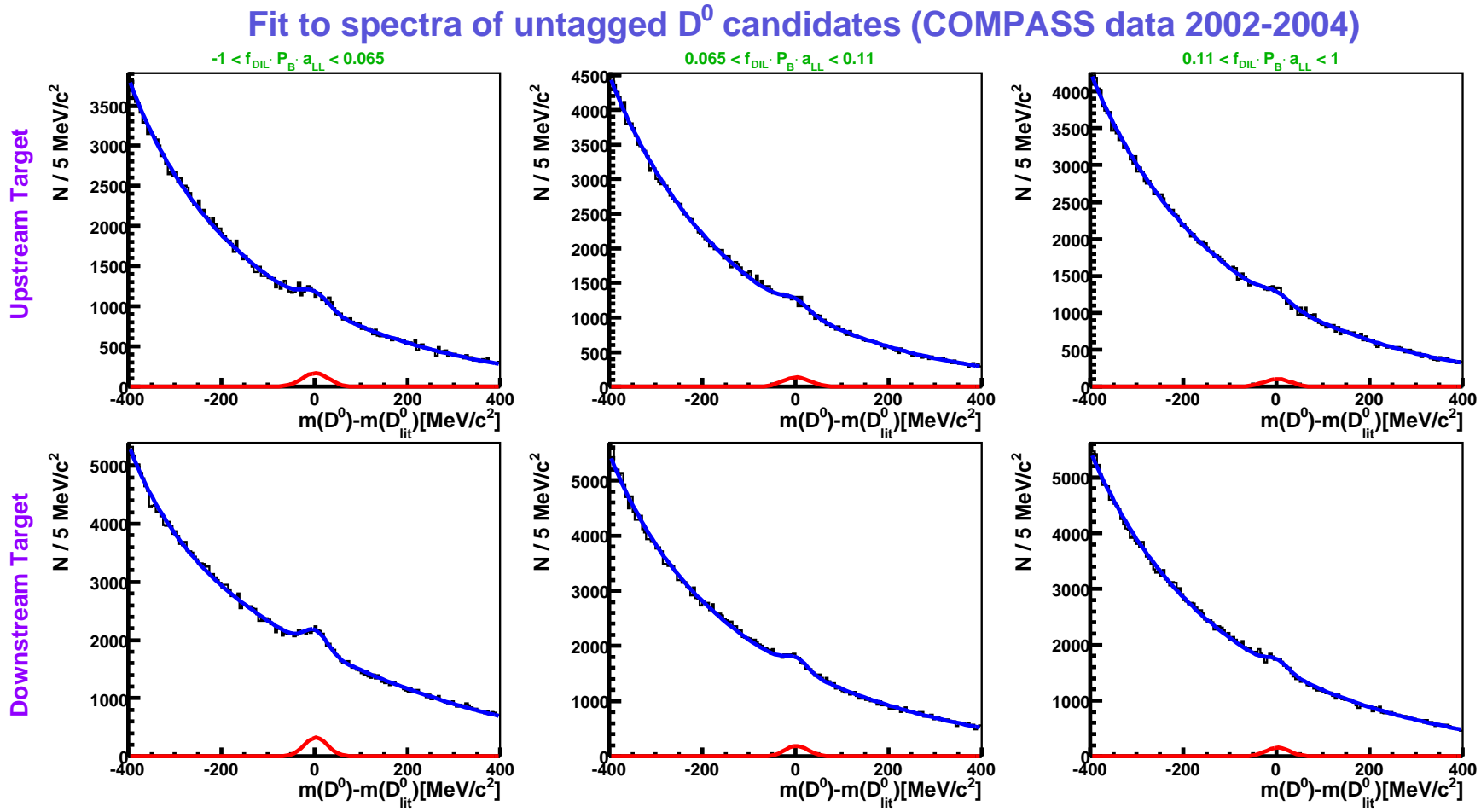


Figure 7.3: The 6 D^0 -mass spectra of the final untagged data sample and the final fit-function.

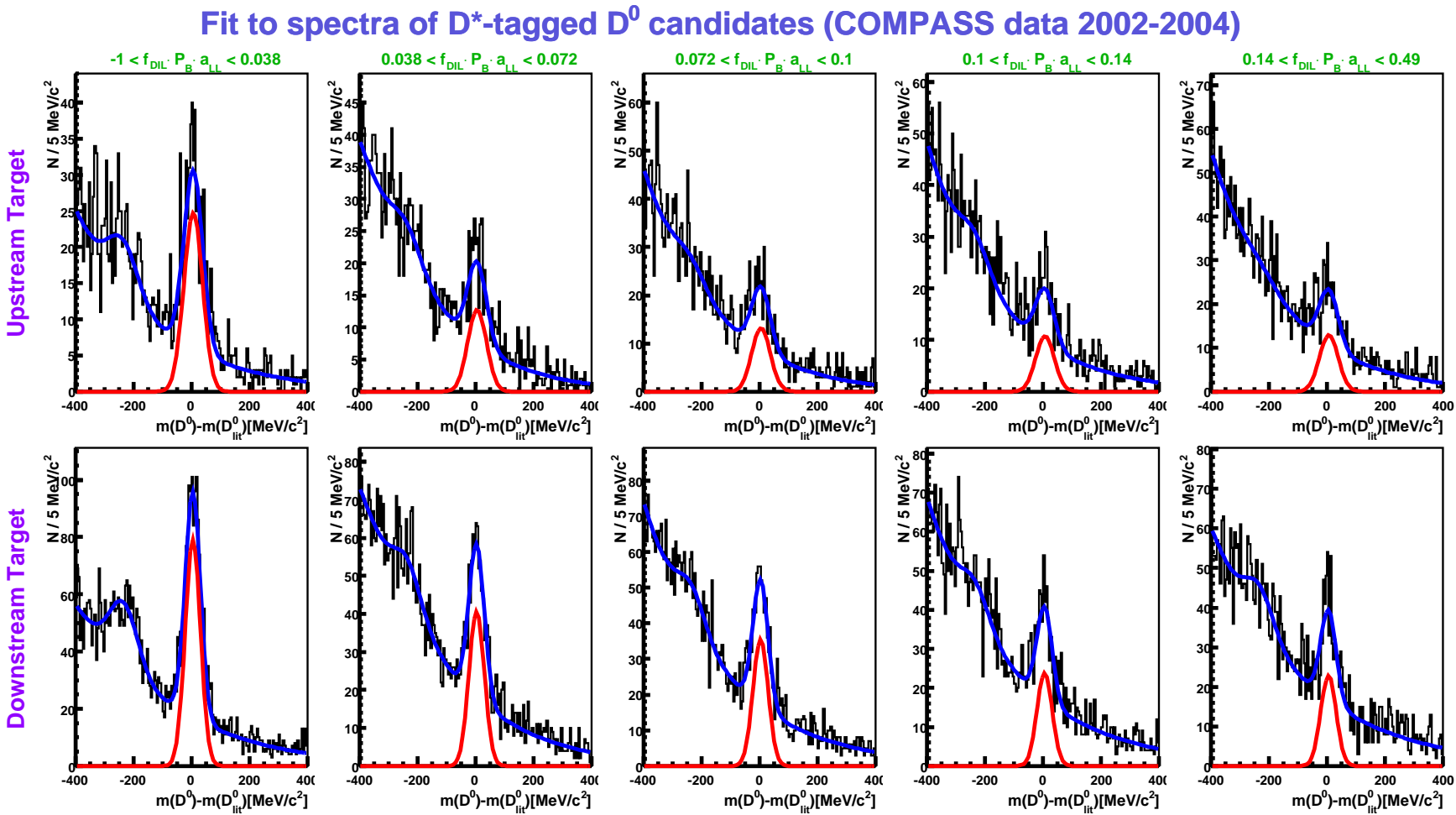


Figure 7.4: The 10 D^0 -mass spectra of the final D^* -tagged data sample and the final fit-function.

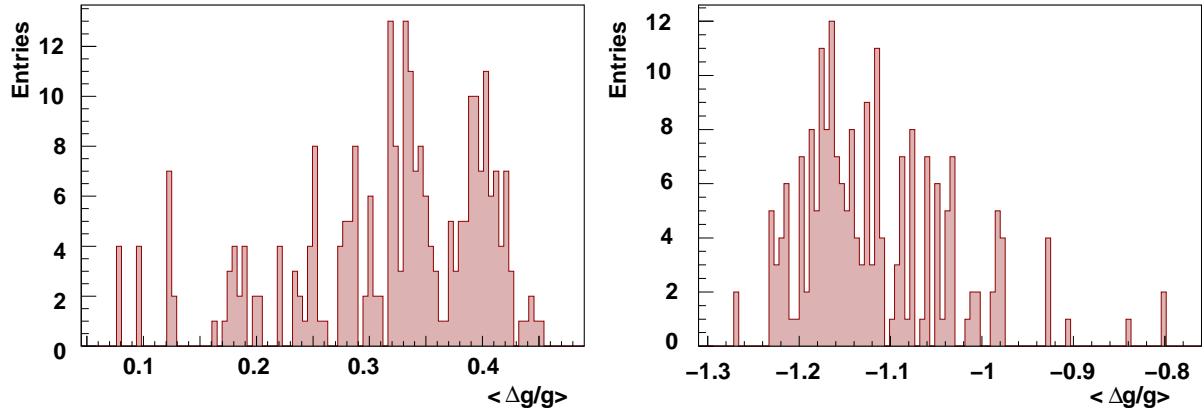


Figure 7.5: The different values of $\langle \frac{\Delta g}{g} \rangle$ obtained from different fit-functions. The left plot shows the values from the untagged sample, the right plot the values for the D^* -tagged sample.

parametrisation of the signal strength. In the left plot the values for the untagged D^0 -sample is shown, the right plot shows the results for the D^* -tagged sample. Both distributions display a spread of the values of $\langle \frac{\Delta g}{g} \rangle$ with an RMS of 0.09. This is significantly smaller than the statistical error of the two values, which is 0.55 (0.75) for the D^* -tagged (untagged) sample.

As a next step, it was checked, whether the value of $\langle \frac{\Delta g}{g} \rangle$ depends on a specific choice of options. This was done simply by looking at the mean values of $\langle \frac{\Delta g}{g} \rangle$ for all fits, where one option was fixed. For example it was compared, if the results for fits with a bin width of 5 MeV was different than for the fits with 10 MeV. This was done for all fit options. No trend could be observed. A systematic influence of the fit-function on the result was therefore excluded. Instead, the largest contribution to the spread of the values of $\langle \frac{\Delta g}{g} \rangle$ is coming from statistical effects in the fits.

Nevertheless, the final result for $\langle \frac{\Delta g}{g} \rangle$ shows a variation with the choice of the fit function. Therefore, the use of one particular function introduces a possible bias, that is estimated using the RMS values of the histograms in figure 7.5, which are both 0.09. This value was used as the contribution from the fitting procedure to the systematic uncertainty of the measurement.

To find the best fit function for the description of the signal strength, the set of good fits was investigated more closely. To settle the question of the best bin width in the mass spectra, the width of the Gaussian describing the D^0 -signal was used. This width lies between 25 MeV and 35 MeV. For a good fit, the bin width should be smaller than the signal width. It was decided, to use a bin width of 5 MeV, which is small enough for a good description of the peak, but large enough to avoid large statistical fluctuations between the bins.

To select a good minimisation method, not much study was needed. The two methods showed the same results. Therefore it was decided to use the standard method, where the value of the fit-function is compared with the histogram entries. The selection of the background function and a possible parameter correlation was more complex, and will be discussed in the following.

Because the D^0 -signals in the 10 (6) histograms are not completely independent, the possibility to use the same fit parameters for a subset of the histograms was studied. This study is motivated

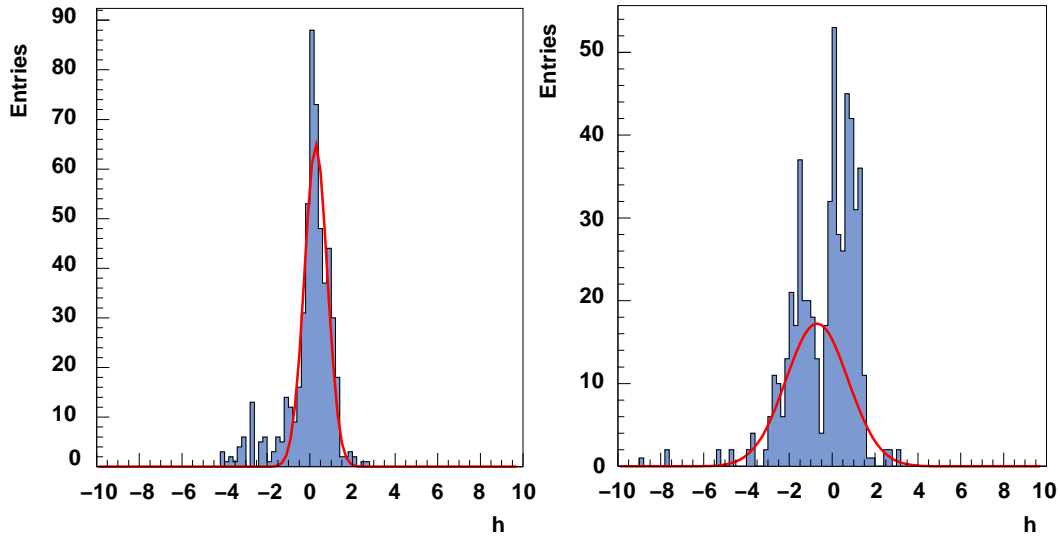


Figure 7.6: Distribution of the pulls h for the width of the signal Gaussian in the D^* -tagged sample. The left plots shows the pull in the case, where all histograms from the same cell are compared, the right plot the comparison of the histograms in the same a_{LL} -bin.

by the fact, that all histograms contain the invariant mass signal of the D^0 -decay. In principle, the mass position and mass resolution should be the same for all histograms. However, especially the mass resolution can show a dependence on the vertex position or the momenta of the decay products. As a result, mass position and mass resolution would be different in different histograms. Nevertheless, it is possible, that a subset of the 10 (6) histograms has the same reconstructed mass and mass resolutions. In this case, the fit becomes more reliable, if only parameter is fitted for the mass position of these histograms and one for the mass resolution. Naturally, the parameters for the amplitudes of the signals were kept independent.

In principle, there are four possibilities, how mass position and resolution could be correlated between the different histograms. One could expect the shape of the D^0 -signal to depend only on the target cell, only on the kinematics of the decay products, on both criteria or on neither. Therefore, different fits were performed, where all four possibilities were implemented, and the results were compared. No difference was observed in the χ^2 values of the fit results.

To understand, whether the data show a preference for combining the parameters for a subset of histograms, the fit-parameters from the fits, where all parameters were kept independent, were investigated. The idea was to check, if the fit parameters from the independent fits are compatible with the hypothesis, that the group of histograms from the same a_{LL}^{PGF} -bin or from the same target cell have the same fit-parameters. This was done using the pulls h of the fit-parameters, which is given by

$$h = \frac{r - \langle r \rangle_{group}}{\Delta r} , \quad (7.26)$$

where r is the value for the fit-parameter of one histogram in the group, Δr is the error of r obtained from the fit and $\langle r \rangle_{group}$ is the mean of the values from the fits of all histograms in the group. The pull h can be used to evaluate the compatibility of a fit parameter with the mean value from a group. Two distributions of h for the fit parameter describing the width of the signal Gaussian are shown for the fits to the D^* -tagged sample. The left distribution is for the pulls calculated by grouping the histograms according to the target cell, i.e. the five histograms from the upstream cell and the five histograms from the downstream cell. The right distribution shows the pulls where the two histograms for the same a_{LL} -bin were grouped together. Both pull distributions were calculated from the same parameters. Each entry corresponds to the fit-parameter of one histogram. One can see a clear difference in the distributions. While in the left figure, most pulls are centred around 0, indicating a good compatibility of the different values in the group, the pulls on the right figure show two separate maxima at about -2 and 1. The appearance of these two peaks is not really surprising, since the pulls in the right figure were calculated by only comparing two values. However the large distance between the two maxima is very large. This indicates, that the two histograms from the same a_{LL} bins but different cells should not be fitted together.

The pulls were studied for the fit-parameters describing the position and the width of the signal Gaussian for the D^* -tagged and the untagged sample separately. For each parameter, the three possible combinations were considered. In all cases, the same results were obtained. The pulls calculated for the histograms in the same cell showed a good compatibility of the parameters with each other, the pulls calculated for histograms from both cells together had clear signs of an incompatibility of the data from the two cells. It was therefore decided to use the same fit-parameters to describe the mass position and the width of the Gaussian describing the D^0 -signal for the histograms belonging to the same cell but different bins of a_{LL}^{PGF} .

The function describing the combinatorial background in the invariant mass distribution was selected by looking at the χ^2 values for fits performed with different fit-functions. The general form of the fit-function was

$$f_{background}(m) = B_1 \exp(-B_2 m) \cdot (1 + a_1 m + a_2 m^2 + \dots) \quad (7.27)$$

It was established based on the observation, that the background could be well approximated with an exponential function. A closer look to the fit-function revealed, that the data were distributed a bit steeper, than a mere exponential distribution. Therefore, a better description can be achieved with a polynomial of the form shown above. To decide on the order of the polynomial, the χ^2 -values for fits with first-, second-, third-, and fourth-degree polynomials were compared. For the D^* -tagged sample, the best values were obtained for the first- and the second-order polynomial. To keep the number of fit-parameters smaller, it was decided to use the first-order polynomial for the final fit-function. For the untagged sample, good χ^2 values were obtained for polynomials of second degree or higher. Thus, the second degree-polynomial was selected.

To summarise the results for the fitting procedure: The fit is used to extract the signal strength $\sigma_{PGF}/(\sigma_{PGF} + \sigma_{BG})$ from the data. For the fit, the data are subdivided into 10 or 6 histograms according to the target cell and the a_{LL} -bin of the event to obtain a good description of the data. All 10 (6) histograms of the D^* -tagged (untagged) sample are fit together, and the same fit-parameter is used to describe the position and the width of the D^0 -signal for the histograms belonging to the same target cell. The fit-function is a sum of one or two Gaussians describing the signal of the

D^0 -meson and in the D^* -tagged sample the reflection of a second D^0 -decay, and an exponential distribution, which was multiplied by a polynomial to better describe the shape of the combinatorial background.

Besides the fitting procedure itself, also the influence of the binning in a_{LL} was studied. This was done by changing the number of bins in a_{LL} used for the fit. In principle, it is expected, that with an increasing number of bins, the anti-correlation of the analysing power and the signal strength is better describe by the fit. Therefore, for a sufficient high number of bins, the result for $\langle \frac{\Delta g}{g} \rangle$ should not depend on the number of bins.

This expectation was fully confirmed by the data. Starting from 3 (2) bins of a_{LL} for the D^* -tagged (untagged) sample no large change in the result was seen [107]. From the remaining statistical fluctuations the possible influence of the choice for this binning was estimated to be 0.04 for both samples. It was chosen to use 5 and 3 bins of the analysing power for the fitting procedure, to have a sufficiently large amount of events in each histogram for a reliable fit of the mass spectra.

7.4 False Asymmetries

To verify, that the asymmetry used for the extraction of $\langle \frac{\Delta g}{g} \rangle$ is not the result of an unstable spectrometer, the final event samples are investigated for false asymmetries. In the measurement presented here, a false asymmetry can be induced by an instability in the detector performance that invalidates the assumption in equation 7.8. To detect such an instability, asymmetries are calculated for event samples, where no physical asymmetry is expected. This is done for example by dividing the target into an upper and a lower half instead of the two target cells, or by splitting the event sample using event properties. An example for this kind of asymmetry is given in figure 7.7, where for the three years an asymmetry was calculated between events, where the kaon went into different directions in the spectrometer. The data points in the figures show the asymmetries between the left (Saleve) and the right (Jura) direction and the asymmetries between the up and down direction of the kaon. Each of these two false asymmetries were calculated for the three years and the D^* -tagged and the untagged D^0 -samples separately. Naturally, the expected result for these false asymmetries is 0. A deviation from this expectation could indicate, that detector instabilities introduce a bias to the measurement of the physics asymmetry.

In a few cases of the studied false asymmetries, deviations from 0 that are larger than their statistical error were observed, as shown in figure 7.7. In the context of the statistical spread of the false asymmetries in the three years, these deviations are within the limits of the expected statistical fluctuations. Therefore, no significant false asymmetry was observed. However, the large error bars of the data points indicate, that the overall significance of this result is limited by the available statistics.

To improve the significance of the results, the event weight for the signal strength was excluded from the event weighting. As a result, signal and background events entered the asymmetry calculation with the same weight, which increased the statistics. Since false asymmetries are an effect of the spectrometer, no dependence on the event type is expected. Signal and background events are equally sensitive to false asymmetries. Also for the samples with increased statistics no significant

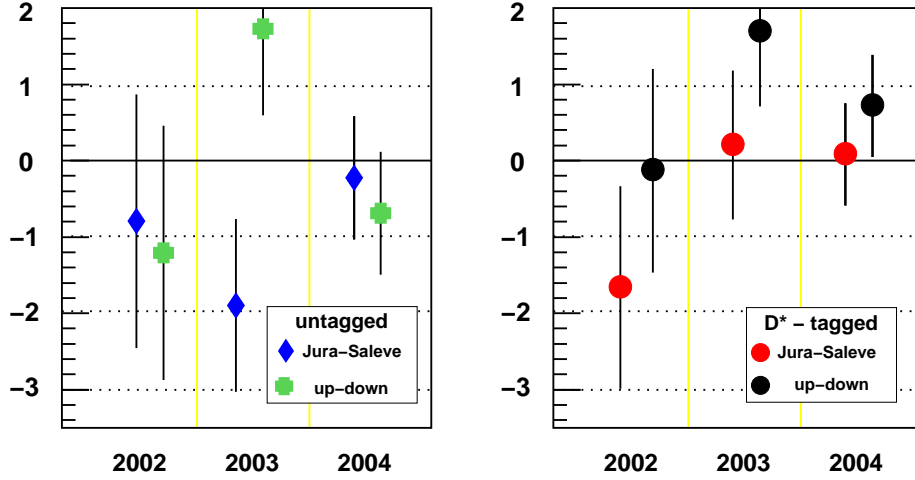


Figure 7.7: Example for non-physical asymmetries determined for the D^* -tagged and untagged D^0 -samples. The data points show the asymmetry calculated for a kaon going the upper or lower part of the detector as well as the asymmetry for the kaon in the right (Saleve) or in the left (Jura) part of the detector calculated for the three data taking years 2002-2004 as well as the combined values for all years and both samples.

false asymmetries were observed. It is therefore concluded, that no false asymmetries are present in the data used for the measurement of the gluon polarisation.

Since the checks for false asymmetries only allowed estimation of a possible bias in the measurement on the level of the statistical uncertainty of $\langle \frac{\Delta g}{g} \rangle$, a different method was used to estimate with which precision a false asymmetry can be excluded. This method is based on the statistical spread of the measurements of $\langle \frac{\Delta g}{g} \rangle$ obtained with the method described in section 7.2 for each data taking week. The method is based on the pulls of the measured asymmetries, where for each measured value of $\langle \frac{\Delta G}{G} \rangle_i$ with a statistical error of $\delta \langle \frac{\Delta G}{G} \rangle_i$ the pull, $h_{\Delta G/G}^i$, is defined by

$$h_{\Delta G/G}^i = \frac{\langle \frac{\Delta G}{G} \rangle_i - \langle \frac{\Delta G}{G} \rangle}{\delta \langle \frac{\Delta G}{G} \rangle_i} . \quad (7.28)$$

For an unbiased measurement, the distribution of the pulls calculated from the results of the 29 data taking weeks follows a Gaussian with a mean of $\mu = 0$ and a spread of $\sigma = 1$. If this distribution is observed, false asymmetries can be excluded with a higher precision than the statistical uncertainty of the measurement, which takes into account the number of individual measurements. A detailed description of how the statistical precision can be estimated using the pulls method can be found in [109].

In the case of the simultaneous extraction of $\langle \frac{\Delta g}{g} \rangle$ and A_{CBG} from the data, one can make use of the fact, that false asymmetries would bias not only the measurement of $\langle \frac{\Delta g}{g} \rangle$ but also the measured background asymmetries. They should therefore lead to a distortion of the pull distributions for $\langle \frac{\Delta g}{g} \rangle$ and A_{CBG} . This increases the number of measurement entering the estimation of the statisti-

cal precision with which false asymmetries can be excluded. However, while $\langle \frac{\Delta g}{g} \rangle$ and A_{CBG} are considered to be completely independent in the measurement procedure, this is not the case, in the presence of a false asymmetry. This can be understood from the fact, that a false asymmetry would invalidate the assumptions of equation 7.17, which both are needed to determine $\langle \frac{\Delta g}{g} \rangle$ and A_{CBG} . Therefore, the possible correlation of the two measurements has to be considered when applying the pulls method.

This is complicated by the fact, that in the absence of a false asymmetry, this correlation cannot be determined. Therefore, the pulls method was evaluated assuming a complete correlation of the $\langle \frac{\Delta g}{g} \rangle$ and A_{CBG} as well as under the assumption of uncorrelated $\langle \frac{\Delta g}{g} \rangle$ and A_{CBG} [110]. For both assumptions the statistical precision, with which a bias from false asymmetries in the measurement of $\langle \frac{\Delta g}{g} \rangle$ and A_{CBG} can be excluded, was estimated. As a conservative upper limit for an observed false asymmetry, the average value of the two estimations was used for the final result. This was motivated by the idea, that in the presence of a false asymmetry only a small correlation between $\langle \frac{\Delta g}{g} \rangle$ and A_{CBG} would be likely. The conservative upper limit for a bias due to false asymmetries in the data samples was determined for the D^* -tagged and the untagged sample separately. For both channels, this resulted in a value of 0.09 for the maximum contribution from false asymmetries to the $\langle \frac{\Delta g}{g} \rangle$ measurement.

7.5 Result for the gluon polarisation

As mentioned in section 7.2 $\langle \frac{\Delta g}{g} \rangle$ is determined for each data taking week individually. The results for each week are shown in figure 7.8. The upper two plots show the results of $\langle \frac{\Delta g}{g} \rangle$ and A_{CBG} for the D^* -tagged channel, the lower two plots show $\langle \frac{\Delta g}{g} \rangle$ and A_{CBG} for the untagged sample. It is obvious, that the results for each week have large statistical uncertainties and no conclusion about the gluon polarisation can be drawn from individual points. When comparing the error bars showing the statistical errors for the two event samples, one can see, that for $\langle \frac{\Delta g}{g} \rangle$ the error bars of the D^* -tagged samples are smaller, than for the untagged sample. This shows again the importance of the D^* -tag for the measurement of the gluon polarisation. For A_{CBG} the situation is opposite. Because of the large background in the untagged sample, the background asymmetry can be determined to a much higher precision from these events.

The final result for $\langle \frac{\Delta g}{g} \rangle$ and A_{CBG} are determined from the weighted mean of the results shown in figure 7.8. For the untagged sample, this gives

$$\langle \frac{\Delta g}{g} \rangle (\text{untagged sample, 2002} - 2004) = 0.53 \pm 0.75 (\text{stat.})$$

with a background asymmetry of $A_{CBG} = -0.005 \pm 0.009 (\text{stat.})$. In the case of the D^* -tagged sample, the precision for the measured $\langle \frac{\Delta g}{g} \rangle$ is slightly higher. The result is

$$\langle \frac{\Delta g}{g} \rangle (D^* \text{-tagged sample, 2002} - 2004) = -1.01 \pm 0.55 (\text{stat.})$$

with a background asymmetry of $A_{CBG} = -0.00 \pm 0.06 (\text{stat.})$. Although the actual values obtained from the two samples are very different, they are statistically compatible with a difference of 1.7

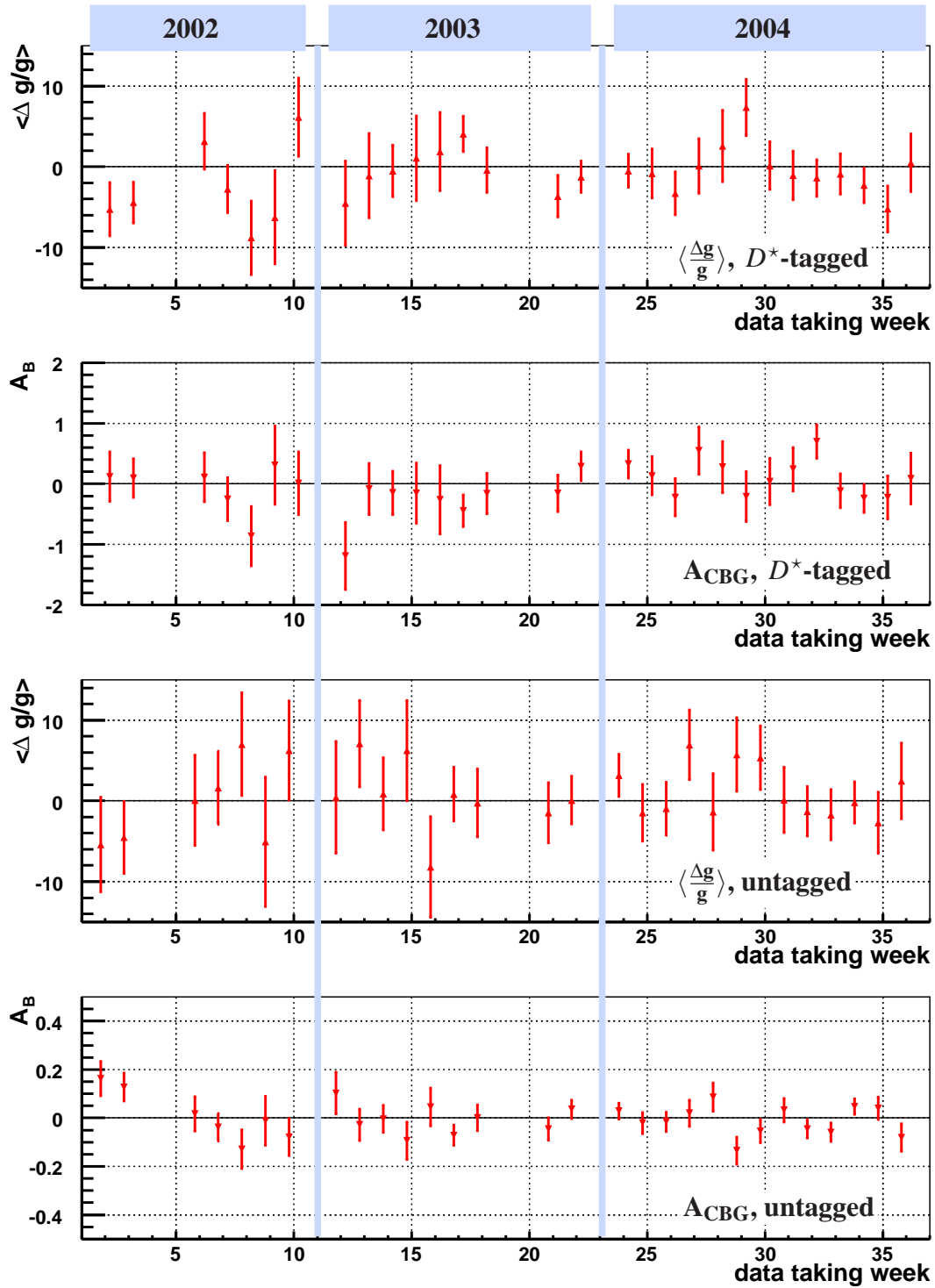


Figure 7.8: This plots shows the measured $\langle \frac{\Delta g}{g} \rangle$ and A_{CBG} values for all 29 data taking weeks with longitudinal target polarisation of the 2002,2003 and 2004 data taking. The weeks without a result correspond to weeks where no data with longitudinal target polarisation were taken.

Source of systematic uncertainty	$\delta\langle\frac{\Delta g}{g}\rangle$	
	D^* -tagged	untagged
False asymmetries	0.09	0.09
Fitting procedure	0.09	0.09
Monte Carlo parameters	0.05	
Binning in a_{LL}	0.04	0.04
Beam polarisation P_μ	0.02	
Target polarisation P_T	0.02	
Dilution factor f	0.02	
Total Error	0.15	

Table 7.1: Overview of the different contributions to the systematic error. Where two values are given, the contribution was determined independently for the two channels. The different contributions are discussed in more detail in the previous sections of this chapter.

standard deviations. Nevertheless, it was carefully checked, whether the difference of the two results could be a systematic effect, but no evidence was found. Also figure 7.8 shows no evidence for a significant difference between the D^* -tagged sample and the untagged sample.

The final result for the open charm measurement of $\langle\frac{\Delta g}{g}\rangle$ is determined from the mean of the results from the two data samples. The value of the gluon polarisation averaged over the region of x covered by the data from the open charm events taken in the years 2002, 2003 and 2004 is

$$\langle\frac{\Delta g}{g}\rangle(\text{COMPASS Open Charm, 2002} - 2004) = -0.47 \pm 0.44(\text{stat.}) \pm 0.15(\text{syst.}) \quad . \quad (7.29)$$

The measured background asymmetry $A_{CBG} = -0.005 \pm 0.009(\text{stat.})$ is consistent with 0. The average x of this measurement was $x = 0.11^{+0.11}_{-0.05}$ and the hard scale μ^2 is given by $\mu^2 = \hat{s} \approx 13 \text{ GeV}^2$.

The different contributions to the systematic error are discussed in the previous sections and summarised in table 7.1. The three largest contributions are coming from the upper limit for false asymmetries in the data sample, the influence of the fitting procedures and the different settings for the Monte Carlo parameters. For all three contributions, the studies made to determine the contribution to the systematic error were limited by the statistical uncertainty of the available data. They are therefore expected to become smaller, when more data is used in the analysis.

For the quantities that are specific for the two data samples, the contributions are determined independently for the D^* -tagged and the untagged sample. As can be seen in table 7.1, the values obtained for the two samples are quite similar. For the individual contributions, where the systematic

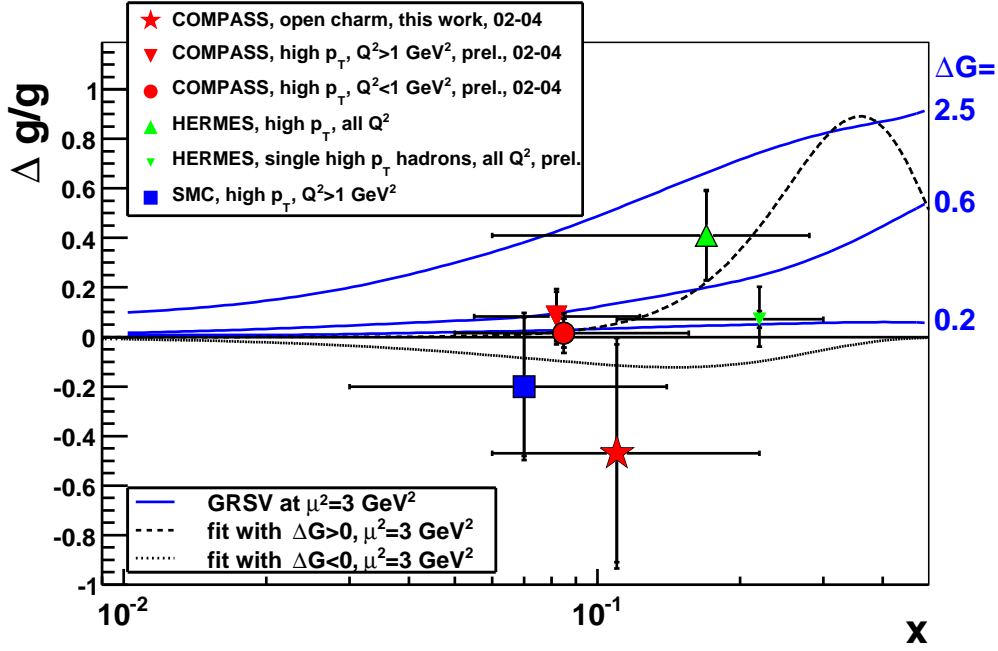


Figure 7.9: Comparison of the direct measurement of $\langle \frac{\Delta g}{g} \rangle$ in the “open charm” channel to measurements from the high- p_t channel and predicted curves of $\Delta G/G(x)$. The “COMPASS, open charm” point is the result of the analysis presented in this thesis, the other points show recent results in the high- p_t channel from COMPASS [111] and HERMES [112] as well as older points from COMPASS, SMC and HERMES. The blue curves show the predicted functions of $\Delta G/G(x)$ for three different gluon polarisations ΔG obtained with a parametrisation from [39], the black lines show the results of the QCD-analysis [24] of the inclusive measurements performed by COMPASS. The two curves correspond to two equally significant solutions of the fit, where one curves gives a positive gluon polarisation, the other a negative. It should be noted, that all curves and data points are given at $\mu^2 = 3 \text{ GeV}^2$, except the “COMPASS open charm” point, where $\mu^2 = 13 \text{ GeV}^2$.

error is determined independently for the D^* -tagged and the untagged sample, the conservative assumption is made, that the two results are fully correlated. The systematic uncertainty of the combined result was therefore estimated by the larger value for the two samples. The total systematic error of the final result is obtained from the quadratic sum of the individual contributions.

The result of the measurement of $\langle \frac{\Delta g}{g} \rangle = -0.47 \pm 0.47$ at $x \sim 0.1$ points to a small or negative value of the polarised gluon distribution $\Delta G/G$ in the x -region of the measurement. Therefore, the measurement disfavors a large positive polarisation of the gluon, which would be observed in the situation, where the gluon spins give a large contribution to the nucleon spin. Since the x -range covered by the measurement is limited, a more precise conclusion about the total polarisation of gluons in the nucleon cannot be made.

Figure 7.9 shows a comparison of the measurement from the “COMPASS, open charm” channel

is to measurements of $\langle \frac{\Delta g}{g} \rangle$ from the high- p_t channel in lepton-nucleon scattering as well as different curves of $\Delta G/G(x)$. The other data points show a recent analysis from the high- p_t channel in COMPASS [111] and the result from longitudinal asymmetries for inclusive charged hadrons measured by HERMES [112]. In addition, older results from COMPASS, HERMES and SMC are shown. All measurements agree within their statistical precision. However, it should be noted, that the measurement in the open charm channel was performed at a different scale with $\mu^2 = 13 \text{ GeV}^2$ instead of $\mu^2 = 3 \text{ GeV}^2$ as for the high- p_t results. Nevertheless, a comparison of the results shown in figure 7.9 is possible, because the change of the polarised gluon distribution through the Q^2 -evolution from 3 GeV^2 to 13 GeV^2 is expected to be smaller than the statistical uncertainty of the open charm measurement.

The open charm point displays a larger statistical uncertainty than the other measurements. However, since the measurement of the gluon polarisation in the open charm channel has the smallest model dependence of all, it provides the most direct access to the gluon polarisation. The measured asymmetry, which is the basis of the determination of the gluon polarisation, was extracted without any assumption on the production process for charm events. The asymmetry itself is therefore independent of the order of the perturbative calculation for the underlying production process. Only to relate the measured asymmetry for the open charm channel with gluon polarisation, the partonic asymmetry $\Delta \hat{\sigma} / \hat{\sigma}$ is needed. Its calculation is based on a model for charm production in muon-nucleon scattering. At this point, the assumptions about the production process and the order of the perturbative calculation enter into the measurement of the gluon polarisation. As discussed in section 1.4, in leading order perturbative QCD, the PGF-process is the only process for charm production in lepton-nucleon scattering. All other contributions are estimated to be small enough to be neglected in the context of this measurement.

Figure 7.9 also displays five different curves with predictions for the dependence of $\Delta G/G(x)$. The three blue curves correspond to three predictions for $\Delta G/G(x)$ at $\mu^2 = 3 \text{ GeV}^2$ for the three different values of the gluon polarisation in the nucleon quoted on the right side of the diagram. The curves were determined using the parametrisations from [39]. The two dashed, black curves show the results from [24] that correspond to a negative and positive polarisation of the gluons. The two curves have similar integrals of $|\int_0^1 \Delta G(x) dx| = 0.2 - 0.3$. It is clear from figure 7.9, that the open charm measurement agrees with all curves shown in the diagram, but its statistical uncertainty is too large to exclude one of the predictions. The same is also true for the older measurements in the high- p_t channel. The newer high- p_t results are more precise and exclude very large values for the gluon polarisation in the measured region. The different measurements of $\langle \frac{\Delta g}{g} \rangle$ seem to prefer a small value of $|\int_0^1 \Delta G(x) dx|$, but a distinction between positive and negative gluon polarisation is so far not possible. Such a distinction might become possible, when the data taken by COMPASS in 2006 are fully analysed. A first analysis of the open charm channel has already started and can be found in [113].

The comparison of the open charm measurement to results from proton-proton scattering at RHIC more complex. Due to the different procedure of the measurement, a direct comparison between the open charm measurement and results from polarised proton-proton scattering is not possible. However, a comparison can be made with the conclusions taken from a QCD-analysis including not only the existing inclusive measurements, but also the different measurements from RHIC [114]. This QCD-analysis used the p_t -dependence of the measured asymmetries from polarised

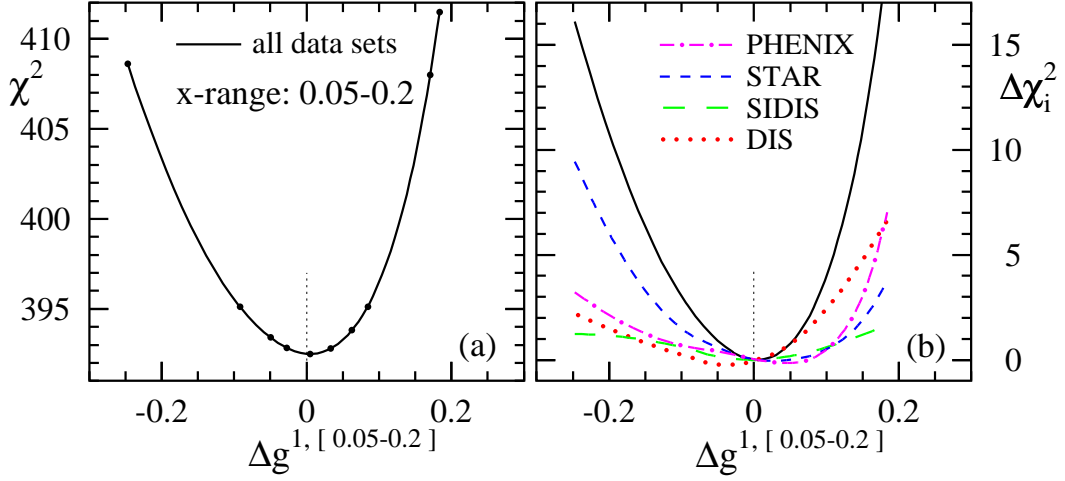


Figure 7.10: The χ^2 distribution for $\Delta g^{1, [0.05, 0.2]} = \int_{0.05}^{0.2} \Delta g(x, Q^2) dx$ at $Q^2 = 10 \text{ GeV}^2$ obtained from a global analysis of inclusive and semi-inclusive lepton-nucleon asymmetries and polarised proton-proton asymmetries [114]. As shown in the diagram, the fit of the global data prefers small values of $\langle \frac{\Delta g}{g} \rangle$ for $0.05 < x < 0.2$.

proton-proton scattering to constrain the polarised gluon distribution in the region of x covered by the data from RHIC. This range of x almost coincides with the range covered by the open charm data. The constraint on $\Delta g^{1, [0.05, 0.2]} = \int_{0.05}^{0.2} \Delta g(x, Q^2) dx$ extracted from this QCD-analysis is shown in figure 7.10 in the form of a χ^2 -function. One can see, that the data from polarised proton-proton scattering prefer very small values of the gluon polarisation for x around 0.1. This result is compatible with the open charm measurement presented in this thesis as well as the other direct measurements of $\langle \frac{\Delta g}{g} \rangle$ shown in figure 7.9.

Summary

Over the past decades, the study of lepton-nucleon scattering has provided the means to investigate the internal structure of the nucleon. Our current understanding of the nucleon is very well described by the QCD improved parton model, where the nucleon consists of quarks and gluons. QCD analyses of the existing measurements of unpolarised lepton-nucleon scattering resulted in precise determinations of unpolarised parton distribution functions.

In polarised lepton-nucleon scattering, the polarised parton distributions that shed light on the spin composition of the nucleon can be measured. However, the existing measurements only cover a small kinematic range, as they have so far only been performed by fixed target experiments. This limits the precision of polarised parton distribution functions obtained in QCD analyses. While the polarised quark distributions are relatively well constrained in recent QCD-fits, the polarised gluon distribution, and with it the gluon spin contribution to the nucleon spin, remain uncertain.

A complementary approach to determine the gluon polarisation in the nucleon is pursued using the direct measurement. In lepton-nucleon scattering, this is done by measuring double spin asymmetries for the photon-gluon fusion process (PGF). In this process, the virtual photon interacts with a gluon from the nucleon creating a quark-antiquark pair. The PGF-process can be tagged through hadrons with high transverse momenta or through charmed hadrons in the final state. The advantage of the open charm channel is that, in leading order, the PGF-process is the only process for charm production, thus no physical background contributes to the selected data sample.

In this analysis, charm production is tagged through a reconstructed D^0 -meson decaying in $D^0 \rightarrow K^- \pi^+$. The reconstruction is done on a combinatorial basis, since the thick solid state target of the COMPASS experiment does not allow for the detection of the D^0 -decay vertex. To reduce the background of wrong track-combinations, kinematic cuts are applied to the reconstructed D^0 -candidate and the information on particle identification from the RICH is used. In addition, the event sample is separated into D^0 -candidates, where a soft pion from the decay of the D^* -meson to a D^0 -meson, $D^{*+} \rightarrow D^0 \pi_{soft}^+$, is found, and the D^0 -candidates without this tag. Due to the small mass difference between D^* -meson and D^0 -meson the signal purity of the D^* -tagged sample is about 7 times higher than in the untagged sample.

To reduce systematic uncertainties in the measured asymmetries, a good knowledge of the data quality is of great importance. During this thesis a lot of effort was made to improve this knowledge under two aspects. In the course of the data stability studies, the influence of individual detectors on the stability of the spectrometer acceptance was studied. The stability of the spectrometer acceptance is essential for the suppression of false asymmetries in the measurement. As part of the stability studies, new procedures were developed to remove data that could possibly introduce

false asymmetries. Besides this investigation of the quality of the recorded data, a first estimation of the cross-section for D^* -production in COMPASS was made. Although the precision of the result is low, a comparison to other measurements of charm production in lepton-nucleon scattering shows a good agreement. The knowledge of the charm production cross-section is important when discussing processes contributing to charm production at higher orders. This will be one of the future steps in the open charm analysis.

The gluon polarisation $\langle \frac{\Delta g}{g} \rangle$ is measured from the event asymmetries for the different spin configurations of the COMPASS target. To improve the statistical precision of the final results, the events in the final sample are weighted. The use of a signal and a background weight allows the separation of the signal asymmetry, corresponding to $\langle \frac{\Delta g}{g} \rangle$, and a possible asymmetry in the combinatorial background. To relate the asymmetry in the signal events with $\langle \frac{\Delta g}{g} \rangle$, the target and the beam polarisation, the dilution factor, the signal purity and the analysing power a_{LL}^{PGF} are needed. With the exception of the analysing power, these quantities can be determined from the event information. The analysing power, containing the partonic photon-gluon asymmetry, is calculated using the kinematics of the hard scattering process. It can therefore only be determined for Monte Carlo generated events. A neural network is used to parametrise the analysing power as a function of event observables, which can then be applied to reconstructed events.

This method results in an average value of the gluon polarisation in the x -range covered by the data of the used event sample. For the data from 2002-2004, analysed in this thesis, the resulting value of the gluon polarisation is

$$\langle \frac{\Delta g}{g} \rangle (\text{COMPASS Open Charm, 2002} - 2004) = -0.47 \pm 0.44 (\text{stat.}) \pm 0.15 (\text{syst.}) \quad ,$$

at an average $x = 0.11_{-0.05}^{+0.11}$ and a scale of $\mu^2 = 13 \text{ GeV}^2$. The result has a larger statistical uncertainty than measurements from the high- p_t channel, where more events to tag the PGF-process can be found. The advantage of the open charm measurement is a very small model dependence. While for high- p_t measurements Monte-Carlo models are needed to determine the fraction of PGF events as well as the underlying partonic asymmetries, in the open charm analysis model calculations are only needed to relate the measured asymmetry of PGF events to the gluon polarisation. The open charm measurement is statistically compatible with the existing measurements of the high- p_t channel.

These first results from COMPASS start to constrain the polarised gluon distribution. In both channels, the results point to small or negative values of $\Delta G/G(x)$ around a value of $x \sim 0.1$, which could point to a small gluon polarisation in the nucleon. To improve the impact of the measurements on the gluon polarisation, the statistical uncertainties have to be reduced. Therefore, the current analysis efforts aim at an increase of the statistics available for the $\langle \frac{\Delta g}{g} \rangle$ measurements. This is achieved with the addition of the COMPASS data taken in 2006. In the open charm analysis, where the increase in statistics will reduce several contributions to the systematic error, the addition of new decay channels is also investigated. In both channels, the statistical precision of the measurements is increased through improvements of the analysis method that allow a better separation of signal and background events through more elaborate event weighting.

Bibliography

- [1] Martin Breidenbach et al. *Observed Behavior of Highly Inelastic electron-Proton Scattering*. Phys. Rev. Lett., **23**:935–939, 1969.
- [2] R. N. Cahn and G. Goldhaber. *The Experimental Foundations of Particle Physics*. Cambridge, UK: Univ. Pr. (1989) 428 p.
- [3] Anthony William Thomas and Wolfram Weise. *The Structure of the Nucleon*. Berlin, Germany: Wiley-VCH (2001) 389 p.
- [4] Peter Schmueser. *Feynman Graphs and Gauge Theories for experimental Physicists. (in german)*. Lect. Notes Phys., **295**:1–217, 1988.
- [5] W. M. Yao et al. *Review of particle physics*. J. Phys., **G33**:1–1232, 2006.
- [6] Murray Gell-Mann. *A Schematic Model of Baryons and Mesons*. Phys. Lett., **8**:214–215, 1964.
- [7] G. Zweig. *An SU(3) model for strong interaction symmetry and its breaking*. CERN-TH-401.
- [8] G. Zweig. *AN SU(3) MODEL FOR STRONG INTERACTION SYMMETRY AND ITS BREAKING. 2*. CERN-TH-412.
- [9] John C. Collins, Davison E. Soper, and George Sterman. *Factorization of Hard Processes in QCD*. Adv. Ser. Direct. High Energy Phys., **5**:1–91, 1988.
- [10] V. N. Gribov and L. N. Lipatov. *Deep inelastic e p scattering in perturbation theory*. Sov. J. Nucl. Phys., **15**:438–450, 1972.
- [11] Yuri L. Dokshitzer. *Calculation of the Structure Functions for Deep Inelastic Scattering and e+ e- Annihilation by Perturbation Theory in Quantum Chromodynamics. (In Russian)*. Sov. Phys. JETP, **46**:641–653, 1977.
- [12] Guido Altarelli and G. Parisi. *Asymptotic Freedom in Parton Language*. Nucl. Phys., **B126**: 298, 1977.
- [13] M. Gluck, E. Reya, and A. Vogt. *Dynamical parton distributions revisited*. Eur. Phys. J., **C5**:461–470, 1998.

- [14] H. L. Lai et al. *Global QCD analysis of parton structure of the nucleon: CTEQ5 parton distributions*. Eur. Phys. J., **C12**:375–392, 2000.
- [15] A. D. Martin, R. G. Roberts, W. J. Stirling, and R. S. Thorne. *Parton distributions incorporating QED contributions*. Eur. Phys. J., **C39**:155–161, 2005.
- [16] A. D. Martin, W. J. Stirling, R. S. Thorne, and G. Watt. *Update of Parton Distributions at NNLO*. Phys. Lett., **B652**:292–299, 2007.
- [17] R. L. Jaffe. *G(2): The Nucleon's Other Spin Dependent Structure Function*. Comments Nucl. Part. Phys., **19**:239, 1990.
- [18] Gerhard K. Mallot. *The Spin Structure of the Nucleon from the SMC Experiments*. Habilitation thesis, Universität Mainz, August 1996.
- [19] R. Windmolders. *Review of recent results in spin physics*. Nucl. Phys. Proc. Suppl., **79**: 51–64, 1999.
- [20] A. Airapetian et al. *Measurement of the proton spin structure function $g_1(p)$ with a pure hydrogen target*. Phys. Lett., **B442**:484–492, 1998.
- [21] B. Adeva et al. *Spin asymmetries A_1 and structure functions g_1 of the proton and the deuteron from polarized high energy muon scattering*. Phys. Rev., **D58**:112001, 1998.
- [22] A. Airapetian et al. *First measurement of the tensor structure function b_1 of the deuteron*. Phys. Rev. Lett., **95**:242001, 2005.
- [23] E. S. Ageev et al. *Measurement of the spin structure of the deuteron in the DIS region*. Phys. Lett., **B612**:154–164, 2005.
- [24] V. Yu. Alexakhin et al. *The deuteron spin-dependent structure function $g_1(d)$ and its first moment*. Phys. Lett., **B647**:8–17, 2007.
- [25] P. L. Anthony et al. *Deep inelastic scattering of polarized electrons by polarized He-3 and the study of the neutron spin structure*. Phys. Rev., **D54**:6620–6650, 1996.
- [26] K. Abe et al. *Measurements of the proton and deuteron spin structure functions g_1 and g_2* . Phys. Rev., **D58**:112003, 1998.
- [27] K. Abe et al. *Measurement of the neutron spin structure function $g_2(n)$ and asymmetry $A_2(n)$* . Phys. Lett., **B404**:377–382, 1997.
- [28] P. L. Anthony et al. *Measurement of the deuteron spin structure function $g_1(d)(x)$ for $1-(\text{GeV}/c)^2 < Q^2 < 40-(\text{GeV}/c)^2$* . Phys. Lett., **B463**:339–345, 1999.
- [29] J. Ashman et al. *An investigation of the spin structure of the proton in deep inelastic scattering of polarized muons on polarized protons*. Nucl. Phys., **B328**:1, 1989.

- [30] B. Adeva et al. *Spin asymmetries $A(1)$ of the proton and the deuteron in the low x and low Q^2 region from polarized high energy muon scattering*. Phys. Rev., **D60**:072004, 1999. erratum ibid. Phys. Rev. **D62**, 079902(E) (19yy).
- [31] A. Airapetian et al. *Quark helicity distributions in the nucleon for up, down, and strange quarks from semi-inclusive deep-inelastic scattering*. Phys. Rev., **D71**:012003, 2005.
- [32] K. Ackerstaff et al. *Measurement of the neutron spin structure function $g_1(n)$ with a polarized He-3 internal target*. Phys. Lett., **B404**:383–389, 1997.
- [33] X. Zheng et al. *Precision measurement of the neutron spin asymmetry $A(1)(n)$ and spin-flavor decomposition in the valence quark region*. Phys. Rev. Lett., **92**:012004, 2004.
- [34] W. Vogelsang. *The spin structure of the nucleon*. J. Phys., **G34**:S149–S171, 2007.
- [35] R. L. Jaffe and Aneesh Manohar. *The $G(1)$ Problem: Fact and Fantasy on the Spin of the Proton*. Nucl. Phys., **B337**:509–546, 1990.
- [36] T. Yamanishi. *F and D Values with Explicit Flavor Symmetry Breaking and Δs Contents of Nucleons*. Phys. Rev., **D76**:014006, 2007.
- [37] B. Adeva et al. *A next-to-leading order QCD analysis of the spin structure function g_1* . Phys. Rev., **D58**:112002, 1998.
- [38] J. Bluemlein and H. Bottcher. *QCD analysis of polarized deep inelastic scattering data and parton distributions*. Nucl. Phys., **B636**:225–263, 2002.
- [39] M. Gluck, E. Reya, M. Stratmann, and W. Vogelsang. *Models for the polarized parton distributions of the nucleon*. Phys. Rev., **D63**:094005, 2001.
- [40] M. Hirai, S. Kumano, and N. Saito. *Determination of polarized parton distribution functions and their uncertainties*. Phys. Rev., **D69**:054021, 2004.
- [41] John C. Collins. *Hard scattering in QCD with polarized beams*. Nucl. Phys., **B394**:169–199, 1993.
- [42] C. Bernet. *Caractérisation des Mircomégas et mesure de la polarisation des gluons sur COMPASS*. PhD thesis, Université Paris VII, Denis Diderot, May 2005.
- [43] Jörg Pretz. *At which average gluon momentum fraction x do we probe the polarized gluon distribution $\Delta G/G$?* COMPASS internal note, 2008-3.
- [44] M. Alekseev et al. *Direct Measurement of the Gluon Polarisation in the Nucleon via Charmed Meson Production*. 2008.
- [45] E. S. Ageev et al. *Gluon polarization in the nucleon from quasi-real photoproduction of high- $p(T)$ hadron pairs*. Phys. Lett., **B633**:25–32, 2006.

- [46] B. Adeva et al. *Spin asymmetries for events with high $p(T)$ hadrons in DIS and an evaluation of the gluon polarization*. Phys. Rev., **D70**:012002, 2004.
- [47] A. Airapetian et al. *Measurement of the spin asymmetry in the photoproduction of pairs of high $p(T)$ hadrons at HERMES*. Phys. Rev. Lett., **84**:2584–2588, 2000.
- [48] Brookhaven National Laboratory (BNL). *RHIC*. <http://www.bnl.gov/rhic/>.
- [49] B. I. Abelev et al. *Longitudinal double-spin asymmetry for inclusive jet production in $p+p$ collisions at $\sqrt{s}=200$ GeV*. Phys. Rev. Lett., **100**:232003, 2008.
- [50] A. Adare et al. *Inclusive cross section and double helicity asymmetry for π^0 production in $p+p$ collisions at $\sqrt{s}=200$ GeV: Implications for the polarized gluon distribution in the proton*. Phys. Rev., **D76**:051106, 2007.
- [51] Stephen Scott Adler et al. *Improved measurement of double helicity asymmetry in inclusive midrapidity π^0 production for polarized $p + p$ collisions at $s^{**}(1/2) = 1200$ -GeV*. Phys. Rev., **D73**:091102, 2006.
- [52] B. I. Abelev et al. *Longitudinal double-spin asymmetry and cross section for inclusive jet production in polarized proton collisions at $s^{**}(1/2) = 200$ -GeV*. Phys. Rev. Lett., **97**:252001, 2006.
- [53] Stephen Scott Adler et al. *Mid-rapidity neutral pion production in proton proton collisions at $s^{**}(1/2) = 200$ -GeV*. Phys. Rev. Lett., **91**:241803, 2003.
- [54] John Adams et al. *Forward neutral pion production in $p+p$ and $d+Au$ collisions at $s(NN)^{**}(1/2) = 200$ -GeV*. Phys. Rev. Lett., **97**:152302, 2006.
- [55] Stephen Scott Adler et al. *Measurement of direct photon production in $p + p$ collisions at $s^{**}(1/2) = 200$ -GeV*. Phys. Rev. Lett., **98**:012002, 2007.
- [56] Steven D. Bass and Christine A. Aidala. *Towards an understanding of nucleon spin structure: From hard to soft scales*. Int. J. Mod. Phys., **A21**:4407–4424, 2006.
- [57] J. J. Aubert et al. *Production of charmed particles in 250-GeV μ^+ - iron interactions*. Nucl. Phys., **B213**:31, 1983.
- [58] Johan Alwall. *Quark asymmetries and intrinsic charm in nucleons*. 2005.
- [59] B. W. Harris, J. Smith, and R. Vogt. *Reanalysis of the EMC charm production data with extrinsic and intrinsic charm at NLO*. Nucl. Phys., **B461**:181–196, 1996.
- [60] M. Stratmann and W. Vogelsang. *Photoproduction of jets and heavy flavors at future polarized $e p$ colliders*. Z. Phys., **C74**:641–650, 1997.
- [61] Krzysztof Kurek. *Resolved Photon studies, talk at COMPASS analysis meeting, April 2007*.

-
- [62] M. Derrick et al. *Study of D^{*+-} (2010) production in $e p$ collisions at HERA*. Phys. Lett., **B349**:225–237, 1995.
- [63] Leonid Gladilin. *Charm hadron production fractions*. 1999.
- [64] P. Abbon et al. *The COMPASS Experiment at CERN*. Nucl. Instrum. Meth., **A577**:455–518, 2007.
- [65] N. Doble, L. Gatignon, G. von Holtey, and F. Novoskoltsev. *The Upgraded muon beam at the SPS*. Nucl. Instrum. Meth., **A343**:351–362, 1994.
- [66] N. Takabayashi. *Polarized target for the measurement of the gluon contribution to the nucleon spin in the COMPASS experiment*. PhD thesis, Nagoya University, March 2003.
- [67] Anatole Abragam. *The principles of nuclear magnetism*. International series of monographs on physics. Clarendon Press, Oxford, 1961.
- [68] E. Albrecht et al. *Status and characterisation of COMPASS RICH-1*. Nucl. Instrum. Meth., **A553**:215–219, 2005, and references within.
- [69] E. Albrecht et al. *COMPASS RICH-1*. Nucl. Instrum. Meth., **A504**:354–355, 2003, and references within.
- [70] R. Kuhn. *A Measurement of Spin Asymmetries in Quasi-Real Photo-Production of Hadrons with High Transverse Momentum at COMPASS*. PhD thesis, Technische Universität München, July 2007.
- [71] C. Bernet et al. *The COMPASS trigger system for muon scattering*. Nucl. Instrum. Meth., **A550**:217–240, 2005.
- [72] P. Astbury et al. *MEASUREMENT OF DEEP INELASTIC COMPTON SCATTERING OF HIGH- ENERGY PHOTONS*. Phys. Lett., **B152**:419, 1985.
- [73] M. Adamovich et al. *WA92: A fixed target experiment to trigger on and identify beauty particle decays*. Nucl. Instrum. Meth., **A379**:252–270, 1996.
- [74] W. Bruckner et al. *The Electromagnetic calorimeter in the hyperon beam experiment at CERN*. Nucl. Instrum. Meth., **A313**:345–356, 1992.
- [75] F. Binon et al. *HODOSCOPE MULTI-PHOTON SPECTROMETER GAMS-2000*. Nucl. Instr. Meth., **A248**:86, 1986.
- [76] C. Kurig. *Aufbau, Test und Weiterentwicklung des Triggersystems für das elektromagnetische Kalorimeter ECAL1 des COMPASS-Experiments*. Diploma thesis, Universität Mainz, August 2007.
- [77] V. Kolosov et al. *Present performances of COMPASS electromagnetic calorimetry from data analysis*. COMPASS internal note, 2008-5.

- [78] R. Panknin. *Bau und Installation eines neuen Veto-Detektors am COMPASS-Experiment am CERN*. Diploma thesis, Universität Bonn, December 2006.
- [79] B. et al. Gobbo. *The CORAL web page*. <http://coral.web.cern.ch/coral>.
- [80] Y. et al. Bedfer. *COMPASS's track reconstruction algorithm*. COMPASS internal note, 2004-1.
- [81] V. Yu. Aleksakhin, Y. Bedfer, S. Gerasimov, and A. Yu. Korzenev. *Geometrical event reconstruction in the COMPASS experiment*. Phys. Part. Nucl. Lett., **4**:350–362, 2007.
- [82] R. Fruhwirth. *Application of Kalman filtering to track and vertex fitting*. Nucl. Instrum. Meth., **A262**:444–450, 1987.
- [83] A. A. Lednev. *Electron shower transverse profile measurement*. Nucl. Instrum. Meth., **A366**:292–297, 1995.
- [84] Guenter Baum et al. *RICHONE: A software package for the analysis of COMPASS RICH-1 data*. Nucl. Instrum. Meth., **A502**:315–317, 2003.
- [85] P. Schiavon. *Summary of the main steps of the RICH-1 analysis*. <http://cern.ch/schiavon/rich1/PID/PID.ps.gz>. COMPASS internal note, January 2006.
- [86] S. Panebianco. *Mesure de la polarisation des gluons par l'asymetrie de spin dans la production de mesons charmes*. PhD thesis, Universite Paris XI Orsay, September 2005.
- [87] T. Carli and B. Koblitz. *A multi-variate discrimination technique based on range- searching*. Nucl. Instrum. Meth., **A501**:576–588, 2003.
- [88] Robert Sedgewick. *Algorithms in C*. Addison-Wesley, Reading, MA, 1990.
- [89] N. et al. Doshita. *Target material data of run 2002 and 2003*. COMPASS internal notes, 2003-5 and 2003-8.
- [90] Fritz-Herbert Heinsius and Susanne Koblitz. *COMPASS Luminosity for 2002-2004*. COMPASS internal note, 2006-5.
- [91] S. Trippel. *Aufbau einer Messeinrichtung zur Bestimmung des Myonenflusses bei COMPASS*. Diploma thesis, Universität Freiburg, March 2005.
- [92] M. von Hodenberg. *First measurement of the gluon polarisation in the nucleon using D mesons at COMPASS*. PhD thesis, Universität Freiburg, November 2005.
- [93] G. Ingelman, J. Rathsman, and G. A. Schuler. *AROMA 2.2 - A Monte Carlo Generator for Heavy Flavour Events in ep Collisions*. Comput. Phys. Commun., **101**:135–142, 1997.
- [94] A. Aktas et al. *Inclusive production of D^+ , D^0 , D/s^+ and D^{*+} mesons in deep inelastic scattering at HERA*. Eur. Phys. J., **C38**:447–459, 2005.

-
- [95] A. Aktas et al. *Inclusive D^{*+-} meson cross sections and D^{*+-} jet correlations in photoproduction at HERA*. Eur. Phys. J., **C50**:251–267, 2007.
- [96] B.Naroska V. Blobel, A. Meyer. *Elementarteilchenphysik (in german)*. Notizen zur Vorlesung, 2002.
- [97] Jörg Pretz. *The Gluon Polarization in the Nucleon from the COMPASS Experiment*. Habilitation thesis, Universität Bonn, April 2007.
- [98] J.-M. Le Goff. *Asymmetry extraction*. COMPASS internal note, 2004-3.
- [99] Jörg Pretz. *A New Method for Asymmetry Extraction*. COMPASS internal note, 2004-11.
- [100] F. James and M. Roos. *Minuit: A System for Function Minimization and Analysis of the Parameter Errors and Correlations*. Comput. Phys. Commun., **10**:343–367, 1975.
- [101] Jörg Pretz. *Asymmetry Extraction in Presence of a Polarized Background*. COMPASS internal note, 2005-12.
- [102] K. Kondo et al. *Polarization measurement in the COMPASS polarized target*. Nucl. Instrum. Meth., **A526**:70–75, 2004.
- [103] B. Adeva et al. *Measurement of the polarization of a high-energy muon beam*. Nucl. Instrum. Meth., **A343**:363–373, 1994.
- [104] D. Adams et al. *Measurement of the SMC muon beam polarisation using the asymmetry in the elastic scattering off polarised electrons*. Nucl. Instrum. Meth., **A443**:1–19, 2000.
- [105] Kenneth Gustafsson. *Computation of the Dilution Factor for the Year 2002 COMPASS Data*. COMPASS internal note, 2003-3.
- [106] Alessandro Bravar, Krzysztof Kurek, and Roland Windmolders. *POLDIS: A Monte Carlo for polarized (semi-inclusive) deep inelastic scattering*. Comput. Phys. Commun., **105**:42–61, 1997.
- [107] G. Brona. *Hadron production and polarisation of gluons in the nucleon in $\mu-N$ interactions in the COMPASS experiment at CERN*. PhD thesis, Warsaw University, 2007.
- [108] Torbjorn Sjostrand. *High-energy physics event generation with PYTHIA 5.7 and JETSET 7.4*. Comput. Phys. Commun., **82**:74–90, 1994.
- [109] M. Stolarski. *Spin structure of the nucleon at low x and low Q^2 in the COMPASS experiment at CERN*. PhD thesis, Warsaw University, 2006.
- [110] Florent Robinet J.-M. Le Goff, J.Pretz. *Systematic Error due to False Asymmetries in the Open Charm Measurement*. COMPASS internal note, 2008-4.

- [111] Marcin Stolarski. *Measurement of Delta G/G from high transverse momentum hadron pairs in COMPASS*. 2008.
- [112] P. Liebing. *Extraction of Delta(g)/g from HERMES data on inclusive charged hadrons*. AIP Conf. Proc., **915**:331–334, 2007.
- [113] F. Robinet. PhD thesis, in preparation, 2008.
- [114] Daniel de Florian, Rodolfo Sassot, Marco Stratmann, and Werner Vogelsang. *Global Analysis of Helicity Parton Densities and Their Uncertainties*. 2008.